

Symmetric Grey Box Identification and Distributed Beam-Based Controller Design for Free-Electron Lasers

Vom Promotionsausschuss der
Technischen Universität Hamburg-Harburg
zur Erlangung des akademischen Grades
Doktor-Ingenieur (Dr.-Ing.)
genehmigte Dissertation

von
Sven Pfeiffer

aus
Finsterwalde

2014

Gutachter: Prof. Dr. Herbert Werner
Prof. Dr.-Ing. Gerwald Lichtenberg
Dr. Holger Scharb

Vorsitzender des Prüfungsausschusses: Prof. Dr.-Ing. Arne Jacob

Tag der mündlichen Prüfung: 11.02.2014

Für Kathleen

Jede Lösung eines Problems ist ein neues Problem.
(Johann Wolfgang von Goethe)

Abstract

The European X-ray Free-Electron Laser (XFEL) at the *Deutsches Elektronen Synchrotron* (DESY) in Hamburg will, starting in 2015, open up completely new research opportunities for scientist and industrial users by exploiting ultrashort X-ray laser pulses. Bunches of electrons are accelerated by a radio frequency field inside superconducting cavities up to an energy of 17.5 GeV. A periodic arrangement of magnets forces the accelerated electrons onto a tight slalom path leading to a process in that the electrons emit extremely short and intense X-ray flashes. The generation of equidistant X-ray flashes with a constant intensity requires an extremely high precision field control in combination with beam-based signals. FLASH, which can be seen as a pilot test facility, allows to develop and test controller concepts even before the European XFEL is in operation.

In this thesis it is shown that a physical white box model structure, which describes the behavior of each subsystem within the radio frequency field control loop, obeys as first-order approximation the special orthogonal group of dimension two ($SO(2)$). Presented is a grey box identification approach, which combines the physical model structure with general identification methods. The accelerator modules are operated in a pulsed mode. Thus, the excitation of the system and therefore the identification of the input-output behavior is only possible within a short time period. Developed is an adaptive identification approach with a specified $SO(2)$ symmetric model structure. The proposed controller design strategy fulfills the requirements of a high precision field performance. Adapting the feedforward signal by using an iterative learning control (ILC) algorithm reduces remaining repetitive field errors from pulse to pulse. It is shown, that exploiting the $SO(2)$ symmetric structure and using the developed tensor based ILC representation simplifies the feedforward update computation. Magnetic chicanes, so-called bunch compressors, are used for a longitudinal compression of the electron bunches. Depending on the beam energy distribution, the electrons travel on different trajectories through the bunch compressor. This allows to control the mean beam energy and energy distribution to minimize the bunch arrival time and bunch compression error at the expense of a non-constant beam energy. Besides controlling the latter beam-based signals, a distributed control scheme is presented which minimizes beam energy variations by an information exchange with neighboring controller modules, leading to an improvement of the beam energy performance.

The presented results were achieved and measurements were carried out at FLASH. Further important plant upgrades for the XFEL project are a completely new hardware platform, providing a higher sampling rate and measurement precision. The proposed system identification and controller approaches have been validated experimentally and in simulation for both hardware platforms.

Zusammenfassung

Der Europäische Röntgenlaser XFEL des Deutschen Elektronen Synchrotron (DESY) in Hamburg ist eine Röntgenquelle zur Erzeugung ultrakurzer Laserlichtblitze. Diese wird ab dem Jahr 2015 einzigartige Forschungsmöglichkeiten eröffnen. Elektronen werden in Paketen mittels eines Hochfrequenzfeldes bis zu einer Energie von 17.5 GeV beschleunigt. Anschließend senden die Elektronenpakete laserartig gebündelte Strahlung aus, indem diese durch eine besondere Magnetanordnung auf einen Slalomkurs gezwungen werden. Die Regelung der Ankunftszeit und Dichte der Elektronenpakete und dementsprechend die Erzeugung abstands- und intensitätsgleicher Röntgenlaserblitze erfordert die Kombination einer hochpräzisen Regelung des Hochfrequenzfeldes innerhalb der supraleitenden Hohlraumresonatoren mit zusätzlichen Strahlinformationen. FLASH, der als Pilotanlage des XFEL betrachtet werden kann, ermöglicht es die notwendigen Regelungskonzepte bereits vor der Fertigstellung des XFEL zu testen.

Im Rahmen dieser Arbeit wird gezeigt, dass die Kombination des physikalischen Verhaltens der einzelnen Komponenten innerhalb der Regelungsschleife einer speziellen orthogonalen Gruppe ($SO(2)$) gehorcht. Basierend auf der Modellierung des Gesamtsystems wird gezeigt, wie das System mittels eines $SO(2)$ symmetrischen modelbasierten Ansatzes in allen Frequenzbereichen identifiziert werden kann. Die Beschleunigungsmodule werden im gepulsten Modus betrieben, welches die Identifikation des Systems lediglich in einem kleinen Zeitintervall ermöglicht. Das daraufhin entwickelte symmetrische Regelungskonzept erfüllt die Anforderungen an eine hochpräzise Regelung des Hochfrequenzfeldes. Wiederkehrende Feldfehler von Puls zu Puls werden minimiert, indem ein iterativ lernender Algorithmus die Vorsteuerung der Beschleunigungsmodule anpasst. Dieser Algorithmus konnte durch die Ausnutzung des $SO(2)$ symmetrischen Systemverhaltens und mittels einer Tensor Darstellung vereinfacht werden. Um die geforderte Intensität des Laserlichts zu erzielen, werden magnetische Schikanen zur longitudinalen Kompression der Elektronenpakete eingesetzt. Abhängig von der Energieverteilung innerhalb eines Elektronenpaketes, legen die Elektronen einen unterschiedlich langen Weg innerhalb dieser Schikane zurück. Demzufolge führt eine Elektronenenergieanpassung vor einer Schikane zu der Möglichkeit die Ankunftszeit und Kompression der Elektronen zu regeln. Es wird gezeigt, dass die Vereinigung der strahlbasierten Messdaten mit dem Hochfrequenzfeld zu einer Verbesserung der Ankunftszeit und Kompression der Elektronenpakete führt. Durch diese Energiemodulation ist es notwendig die Endenergie der Elektronenpakete anzupassen. Ein verteiltes Regelungskonzept wurde entwickelt, welche es ermöglicht diese Energievariationen modelbasiert mittels der Kommunikation benachbarter Regelungsmodule zu minimieren.

Die gezeigten Ergebnisse und Messungen wurden am FLASH durchgeführt. Die verwendete Hardware am FLASH ist während der Entstehung dieser Arbeit weiterentwickelt worden. Parallel wurde die Umsetzbarkeit der entwickelten Konzepte unter Verwendung der neuen Hardware experimentell anhand von Messdaten und in Simulationen validiert.

Contents

1	Introduction	1
1.1	Motivation and Objectives	1
1.2	Scope and Contribution	2
1.3	Structure of this Thesis	3
2	Free-Electron Lasers	5
2.1	European XFEL	5
2.2	Free-Electron Laser FLASH	7
2.3	Overview of an RF Station	7
2.4	Beam-Based Measurements	12
2.5	SASE Process and Pump-Probe Experiment	14
2.6	Sources of Perturbations	15
3	System Identification	17
3.1	RF Field Modeling	18
3.1.1	Introduction	18
3.1.2	Grey Box Modeling with SO(2) Symmetric Structure	23
3.1.3	Example at FLASH	28
3.1.4	SO(2) Symmetry Validation	38
3.2	Beam Modeling	42
3.2.1	Bunch Compressor	42
3.2.2	Example at FLASH	44
3.3	Combination of RF Field and Beam Model	46
3.4	Conclusion	48
4	RF Field Controller Design	49
4.1	RF Field Feedback Controller	50

4.1.1	Introduction	50
4.1.2	General Approach	51
4.1.3	Example at FLASH	55
4.2	Iterative Learning Control	65
4.2.1	Introduction	66
4.2.2	Norm Optimal ILC for SO(2) Symmetric Systems	67
4.2.3	Norm Optimal Tensor ILC (NO-T-ILC)	71
4.3	Conclusion	79
5	Beam-Based Feedback	81
5.1	Bunch Arrival Time and Compression Control	81
5.1.1	Beam-Based Controller Design	82
5.1.2	Example at FLASH	86
5.2	Beam Energy Control with Information Exchange	97
5.2.1	Introduction	97
5.2.2	Distributed Controller Design	99
5.2.3	Simulation Results for XFEL	110
5.2.4	Outlook - Communication Delays	114
5.3	Conclusion	116
6	Summary and Outlook	117
6.1	Outlook	118
A	Introduction Lie Groups and Subgroup SO(2)	121
B	3rd Harmonic RF Module at FLASH	123
B.1	Phase Space Linearisation	123
B.2	Modeling the 3rd Harmonic RF Module	125
C	Iterative Learning Control - Proofs	127
D	Amplitude/Phase to I/Q Linearisation	131
E	Introduction to Distributed Control	133
F	Symbols and Abbreviations	137
	Bibliography	141

Chapter 1

Introduction

1.1 Motivation and Objectives

A device in which charged particles are accelerated on a linear path by a time-dependent electromagnetic field is called linear accelerator, [Wangler, 1998]. Linear acceleration was first mentioned by G. Ising in 1924, [Ising, 1925]. The first experimental test by R. Wideröe in 1928, [Wideröe, 1928], is the forerunner of today's linear accelerators. During this time acceleration frequencies in the megahertz range were used, not suitable to accelerate light particles such as electrons, since the distances between acceleration gaps would be impracticably large. Nevertheless, with the development of high-frequency power generators in the gigahertz range and new efficient accelerating structures the first modern linear accelerators were born and over years their number has grown continuously. The fundamentals of Free-Electron Lasers (FELs), i.e. acceleration of electrons and the energy transfer to light flashes by a stimulated emission of synchrotron radiation in a periodic magnetic field, was invented by J. Madey in 1971, [Madey, 1971]. The first stimulated emission of radiation by relativistic electrons in a periodic magnetic field has been observed in 1975 with a wavelength of about 11 μm , [Elias et al., 1976]. The first FEL oscillator with a spontaneous radiation emitted by the electron beam was operated with a wavelength of about 3.4 μm in 1977, [Deacon et al., 1977]. Enormous improvements have been done in this scientific field over the last few decades. Currently FELs generate laser light with a wavelength down to X-ray range of 0.1 nm (1 \AA) by the self-amplified spontaneous emission (SASE) process from a high-energy electron beam. This has been demonstrated at various linear accelerators, e.g. at the Stanford Linear Accelerator Center (SLAC) by using normal conducting accelerator modules. Since 2004 the free-electron laser facility FLASH in Hamburg, a former project of the TeV-Energy Superconducting Linear Accelerator (TESLA) collaboration for research with superconducting accelerator modules, delivers soft X-ray radiation as an user facility.

Scientists and researchers from all over the world appreciate the FEL pulses which can be as short as 10 fs, with a peak brilliance up to 10^{33} photons/s/mrad²/mm²/(0.1% bandwidth) and a high transverse coherence, [XFEL, 2013]. Achieving a stable and reliable production of X-ray laser pulses with a pulse-duration in the femtosecond timescale im-

poses completely new demands. Perturbations, e.g. acceleration field errors in amplitude and phase, can cause undesired fluctuations of the electron beam peak-current, longitudinal charge fluctuations and variations in the arrival time of the electron beam at the end of the linear accelerator section. The work of this thesis includes strategies to control the beam directly by adjusting the radio frequency field inside the accelerator modules. This includes controlling the bunch arrival time to guarantee equidistant light pulses, the bunch compression to ensure a constant peak brilliance and the beam energy leading to the same laser light wavelength for each electron bunch.

1.2 Scope and Contribution

In parallel to the improvements of linear accelerators, several publications are available which collect an amount of physical system descriptions. In this thesis it is shown how the physical insight can be exploited not only in the system identification, e.g. the fact that the acceleration field, which is used to control the beam properties, displays certain symmetries, i.e. *special orthogonal group of dimension two*, [Gilmore, 1974]; as short hand notation $SO(2)$, an introduction to this special Lie group is given in Appendix A. The work of this thesis is motivated by the demand of high quality laser flashes, Section 1.1, and symmetric systems, which has been shown as an advantage in many contexts, e.g. the behavioral framework, [Fagnani and Willems, 1991]. A more general nonlinear case for an identification of a symmetric oscillator network model is described in [Barany, 2001]. Multi-input multi-output systems with a similar symmetry have also been investigated before, see [Jugo and Arredondo, 2005]. This thesis presents a systematic system identification and controller design by making use of the symmetric plant properties, reaching a high performance electron beam. The contributions are summarized as follows:

- Systematic system identification of linear time-invariant models with the focus on $SO(2)$ symmetric plant behavior and the ability to block-wise extend the internal model structure such that additional eigenvalues can be identified independently.
- Interconnection of beam-based signals to RF field properties, a necessary condition for optimal beam control.
- Fixed order discrete-time controller design strategy by exploiting the $SO(2)$ symmetric plant and reliable optimal controller synthesis.
- Integration of beam-based signals within a lumped RF field controller design to control the arrival time and compression of electron bunches.
- Interaction of neighboring controller units within a distributed observer based control scheme to ensure a high beam energy performance.
- Simplification regarding iterative learning control (ILC) algorithm usable for $SO(2)$ symmetric plant models.
- Streamline the norm optimal ILC by using tensor representation.

1.3 Structure of this Thesis

This thesis is structured as follows: Chapter 2 introduces the free-electron lasers, which are a part of this thesis, at DESY in Hamburg. First, an overview of the European XFEL and FLASH is given. A more detailed description of an RF station, the considered beam related measurements, the SASE process and possible sources of beam perturbations conclude this chapter. The system identification problem is addressed in Chapter 3 and separated in an RF field and beam model. It is shown, that the main RF field system dynamics obeys a special orthogonal group symmetry, which connects physical modeling with a mathematical identification problem. The second part covers the beam model which includes the bunch arrival time and bunch compression. The interaction between the RF field and beam models are outlined in the third part. In the following, each chapter is finalized by a conclusion. Based on the mathematical description of the RF field model, a systematic RF field controller design is presented in Chapter 4. The RF field controller needs to be optimized to guarantee an optimal RF field performance. In addition, simplifications of the used norm optimal iterative learning control algorithm, which improves the feedforward drive to cope with repetitive errors, are given: On the one hand by exploiting the RF field symmetry and on the other hand by rewriting the algorithm by tensors. Chapter 5 considers the interconnection of beam-based signals to the RF field controller to improve the beam performance. This chapter is separated into two parts depending on the location of action. First, control strategies to improve the performance for the bunch arrival time and bunch compression, which can only be controlled within the first part of a linear accelerator, are given and compared to each other. The second part of a linear accelerator increases the beam energy up to a desired value. It will be shown that interconnections of the RF controllers are necessary to ensure high beam energy performance. Firstly, the beam energy may be corrupted by controlling the beam-based signals within the first acceleration part. Secondly, additional events affecting the control variable are discussed and a strategy of an interconnected control scheme is presented, which helps to improve the beam energy performance. Finally, Chapter 6 summarizes the results and discusses the directions for future developments.

Chapter 2

Free-Electron Lasers

This chapter gives an overview of the European XFEL and FLASH at DESY. Both free-electron lasers (FELs) are linear accelerators, while FLASH is currently in operation and the European XFEL is under construction. The main function of FELs is to generate thousands of X-ray flashes per second with an outstanding brilliance. The considered FELs are equipped with superconducting cavities, operated at around 2 Kelvin, which accelerate electron bunches almost to speed of light. At the end of the main acceleration section, the electron beam energy is transferred to X-ray flashes, which allows scientists from all over the world to e.g. map atomic details of viruses or take three dimensional movies of the nanoworld.

How this exactly works is briefly outlined in the following sections. First an introduction to the European XFEL and FLASH is given in Section 2.1 and Section 2.2, respectively. Section 2.3 points out the details and current state of the low level radio frequency (LLRF) system, used to control the radio frequency (RF) field inside the cavities. The used beam-based signals within this thesis are briefly discussed in Section 2.4. The process of converting an electron beam into X-ray flashes and an example of using the latter is outlined in Section 2.5. Possible perturbations which act as disturbances on the beam quality are discussed in the last section.

2.1 European XFEL

During the time of writing, the European XFEL, an **X**-ray **F**ree-**E**lectron **L**aser for research with X-ray flashes, is under construction with a total length of 3.4 km. The basic layout is depicted in Figure 2.1.1, initially defined in [Brinkmann et al., 2002] and [Altarelli et al., 2006]; parts are frequently updated by [FEL Beam Dynamics Group, 2013]. Within this thesis the latest XFEL layout version is used. Nevertheless, further changes will not have an impact on the developed system identification and controller design strategies.

The first 1.7 km section of the XFEL accelerates the electrons and can be separated into four linear acceleration (Linac) parts. Within the Injector 1, an RF Gun together with an accelerator module I1 and a third harmonic module A3H are used to optimize the

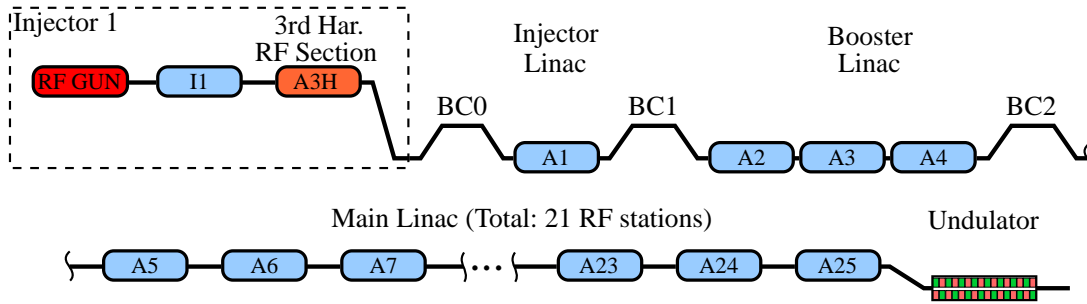


Figure 2.1.1: Basic overview of the European XFEL.

longitudinal phase space (Appendix B.1) and to accelerate the electrons to a beam energy of about 120 MeV. The electron bunch length is reduced by a bunch compressor BC0. The *Injector Linac* consists of the accelerator module A1. The bunch compressor BC1 compresses the electron bunch at an energy of 500 MeV by a factor of about 20. The *Booster Linac* further accelerates the electrons up to 2 GeV, followed by an additional bunch compressor BC2, which compresses the bunch by a factor of about five. Hence, an electron bunch leaving the RF Gun with an initial length of about 2 mm (rms) is compressed by a factor of 100, i.e. to a bunch length of 0.02 mm (rms) to achieve a peak current of about 5 kA. The *Main Linac* increases the bunch energy to a maximum final value of 17.5 GeV. Eventually, the electron bunch enters the Undulator part introduced in Section 2.5. A further detailed description can be found in [Altarelli et al., 2006].

After the main linac, the electron beam generates laser light by e.g. the SASE process, see Section 2.5 for a short introduction. This part is not considered within this thesis, since the main focus is on controlling the accelerator modules and the electron beam itself.

The European XFEL is constructed underground in a tunnel, depicted in Figure 2.1.2. The hardware driving each accelerator module, see Section 2.3, must fulfill the requirement

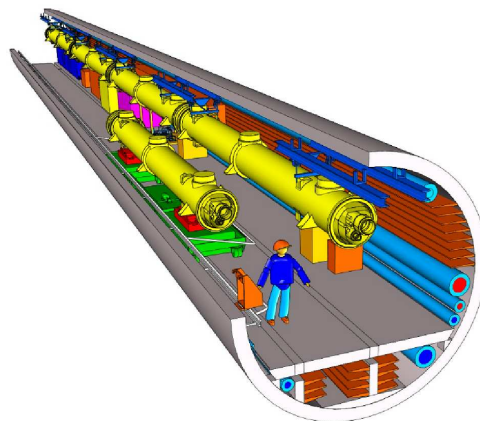


Figure 2.1.2: Layout of the linac tunnel, including the accelerator modules (yellow) and roughly the tunnel diameter, [Altarelli et al., 2006].

to be placed into the tunnel, more precisely below the accelerator modules. New hardware with a smaller form factor is developed, based on *Micro Telecommunications Computing*

Architecture standard; in the following called *MTCA system* [MTCA.4, 2013]. The basic improvements compared to the old hardware, based on *Versa Module Eurocard* standard in the following called *VME system*, are given in Section 2.3.

2.2 Free-Electron Laser FLASH

The **F**ree-**e**lectron **L**ASer in **H**amburg (FLASH) is a smaller version of the European XFEL and can be seen as pilot test facility. The basic layout is depicted in Figure 2.2.1. Especially the first part is very similar to the XFEL injector and booster section. First, the

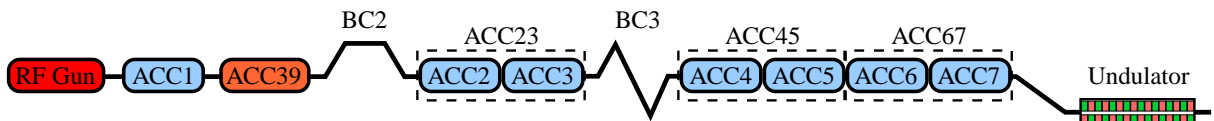


Figure 2.2.1: Basic overview of FLASH, a more detailed sketch can be found in [FLASH, 2013].

electrons are pre-accelerated by the RF Gun, followed by the accelerator module ACC1. The longitudinal phase space is optimized by a third harmonic module ACC39, operated at a 3 times higher frequency than ACC1. A bunch compressor, for historical reasons BC2, reduces the bunch length and the module ACC23, consisting of ACC2 and ACC3, further accelerates the electrons. The second bunch compressor BC3 further reduces the bunch length and the following accelerator modules accelerate the electrons up to their final energy of maximum 1.25 GeV, corresponding to a laser light wavelength of 4.12 nm, [FLASH, 2013].

2.3 Overview of an RF Station

The main components of the RF Station can be found in Figure 2.3.1 and will be outlined in the following. They are distributed in physical parts, i.e. master oscillator, vector modulator, klystron, waveguide, cavities, pickup antenna, down converter unit, analog-digital converters (ADC), digital-analog converters (DAC), and software components, i.e. calibration unit, setpoint, feedforward, which is corrected by an iterative learning control algorithm, and the MIMO controller.

The operation of the system can roughly be described as follows: The master oscillator provides a constant RF signal at 1.3 GHz. Within the vector modulator amplitude and phase of this signal is modulated by control signals, before it is amplified with the klystron and distributed inside a waveguide system to the cryomodule hosting eight cavities, i.e. the accelerator modules. The latter are resonators supporting standing electromagnetic waves of the same frequency. To measure the RF fields inside the cavities, each of them contains a pickup antenna. This signal is down-converted by a mixer from 1.3 GHz to an intermediate frequency (IF) and sampled by an ADC, either by an I/Q or

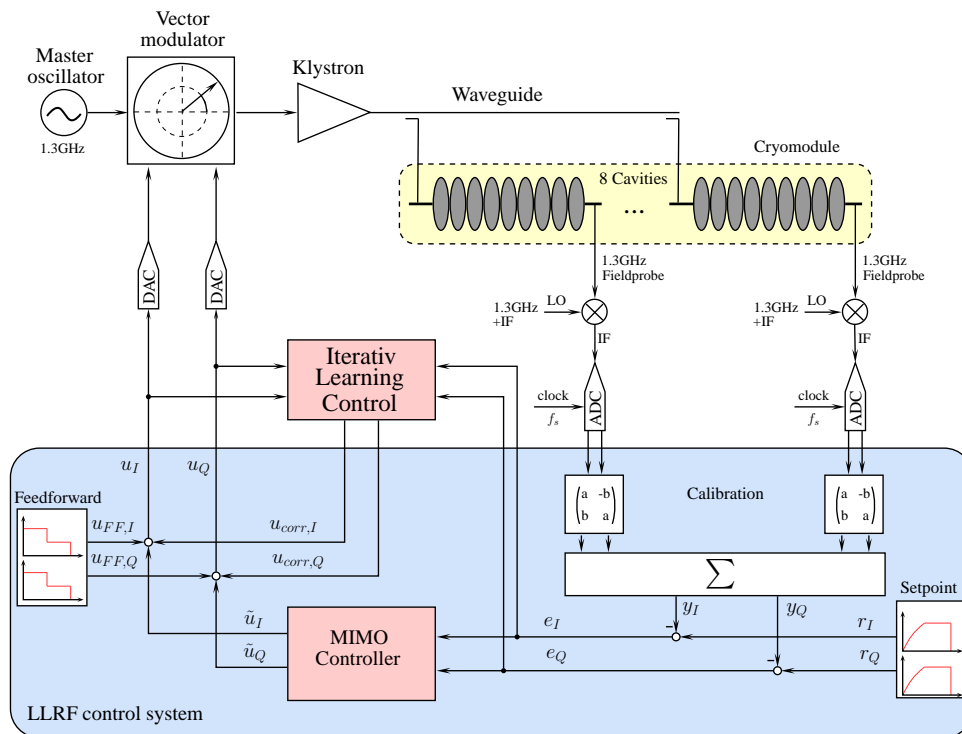


Figure 2.3.1: Signal flow for an RF Station and the associated LLRF control system.

so-called non-I/Q sampling scheme, [Hoffmann, 2008]. The electric field vector is decomposed in its real part I and imaginary part Q , and processed by the control hardware. The indices I and Q denote 'in-phase' and 'quadrature', a common notation not only in accelerator physics. The signals from the cavities enter a software module inside a Field Programmable Gate Array (FPGA). The main advantage of this is parallel, high speed data processing and the possibility of reconfiguration without hardware changes. Since the measurement equipment is very sensitive to cable movements or different cable lengths, a calibration of the signals is necessary. This is done by rotating the measured field vector of each cavity and processing their sum, because only one actuator drives 8 cavities for economic reasons. Finally, the system outputs y_I , y_Q are subtracted from the setpoints r_I , r_Q and the resulting error enters the multi-input multi-output (MIMO) controller. At the controller output a feedforward signal is added. The linear accelerator is operated in a pulsed mode, hence it is straightforward to minimize repetitive errors by an iterative learning control algorithm, which updates the feedforward signal between the pulses, [Kirchhoff et al., 2008]. Finally the system input signals u_I , u_Q are converted to an analog signal and applied to the vector modulator. Thus, the controller can change the amplitude and phase of the frequency provided by the master oscillator.

The requirements for controlling the RF fields are determined by the X-ray pulses generation, Section 2.5. The relative energy spread $\Delta E/E$ from bunch to bunch and pulse to pulse should be in the order of 10^{-4} at the end of the acceleration section. When an electron beam transverses an undulator, it emits radiation corresponding to a photon

wavelength of

$$\lambda_P = \frac{\lambda_u}{2\gamma^2} \left(1 + \frac{K^2}{2} \right), \quad (2.3.1)$$

with an undulator periodic length λ_u , the relativistic Lorentz factor γ and an undulator specific parameter K , which is in the order of one [Schmüser et al., 2008]. The relativistic factor γ is the ratio between the electron energy E and electron energy at rest E_0

$$\gamma = \frac{E}{E_0} \quad \text{with} \quad E = \gamma m_e c^2 = \gamma E_0,$$

where $E_0 = 0.511$ MeV. The first derivative of photon wavelength (2.3.1) is

$$\frac{\partial \lambda_P}{\partial \gamma} = -\frac{\lambda_u}{\gamma^3} \left(1 + \frac{K^2}{2} \right) \quad (2.3.2)$$

and the emitted photon energy spread can be written as

$$\frac{\partial \lambda_P}{\lambda_P} = -2 \frac{\partial \gamma}{\gamma} = -2 \frac{\partial E}{E}. \quad (2.3.3)$$

Example Assume a maximum relative spectral width of $5 \cdot 10^{-4}$ (FWHM) for relative photon wavelength deviation. The relationship $\text{FWHM} = 2\sqrt{2 \ln(2)} \sigma$ for Gaussian distribution is used to compute the maximum standard deviation as $\sigma = 2.1 \cdot 10^{-4}$. To achieve this photon wavelength stability, a relative beam energy stability at the end of an accelerator of about 0.01 % must be guaranteed, e.g. a beam energy variation of maximum 1.75 MeV at final beam energy of 17.5 GeV for XFEL.

Therefore an RF control system is used to regulate the fields in a disturbed environment.

The main differences between the hardware of the MTCA and VME system can be found in Table 2.1.

Table 2.1: Differences VME and MTCA system

	VME system	MTCA system
Intermediate Frequency (IF)	250 kHz	54 MHz
Sampling Frequency (f_S)	81 MHz	81 MHz
Sampling Method	I/Q	non-I/Q
Decimated Sampling Rate	1 MHz	9 MHz
ADC Resolution	14 bit	16 bit
Cryomodules per RF station	1 or 2	1 or 4

Most of the previously described parts are discussed in detail in several publications and the interested reader is referred to e.g. [Schilcher, 1998] and [Schmidt, 2010]. In the following, an introduction to the pulsed mode operation and the cavity is given.

Pulsed Mode Operation To reach a high beam energy, FLASH and later XFEL are operated in a pulsed mode with an usual repetition rate of 10 Hz, [Altarelli et al., 2006]. A typical pulse pattern is divided into three stages, as shown in Figure 2.3.2, which are *filling*, *flat-top* and *decay*. At first, the power is increased in the filling phase in order to

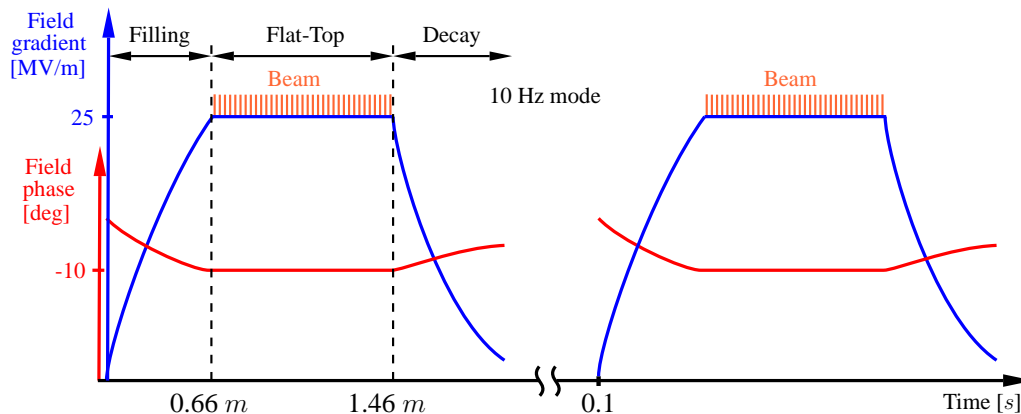


Figure 2.3.2: Example of pulsed operation with 10 Hz repetition rate, 660 μs filling and 800 μs flat-top.

reach a desired level of field gradient. In the following flat-top phase, electron bunches are injected. This is the most important step, in which the field gradient has to be kept constant. At the end of the flat-top phase, power is turned off to avoid overheating and the gradient decays until the next pulse starts.

Cavity A cavity, i.e. a resonator, is used to accelerate the electrons. One can imagine it as a hollow tube consisting of nine cells as presented in Figure 2.3.3. Into this, electromag-

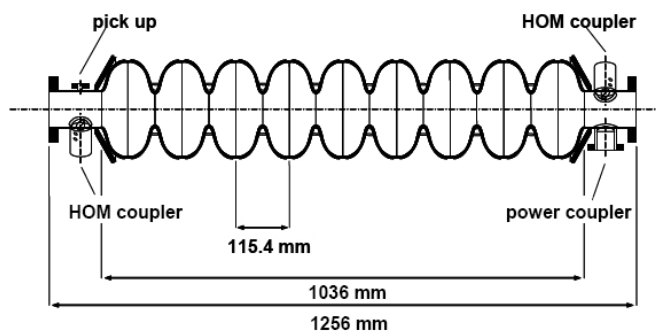


Figure 2.3.3: Cavity with the main power coupler port, the pick up probe, and two higher order mode couplers [Altarelli et al., 2006].

netic energy in form of microwaves at about 1.3 GHz is injected through a power coupler, which is the connection part between the waveguide system and the cavity. The coupling factor can be adjusted inside the power coupler by moving an antenna in a certain range.

As a result of the cavity geometry, the cavities can house different modes of the electromagnetic field applied, see Table 2.2 for frequency location of the fundamental modes.

Table 2.2: Fundamental cavity modes, [Vogel, 2007]

Fundamental mode	Mean eigenfrequency of 116 cavities
π	$f_{\pi} = (1\,300\,444 \pm 303)$ kHz
$8/9 \pi$	$f_{\pi} - (785 \pm 51)$ kHz
$7/9 \pi$	$f_{\pi} - (3\,053 \pm 94)$ kHz
$6/9 \pi$	$f_{\pi} - (6\,501 \pm 157)$ kHz
$5/9 \pi$	$f_{\pi} - (10\,694 \pm 243)$ kHz
$4/9 \pi$	$f_{\pi} - (15\,122 \pm 347)$ kHz
$3/9 \pi$	$f_{\pi} - (19\,237 \pm 430)$ kHz
$2/9 \pi$	$f_{\pi} - (22\,594 \pm 503)$ kHz
$1/9 \pi$	$f_{\pi} - (24\,773 \pm 543)$ kHz

The electric component of that field is responsible for the acceleration of the injected electron bunches. It is intended to transfer as much energy as possible from the field to the electrons; an optimal mode, i.e. π -mode, is shown in Figure 2.3.4. The arrows indicate

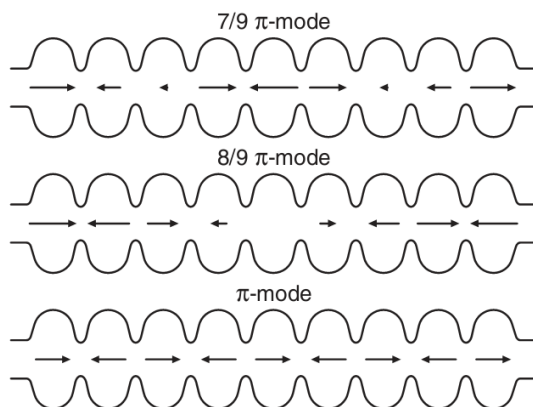


Figure 2.3.4: Cut through a cavity with electric field vectors as example for the π -mode, used for acceleration, and other unwanted fundamental modes, e.g. $8/9 \pi$ -mode and $7/9 \pi$ -mode, [Vogel, 2007].

the electrical component of the RF field in direction of the electron movement and the length indicates the field amplitude. The cavity geometry is such that the π -mode optimally accelerates a relativistic electron beam. This mode shows equal field amplitudes in all cells with changing signs proceeding from cell to cell. While the electron bunches pass from cell to cell, the sign of the field amplitude changes synchronously, leading to beam acceleration over the full cavity length. Beside the fundamental π -mode, several other fundamental modes are present, i.e. $1/9 \pi$ -mode up to the $8/9 \pi$ -mode; an example is depicted in Figure 2.3.4.

The electromagnetic field lines of an ultrarelativistic electron bunch, traveling through a perfectly conducting cylindrical pipe, move together with the particle. Changes of the geometry, e.g. of the cells of a cavity, lead to electromagnetic field lines, generated by the

charge, behind the electrons. When the beam tube narrows again, so-called wake fields occur, i.e. reflections of the field. But even without geometry changes, wake fields can grow up when the beam tube walls have a finite resistivity. An electron following the first one is affected by those fields which may change its energy or result in an orbit deflection, for further details see [Baboi, 2001].

To reduce the effect of wake fields, each cavity is equipped with higher order mode (HOM) couplers, shown in Figure 2.3.3, whereby the stored energy of the HOMs is extracted. Without going into the detail, two HOM couplers, which are adjusted to minimize the energy extraction of the π -mode, are used to reduce the higher order mode effects. Since those are optimized to the π -mode, the additional fundamental modes, e.g. $8/9 \pi$ -mode, may be attenuated by the HOM couplers and the RF field pick up detects a reduced influence of these modes, [Baboi, 2013] and [Vogel, 2013].

2.4 Beam-Based Measurements

In the following, the focus is on beam-based measurements which are used to directly control the electron bunch. A short introduction to each measurement device is given, and further information can be found in the mentioned references.

Bunch Arrival Time Monitor

To measure time-of-flight variations, a bunch arrival time monitor (BAM) has been developed, [Löhl, 2009] and further improved [Bock, 2012]. The operation principle comprises the measurement of the bunch arrival time relative to the optical timing reference (reference laser pulse), which is provided by actively length-stabilized fibre-links of the optical synchronization system. The basic detection scheme is shown in Figure 2.4.1.

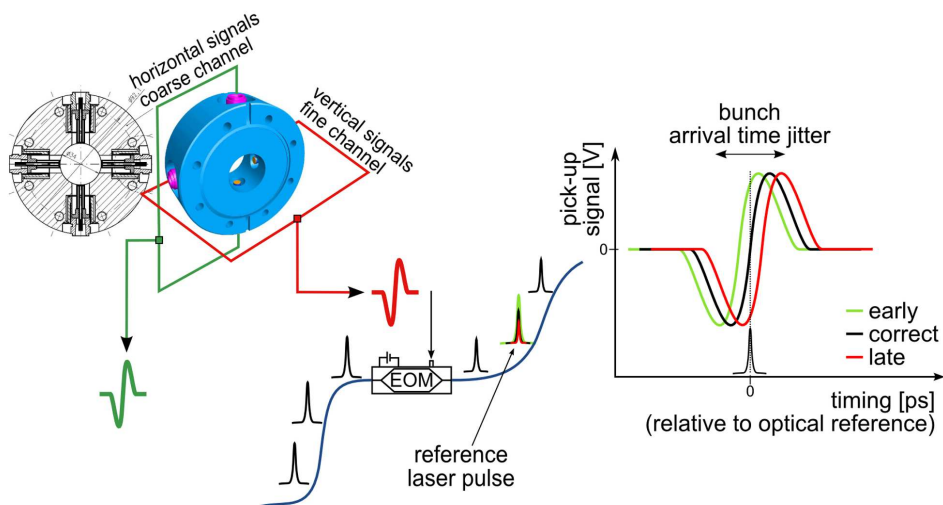


Figure 2.4.1: BAM principle [Bock, 2012].

The upper left side shows the pick-up system which is installed in the beamline. Feed-troughs in the horizontal and vertical plane couple out the beam-induced transient signal which, in both planes, is merged from two opposing antennas into one channel. One is used for high resolution but has only a small temporal dynamic range in the order of a few pico-seconds, the other is utilized for a large dynamic range; i.e. the fine and coarse channel, respectively. The resulting bipolar signals are used to modulate reference laser pulses in amplitude by an electro-optical modulator (EOM). Arrival time changes of the voltage zero-crossing relative to the optical reference are transferred into an amplitude modulation which is detected. Especially the fine channel with a resolution of a few femto-seconds is highly suitable for controlling the bunch arrival time.

Bunch Compression Monitor

Electron bunches are accelerated to ultrarelativistic energies by the first accelerator module. In order to produce photon pulses with a few tens of femto-second duration, the electron bunch is longitudinally compressed in magnetic bunch compressors, see Section 3.2.1. Bunch compression monitors (BCM) were developed [Wesch, 2012] to measure the bunch peak current behind a bunch compressor. The basic detection principle is shown in Figure 2.4.2. An electron passing a metallic slit generates coherent diffraction

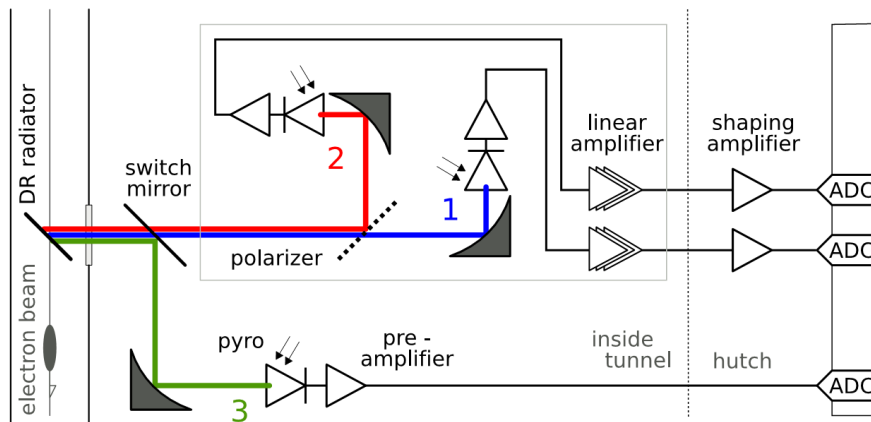


Figure 2.4.2: BCM principle [Behrens et al., 2010].

radiation (CDR), which is used to determine a relative bunch length, thus bunch current. A motorize mirror deflects the diffraction radiation (DR) into different detectors, i.e. either DR path 1 and 2, which is the new detection strategy, or DR path 3 the old detection set-up. For simplicity, only the new detection scheme is considered using two channels for different dynamic ranges. A polarizer separates the vertical and horizontal radiation field components, which are focused by parabolic mirrors onto pyroelectric elements. The outgoing signal is amplified and sampled. For further details, see [Wesch, 2012] and [Behrens et al., 2010]. The BCM signals are used to control the energy spread within an electron bunch by adjusting the RF field phase of the upstream accelerator module.

Orbit based energy measurements

Electron energy changes result in orbit, hence position, changes within a dispersive section. It is foreseen to upgrade all bunch compressors with energy beam position monitors (EBPM), [Hacker, 2010]. Detecting position deviations from the nominal trajectory allows to compute beam energy changes. The basic principle of an EBPM is depicted in Figure 2.4.3. The electron bunch passes the pickup and induces a voltage transient which

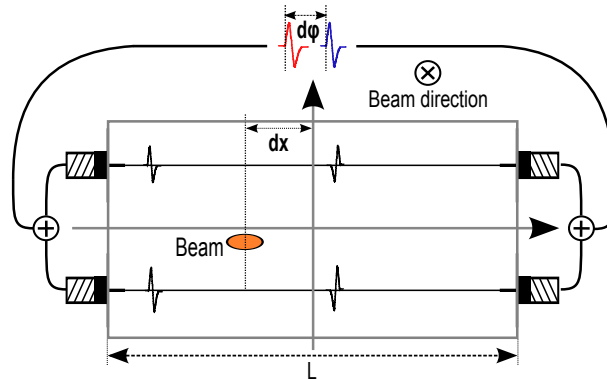


Figure 2.4.3: EBPM principle [Mavrič et al., 2012].

travels to the left and right side of the upper and lower coaxial strip lines. The signals on each side are added to reduce the dependence on the y-direction, i.e. a vertical displacement. The latter is in principle not affected by a bunch compressor, see Section 3.2.1. Fast ADCs detect a phase difference between the incoming signals from the left and right, which is proportional to a bunch displacement dx , hence to an energy change ΔE from its nominal energy, [Hacker, 2010] and [Mavrič et al., 2012].

2.5 SASE Process and Pump-Probe Experiment

SASE Process The main linac accelerates the electron bunches to the target energy. The collimator protects the undulator against mis-steered and off-energy electron bunches. The undulator comprised a periodic magnetic field and forces the electron beam onto a sinusoidal trajectory, depicted in Figure 2.5.1. Hereby the electrons emit photons of high intensity and quality by the *self-amplified spontaneous emission* (SASE) process. To obtain high gain and saturation in the SASE process at nanometer and sub-nanometer wavelength, an electron beam needs to fulfill tight requirements. Especially within the injector and booster linac, the bunch length must be stabilized to about $20 \mu\text{m}$ (rms), leading to a desired peak current of about 5 kA. In addition, the standard deviation of arrival time, the so-called arrival time jitter, of each bunch must be better than 30 fs (rms), further details and requirements can be found in [Altarelli et al., 2006].

The produced X-ray photons with wavelength down to 0.05 nm for XFEL, [XFEL, 2013], and down to 4.12 nm for FLASH, [FLASH, 2013], are used by scientists and researchers to investigate the structure of matter, where often the experiment are carried out in a pump-probe configuration.

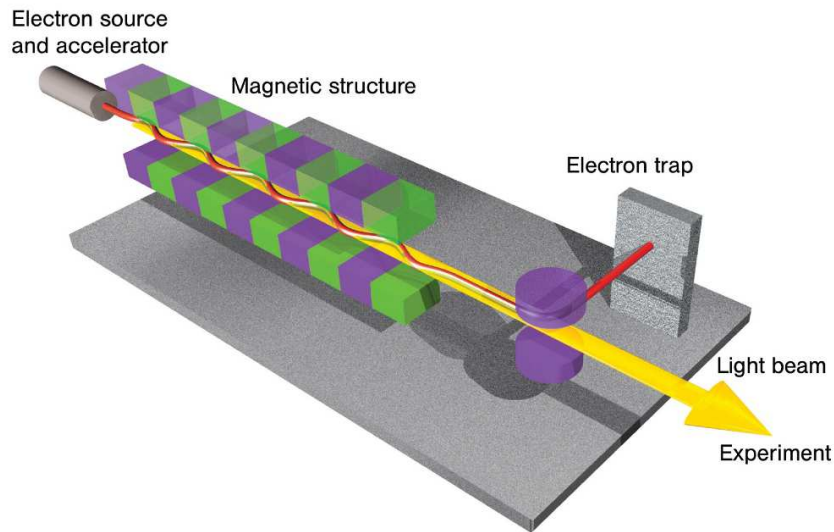


Figure 2.5.1: SASE principle with an electron source, i.e. the FEL, the magnetic structure and the resulting light. The electron bunches are extracted by an electron trap, [XFEL, 2013].

Pump-Probe Experiment This example is taken from [Photon Science DESY, 2013]. Two short pulses are required to explore the temporal evolution of various processes such as atomic motion, expansion of hot plasmas, phase transitions and chemical reactions.

A pump pulse starts the reaction, the probe pulse detects the state of the system. This can be done for defined time delays such that a sequence of probe pulses allows recording a movie of e.g. a molecular reaction. Both pulses could originate from the free-electron laser itself. In this case, the pulse coming from the free-electron laser is split into two pulses, where one of them is delayed by sending it on a longer path. However, often the reaction has to be triggered or probed, e.g. to study the evolution of processes, by ultra-short pulse lasers of optical wavelength with photon energies in the electron volt range; instead of thousands of electron volts providing the free-electron laser. It is much easier to change specific properties of the optical laser, e.g. the pulse duration and shape, the wavelength, the polarization, or the angle of incidence. Nevertheless, those experiments require a precise synchronization and equidistant arrival time of probe and pulse source.

2.6 Sources of Perturbations

In [Schmidt, 2010], an overview of repetitive and non-repetitive disturbances to the control system is given. These include microphonics, i.e. mechanical vibrations caused by e.g. pumps, Lorentz force detuning, i.e. changes of the cavity geometry by the electromagnetic field used for acceleration, and the electron beam itself. These and other disturbances have an impact on the stability of the RF field and were studied in [Schmidt, 2010].

To stabilize the beam, further sources of perturbations must be considered. These can be separated into two groups, as shown in Table 2.3. Within this thesis mainly the fast disturbances, which act within a pulse, are considered.

Table 2.3: Sources of perturbations

Slow Drifts	Fast Fluctuations
Temperature changes within the tunnel or waveguide components	RF field amplitude and phase jitter
Switching in electronics, e.g. vans	Thermal heating within macro-pulse
Aging of components	Photo cathode laser (power, pointing stability, profile)
Ground motions	Vibrations
Electromagnetic interference	Electromagnetic interference
Faults in devices and components	Lorentz force detuning
Cryogenic pressure drifts	Orbit changes due to couples kicks
Stability of magnetic fields	Beam loading effects
	Multi-bunch effects (Higher order modes)

Chapter 3

System Identification

This chapter will focus on the mathematical representation of the considered system. A grey box identification approach, combining a physical white box model structure with engineering identification methods is presented. It will be seen that fixing the internal structure of the model, helps to estimate free parameters in the case of an excited system. The excitation signal itself must be considered as disturbance input. In consequence of pulsed mode operation, not all frequency ranges of interest can be excited within one step. The developed grey box identification approach is flexibly designed, such that the internal model structure can be extended block-wise, depending on estimated models for different frequency ranges. Having a good plant approximation is a necessary step to develop control strategies, like RF field controller or iterative learning control, described in Chapter 4. Model-based controller synthesis allows a systematic tuning procedure which facilitate the achievement of high-performance control objectives, not only for linear accelerators.

Parts of this chapter are published in [Pfeiffer et al., 2011] and [Pfeiffer et al., 2012a].

The chapter is organized as follows. Section 3.1 describes the physical RF field characteristics for the main components within the RF field control loop. It will be seen, that the system behavior, described as real and imaginary part of the RF field amplitude and phase, obeys a *special orthogonal group of dimension two* (SO(2)) symmetric structure. Based on this, a SO(2) symmetric grey box identification approach is presented. Measurement results from tests at the plant conclude this section. Section 3.2 focuses on the response of electron beam properties w.r.t. RF field changes. First, the main behavior of a bunch compressor, a device to change the beam properties, i.e. the bunch arrival time and bunch compression, within the linear accelerator is considered. It will be seen, that the mathematical representation of the RF field to beam response is static in first-order approximation, if RF field changes in amplitude and phase are considered. The combination of an accurate dynamic RF field model and an accurate static beam model, is presented in Section 3.3, a necessary step for optimal beam control, as presented in Section 5.1. The longitudinal phase space of the electron beam is linearised using a third harmonic RF station. The influence and sensitivity to RF field disturbances, e.g. a beam-based correction signal, is studied in Appendix B.1.

3.1 RF Field Modeling

This section is divided into four parts. The first subsection considers the models of the vector modulator and klystron within the RF field chain. Together with the physical equations of a single cavity, a white box model based on the main system behavior is designed. Using only those equations does not provide a complete plant model. Several other components within the signal flow, e.g. the waveguide itself, are not considered. The European XFEL hosts 27 RF stations, which have to be modeled and the controller design for each of these should be done within some minutes. Modeling the overall system behavior on physical equations is not necessary, as will be shown later. In case of maintenance or exchange of components a further modeling process would be necessary. Within the second subsection the result from the white box modeling, which obeys SO(2) symmetry, is used to design a SO(2) symmetric grey box state space model structure which helps to fix and identify a reduced number of parameters. These parameters are estimated by measuring and preprocessing the input/output data. This theoretical approach together with an example will be presented in the third subsection. This section is finalized by SO(2) validation and possible plant simplifications.

3.1.1 Introduction

The system modeling for the main RF components within a linear accelerator is discussed in [Schilcher, 1998], where linear models in Laplace domain with complex variable s of the vector modulator $G_{VM}(s)$, klystron $G_{Kly}(s)$ and cavity $G_{Cav}(s)$ are given. Figure 3.1.1 shows the signal flow for a continuous time input signal $u(t)$, i.e. input to the vector modulator, to the output signal $y(t)$, i.e. the vector sum, see Figure 2.3.1. For com-

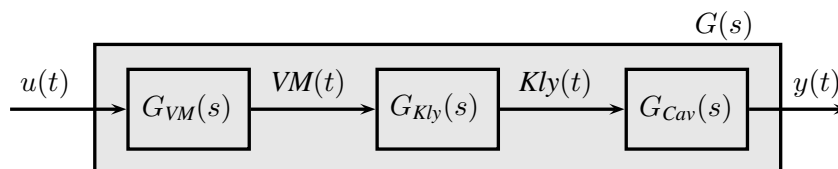


Figure 3.1.1: Signal flow from $u(t)$ to $y(t)$ which forms the model $G(s)$ to be identified.

pleteness, the output of the vector modulator and klystron is down-converted by a mixer from 1.3 GHz to an intermediate frequency and sampled by an ADC, like the 1.3 GHz field probe signal shown in Figure 2.3.1. Additional components like ADC, DAC or pre-amplifier are considered as part of each subsystem.

In this subsection, the developed models will be recalled and discussed with measurement results. These models are given by I/Q representation of the RF field vector, i.e. in-phase or real part (I) and quadrature or imaginary part (Q). It will be shown that couplings from channel I to channel Q and Q to I , respectively, are caused by the vector modulator and klystron, probably in addition by the waveguide system, cables and other components within the signal flow, while the dynamic system behavior is mainly given by the cavity

equation. The series connection of the resulting model

$$G(s) = G_{Cav}(s)G_{Kly}(s)G_{VM}(s)$$

will be used to define an initial model structure for Section 3.1.2.

Vector Modulator Modeling

In [Schilcher, 1998] the model of the vector modulator is given as a first-order approximation in Laplace domain by

$$G_{VM}(s) = \frac{\omega_{VM}}{s + \omega_{VM}} \cdot \mathbf{I}. \quad (3.1.1)$$

The vector modulator has two inputs and two outputs, the in-phase part I and quadrature part Q , respectively. Hereby the given transfer function matrix shows only direct couplings of the input and output, where \mathbf{I} indicates the identity matrix. Previous measurements in [Schilcher, 1998] have shown that $\omega_{VM}/(2\pi) \approx 10$ MHz, which is beyond the maximum Nyquist frequency of 4.5 MHz for the MTCA system. Within this thesis, it will be assumed that the model has a static behavior for frequencies up to the maximum sampling frequency of 9 MHz. Measurements at FLASH with a sampling frequency of 1 MHz, i.e. the VME system, were done. An excitation signal, e.g. pseudo random binary (PRB) signal, is added in closed-loop to the setpoint signal. A gain matrix is estimated by the method of least squares. The measurement and the simulation of the vector modulator is presented in Figure 3.1.2. Here only the time range during the flattop is considered.

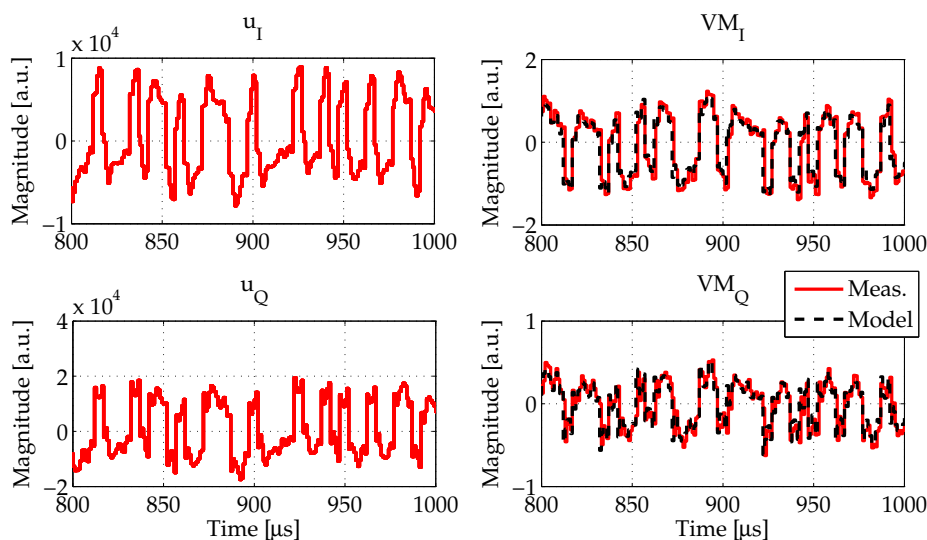


Figure 3.1.2: Vector modulator input and corresponding measured and simulated output signal during flattop as validation with the VME system.

The input signal to the vector modulator is shown on the left side, while the output of the vector modulator is shown on the right side for channel I and Q , respectively. Since

the real and imaginary part of a vector field is given and with the assumption that the vector modulator is static up to the Nyquist frequency ($\omega_{VM} > \omega_{NY}$), the resulting model can be separated into a static scaling and rotation matrix

$$\begin{bmatrix} VM_I(k) \\ VM_Q(k) \end{bmatrix} = K_{VM} \cdot \begin{bmatrix} \cos \phi_{VM} & -\sin \phi_{VM} \\ \sin \phi_{VM} & \cos \phi_{VM} \end{bmatrix} \cdot \begin{bmatrix} u_I(k) \\ u_Q(k) \end{bmatrix}, \quad (3.1.2)$$

where $k = t/T_s$ is a sequence of integer numbers, representing a discrete-time signal with sampling period T_s , K_{VM} as proportional gain and ϕ_{VM} as angle of rotation. This matrix parametrizes a special orthogonal group of dimension two (SO(2)), with the rotation matrix as simplest SO(2) representation. The resulting parameters in this example are identified to be $K_{VM} = 6.6 \cdot 10^{-6}$ and $\phi_{VM} = 135^\circ$.

Klystron Modeling

The model is described in [Schilcher, 1998] and given in Laplace domain as

$$G_{Kly}(s) = \frac{\omega_{Kly}}{s + \omega_{Kly}} \cdot \mathbf{I}. \quad (3.1.3)$$

The bandwidth is estimated by measurements to be $\omega_{Kly}/(2\pi) = 8$ MHz [Schilcher, 1998], which is again above the Nyquist frequency such that only a gain matrix is identified. Figure 3.1.3 shows on the left side the output of the vector modulator, respectively by neglecting preamplifier the input to the klystron and, on the right side, the output of the klystron. Similar to the vector modulator, the static matrix for the klystron ($\omega_{Kly} > \omega_{NY}$)

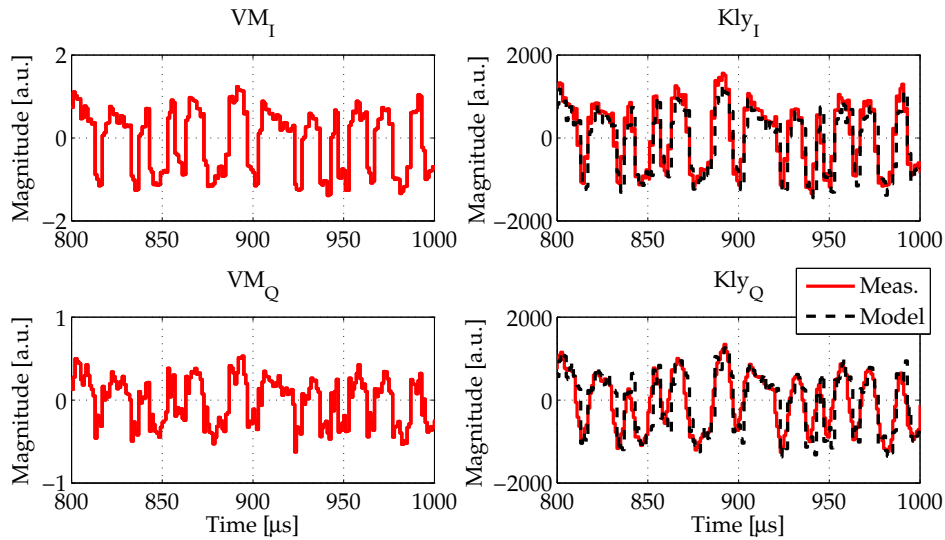


Figure 3.1.3: Klystron input as well as corresponding measured and simulated output signal during flat-top as validation with the VME system.

is given by a SO(2) symmetric structure as

$$\begin{bmatrix} Kly_I(k) \\ Kly_Q(k) \end{bmatrix} = K_{Kly} \cdot \begin{bmatrix} \cos \phi_{Kly} & -\sin \phi_{Kly} \\ \sin \phi_{Kly} & \cos \phi_{Kly} \end{bmatrix} \cdot \begin{bmatrix} VM_I(k) \\ VM_Q(k) \end{bmatrix}, \quad (3.1.4)$$

with a proportional gain $K_{Kly} \approx 1320$ and an angle of rotation $\phi_{Kly} \approx 25^\circ$.

As is now apparent, additional cross-couplings, which in the following are described by a SO(2) symmetric structure, result, among others, from a proportional mapping of the vector modulator and klystron, obeying a SO(2) symmetry.

Cavity Modeling

The dynamical system behavior is modeled by using the physical cavity equation from [Schilcher, 1998]. The latter is well known in accelerator physics and can be described by the differential equation

$$\frac{d}{dt} \begin{bmatrix} V_I(t) \\ V_Q(t) \end{bmatrix} = \begin{bmatrix} -\omega_{1/2} & -\Delta\omega \\ \Delta\omega & -\omega_{1/2} \end{bmatrix} \begin{bmatrix} V_I(t) \\ V_Q(t) \end{bmatrix} + R_L \cdot \omega_{1/2} \begin{bmatrix} 1 & 0 \\ 0 & 1 \end{bmatrix} \begin{bmatrix} I_I(t) \\ I_Q(t) \end{bmatrix}, \quad (3.1.5)$$

in which V is the complex cavity voltage, I the complex driving current, $\omega_{1/2}$ as bandwidth, $\Delta\omega = \omega_0 - \omega$ the detuning and R_L the shunt impedance of the cavity. Lets redefine the output vector $V(t)$ as $y(t)$ and choose the input vector as

$$u(t) = \begin{bmatrix} u_I(t) \\ u_Q(t) \end{bmatrix} = \begin{bmatrix} R_L I_I(t) \\ R_L I_Q(t) \end{bmatrix}, \quad (3.1.6)$$

an usual notation of plant input and output in control theory. This leads to

$$\begin{aligned} \frac{d}{dt} \begin{bmatrix} y_I(t) \\ y_Q(t) \end{bmatrix} &= \underbrace{\begin{bmatrix} -\omega_{1/2} & -\Delta\omega \\ \Delta\omega & -\omega_{1/2} \end{bmatrix}}_A \begin{bmatrix} y_I(t) \\ y_Q(t) \end{bmatrix} + \underbrace{\begin{bmatrix} \omega_{1/2} & 0 \\ 0 & \omega_{1/2} \end{bmatrix}}_B \begin{bmatrix} u_I(t) \\ u_Q(t) \end{bmatrix}, \\ \begin{bmatrix} y_I(t) \\ y_Q(t) \end{bmatrix} &= \underbrace{\begin{bmatrix} 1 & 0 \\ 0 & 1 \end{bmatrix}}_C \begin{bmatrix} y_I(t) \\ y_Q(t) \end{bmatrix}, \end{aligned} \quad (3.1.7)$$

with A as system matrix, B as input matrix and C as output matrix. The transformation of (3.1.7) into the Laplace domain by $G(s) = C(s\mathbf{I} - A)^{-1}B$ is

$$\begin{bmatrix} Y_I(s) \\ Y_Q(s) \end{bmatrix} = \underbrace{\frac{(\omega_{1/2})}{(\Delta\omega)^2 + (s + \omega_{1/2})^2} \begin{bmatrix} s + (\omega_{1/2}) & -\Delta\omega \\ \Delta\omega & s + (\omega_{1/2}) \end{bmatrix}}_{G(s)} \begin{bmatrix} U_I(s) \\ U_Q(s) \end{bmatrix}. \quad (3.1.8)$$

The cavity equation is developed around the baseband frequency, meaning the fundamental π -mode is located at frequency zero. This differential equation holds only for a single fundamental mode, e.g. the π -mode. Since other fundamental modes are present, all cavity mode models are in parallel, thus have to be added to get the overall cavity model. The field probe signal is measured at the end cell of the cavity, thus each even mode, e.g. $8/9 \pi$ -mode, is sign-inverted such that each fundamental mode is represented as

$$G_{\frac{n}{9}\pi}^n(s) = (-1)^{n+1} K_{\frac{n}{9}\pi} \frac{(\omega_{1/2})_{\frac{n}{9}\pi}}{(\Delta\omega_{\frac{n}{9}\pi})^2 + (s + (\omega_{1/2})_{\frac{n}{9}\pi})^2} \begin{bmatrix} s + (\omega_{1/2})_{\frac{n}{9}\pi} & -\Delta\omega_{\frac{n}{9}\pi} \\ \Delta\omega_{\frac{n}{9}\pi} & s + (\omega_{1/2})_{\frac{n}{9}\pi} \end{bmatrix}, \quad (3.1.9)$$

for $n = 1, \dots, 9$. This equation is used to compute the transfer function matrix of the π -mode ($n = 9$) with $K_\pi = 1$. The variation in the coupling and loaded quality factor for the remaining modes ($n \neq 9$) is described in [Vogel, 2007] and requires an adjustment of static gain, bandwidth and detuning by

$$K_{\frac{n}{9}\pi} \stackrel{n \neq 9}{=} 2 \sin^2 \left(\frac{n\pi}{18} \right), \quad (3.1.10)$$

$$(\omega_{1/2})_{\frac{n}{9}\pi} \stackrel{n \neq 9}{=} 2 \sin^2 \left(\frac{n\pi}{18} \right) \frac{\pi f_{\frac{n}{9}\pi}}{Q_L} \text{ and} \quad (3.1.11)$$

$$\Delta\omega_{\frac{n}{9}\pi} = 2\pi \left(f_{\frac{n}{9}\pi} - f_\pi \right), \quad (3.1.12)$$

where Q_L is the loaded quality factor and f_π is the resonance frequency of the π -mode. The cavity baseband model is the superposition of all fundamental modes

$$G_{Cav}(s) = \sum_{n=1}^9 G_{\frac{n}{9}\pi}(s). \quad (3.1.13)$$

Figure 3.1.4 shows the resulting continuous time white box model for the cavity with all fundamental modes.

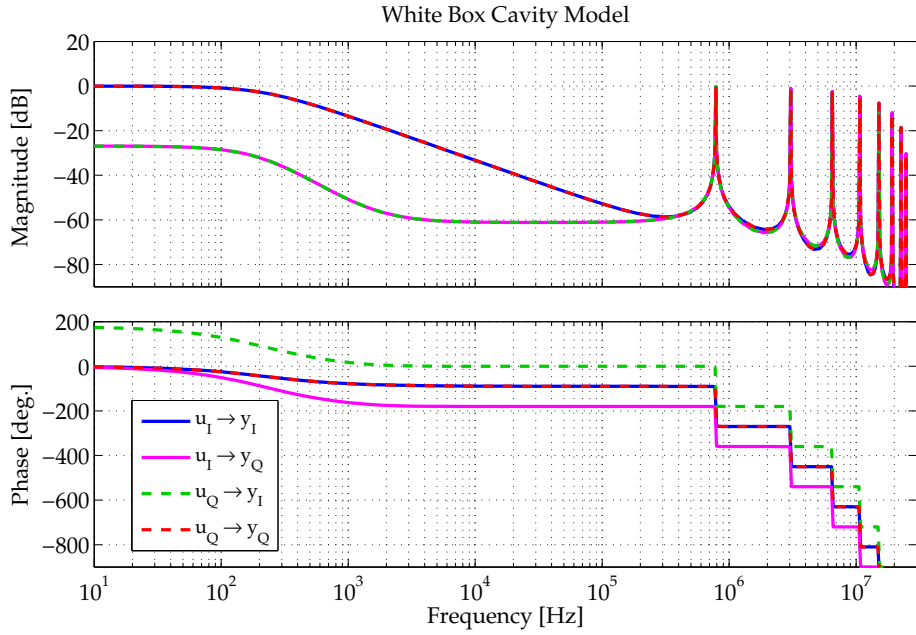


Figure 3.1.4: Continuous time cavity baseband white box model without time delay, an initial detuning of $\Delta\omega_\pi = -2\pi \cdot 10$ Hz and a loaded quality factor of $Q_L = 3 \cdot 10^6$, computed by (3.1.9) to (3.1.13). The fundamental π -mode ($f_\pi = 1.3$ GHz) is located at frequency zero.

The loaded quality factor $Q_L = 3 \cdot 10^6$ of the cavity corresponds to a bandwidth

$$f_{1/2} = \frac{f_\pi}{2Q_L} \quad (3.1.14)$$

of about 217 Hz. Towards higher frequencies the additional fundamental modes are visible, which starts with the $8/9 \pi$ -mode down to the $1/9 \pi$ -mode. Couplings between channel I and Q and vice versa are caused by an imperfectly tuned cavity, i.e. $\Delta\omega_\pi \neq 0$. Detuning is almost negligible, since a piezo controller is in operation, which allows this assumption. Having the detuning information of every pulse and using an adaptive feed-forward strategy, keeps the detuning within a few hertz around zero, see [Przygoda et al., 2010]. Additional cross-couplings are related to the previously described static model of vector modulator and klystron, but also caused by second-order effects, e.g. from the waveguide system. These components are in series with the cavity model as

$$G(s) = G_{Cav}(s)G_{Kly}(s)G_{VM}(s) , \quad (3.1.15)$$

resulting in off-diagonal transfer functions with decreasing magnitude of -20 dB/dec starting at the bandwidth, defined by the cavity model.

3.1.2 Grey Box Modeling with SO(2) Symmetric Structure

Next, a linear time-invariant (LTI) MIMO model structure with inputs u_I, u_Q and outputs y_I, y_Q will be constructed, which should fulfill the following *RF field model requirements*:

- (1) SO(2) symmetric model structure
- (2) Low pass characteristic
- (3) Capability to model additional fundamental modes

The first requirement results from the analysis of the vector modulator and klystron, while the second and third are caused by the cavity equations. Within this section, the discrete-time modeling structure is specified by a reduced number of free parameters, based on a grey box modeling approach.

The system is depicted in Figure 2.3.1 (see page 8) and has an input vector $u(k)$, respectively $U_I(z)$ and $U_Q(z)$, and an output vector $y(k)$, i.e. $Y_I(z)$ and $Y_Q(z)$. Both vectors depend on I and Q , thus represent an amplitude and phase. As seen in the previous section, the MIMO system follows SO(2) symmetry. Therefore a linear discrete-time model, which is SO(2) symmetric, has to have the structure

$$\begin{bmatrix} Y_I(z) \\ Y_Q(z) \end{bmatrix} = \begin{bmatrix} G_1(z) & -G_2(z) \\ G_2(z) & G_1(z) \end{bmatrix} \begin{bmatrix} U_I(z) \\ U_Q(z) \end{bmatrix} , \quad (3.1.16)$$

to fulfill the first required statement. Including the dynamics, the low-pass and additional fundamental modes, into the model structure is discussed in the following part and has been taken into account in [Gdaniec, 2010]. Consider a linear discrete-time state space model

$$\begin{aligned} x(k+1) &= \Phi x(k) + \Gamma u(k) , \\ y(k) &= Cx(k) + Du(k) . \end{aligned}$$

In the following, Φ , Γ and C will be constrained to fulfill the $SO(2)$ symmetry, such that the low pass behavior, denoted by subscript r for real eigenvalue, and additional fundamental modes, denoted by subscript c for complex conjugate pairs of eigenvalues, result in the transfer function matrix given by (3.1.16). The direct feedthrough matrix D is set to zero, which holds, if physically realizable systems are modeled.

Low Frequency Behavior

The discrete-time state space model

$$\begin{aligned} x(k+1) &= \Phi_r x(k) + \Gamma_r u(k) , \\ y(k) &= C_r x(k) , \end{aligned}$$

which fulfills a low pass characteristic is designed by a diagonal system matrix Φ_r with real valued parameter λ

$$\Phi_r = \begin{bmatrix} \lambda & 0 \\ 0 & \lambda \end{bmatrix} . \quad (3.1.17)$$

Choosing the input or output matrix similar to a $SO(2)$ structure, leads e.g. to the following two cases:

(a.i) Antisymmetric off-diagonal input matrix

$$\Gamma_r = \begin{bmatrix} b_1 & -b_2 \\ b_2 & b_1 \end{bmatrix} \quad (3.1.18)$$

Output is chosen as identity matrix

$$C_r = \begin{bmatrix} 1 & 0 \\ 0 & 1 \end{bmatrix} \quad (3.1.19)$$

The designed input and output matrices obey the $SO(2)$ symmetry and result in a discrete-time transfer function matrix

$$G_r(z) = C_r(z\mathbf{I} - \Phi_r)^{-1}\Gamma_r = \begin{bmatrix} \frac{b_1}{z-\lambda} & \frac{-b_2}{z-\lambda} \\ \frac{b_2}{z-\lambda} & \frac{b_1}{z-\lambda} \end{bmatrix} .$$

(a.ii) Antisymmetric off-diagonal output matrix

$$C_r = \begin{bmatrix} c_1 & -c_2 \\ c_2 & c_1 \end{bmatrix} \quad (3.1.20)$$

Input as identity matrix

$$\Gamma_r = \begin{bmatrix} 1 & 0 \\ 0 & 1 \end{bmatrix} \quad (3.1.21)$$

Similar to the previous design, this results in

$$G_r(z) = C_r(z\mathbf{I} - \Phi_r)^{-1}\Gamma_r = \begin{bmatrix} \frac{c_1}{z-\lambda} & \frac{-c_2}{z-\lambda} \\ \frac{c_2}{z-\lambda} & \frac{c_1}{z-\lambda} \end{bmatrix} ,$$

which obeys the $SO(2)$ symmetry.

High Frequency Behavior

Additional fundamental modes are included into the designed low frequency model by extending the structure by complex conjugate pairs of eigenvalues. Through this the model gets the information about resonant modes, i.e. the additional fundamental modes shown within the cavity modeling section. First, one mode is designed without the low frequency behavior to develop the necessary structure such that $SO(2)$ symmetry is fulfilled. This leads to a state space model structure, which is independent of the model structure for real eigenvalues. Hereby, possible additional $SO(2)$ symmetric phase changes can be modeled, without considering the $SO(2)$ symmetric phase for real eigenvalues, applying the freedom to model the system with different phase couplings.

A single high frequency mode can be represented as a state space model with minimal order of two

$$\begin{aligned} x(k+1) &= \overbrace{\begin{bmatrix} \sigma & \omega \\ -\omega & \sigma \end{bmatrix}}^{\tilde{\Phi}_c} x(k) + \overbrace{\begin{bmatrix} \tilde{b}_1 & \tilde{b}_2 \\ \tilde{b}_3 & \tilde{b}_4 \end{bmatrix}}^{\tilde{\Gamma}_c} \cdot \begin{bmatrix} u_I(k) \\ u_Q(k) \end{bmatrix}, \\ \begin{bmatrix} y_I(k) \\ y_Q(k) \end{bmatrix} &= \underbrace{\begin{bmatrix} \tilde{c}_1 & \tilde{c}_2 \\ \tilde{c}_3 & \tilde{c}_4 \end{bmatrix}}_{\tilde{C}_c} x(k). \end{aligned} \quad (3.1.22)$$

The system transfer function matrix of (3.1.22) is given by

$$\begin{bmatrix} Y_I(z) \\ Y_Q(z) \end{bmatrix} = G_c(z) \begin{bmatrix} U_I(z) \\ U_Q(z) \end{bmatrix}, \quad (3.1.23)$$

where

$$G_c(z) = \tilde{C}_c(z\mathbf{I} - \tilde{\Phi}_c)^{-1}\tilde{\Gamma}_c. \quad (3.1.24)$$

Let the transfer function matrix for the given MIMO model be written as

$$G_c(z) = \begin{bmatrix} \frac{N_{II}(z)}{D(z)} & \frac{N_{IQ}(z)}{D(z)} \\ \frac{N_{QI}(z)}{D(z)} & \frac{N_{QQ}(z)}{D(z)} \end{bmatrix}. \quad (3.1.25)$$

The common denominator polynomial of $G_c(z)$ is

$$D(z) = z^2 - 2\sigma z + \sigma^2 + \omega^2, \quad (3.1.26)$$

while the four numerator polynomials differ and are given by

$$N_{II}(z) = (\tilde{c}_1\tilde{b}_1 + \tilde{c}_2\tilde{b}_3) \cdot (z - \sigma) + (\tilde{c}_1\tilde{b}_3 - \tilde{c}_2\tilde{b}_1) \cdot \omega, \quad (3.1.27)$$

$$N_{QQ}(z) = (\tilde{c}_3\tilde{b}_2 + \tilde{c}_4\tilde{b}_4) \cdot (z - \sigma) + (\tilde{c}_3\tilde{b}_4 - \tilde{c}_4\tilde{b}_2) \cdot \omega, \quad (3.1.28)$$

$$N_{IQ}(z) = (\tilde{c}_1\tilde{b}_2 + \tilde{c}_2\tilde{b}_4) \cdot (z - \sigma) + (\tilde{c}_1\tilde{b}_4 - \tilde{c}_2\tilde{b}_2) \cdot \omega \quad \text{and} \quad (3.1.29)$$

$$N_{QI}(z) = (\tilde{c}_3\tilde{b}_1 + \tilde{c}_4\tilde{b}_3) \cdot (z - \sigma) + (\tilde{c}_3\tilde{b}_3 - \tilde{c}_4\tilde{b}_1) \cdot \omega. \quad (3.1.30)$$

For SO(2) symmetry (3.1.27) to (3.1.30) must fulfill the condition

$$\left. \begin{aligned} N_{II}(z) &= N_{QQ}(z) \\ N_{IQ}(z) &= -N_{QI}(z) \end{aligned} \right\} \forall z, \sigma \text{ and } \omega ,$$

which leads to only two non-zero cases with a minimal order of the state space model to combine real values of all parameters \tilde{b} and \tilde{c} :

(b.i) for antisymmetric off-diagonals

$$\tilde{\Gamma}_c = \begin{bmatrix} \tilde{b}_1 & -\tilde{b}_2 \\ \tilde{b}_2 & \tilde{b}_1 \end{bmatrix} , \quad \tilde{C}_c = \begin{bmatrix} \tilde{c}_1 & -\tilde{c}_2 \\ \tilde{c}_2 & \tilde{c}_1 \end{bmatrix} \quad (3.1.31)$$

(b.ii) for antisymmetric diagonal elements

$$\tilde{\Gamma}_c = \begin{bmatrix} \tilde{b}_1 & \tilde{b}_2 \\ \tilde{b}_2 & -\tilde{b}_1 \end{bmatrix} , \quad \tilde{C}_c = \begin{bmatrix} \tilde{c}_1 & \tilde{c}_2 \\ \tilde{c}_2 & -\tilde{c}_1 \end{bmatrix} . \quad (3.1.32)$$

In the case of (b.i), the model can be rewritten as SO(2) rotational part including a scaling factor. Therefore the input and output matrix rotates and scales the corresponding vector. Considering only the rotation part results in $\det(\tilde{\Gamma}_c) = 1$ and $\det(\tilde{C}_c) = 1$, respectively, which is SO(2) with a rotation about the origin. Case (b.ii) represents a glide reflection with $\det(\tilde{\Gamma}_c) = -1$ and $\det(\tilde{C}_c) = -1$, if the determinant is normalized to one. If not, separating a scaling part from this matrix achieves a normalized determinant. For both cases symmetry groups are defined.

Besides both representations, an additional term is introduced, i.e. a block diagonal system matrix with an extended input and output matrix. In principle there exists an infinite set of input and output matrices which combinations obey the SO(2) symmetry. Here, the focus is on two representations with an extended system matrix

$$\Phi_c = \begin{bmatrix} \sigma & \omega & 0 & 0 \\ -\omega & \sigma & 0 & 0 \\ 0 & 0 & \sigma & \omega \\ 0 & 0 & -\omega & \sigma \end{bmatrix} . \quad (3.1.33)$$

(c.i) Input matrix follows SO(2) like symmetry

$$\Gamma_c = \begin{bmatrix} b_{11} & b_{12} & b_{21} & b_{22} \\ -b_{21} & -b_{22} & b_{11} & b_{12} \end{bmatrix}^T \quad (3.1.34)$$

Output matrix chosen as

$$C_c = \begin{bmatrix} 0 & 1 & 0 & 0 \\ 0 & 0 & 0 & 1 \end{bmatrix} \quad (3.1.35)$$

(c.ii) Output matrix follows SO(2) like symmetry

$$C_c = \begin{bmatrix} c_{11} & c_{12} & -c_{21} & -c_{22} \\ c_{21} & c_{22} & c_{11} & c_{12} \end{bmatrix} \quad (3.1.36)$$

Input matrix chosen as

$$\Gamma_c = \begin{bmatrix} 0 & 1 & 0 & 0 \\ 0 & 0 & 0 & 1 \end{bmatrix}^T \quad (3.1.37)$$

Extending the state space model structure has the benefit to model independently transmission zeros, i.e. input coupling for high frequency resonant modes, of the diagonal and off-diagonal transfer functions, sometimes called *multivariable zeros*, [Skogestad and Postlethwaite, 2005]. Numerical experiments show that the results of the grey box parameter identification, which is described later, is improved if the state space model is extended by two additional states. So, the input-output pole direction for cases given by (b) and (c) does not change, while the input-output zero direction may change, which improves the system modeling. Such an extended system representation leads to an increased order of the system and to an independent modeling of the transmission zeros, while the number of parameters remains unchanged.

The discrete-time state space model with low pass character and one resonance frequency is

$$\begin{aligned} x(k+1) &= \begin{bmatrix} \Phi_r & 0 \\ 0 & \Phi_c \end{bmatrix} x(k) + \begin{bmatrix} \Gamma_r \\ \Gamma_c \end{bmatrix} u(k) , \\ y(k) &= \begin{bmatrix} C_r & C_c \end{bmatrix} x(k) . \end{aligned} \quad (3.1.38)$$

The model has two real eigenvalues and either one, for case (b), or two, for case (c), complex conjugate pairs of eigenvalues and obeys the SO(2) symmetry. Slightly non-symmetric system behavior is introduced in Appendix B.2. Additional resonant modes and time delays are considered next by extending the state space model block-wise.

Extension to further resonant modes and time delays

Additional resonant modes can be included by extending the state space model block-wise by additional block diagonal matrices e.g. leading to

$$\begin{aligned} x(k+1) &= \begin{bmatrix} \Phi_r & 0 & 0 \\ 0 & \Phi_{c_1} & 0 \\ 0 & 0 & \Phi_{c_2} \end{bmatrix} x(k) + \begin{bmatrix} \Gamma_r \\ \Gamma_{c_1} \\ \Gamma_{c_2} \end{bmatrix} u(k) , \\ y(k) &= \begin{bmatrix} C_r & C_{c_1} & C_{c_2} \end{bmatrix} x(k) , \end{aligned} \quad (3.1.39)$$

which obeys the SO(2) symmetry for each eigenvalue. This allows to include additional block matrices, while the coupling of the modes, which can vary for different resonant modes, is independent of the previous identified system, input and output matrices.

The *time delay* of the plant will be considered during the identification procedure. The system to be identified is operated in a pulsed mode operation, such that the output vector is shifted with respect to the input vector, corresponding the sampling points. After the system identification, additional states are used to extend the state space model such that the time delay of the plant is included into the model structure, needed e.g. during the controller design, Section 4.1.

The described system identification approximates the RF field plant behavior without time delay to reduce the complexity of the system model. First, the low frequency behavior is identified, followed by the inclusion of additional resonant modes by extending the state space model with block matrices, see (3.1.39). Figure 3.1.5 shows the identified SO(2) symmetric model $G(z)$, in series connection with the time delay T_d . The signal flow for

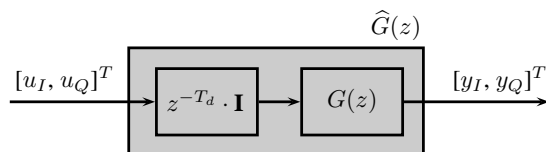


Figure 3.1.5: Identified model $G(z)$, time delay T_d and overall plant model $\hat{G}(z)$, used for the controller design.

both channels is similar, hence the time delay is assumed to be equal, resulting in a SO(2) symmetric model $\hat{G}(z)$. The model extension by inclusion of time delays is not necessary for the identification procedure, while for the controller design it is.

3.1.3 Example at FLASH

The grey box model structure developed within the previous section, will be used to identify a linear time-invariant discrete-time model with an input signal as input to the vector modulator and an output signal as vector sum, i.e. the sum of calibrated cavity probe signals. Such an engineering approach simplifies the complex white box modeling to an identification procedure, which computes the main system behavior within some routine steps. The parameter identification is divided into two steps, a consequence of the pulsed mode operation. The excitation of the system and therefore the identification of the input-output behavior is only possible within a short time period, leading to an adaptive identification procedure.

First the location of the low frequency pole, the bandwidth of the system, is identified by a real eigenvalue with

$$\begin{aligned} x(k+1) &= \Phi_r x(k) + \Gamma_r u(k) , \\ y(k) &= C_r x(k) . \end{aligned} \tag{3.1.40}$$

This provides the low pass characteristic together with its input matrix by using PRB signals.

In the second step, the frequency and damping of one or more complex conjugate pairs of eigenvalues are determined, while the low frequency behavior is fixed. An adaptive exci-

tation scheme that starts with a wide frequency scan, ends with fine sinusoidal excitation and finally the pole location of the considered mode. The identification scheme for the low frequency and high frequency behavior, see (3.1.38), is shown in Figure 3.1.6.

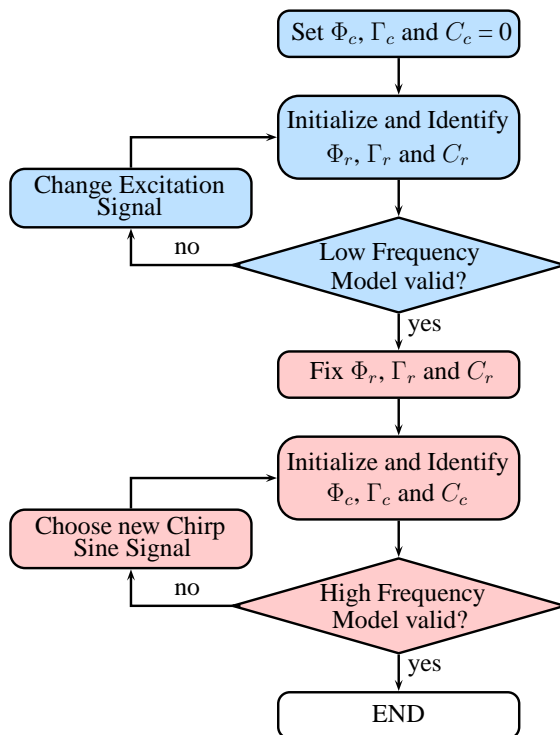


Figure 3.1.6: Adaptive two step system identification using fixed grey box model structure to identify a mathematical model for one real eigenvalue and one complex conjugate pair of eigenvalues.

It is necessary to develop reasonable excitation and preconditioning procedures before identifying parameters by e.g. the iterative prediction-error minimization method, [Ljung, 1999]. The following example shows, how the grey box system identification is used to compute a model. For different amplitude setpoints the system shows slightly nonlinear behavior, caused mainly by the klystron, [Cichalewski and Koseda, 2007]. But in usual operation the amplitude is fixed and further strategies are used to linearise the behavior of the klystron. The model identification operates in open loop at a given amplitude and phase setpoint. Adjusting the feedforward drive before the identification starts, helps to minimize residual field errors. Minimizing those field errors allows to estimate a model around the operating setpoint, i.e. during flattop, where a persistent excitation signal is added to the feedforward signal. By this, the feedforward output signal is overlapped by an arbitrary excitation signal. High amplitudes of the excitation signal lead to a better signal-to-noise ratio, but introduce additional cross couplings caused by cavity detuning. A cavity simulation based on (3.1.8), page 21, point out cross-coupling variations by changing the detuning and loaded Q (Q_L), presented in Figure 3.1.7. Changes in Q_L affect the diagonal channel, variations of detuning Δf mainly the off-diagonal channel, while the ratio of off-diagonal and diagonal coupling is almost constant for both parameters.

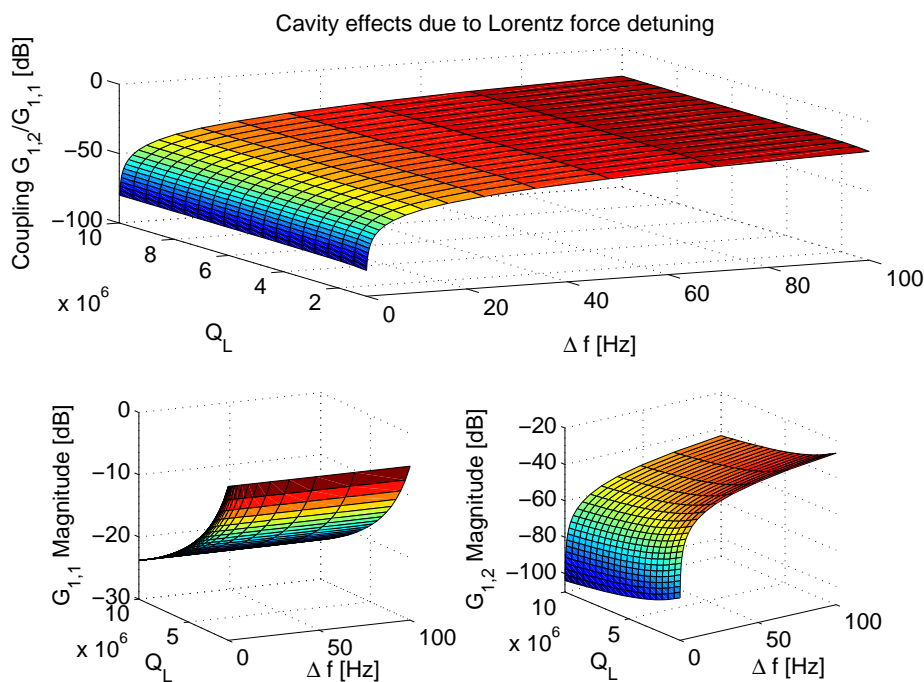


Figure 3.1.7: Coupling of off-diagonal to diagonal channel as function of detuned cavity (Δf) and different loaded Q (Q_L). The lower left plot shows the magnitude changes for the diagonal channel and on the right the off-diagonal channel. These plots show the frequency response at $f = 1$ kHz, which is the minimum frequency for flat-top length of about 1 ms.

During normal operation, i.e. detuning is kept within a few Hertz, the cavity coupling can be neglected, unlike during a system identification, where the cavity is probably slightly detuned by the excitation signal itself. In addition this coupling is constant for Q_L adjustments within the regulation. Therefore, Q_L changes lead to a different low frequency gain, but do not influence the modeling structure. This fact is an important result for the SO(2) validation and is further considered in Section 3.1.4. Getting only the influence of an additional excitation signal, used to identify a small signal model, it is necessary to detrend the measured signal. Drifts and fluctuations are caused by Lorentz force and microphonics, which will be briefly discussed in the following. Further details can be found in [Schmidt, 2010].

Data Preconditioning and Detrending

Microphonics Signal changes from pulse to pulse are primarily caused by microphonics, e.g. introduced by ground vibrations, pumps and so on. It has been shown that this disturbance can be minimized by taking a series of measurements, which are averaged, being a necessary step for system identification [Schmidt, 2010].

Detrend Consider a given setpoint (amplitude and phase), where a linear state space model has to be identified. Assume a stable linear time-invariant system with a persistent zero mean excitation signal. Before the excitation starts and some time after the excitation signal, depending on the system dynamics, the output should be zero with respect to the excitation signal. In this application, changing the amplitude and phase results in different detuning and therefore in additional cross couplings. Changes of the electromagnetic field strength inside the cavities vary their length and thus its resonant frequency. Furthermore, the klystron has shown a nonlinear behavior, which is linearised by a klystron input-output adjustment, [Cichalewski and Koseda, 2007]. Within the grey box modeling process those additional effects are not considered, since this detuning will be removed by a piezo actuator, which changes the length of the cavity for the flattop phase to reach zero detuning, [Przygoda et al., 2010]. It will be checked first, whether these effects will have an influence on the identified parameters. Figure 3.1.8 shows the vector sum in amplitude and phase without and with an added excitation signal.

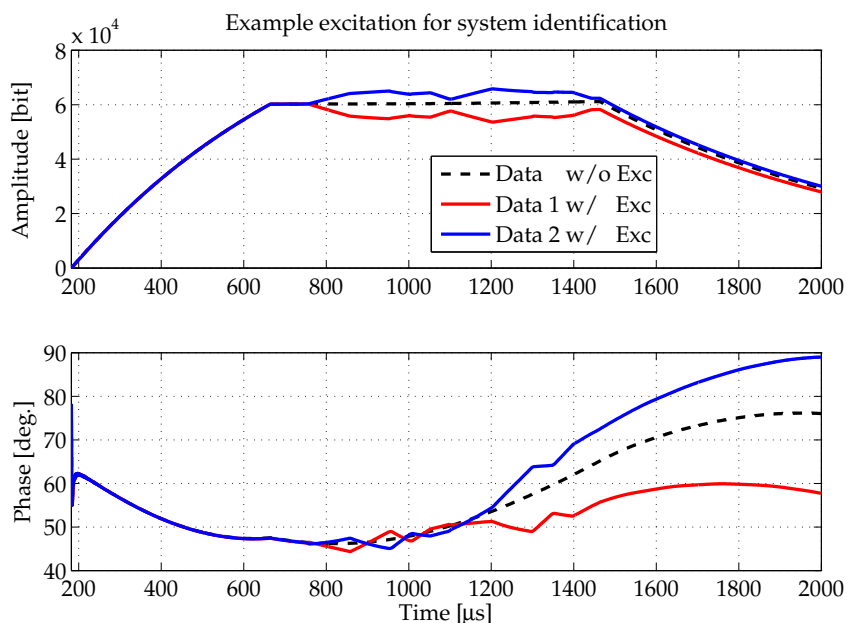


Figure 3.1.8: Excitation during flattop with the same excitation signal, either added (Data 1) or subtracted (Data 2) to the feedforward signal around the operating RF field setpoint (Data w/o Exc) for slightly detuned cavities.

In a second step this excitation is subtracted from the feedforward drive. It is obvious that

the amplitude and phase decrease and increase depending on the sign of the excitation signal. By using the grey box modeling procedure, the small signal model is computed and validated by both excitation signals, shown in Figure 3.1.9. Here the system response

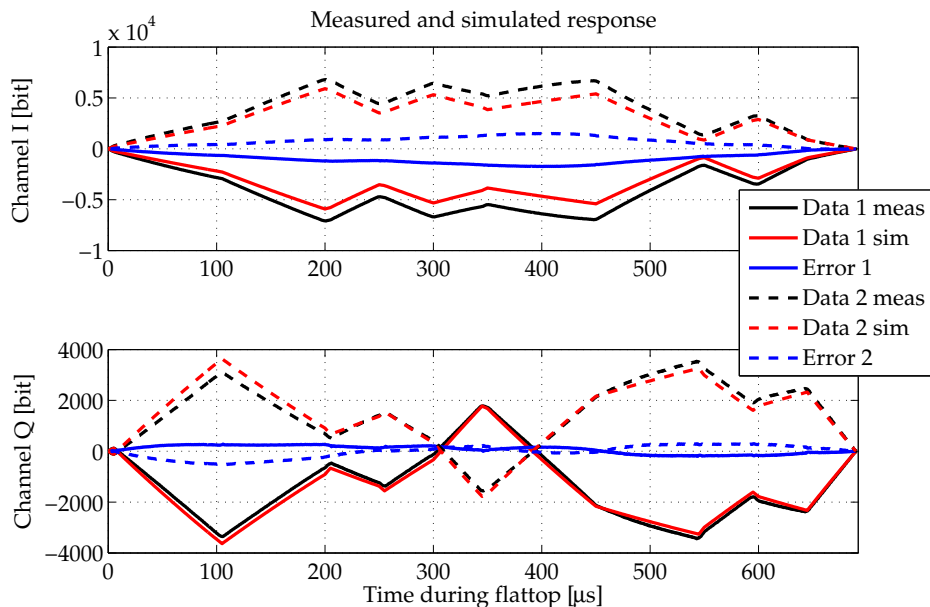


Figure 3.1.9: Small signals for the added (Data 1) and subtracted (Data 2) excitation signal from Figure 3.1.8, used for system identification.

is compensated by a linear detrend, such that the value is zero at both the start and end of the excitation time. It shows that an error in both channels is present between the simulated and measured signal, caused either by a detuned cavity or further effects, e.g. klystron phase drifts caused by non-linear input-output behavior, [Cichalewski and Koseda, 2007]. But since the controller acts only around the operating setpoint, this effect is not critical, since the detuning close to the operating setpoint is compensated. Thus, keeping the $SO(2)$ symmetry within the modeling procedure, reduces detuning effects, which are only present within the system identification, for comparison see the cross-validation on page 37. Minimizing the detuning effects by using an excitation signal with small magnitude, i.e. a lower signal-to-noise ratio (SNR), leads to a non-perfect system identification, while too high magnitudes may change the detuning, thus cross-couplings significantly. A necessary excitation magnitude, which leads to good data cross-validation must be used to increase the signal-to-noise ratio. Nevertheless, small additional cross-coupling effects caused by non-perfect detuning can be compensated within the controller design by changing the off-diagonal components for the multi-input multi-output controller, see Chapter 4. For a controller which fulfills the $SO(2)$ symmetry like the system model, it can be rewritten as scaling and rotation part, shown in Section 3.1.4, such that adjusting the controller phase is sufficient. The linear detrend for both channels leads to the measured small signal response. Based on the system excitation and resulting detrended signals (Data 1 and Data 2), as shown in Figure 3.1.9, the resulting low frequency model for both cases is displayed in Figure 3.1.10. Here only one channel for the direct

and the cross coupling is shown, while the second channel obeys the $SO(2)$ symmetry. Exciting the system by adding or subtracting an additional input signal and using a lin-

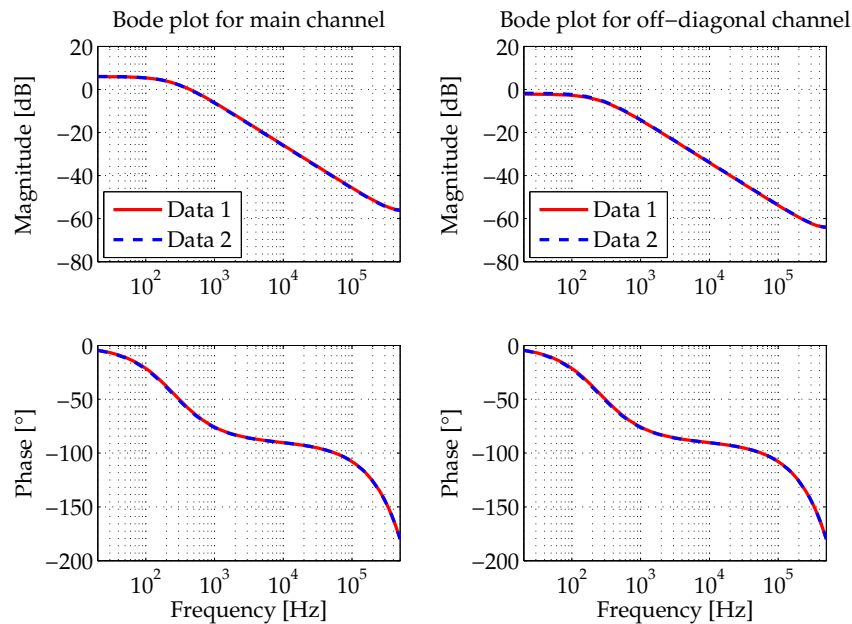


Figure 3.1.10: Bode diagram for the identified model, either with added (Data1) or subtracted (Data2) excitation signal, with system response given in Figure 3.1.9.

ear detrend does not change the plant model as shown in Figure 3.1.10. For reliability and safety reasons only excitation signals, which lower the amplitude are used to identify the plant.

Summary Figure 3.1.11 illustrates the described procedure for preconditioning and detrending the datasets:

1. Operate the machine at an usual operating setpoint.
2. Take a series of 60-80 output signals without excitation, e.g. I w/o Exc.
3. Add an excitation signal to the feedforward signal, e.g. FF w/ Exc.
4. Take a series of 60-80 output signals with excitation, e.g. I w/ Exc.
5. Average the output data without and with excitation to get two signals, one without and one with added excitation.
6. Calculate the difference signal, i.e. ΔI , between the data with and without excitation computed in Step 5.
7. Shift the signal computed in Step 6 accordingly to the time delay of the plant.
8. Linearly detrend the signal ΔI of Step 7 resulting in $\Delta I_{\text{Detrend}}$ such that the difference signal is zero at beginning and end of a non-zero excitation signal.

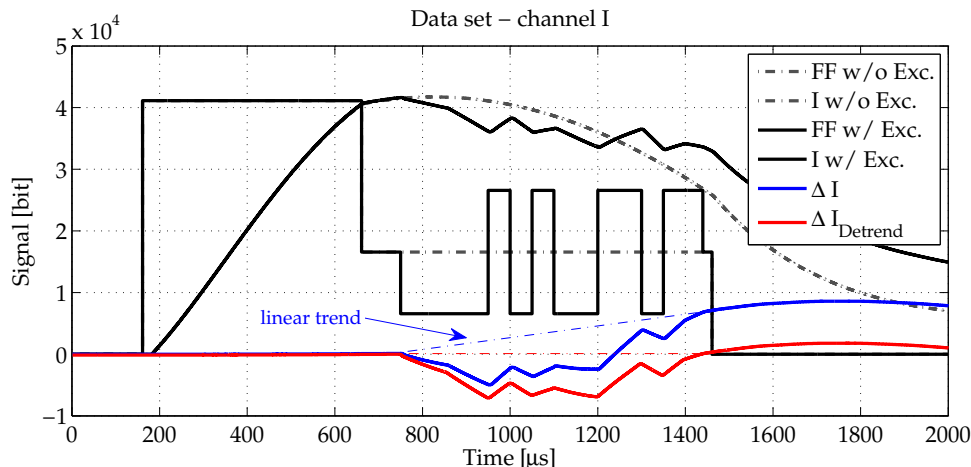


Figure 3.1.11: An example for detrending the signal of channel I based on the excitation and the resulting system response.

This procedure is necessary to generate the preconditioned set of signals used by the parameter estimation method shown in Figure 3.1.6.

Parameter Identification at FLASH for VME System

Using the system identification toolbox of MATLAB, the structure, including fixed and free parameters, of a linear discrete-time-invariant grey box model can be defined. Using the function `idgrey` and estimating a grey box model by the prediction error minimization method `pem`, [Ljung, 1999], allows to optimize the frequency output spectrum accordingly to its input spectrum. The first goal is to estimate the real pole (3.1.17) for low frequency behavior and its corresponding input matrix (3.1.18). Thus, the model has the form of (3.1.40). Assume, all parameters are unknown and set the pole and the input matrix as described in Section 3.1.2. First, initialize the free parameters such that the diagonal elements should dominate, e.g. initialize b_1 to a higher value, e.g. 0.1, b_2 as zero or close to zero and the real pole at around 200 Hz. By assuming that many pulses and thus columns are combined to a single one, the disturbance caused by microphonics can be neglected such that the disturbance model is set to zero.

The estimation of the parameters of the low frequency grey box model with two real eigenvalues, leads by way of example to values

$$\lambda_1 = 0.9996, b_1 = 0.0028, b_2 = 0.0014 .$$

Besides, the parameter λ_1 can be calculated by analyzing the decay of the RF field amplitude. During this decay phase (see Figure 2.3.2), the feedforward signal is set to zero and the system is driven in open loop. Using a first-order approximation of the amplitude decay

$$A = A_0 \cdot e^{-\frac{t}{\tau}}$$

and a linear fitting of the natural logarithm of the field amplitude leads to a continuous time eigenvalue of $1/\tau$, which corresponds to the system bandwidth $\omega_{1/2}$ for low frequency behavior. Hence, the initial discrete-time eigenvalue of the low frequency behavior can be computed leading to three free parameters or the computed eigenvalue can be fixed such that only the input matrix is estimated with two free parameters. As long as the loaded quality factor Q_L of each cavity is not changed, the system bandwidth does not change, see relation in (3.1.14). If the cross validation between measured and simulated data, an example is shown in Figure 3.1.14, is sufficient for the low frequency behavior, the model given by (3.1.40) is fixed such that resonant modes, i.e. additional fundamental modes, can be included and estimated.

High Frequency Parameter Estimation From the baseband cavity model, given in (3.1.13), it is known that additional resonant modes are present. Using high frequency excitation signals allows to excite resonances that are difficult to find by PRBS. Chirp sine signals with a linear increasing frequency constrain the frequency region of interest.

Example: Assume, the resonant mode is located around 200 kHz. Starting with a rough chirp sine signal, e.g. with a frequency range from 150 kHz up to 250 kHz, shown in Figure 3.1.12 the region of possible resonances will be scanned first. Analyzing the spectrum of the output dataset leads to small peaks, which are, verified by decreasing the frequency range of the chirp sine signal, shown in Figure 3.1.12. Shrinking the frequency range of

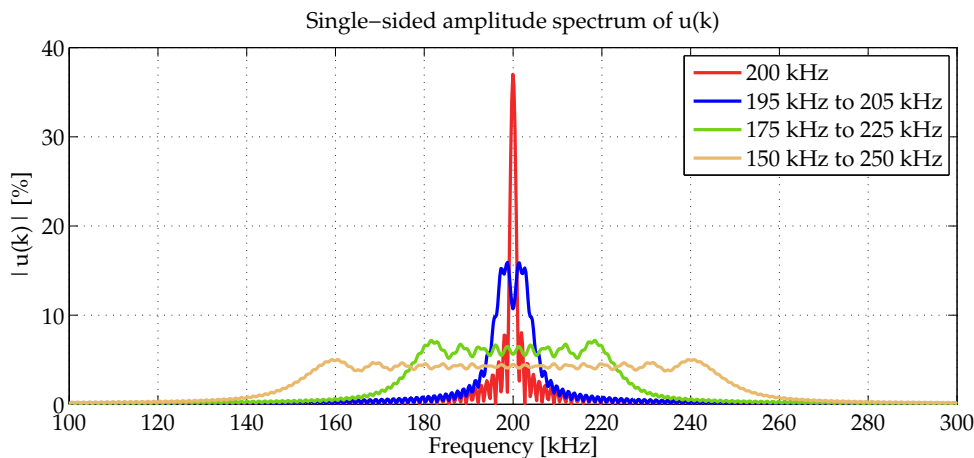


Figure 3.1.12: Excitation signal spectrum for chirp sine signals with given frequency range and a sinusoidal signal of 200 kHz. The excitation signal length is 800 μs , an usual flattop length at FLASH, the sampling time is 1 μs , which corresponds to the VME system.

the excitation signal of fixed length leads to a higher amplitude of the appropriate frequency within the frequency spectrum and thus the system response is more reliable in that range.

Exciting those modes is difficult since cavities with a high quality factor are used, leading to a narrow frequency bandwidth. The additional fundamental modes are given in Section 2.3, Table 2.2 on page 11. Obviously, the first mode, located at $f_{8/9} \pi \approx$

785 kHz \pm 51 kHz (see Table 2.2 on page 11), is above the Nyquist frequency of 500 kHz for VME system and hence, an aliased mode should be found around 200 kHz. After evaluating the input-output datasets, one can identify at least one additional resonant mode by augmenting the states and matrices from (3.1.40) to the structure of (3.1.38). Including additional resonant peaks into the model structure is done by further extending the state equations given in (3.1.38) with block matrices given in (3.1.33)–(3.1.35). The previous verified and modeled state space matrices will be fixed and the identification of a second complex conjugate pair of eigenvalues starts at the next frequency region of interest. Figure 3.1.13 shows the resulting bode diagram of the identified model with a sampling frequency of 1 MHz. As seen in the previously described data preconditioning

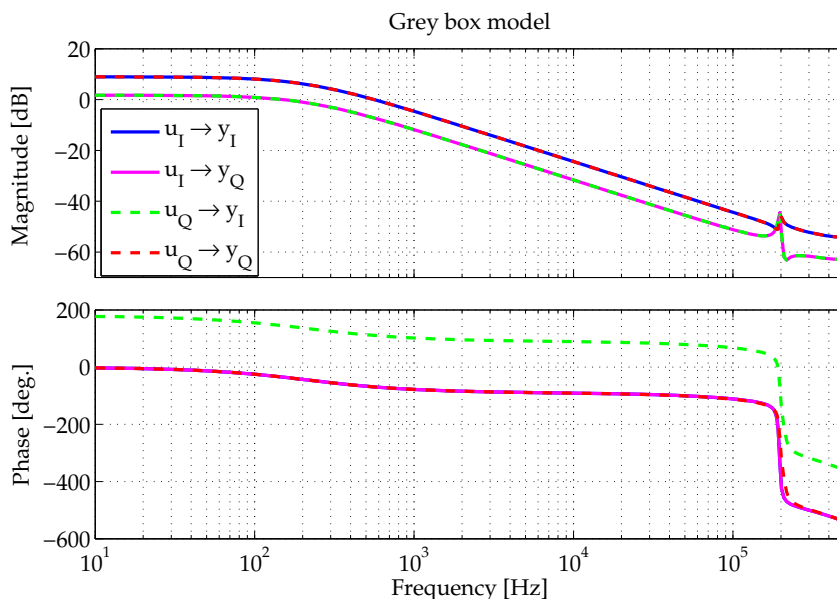


Figure 3.1.13: Bode diagram for the identified model of the VME system, containing a real eigenvalue representing the system bandwidth and a complex conjugate pair of eigenvalues, i.e. the aliased $8/9 \pi$ -mode.

and detrending subsection, the simulated system response compared with the measured signal has an error which is caused by e.g. detuning and klystron non-linearities. A cross validation in Figure 3.1.14 shows a reduced error if the amplitude and phase of the RF field is excited close to the operating setpoint by using a higher frequency excitation signal, i.e. lower detuning effect due to smaller changes of the RF field amplitude. By reducing RF field errors, e.g. by a MIMO RF field controller presented in Section 4.1, the operating RF field is kept constant. In addition, further control loops minimize mechanical deformations of the cavity, caused by the detuning. These additional feedback loops ensure a linear and time-invariant system behavior.

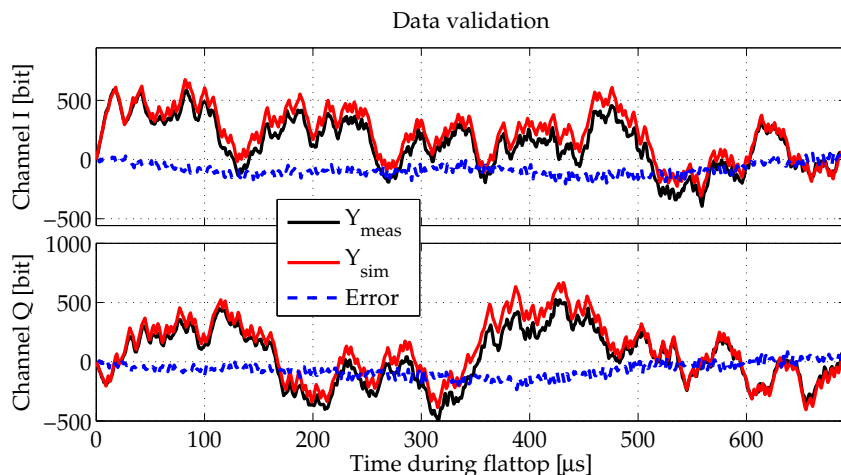


Figure 3.1.14: A system cross-validation with a high-frequency PRB signal shows small deviation of the error signal, i.e. the difference between measurement and simulation.

Parameter Identification for MTCA System

The same modeling procedure is used with the MTCA system, see Section 2.3. From the white box modeling of the cavities it is obvious, that the new model contains a sampled and non-aliased $8/9 \pi$ -mode and $7/9 \pi$ -mode. Here, the system bandwidth and the two mentioned modes are estimated. Starting at low frequencies, first the real eigenvalue is estimated, followed by the $8/9 \pi$ -mode, around 800 kHz, next the $7/9 \pi$ -mode around 3 MHz. This example shows the result of an identification by adding and estimating block-wise additional high frequency matrices; (3.1.33)–(3.1.35).

The low frequency behavior should be almost the same for both systems. The bode diagrams of the VME and MTCA system are overlapped for comparison in Figure 3.1.15. The frequency response for the identified model of the MTCA system is indicated by the normal lines, whereas the grey lines are identified with the VME system. It is clearly visible that the $8/9 \pi$ -mode is mapped to the left at the Nyquist frequency, which is marked by the black line.

In addition, the magnitude of the aliased mode for the VME system is attenuated by the sampling method itself, i.e. I/Q-sampling scheme with data averaging, see [Schmidt, 2010], and by destructive interference of eight cavity signals which are added to the vector sum signal, [Hoffmann, 2008]. Furthermore, a frequency scan with the MTCA system for both identified resonant modes is presented in [Schmidt et al., 2012], where the $8/9 \pi$ -mode is found at $f_{8/9\pi} = 777 \text{ kHz} \pm 25 \text{ kHz}$ and the $7/9 \pi$ -mode at $f_{7/9\pi} = 3035 \text{ kHz} \pm 60 \text{ kHz}$. These frequency ranges are covered by the frequency width of the complex conjugate pairs of eigenvalues for the MTCA system as shown in Figure 3.1.15. However, the resonant frequency for the aliased $8/9 \pi$ -mode should be found at $f_{8/9\pi} = 222 \text{ kHz} \pm 25 \text{ kHz}$, while it is found at 197 kHz for the VME system. This is explainable by the ADC detection scheme which, without going into the details, is based on 250 kHz sampling frequency [Hoffmann, 2008]. Hence, resonance frequencies close to this sampling frequency are further attenu-

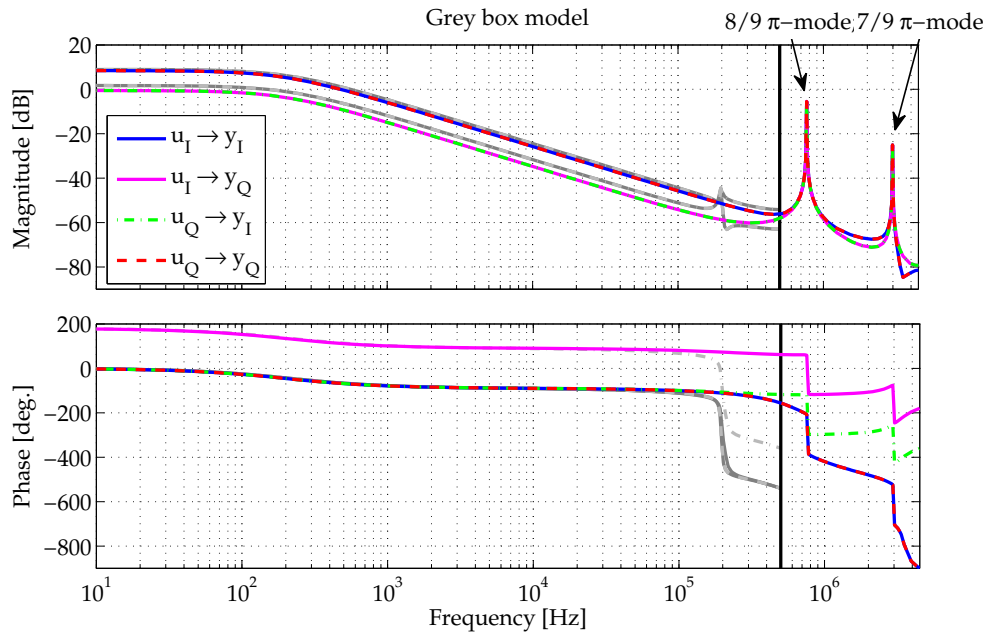


Figure 3.1.15: Bode diagram for the identified model of the MTCA system, containing a real eigenvalue and two complex conjugate pairs of eigenvalues, i.e. $7/9 \pi$ -mode and $8/9 \pi$ -mode. Overlapped for comparison is the identified frequency response of the VME system, i.e. grey lines, up to the Nyquist frequency which is marked by the black line; see Figure 3.1.13.

ated by the Nyquist-Shannon sampling theorem. As a result, the $8/9\pi$ mode for the VME system is found at the lowest frequency within the frequency spread of eight cavities, i.e. $f_{8/9\pi} = 197$ kHz.

A cross validation compares the low and the high frequency behavior between the measured and simulated system response, which includes both identified additional modes, see Figure 3.1.16.

3.1.4 SO(2) Symmetry Validation

In Section 3.1.1 it is shown, by physical equations for the vector modulator, klystron and the cavities, that the open loop structure for the RF field chain follows a SO(2) symmetric structure. Within Section 3.1.2, the mathematical state space model structure, based on a linear time-invariant model in discrete time, is developed to identify a mathematical approximation of the RF field chain. The frequency spectrum is divided into several frequency ranges, where for each region of interest, e.g. around bandwidth and additional fundamental modes, a model could be found. The block-wise extension of the resulting models shows an improvement in finding the resonant modes. Each block of the state space model fulfills a SO(2) symmetric structure, with the freedom to model different couplings, i.e. the phase of the SO(2) structure for each frequency region may change, which will be checked next. The example in Section 3.1.3 presents the precise system

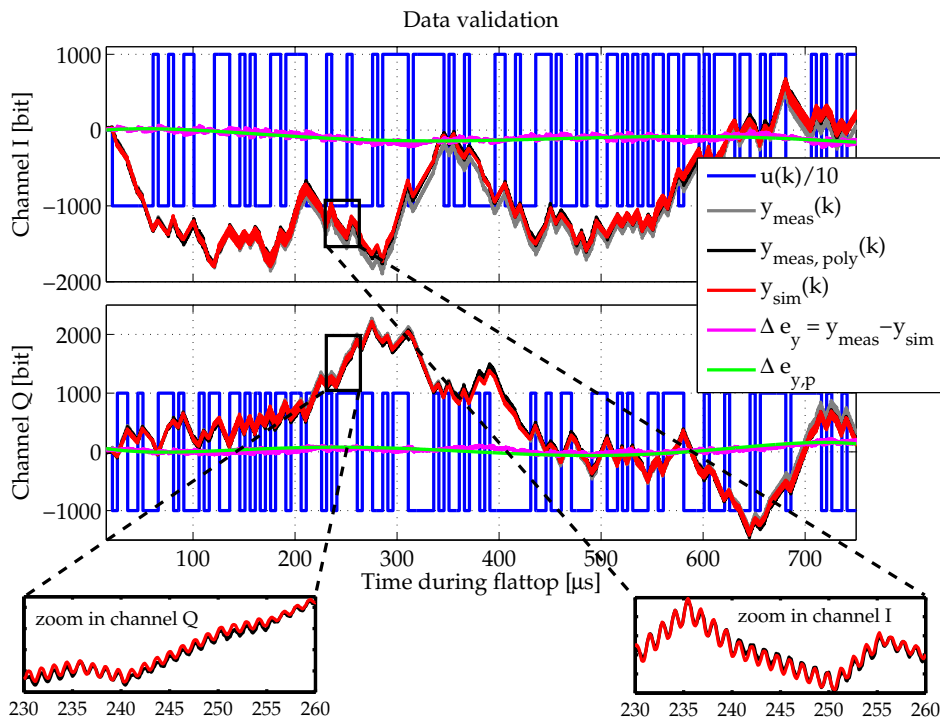


Figure 3.1.16: System cross-validation for the MTCA system with excitation signal $u(k)$. A 5th order polynomial fit of the error signal Δe_y , i.e. $\Delta e_{y,p}$, is used to correct detuning and other second-order effects of the measured signal $y_{meas}(k)$, resulting in $y_{meas,poly}(k)$. The simulated response $y_{sim}(k)$ is displayed for comparison. In addition, two subplots, one for channel I and one for Q, are presented with zoomed into time range, where clearly the $8/9 \pi$ -mode is visible and excited by the PRB signal.

modeling by a cross validation, especially for the MTCA system, where both resonant modes could be identified successfully.

As presented earlier, the model of the MTCA system is well identified and will be used to study the SO(2) symmetry. Recall, that the defined SO(2) symmetric linear discrete-time model has to have the structure

$$\begin{bmatrix} Y_I(z) \\ Y_Q(z) \end{bmatrix} = \begin{bmatrix} G_1(z) & -G_2(z) \\ G_2(z) & G_1(z) \end{bmatrix} \begin{bmatrix} U_I(z) \\ U_Q(z) \end{bmatrix}.$$

Based on the model structure each frequency region is SO(2) symmetric. Computing the response for a considered frequency ω_i , leads to a transition matrix

$$F(\omega_i) = \begin{bmatrix} f_{(1,1)_i} & f_{(1,2)_i} \\ f_{(2,1)_i} & f_{(2,2)_i} \end{bmatrix},$$

in which the elements obey a SO(2) symmetry, claimed by the model structure

$$F(\omega_i) = \begin{bmatrix} f_{(1,1)_i} & -f_{(1,2)_i} \\ f_{(1,2)_i} & f_{(1,1)_i} \end{bmatrix} = \begin{bmatrix} \chi_{1,i} + i\zeta_{1,i} & -(\chi_{2,i} + i\zeta_{2,i}) \\ \chi_{2,i} + i\zeta_{2,i} & \chi_{1,i} + i\zeta_{1,i} \end{bmatrix}.$$

Based on the fundamentals of a SO(2) symmetric matrix and the developed system structure, $F(\omega_i)$ can be written as

$$\tilde{F}(\omega_i) = (\tilde{\chi}_i + i\tilde{\zeta}_i) \begin{bmatrix} \cos(\phi_i) & -\sin(\phi_i) \\ \sin(\phi_i) & \cos(\phi_i) \end{bmatrix},$$

which decomposes the matrix into a complex scaling factor and a real valued rotation matrix. Assuming, that the rotation part does not change for all frequencies, leads to a model representation which is SO(2) symmetric with a fixed plant phase $\phi_G = \phi_i$.

Consider frequencies below the 8/9 π -mode and compute $\phi_G = \phi_i$ for $\omega_i \ll \omega_{\frac{8}{9}\pi}$, then

$$G(z) = A_G(z) \cdot R(\phi_G) \quad (3.1.41)$$

holds, with

$$A_G(z) = \frac{G_1(z)}{\cos(\phi_G)} \quad \text{and} \quad (3.1.42)$$

$$R(\phi_G) = \frac{1}{\sqrt{\det(G(\omega_i))}} G(\omega_i) = \begin{bmatrix} \cos(\phi_G) & -\sin(\phi_G) \\ \sin(\phi_G) & \cos(\phi_G) \end{bmatrix}, \quad \text{for } \omega_i \ll \omega_{\frac{8}{9}\pi}. \quad (3.1.43)$$

This separation is finite for a diagonal dominant system, while for an off-diagonal dominant system, i.e. $\cos(\phi_G) \rightarrow 0$, the scaling part must be redefined as

$$A_G(z) = \frac{G_2(z)}{\sin(\phi_G)}.$$

Figure 3.1.15 shows the identified model. One off-diagonal channel has a phase shift of 180 degree, leading to a SO(2) symmetric structure. Close to the first resonant mode, the phases of the off-diagonal channels are changing its phase relation with the frequency. Hence, the off-diagonal channel which has a phase shift of 180 degree for low frequencies is, between the first and second resonant mode, in-phase with the diagonal channels. As a consequence, caused by the measured signal at the end of a cavity, each even mode has an inverted sign and therefore an additional phase shift of 180 degree, as presented in (3.1.9) on page 21. Caused by the SO(2) symmetric model approach, the diagonal channels are the same and one of the off-diagonal channels is sign-inverted. Nevertheless, since the dynamic behavior for both, the diagonal and off-diagonal channels are the same, it is sufficient to consider only one diagonal and one off-diagonal channel. Mapping the model, shown on the left side of Figure 3.1.17, into a SO(2) symmetric structure with a fixed phase as described above, leads to the bode diagram on the right side of Figure 3.1.17. In the upper plot, the black line sketches the ratio of the diagonal and off-diagonal channel, i.e. variations of the magnitude, which should be constant. In the lower plot, the difference of the diagonal and off-diagonal channels are shown, i.e. phase drifts between both channels, which should be zero. Obviously, for a SO(2) symmetric model with fixed phase ϕ_G , the magnitude ratio and the phase change are constant over all frequencies, while for the identified model it is not. For high frequencies, i.e. frequencies close to the resonant modes, changes of the phase difference and a stronger coupling between the magnitudes

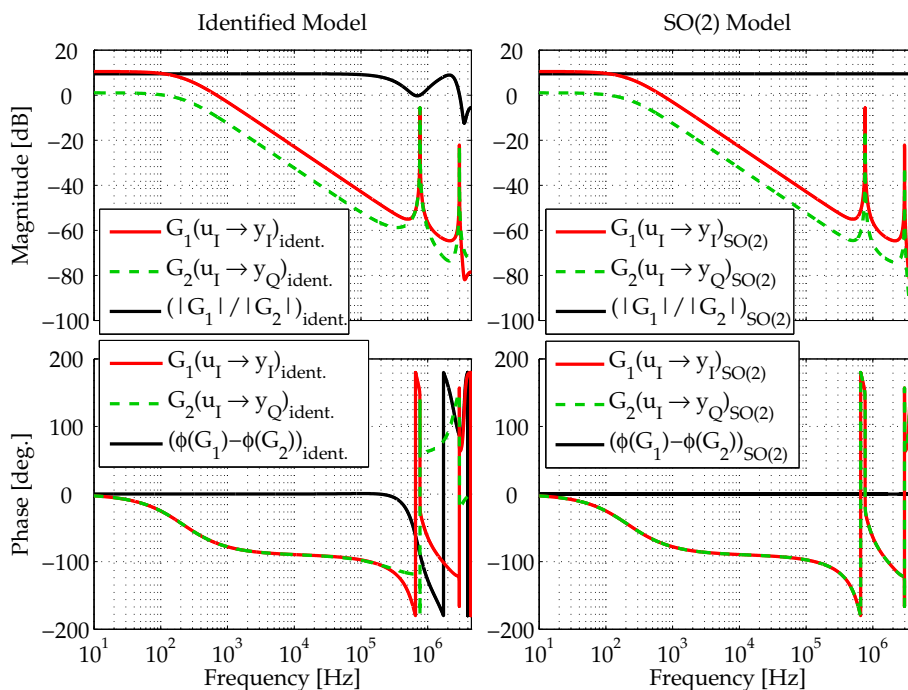


Figure 3.1.17: Identified model as comparison to SO(2) model with fixed rotation matrix $R(\phi_G)$.

with a ratio close to 0 dB is present; with a ratio in magnitude of one, the resonant modes rotates in I/Q plant on a perfect circle with same amount in I and Q .

Beside SO(2) symmetric model with fixed phase, the high frequency part follows (3.1.26)-(3.1.30) and has a common denominator polynomial $D(z)$. The numerator polynomials are independently modeled for the diagonal and off-diagonal channels, such that a model separation leads to

$$G(z) = \frac{1}{D(z)} \begin{bmatrix} N_1(z) & -N_2(z) \\ N_2(z) & N_1(z) \end{bmatrix}. \quad (3.1.44)$$

The ratio of the magnitude ($|G_1|/|G_2|$) and the phase difference ($\phi(G_1) - \phi(G_2)$) differ for the identified model. This is caused by unequal zeros, i.e. $N_1(z) \neq N_2(z)$, especially for frequencies close to resonant modes, here the $8/9 \pi$ -mode and $7/9 \pi$ -mode.

Nevertheless, for frequencies below the first resonant mode the system can be represented as dynamic scaling and fixed SO(2) symmetric rotation part. Even in case of Q_L changes within the cavities, as shown in Figure 3.1.7 on page 30, the plant phase ϕ_G needs not to be updated, while an adjustment of the proportional gain for the dynamic scaling part is necessary. This example is performed during the first MTCA tests and the high frequency behavior, especially the coupling of the resonant modes, must further be studied. Within the controller design first the fixed SO(2) symmetric model, followed by a controller optimization with the identified model is considered. It will be shown, that a controller design based on the SO(2) symmetric model is sufficient as long as passive controllers, e.g. resonant mode suppression by band-stop filters, are considered.

3.2 Beam Modeling

Within this section, the knowledge of the RF field system model is used to identify the relation between RF field and beam in terms of a transfer function model. Within the first section the focus is set to the physical equations of the bunch compressor (BC). At FLASH two BCs are installed, which can be used to control the beam. For the European XFEL it is planned to install three BCs, which will not change the fundamental idea of beam modeling.

3.2.1 Bunch Compressor

A bunch compressor is a magnetic chicane, where the electrons travel on different trajectories depending on the electron energy. The physical equations of a BC consider path length changes l , energy deviations δ_E , orbit changes in x and y and changes of the orbit derivative, e.g. $x' = \partial x / \partial z$, with z as longitudinal position. A first-order approximation, see [Brown, 1975], for a single electron passing a magnetic chicane, is given by

$$\begin{bmatrix} x_f \\ x'_f \\ y_f \\ y'_f \\ l_f \\ \delta_{E,f} \end{bmatrix} = \begin{bmatrix} R_{11} & R_{12} & 0 & 0 & 0 & R_{16} \\ R_{21} & R_{22} & 0 & 0 & 0 & R_{26} \\ 0 & 0 & R_{33} & R_{34} & 0 & 0 \\ 0 & 0 & R_{43} & R_{44} & 0 & 0 \\ R_{51} & R_{52} & 0 & 0 & 1 & R_{56} \\ 0 & 0 & 0 & 0 & 0 & 1 \end{bmatrix} \begin{bmatrix} x_i \\ x'_i \\ y_i \\ y'_i \\ l_i \\ \delta_{E,i} \end{bmatrix}, \quad (3.2.1)$$

where i denotes an initial and f the final vector. The orbit in x and y of each electron changes with respect to the initial orbit, respectively the first derivative by (3.2.1). First, consider only the traveling path of an electron. The final path length l_f depends on the initial path length l_i , the initial electron energy deviation $\delta_{E,i}$ and x_i , x'_i , respectively. The path changes are given by the fifth row of (3.2.1) as

$$l_f = R_{51}x_i + R_{52}x'_i + l_i + R_{56}\delta_{E,i}.$$

The contributions of x_i and x'_i to path changes are small, compared with the relative energy deviation $\delta_{E,i}$, and can be neglected, [Stulle, 2004]. Thus it is sufficient to consider the path difference to compute the final longitudinal position

$$z_f = z_i - (l_f - l_i) = z_i - R_{56}\delta_{E,i} \quad (3.2.2)$$

of the electron with respect to the bunch center after a BC section [Stulle, 2004]. The relative energy deviation is related to the nominal energy and given by $\delta_E = \Delta E / E_0$. The matrix element R_{56} is called the momentum compaction factor or longitudinal dispersion, [Stulle, 2004]. An electron entering the BC changes its output position depending on energy deviations. Hereby, the focus is set to bunch position and therefore bunch arrival time changes. Electrons, which are leaving the first accelerator module, are accelerated to almost speed of light, thus are ultrarelativistic. Time-of-flight changes are

proportional to energy variations by

$$\Delta t_A = \frac{(z_f - z_i)}{v_e} = \frac{\Delta z}{v_e} = -\frac{R_{56} \frac{\Delta E_i}{E_{0i}}}{v_e}, \quad (3.2.3)$$

with an electron velocity $v_e \approx c$. The first bunch compressor at FLASH has a R_{56} of about -180 mm, thus the expected bunch arrival time variation is about 6 ps per percent energy variation (3.2.3). Consider electron bunches where the size and length of each bunch depends on the bunch charge, thus the number of electrons. Therefore (3.2.3) must be computed for each electron or simplified for the center of mass. It is obvious that arrival time changes are caused by energy changes for the center of mass, while energy chirps along the bunch results in rotation of longitudinal phase space or longitudinal compression changes, which is straight forward to show by (3.2.3). Figure 3.2.1 sketches a so-called off-crest acceleration. The leading electrons get less energy than the trailing electrons, resulting in path length differences for the head and tail of the electron bunch. Therefore the longitudinal bunch length is reduced after a BC. This leads to path length and thus arrival time relations of the average beam energy, while the beam energy distribution is related to the energy spread. Converting those energy properties to field properties leads to RF field amplitude and phase relations of the RF modules in front of each BC. Figure 3.2.1 shows the relation of an RF field phase change, thus amplitude, bunch arrival time and compression changes, respectively. Consider the two upper plots, where

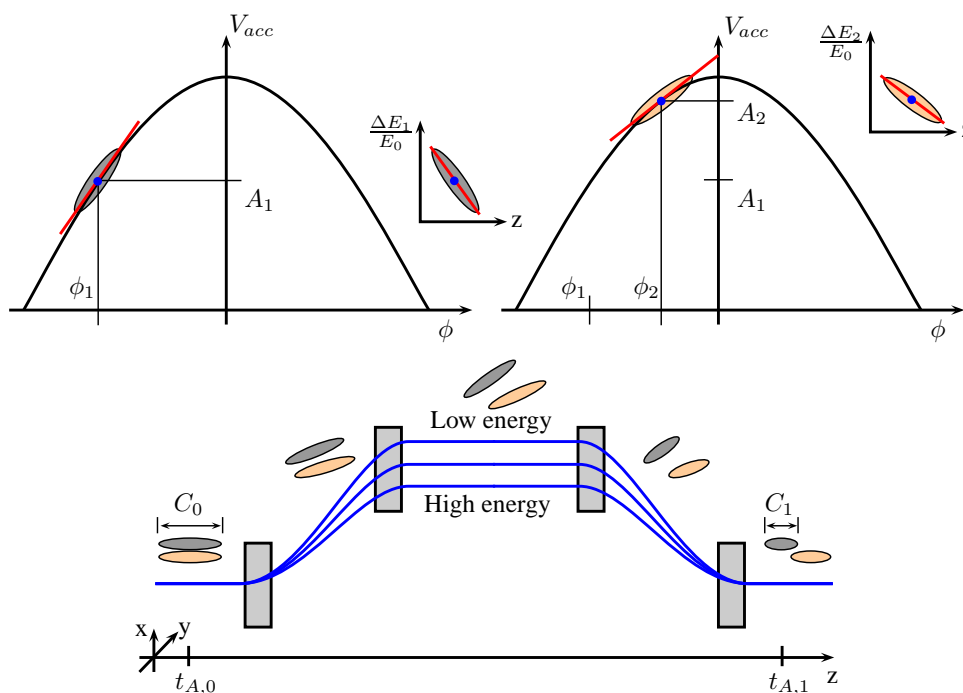


Figure 3.2.1: Sketched bunch compressor with a phase change of the RF field within the previous RF module.

the electron beam energy distribution is shown. Bunch 1, left side, is accelerated by an amplitude A_1 and a phase ϕ_1 . The bunch length extends over a certain RF field phase

and thus amplitude range, which leads to an electron energy spread within the bunch, which is usually normalized by the center of mass energy E_0 . Changing only the RF field phase from ϕ_1 to ϕ_2 , changes the amplitude to A_2 , shown on the right side. Thus, by changing the RF field phase the amplitude changes accordingly. Changing only the amplitude is not affecting the normalized electron energy distribution over the bunch. The lower plot sketches the electron path through a bunch compressor, e.g. for bunch 1, upper left sketch, and for a second bunch, upper right sketch. Depending on the initial beam energy distribution, the bunch arrival time and bunch compression changes are given as linear approximation by

$$\begin{bmatrix} \Delta t_A \\ \Delta C \end{bmatrix} = \underbrace{\begin{bmatrix} t_{11} & t_{12} \\ t_{21} & t_{22} \end{bmatrix}}_{G_B} \begin{bmatrix} \frac{\Delta A}{A} \\ \Delta \phi \end{bmatrix}. \quad (3.2.4)$$

This holds for energy and energy spread changes, respectively amplitude and phase changes of the RF field around the operating setpoint. This transformation matrix converts relative amplitude and absolute phase deviations to bunch arrival time and bunch compression changes of a single bunch and will be seen as static beam model G_B .

Consider a bunch train, e.g. the whole flattop is loaded with bunches with a bunch repetition rate of 1 MHz, such that (3.2.4) is written as discrete-time sequence of beam property changes, as a direct result from field changes,

$$\begin{bmatrix} \Delta t_A(k) \\ \Delta C(k) \end{bmatrix} = [G_B] \begin{bmatrix} \frac{\Delta A}{A}(k) \\ \Delta \phi(k) \end{bmatrix}. \quad (3.2.5)$$

Rewriting the relative amplitude changes to absolute ones leads to

$$\underbrace{\begin{bmatrix} \Delta t_A(k) \\ \Delta C(k) \end{bmatrix}}_{y_B(k)} = [G_B] \cdot \overbrace{\begin{bmatrix} \frac{1}{A} & 0 \\ 0 & 1 \end{bmatrix}}^{\tilde{G}_B} \underbrace{\begin{bmatrix} \Delta A(k) \\ \Delta \phi(k) \end{bmatrix}}_{\tilde{e}_F(k)}, \quad (3.2.6)$$

where a part of the relative amplitude deviation, i.e. $1/A$, is separated into the static beam model \tilde{G}_B . Thus for given deviations of RF field amplitude and phase, possible bunch arrival time and bunch compression deviations are computed.

Note: For an off-crest acceleration, i.e. the beam phase w.r.t. RF field phase is non-zero, the static beam models G_B and \tilde{G}_B are nonsingular.

3.2.2 Example at FLASH

In principle, the identification of the beam model can be done in the same way like the RF field system. Exciting the system by well known identification input signals, e.g. PRB or chirp sine signals, leads to a system response in a desired frequency range. Unfortunately, the electron beam is not always available and especially for long bunch trains, e.g. a fully

loaded flattop, not easily set up, such that losses within the accelerator are minimal. Thus, only a static matrix, which maps the RF field to beam properties will be identified. Next, the dynamic part is superimposed by the field model. Figure 3.2.2 shows an example for the behavior of bunch arrival time and bunch compression, respectively, depending on changes in RF field amplitude and phase. Based on this, a transformation matrix,

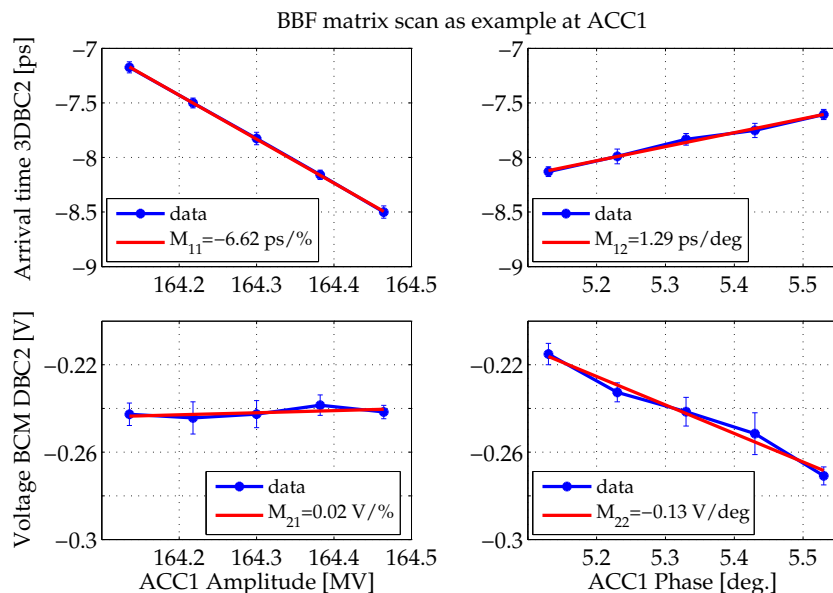


Figure 3.2.2: Example for estimating the beam model by a BBF matrix as variation of the RF field amplitude and phase within the accelerator module ACC1 at FLASH.

mapping field to beam properties, is estimated, using the method of least squares. It has to be mentioned that ACC1 is operated in series with the third harmonic module ACC39, which decelerates the bunch by an amplitude of $1/9$ of the amplitude of ACC1. As a consequence, the factor $1/A$ needs to be defined as

$$\frac{1}{A} = \frac{1}{A_{ACC1} + A_{ACC39}} = \frac{1}{A_{ACC1} - \frac{1}{9}A_{ACC1}} = \frac{1}{\frac{8}{9}A_{ACC1}} \approx 1.1 \frac{1}{A_{ACC1}},$$

which means that the estimated bunch arrival time change is 1.1 times too high. By this a bunch arrival time change of about 6 ps per percent energy deviation in ACC1 is expected and estimated. Here only ACC1 is considered, while the third harmonic RF module is driven as described in Appendix B.1, i.e. no correction is done.

3.3 Combination of RF Field and Beam Model

The RF field model contains the dynamics, e.g. the 8/9 π -mode of the system and was derived within the previous section as

$$\underbrace{\begin{bmatrix} y_I(k) \\ y_Q(k) \end{bmatrix}}_{y_F(k)} = \begin{bmatrix} G_{II}(z) & G_{IQ}(z) \\ G_{QI}(z) & G_{QQ}(z) \end{bmatrix} \cdot \underbrace{\begin{bmatrix} u_I(k) \\ u_Q(k) \end{bmatrix}}_{u(k)}. \quad (3.3.1)$$

Converting y_F to amplitude and phase, leads to

$$\tilde{y}_F(k) = |y_F(k)| \cdot e^{i \cdot \arg(y_F(k))} \quad (3.3.2)$$

$$= \sqrt{y_I^2(k) + y_Q^2(k)} \cdot e^{i \cdot \arctan\left(\frac{y_Q(k)}{y_I(k)}\right)}, \quad (3.3.3)$$

such that the RF field model can be combined with the beam model. Figure 3.3.1 shows the basic idea obtaining the beam model, with the input to the vector modulator as input signal and the beam properties as output signal. Subtracting the reference of the RF field

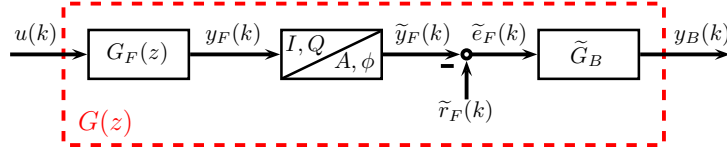


Figure 3.3.1: Model based plant design which combines the RF field and beam properties.

operating setpoint leads to field variations in amplitude and phase, $\tilde{e}_F(k)$. These small amplitude and phase deviations change the beam properties, such that a beam model can be derived. Since the field dynamics are known, the identification of the static matrix G_B or \tilde{G}_B is sufficient. This model based approach considers changes of the RF field in amplitude and phase with respect to the bunch arrival time and compression. The latency from the input signal $u(k)$ to $y_F(k)$ is part of the field model $G_F(z)$. Next, compare the latency between the measured RF field and the measured beam-based signal, shown in Figure 3.3.2. An excitation signal $u(k)$ is added to the feedforward signal of ACC1 for visualizing the resulting relative amplitude and thus bunch arrival time changes. The latter are mapped to relative amplitude deviations by dividing Δt_A by R_{56} . Shifting this signal by 2 μs fits almost to the RF field amplitude changes, thus the bunch arrival time signal is sampled and preprocessed faster than the RF field signal.

Consider the geometry of each cavity. Only the π -mode is used to accelerate the electrons. Other fundamental modes, which are present in a nine cell cavity, will be considered as disturbances of the RF field. An ultrarelativistic electron flying through a cavity is further accelerated by this disturbed RF field. Consider only the 8/9 π -mode of the cavity. For this mode, the acceleration field is theoretically superimposed by 4 sinusoidal functions, in which each electron gets four times more and four times less energy. Assume based on the latter, each even additional fundamental mode is not seen by the electron if each

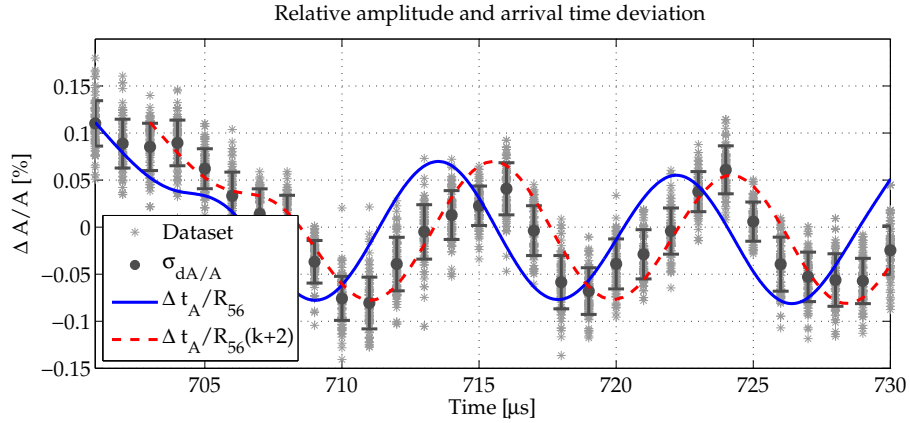


Figure 3.3.2: Latency between measured RF field (VME system) and bunch arrival time for an excitation signal on the amplitude of ACC1 at FLASH.

cavity is well tuned, i.e. a detuning close to zero. As a consequence, each even additional fundamental mode has to be removed from the beam model, e.g. by extending the RF field model by a band-stop filters which removes these mode. This consideration must further be studied and verified by beam measurements with a high bunch repetition rate.

3.4 Conclusion

This chapter has shown the system identification of the RF field and beam model, i.e. the bunch arrival time and bunch compression. First, a small signal model for the RF field is identified by exploiting symmetries of the RF-system. The excitation signal is applied during the flattop phase, i.e. with bounded excitation time, where the RF field performance must be within predefined specifications, [Altarelli et al., 2006]. As the high frequency characteristic is only roughly estimated by black box identification, [Schmidt, 2010], a grey box model based on a $SO(2)$ symmetric structure is developed to cope with this limitation. The identification procedure is separated into two parts, one for the low frequency characteristic and one for the high frequencies. By analyzing the resulting grey box model it has been shown, that the model is $SO(2)$ symmetric for all frequencies and with the limitation of a not changing plant phase it is $SO(2)$ up to the $8/9 \pi$ -mode. The specified symmetric model structure is already successfully used during identification of the FLASH plant. An example by extending the identification structure by two additional parameters to cope with non-symmetric plants is presented in Appendix B.2.

Beside the RF field model, the physical equations of the bunch compressor show a direct mapping from RF field amplitude and phase deviations to bunch arrival time and bunch compression deviations, which is in first-order approximation a static matrix operation. This has been verified by measurements at FLASH. The combination of RF field and beam model is a necessary condition for optimal beam-based feedback, presented in Section 5.1. One has to take into account, that in theory the even additional fundamental modes of a cavity are not changing the electron energy during acceleration by a cavity. This must be further studied and validated by measurements.

Chapter 4

RF Field Controller Design

This chapter describes the systematic RF field controller design based on the identified RF field plant model, Section 3.1. Having a good controller minimizes residual errors within a pulse as well as from pulse to pulse, i.e. intra-train control and adaptive feedforward strategies, respectively. During the last years RF field control strategies were developed and included in the LLRF controller [Schmidt, 2010]. In consequence of pulsed mode operation, two control strategies are necessary. On one hand a multi-input multi-output (MIMO) controller minimizes RF field amplitude and phase errors within the pulse. On the other hand iterative learning control (ILC) corrects the feedforward signal to minimize repetitive errors from pulse to pulse. Both kinds of controllers are essential to achieve high RF field performance. Optimal RF field control is a necessary step for optimal beam control.

This chapter is divided into three parts. Section 4.1 considers the RF field feedback controller, acting within a pulse. It will be shown, that making use of the $SO(2)$ symmetric RF field model helps to optimize the RF field controller. Special controller requirements are given with respect to the later used beam-based feedback controller. Within Section 4.2 the norm optimal iterative learning control algorithm is recalled and simplifications regarding the possibility to implement this algorithm on an FPGA are given. It will be shown, that the RF field model and the RF field controller leads to a closed-loop plant which is $SO(2)$, hence the algorithm can be simplified by exploiting the $SO(2)$ symmetry. Furthermore, the algorithm can be expressed by a tensor based scheme which further simplifies the algorithm and makes an FPGA implementation possible. The last section concludes this chapter.

Parts of this chapter are published in [Pfeiffer et al., 2012b], [Pfeiffer et al., 2012c] and [Pfeiffer and Lichtenberg, 2013].

4.1 RF Field Feedback Controller

The section is divided into three parts. First, an introduction to the considered RF field plant properties and the RF field controller requirements is given. Section 4.1.2 considers the general controller design strategy fulfilling a plant decoupling. This is followed by a controller extension to avoid the excitation of additional fundamental modes. The proposed controller design follows a two-step method, i.e. an analytical controller computation, based on the SO(2) symmetric plant structure, is optimized in a second step by a mixed-sensitivity design. An example for the VME and MTCA system completes this section.

4.1.1 Introduction

The RF field feedback controller, based on a black box RF field model, are described in e.g. [Langkowski, 2008] and [Schmidt, 2010].

Within this section, the proposed controller design is on:

- SO(2) symmetric plant model for all frequencies
- Discrete-time eigenvalues inside unit disc
- Discrete-time zeros inside, on, or outside unit disc

Based on the system model, a controller has to be designed, which must fulfill the following *RF field controller requirements*:

- (1) Low order controller design
- (2) Decouple the channels I and Q from reference to vector sum signal
- (3) Avoid the excitation of additional fundamental modes
- (4) Optimal closed-loop behavior for fixed controller order

These requirements are further necessary steps for an optimal intra-train longitudinal beam-based feedback controller, see Section 5.1.

First, the controller design of $C(z)$ for a general SO(2) symmetric plant $\hat{G}(z)$, see Figure 3.1.5 on page 28, is considered and visualized in Figure 4.1.1, where the SO(2) grey box model of the system containing an input-output time delay T_d fulfills

$$\hat{G}(z) = \begin{bmatrix} \hat{G}_1(z) & -\hat{G}_2(z) \\ \hat{G}_2(z) & \hat{G}_1(z) \end{bmatrix}.$$

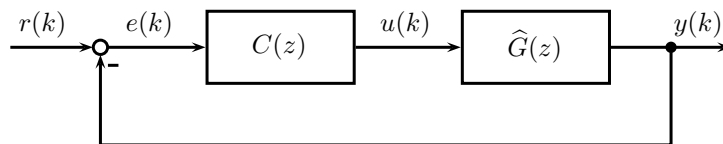


Figure 4.1.1: Closed-loop model containing the plant model $\hat{G}(z)$ and the controller $C(z)$ to be designed.

4.1.2 General Approach

The general controller design for a $SO(2)$ symmetric plant model is considered to fulfill the given *RF field controller requirements*. The designed MIMO controller will be implemented on an FPGA, thus the controller order is limited by constraints, i.e. the FPGA resource limitation and acceptable processing delays.

Fixed Order Controller Based on the restrictions within the FPGA, each transfer function of the two-input, two-output controller is implemented with a fixed order. Currently, the controller is given as

$$C(z) = \begin{bmatrix} C_{11}(z) & C_{12}(z) \\ C_{21}(z) & C_{22}(z) \end{bmatrix}, \quad (4.1.1)$$

where each element is implemented as a second order transfer function, following

$$C_{ij}(z) = \frac{b_{0,ij} + b_{1,ij}z^{-1} + b_{2,ij}z^{-2}}{1 + a_{1,ij}z^{-1} + a_{2,ij}z^{-2}}, \quad i, j = 1, 2.$$

The following sections consider decoupling and mode suppression within the controller $C(z)$, shown in Figure 4.1.2.

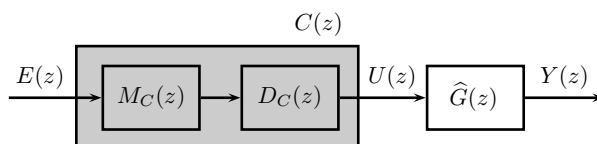


Figure 4.1.2: Design of the controller $C(z)$, which is separated in mode suppression part $M_C(z)$ and a decoupling part $D_C(z)$.

Decoupling The closed-loop behavior is designed such that a decoupling of the processed signals, here between the real and imaginary part of error signal $E(z)$ and the real and imaginary part of vector sum signal $Y(z)$, is fulfilled. A strategy for such decoupling of system is studied in the following. Assume $M_C(z)$ is set as identity matrix.

Consider $G(z)$ to be a plant model without time delay which should result in a low order decoupling part $D_C(z)$. The proposed strategy present a system decoupling which comes with the benefit of a low order decoupling implementation within the FPGA and results in a *controller design by exploiting the $SO(2)$ symmetric plant model*.

We now consider frequencies below the additional fundamental modes, e.g. for the MTCA system frequencies up to 100 kHz, of the plant model given in Section 3.1. In Section 3.1.4 it is shown that the coupling from the diagonal to the off-diagonal channel is constant up to a certain frequency and that the ratio is given by the plant model phase ϕ_G . This allows a static decoupling by assuming a constant rotation matrix $R(\phi_G)$ for all frequencies.

The plant is approximated by

$$G(z) = \begin{bmatrix} G_1(z) & -G_2(z) \\ G_2(z) & G_1(z) \end{bmatrix} = A_G(z) \cdot \overbrace{\begin{bmatrix} \cos(\phi_G) & -\sin(\phi_G) \\ \sin(\phi_G) & \cos(\phi_G) \end{bmatrix}}^{R(\phi_G)}, \quad (4.1.2)$$

see (3.1.41)-(3.1.43), leading to a static decoupling matrix

$$D_C = \overbrace{\begin{bmatrix} \cos(\phi_G) & \sin(\phi_G) \\ -\sin(\phi_G) & \cos(\phi_G) \end{bmatrix}}^{R(\phi_G)^T},$$

to ensure the system is sufficiently decoupled. Hence, the loop gain for the approximated system is in low frequency

$$L(z) = D_C G(z) = A_G(z) R(\phi_G)^T R(\phi_G) = A_G(z) \mathbf{I},$$

which is decoupled. Since the model is chosen to be SO(2) symmetric with a fixed rotation matrix, the real system is decoupled up to a certain frequency. The advantage of using a static matrix for decoupling comes with the benefit that no additional dynamics must be inserted in $C(z)$.

During the further RF field controller design only this static decoupling is used. It is sufficient to describe the model by (3.1.43), page 40, with a constant rotation matrix $R(\phi_G)$, since the system behavior up to the desired closed-loop bandwidth for this application is almost perfectly modeled. The contribution of slight cross-couplings can be neglected to fulfill the requirement of a low order controller implementation, which is just a static gain corresponding to $R(\phi_G)^T$.

Mode suppression As known from the white box model, additional fundamental modes are present. These are the 8/9 π -mode down to the 1/9 π -mode. Exciting these modes leads to oscillations of the vector sum, while each cavity mode has a narrow bandwidth, [Schmidt et al., 2012]. One can think of two different strategies:

- 1: Active mode suppression
- 2: Passive mode suppression

In presence of oscillations and thus excited resonant modes, an *active mode suppression* has to be used to suppress the regarding oscillations, e.g. in simplified terms by feeding back the oscillations with a phase shift of 180 degree. Here the vector sum, the sum of

up to 32 cavity signals, is controlled. It cannot be guaranteed that each resonant mode is exactly at the same frequency, hence the vector sum can host multiple modes of the same type. Each identified resonant mode of the RF field model is a distribution of several resonant modes, where the frequency spread of these modes is given by the width of the identified resonant mode.

In the following, a *passive mode suppression* is considered, i.e. the excitation of these modes is avoided. As presented in Section 3.1.3, each resonant mode is identified as complex conjugate pair of eigenvalues within one step. The SISO transfer function $A_G(z)$ of $G(z)$, see (4.1.2), contains the dynamics, i.e. the eigenvalue for low frequency behavior and complex conjugate pairs of eigenvalues as additional resonant modes. Using an inverse dynamics and setting the complex conjugate pairs of eigenvalues p_i for $i = 1, \dots, m$ as zeros, leads to a SISO transfer function

$$M_C(z) = K_{M_C} \frac{(z - p_1)(z - p_2) \cdots (z - p_m)}{(z - \hat{p}_1)(z - \hat{p}_2) \cdots (z - \hat{p}_m)}, \quad (4.1.3)$$

with K_{M_C} as proportional gain and additional poles \hat{p}_i for $i = 1, \dots, m$ to guarantee a bi-proper system, i.e. an equal number of poles and zeros. The zeros impose band-stop filters at frequency regions which should not be excited. The real eigenvalue, describing the system bandwidth, is not considered to keep the controller order low. Select the necessary poles to be suppressed by defining a frequency range and determine their natural frequency by

$$\omega_{n_i} = \text{Im} \left\{ \frac{\ln(p_i)}{T_s} \right\}, \quad (4.1.4)$$

where p_i is a pole of $A_G(z)$ and T_s is the sampling time. The dynamic mode suppression part is normalized to a low-frequency gain of one by computing

$$K_{M_C} = \frac{(1 - \hat{p}_1)(1 - \hat{p}_2) \cdots (1 - \hat{p}_m)}{(1 - p_1)(1 - p_2) \cdots (1 - p_m)}, \quad (4.1.5)$$

which follows from the final value theorem in discrete time. The SO(2) symmetric controller is designed by a dynamic transfer function, which is a SISO band-stop filter containing all resonant modes and a static matrix, which maps the SISO transfer function to a MIMO controller, i.e. $M_C(z)$ and D_C , respectively. An additional proportional diagonal gain K_P is included to further reduce the RF field error, while further increasing this gain causes additional beam energy fluctuations, as presented in [Gerth et al., 2009]. The proportional gain is initially adjusted regarding the minimal energy fluctuations. Up to this point, the MIMO controller contains a proportional gain and band-stop filters, while the controller is designed only by the SO(2) symmetric plant approximation with constant rotation matrix and without time delay. Hence, this analytically computed controller

$$C_{ana}(z) = \frac{U(z)}{E(z)} = K_P M_C(z) D_C \quad (4.1.6)$$

is further improved with an optimization algorithm based on the plant model with time delay $\hat{G}(z)$, considered in the following.

Controller Optimization using HIFOOd

Optimality Several optimization algorithms are used to optimize the closed-loop system behavior, e.g. a mixed sensitivity design by H_∞ optimization, depicted in Figure 4.1.3.

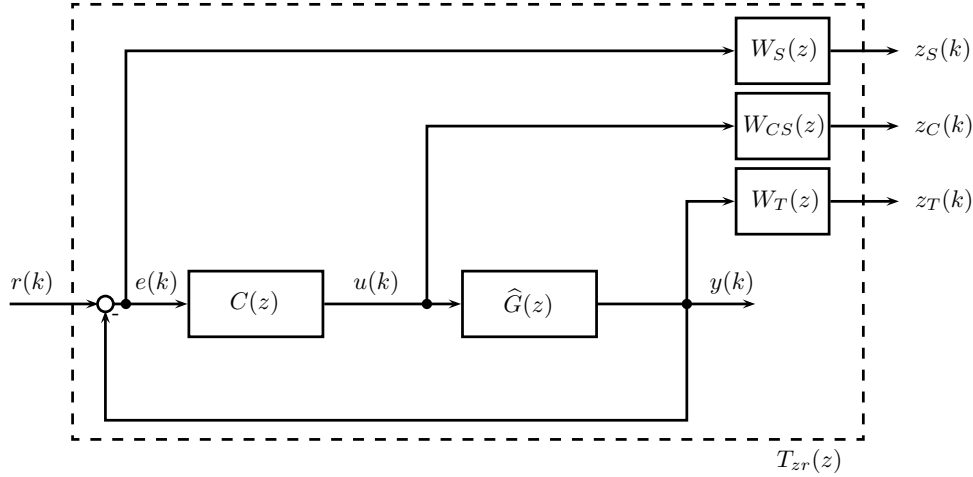


Figure 4.1.3: H_∞ controller design with constraints from $r(k)$ to $e(k)$, i.e. sensitivity $S(z)$ weighted by $W_S(z)$, control sensitivity $C(z)S(z)$ from $r(k)$ to $u(k)$ is weighted by $W_{CS}(z)$ and from $r(k)$ to $y(k)$ as complementary sensitivity $T(z)$ weighted by $W_T(z)$.

Since the controller order is fixed, an H_∞ fixed order optimization in discrete time (HIFOOd) [Popov et al., 2010] is used. The goal is to find a controller $C(z)$ such that

$$\|T_{zr}(z)\|_\infty = \left\| \begin{bmatrix} W_S(z) \cdot S(z) \\ W_{CS}(z) \cdot C(z)S(z) \\ W_T(z) \cdot T(z) \end{bmatrix} \right\|_\infty < 1, \quad (4.1.7)$$

where $z(k) = [z_S(k), z_C(k), z_T(k)]^T$ is a fictitious output vector, filtered by $W_S(z)$, $W_{CS}(z)$ and $W_T(z)$ to describe the relative importance and frequency content of disturbance, setpoint and noise signals [Skogestad and Postlethwaite, 2005]. From the definition of H_∞ norm, (4.1.7) is equivalent to

$$\sup_{\theta \in [0, \pi]} \bar{\sigma} \left(\begin{bmatrix} W_S(e^{i\theta}) \cdot S(e^{i\theta}) \\ W_{CS}(e^{i\theta}) \cdot C(e^{i\theta})S(e^{i\theta}) \\ W_T(e^{i\theta}) \cdot T(e^{i\theta}) \end{bmatrix} \right) < 1, \quad (4.1.8)$$

with $\bar{\sigma}$ as maximum singular value of the transfer function matrix $T_{zr}(e^{i\theta})$.

Without going into detail, the choice of the weighting functions can be summarized as follows:

- Shaping the *sensitivity* $S(z)$ by $W_S(z)$ covers the low frequency design, including reference tracking and system bandwidth.

- The attenuation of measurement noise at high frequencies is expressed by introducing $W_T(z)$ which shapes the *complementary sensitivity* $T(z)$.
- The *control sensitivity* $C(z)S(z)$ impose limits on the control effort typically at high frequencies; here it is used to ensure the resonant mode suppression.

The interested reader is referred to [Skogestad and Postlethwaite, 2005] for further information concerning mixed sensitivity design.

The HIFOOD controller optimization is initialized, since HIFOOD typically tends to converge towards local minima, with the previously designed analytically determined controller based on $G(z)$ and in addition the controller structure is specified by

$$\begin{aligned} x(k+1) &= \begin{bmatrix} \Phi_c & 0 \\ 0 & \Phi_c \end{bmatrix} x(k) + \begin{bmatrix} \Gamma & 0 \\ 0 & \Gamma \end{bmatrix} e(k), \\ u(k) &= \begin{bmatrix} C_1 & C_2 \\ -C_2 & C_1 \end{bmatrix} x(k) + \begin{bmatrix} D_1 & D_2 \\ -D_2 & D_1 \end{bmatrix} e(k) \end{aligned} \quad (4.1.9)$$

to ensure $SO(2)$ symmetry and therefore decoupling. The parameter block Φ_c defines a complex conjugate pair of eigenvalues, Γ the input matrix, C_i the output matrix and D_i the direct feedthrough for $i = 1, 2$, respectively. Besides specifying the controller structure, one can penalize the sensitivity using the off-diagonal weighting functions, which is not studied further. Such a $SO(2)$ symmetric approach reduces the set of parameters, which must be optimized, by a factor of two.

To recap: The controller design is divided into two steps. First, an analytically calculated MIMO controller, based on the plant approximation without time delay $G(z)$ as shown in the previous part, followed by a controller optimization with a mixed-sensitivity design based on the plant model $\hat{G}(z)$ containing the time delays.

4.1.3 Example at FLASH

The main parts of the previously described controller design strategy are validated for the VME and MTCA system, where the focus is on decoupling and suppression of additional fundamental modes. The latter is mainly important for the MTCA system, where these modes are located within the Nyquist frequency, see Section 3.1. The first subsection gives an example for the VME system. Here, it is shown how decoupling improves the system performance. Afterwards, the proposed controller design is shown with measurements and simulations for the MTCA system, where the focus is on decoupling, mode suppression and optimal control. To keep repetitive RF field errors around zero, iterative learning control (ILC) [Rogers et al., 2010] is used to adapt the feedforward tables from pulse to pulse, [Kirchhoff et al., 2008] and [Schmidt, 2010], such that only the designed MIMO controller acts within the pulse. Further ILC details can be found in Section 4.2.

RF Field Controller Design for VME System

The bode diagram of the identified model with a sampling frequency of 1 MHz, here ACC1, is shown in Figure 3.1.13 on page 38. It can be seen that the difference of the magnitude is constant over the frequency up to the aliased additional fundamental mode around $f_{8/9 \pi} \approx 200$ kHz. Due to the aliased mode and low resonant peak in frequency domain, the effect of this mode is negligible for the VME system, in contrast to the identified model for the MTCA system. Thus, a proportional controller will not excite the aliased $8/9 \pi$ -mode and is in principle sufficient for this sampling time. The designed SO(2) symmetric controller

$$C(z) = \begin{bmatrix} C_1(z) & C_2(z) \\ -C_2(z) & C_1(z) \end{bmatrix}, \quad (4.1.10)$$

which is optimized by HIFOOD, is tested at FLASH and compared with a standard diagonal proportional controller

$$K_P = \begin{bmatrix} K_{P,I} & 0 \\ 0 & K_{P,Q} \end{bmatrix}, \quad (4.1.11)$$

as shown in Figure 4.1.4. During flattop, a PRB signal is added to the reference signal

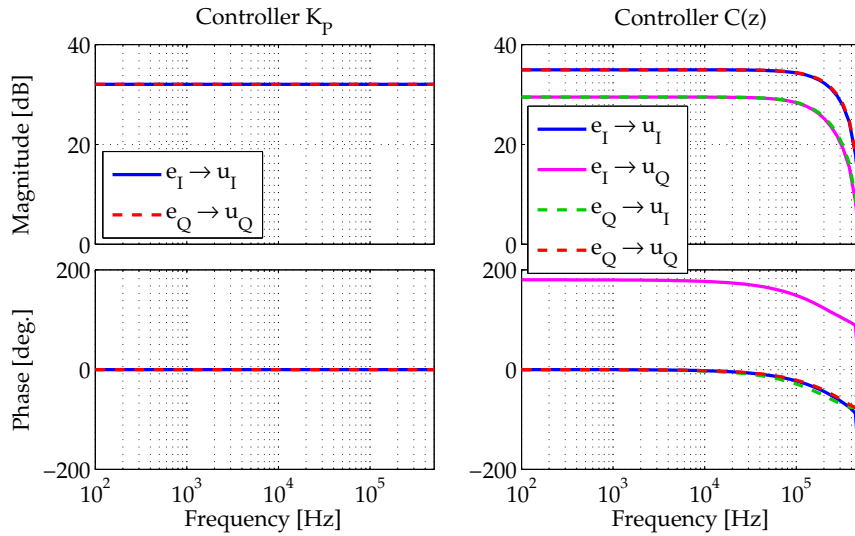


Figure 4.1.4: The left side shows the MIMO controller as diagonal proportional controller with $K_{P,I} = K_{P,Q} = 40$ (≈ 32 dB), the right side the SO(2) symmetric controller optimized by HIFOOD with a low frequency gain of 56 (≈ 35 dB) and 29 (≈ 29 dB) on diagonal and off-diagonal channel, respectively.

of the real channel and the effect on the vector sum signal is analyzed, see Figure 4.1.5. Such a reference change is similar to an error signal on the considered channel. It can be seen that couplings and therefore remaining errors are reduced by a decoupled closed-loop plant.

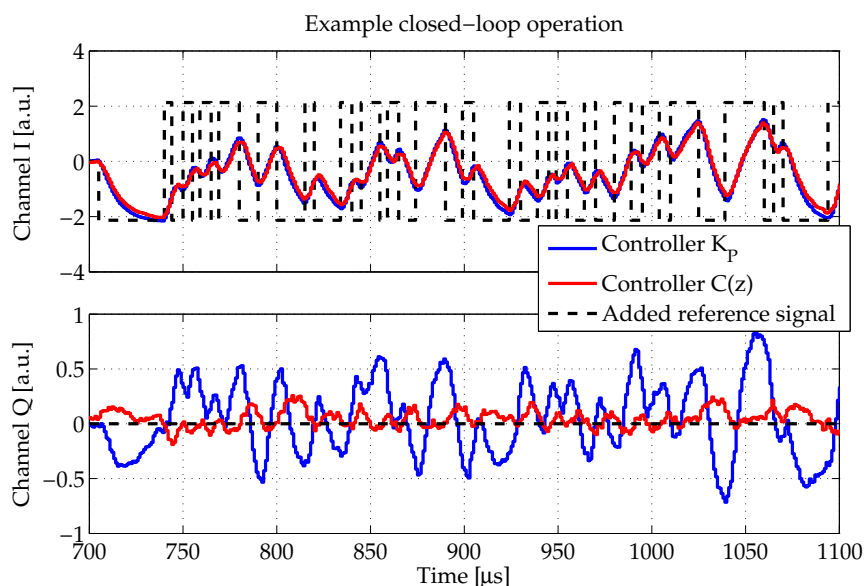


Figure 4.1.5: Controller decoupling with defined reference trajectory as comparison of diagonal proportional and designed SO(2) MIMO controller during flattop time.

The designed SO(2) symmetric controller is permanently in normal operation at FLASH and improves the RF field performance. Figure 4.1.6 shows the improvements of a standard diagonal proportional controller and the computed SO(2) controller for the VME system. Due to the aliased $8/9 \pi$ -mode, the performance is mainly affected by a decoupled

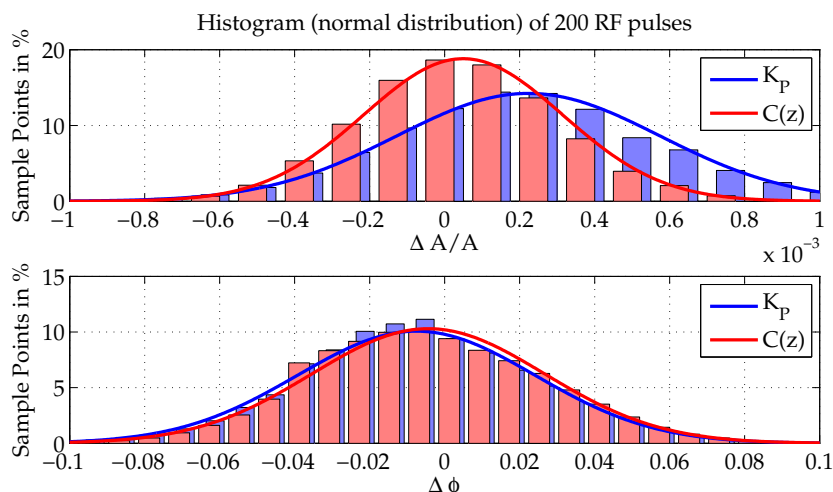


Figure 4.1.6: Controller comparison for ACC45 driven by the VME system at FLASH. The RF field performance, given as standard deviation, for K_P are $\Delta A/A = 0.046\%$ and $\Delta\phi = 0.031^\circ$ and for $C(z)$ given by $\Delta A/A = 0.027\%$ and $\Delta\phi = 0.031^\circ$.

closed-loop plant and minimal by the $8/9 \pi$ -mode. Each bar of the histogram corresponds to a quantization step of the measured vector sum signal, see Figure 4.1.7.

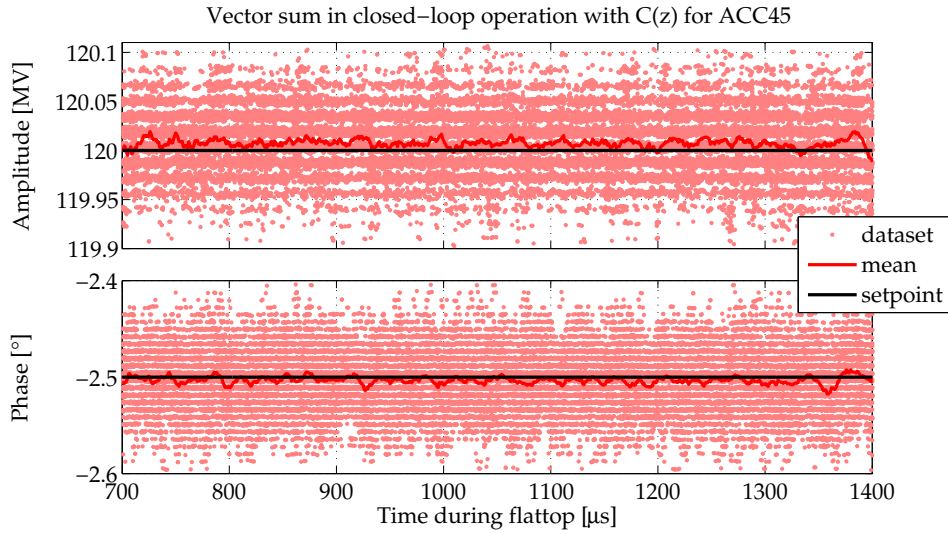


Figure 4.1.7: Measured vector sum signal of ACC45 during flattop in closed-loop operation with $C(z)$. The plot over time corresponds to the histogram given in Figure 4.1.6.

Since the RF field performance limit is almost reached and could not be further improved, the next subsection gives an outlook on the controller design for the MTCA system.

RF Field Controller Design for MTCA System

During this research project, one RF station at FLASH was experimentally equipped with the MTCA system and the main controller performance result, based on the proposed SO(2) symmetric controller design strategy, is presented.

In the following, a mixed sensitivity H_∞ controller design will be shown, which uses the SO(2) symmetric RF field structure to suppress the $7/9 \pi$ -mode. The $8/9 \pi$ -mode, which does not couple to the beam, see Section 3.3, page 46, is removed from each individual cavity signal using a notch filter, i.e. band-stop filter with a narrow stopband, [Schmidt et al., 2012]. Hence, it is assumed that the plant model consists of a real eigenvalue, representing the bandwidth, and one complex conjugate pair of eigenvalues, i.e. $7/9 \pi$ -mode. An example for using the proposed RF field controller design to suppress the $8/9 \pi$ -mode can be found in [Pfeiffer et al., 2012c]. The controller design includes plant decoupling, which is needed for additional longitudinal beam-based feedbacks, shown in Section 5.1. Furthermore, unwanted additional fundamental modes leading to a degradation of the regulation performance should be suppressed or at least not excited. In [Vogel, 2007] the theoretical background for time delay changes within the LLRF system is given, which is briefly validated with measurements at FLASH for the $7/9 \pi$ -mode and $8/9 \pi$ -mode. Further information regarding the influence and the frequency spread of both modes can be found in [Schmidt et al., 2012].

Characterization of Feedback Loop for Different Time Delays As is known, time delays of the plant change the phase for high frequencies, where the additional fundamental modes are located. Those phase changes feed back excited resonant modes with a corresponding phase, in worst case with a phase shift of 180 degree, resulting in a positive feedback. Assume that the controller $C(z)$ is set as proportional gain $C(z) = K_P \mathbf{I}$. An additional time delay, to display e.g. changes in cable length or different processing times, is introduced by shifting the output signal in steps corresponding to 81 MHz clock cycles. Figure 4.1.8 shows on the left side the amplitude stability of the 8/9 π -mode for a feedback gain scan with different additional time delays. The color code represents the

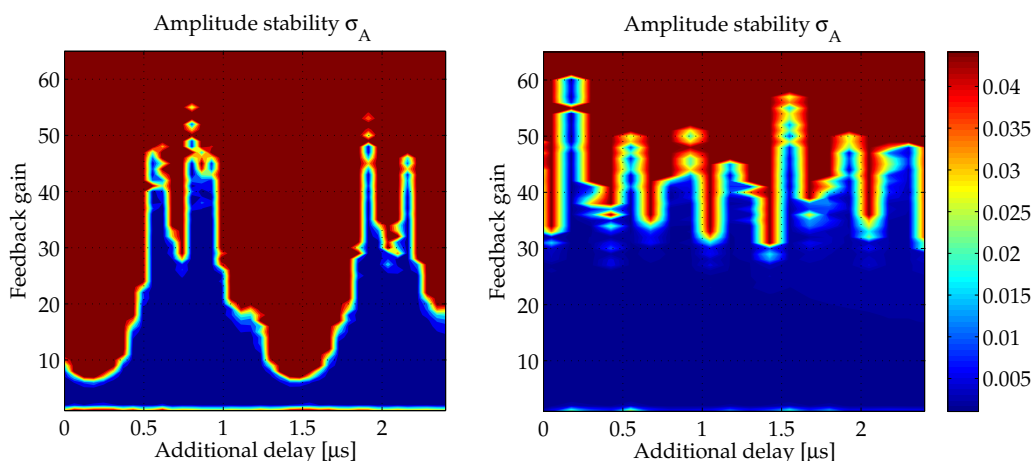


Figure 4.1.8: Feedback gain scan as function of an additional delay for a diagonal proportional controller without (left plot) and with (right plot) applied 8/9 π -mode notch filters. The difference between the minimal feedback gain which causes an amplitude instability corresponds to the magnitude of occurring resonant modes, see Figure 3.1.15 on page 38.

standard deviation of the RF field amplitude error. The red area is unstable consequently the blue one is the desired stable operating point for proportional feedback controller. It can be seen, that one important point within the controller design is to avoid the excitation of this mode and therefore the resulting positive feedback, e.g. by using a notch filter. The frequency location of this mode is computed by inverting the absolute value of time difference between two unstable areas, here for an additional time delay of 0.2 μs and 1.5 μs , corresponding 770 kHz. Between these two areas an additional unstable area is found.

Assume, the 8/9 π -mode is filtered for each cavity signal, thus it is not measurable on the vector sum signal to be controlled. Figure 4.1.8 presents on the right side the amplitude stability of the 7/9 π -mode for an increasing proportional gain with different additional delays. The corresponding resonant mode of about 3 MHz is determined for an additional time delay of about 0.7 μs and 1.05 μs . With the current signal processing, i.e. without additional time delay, and by increasing the proportional gain, this mode is fed back with a positive feedback, such that the amplitude stability is limited by the 7/9 π -mode. For

the basic controller design, it is sufficient to show how this mode can be suppressed or at least not excited by using the current controller implementation, following next.

Controller Design with SO(2) Symmetry

First, separate the plant into a scaling $A_G(z)$ and rotation matrix $R(\phi_G)$, see (4.1.2). The complex conjugate pairs of eigenvalues, i.e. the resonant modes, can be computed directly from $A_G(z)$. Place a band-stop filter at these modes, realized as a second order transfer function in $M_C(z)$. The multiplication of $M_C(z)$, (4.1.3), with the transpose of plant rotation matrix R_G^T , maps the designed SISO controller back to the MIMO controller, fulfilling the SO(2) symmetry, thus the decoupling. Figure 4.1.9 shows the bode plot for the transfer function matrix of the analytically computed controller $C_{ana}(z)$.

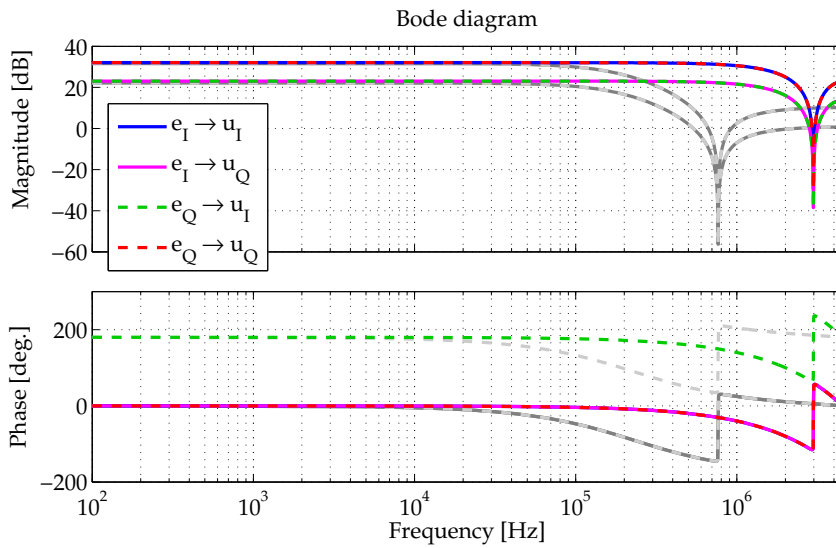


Figure 4.1.9: Bode plot for the analytically computed controller. The colored lines indicate the 7/9 π -mode filter set in MIMO controller (Data 1 in Figure 4.1.10); the grey lines visualizes the 8/9 π -mode suppression within the MIMO controller (Data 2 in Figure 4.1.10), where in addition two poles are set as low-pass filter with $\hat{p}_1 = \hat{p}_2 = 0.85$.

The controller performance when using both filters in comparison to the controller which only suppresses the 8/9 π -mode is shown in Figure 4.1.10. The RF field performance, given as standard deviation, is improved from

$$\Delta A/A = 0.007\% \quad \text{and} \quad \Delta\phi = 8 \text{ mdeg}$$

to

$$\Delta A/A = 0.0057\% \quad \text{and} \quad \Delta\phi = 6.6 \text{ mdeg} .$$

Remember, the RF field requirement for the European XFEL is $\Delta A/A < 0.01\%$ and $\Delta\phi < 1 \cdot 10^{-2} \text{ deg} = 10 \text{ mdeg}$, which is already reached by using the analytically computed controller.

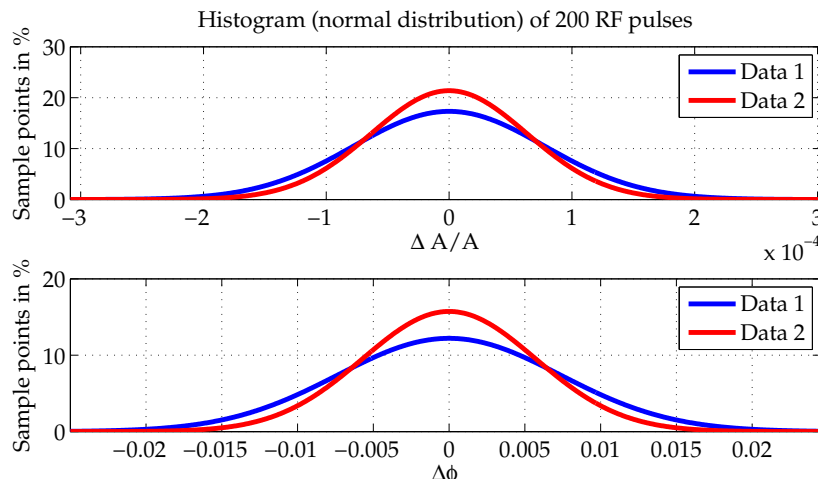


Figure 4.1.10: MIMO Controller with $8/9$ π -mode filter (Data 1), see [Pfeiffer et al., 2012c], and for comparison the $7/9$ π -mode filter set in MIMO controller and an additional $8/9$ π -mode filter (Data 2). The histogram presents the RF field performance for both analytically computed controllers.

As shown in Figure 3.1.17, the resonant modes destroy the $SO(2)$ symmetry, if the rotation matrix is static, while the analytical controller design uses this symmetry. Nevertheless, this analytical approach works fine for the controller design, especially for low frequencies. A controller optimization with the identified system model $\hat{G}(z)$ is introduced in the following. Using an optimization algorithm, e.g. HIFOOd, should optimize the feedback controller at high frequencies, where the performance improvements depend strictly on the decoupling and suppression of the passband modes.

Controller Optimization with HIFOOd

For the implemented controller, given in (4.1.1), one has to optimize 20 parameters, 5 for each controller transfer function. Using the $SO(2)$ symmetric controller, given in Section 4.1.2, only half of these parameters are free. The other half set of parameters is related to the free parameter such that the $SO(2)$ symmetry is fulfilled. The analytically computed controller is used as initial controller and can be included as input parameter by using the optional controller initialization of HIFOOd. To fix the $SO(2)$ structure and therefore ensure decoupling, specify the controller structure according to (4.1.9). For this example the shaping filters are visualized in Figure 4.1.11. The controller sensitivity $W_{CS}^{-1}(z)$ is chosen as analytical controller in series to a low pass filter, which slightly suppresses the $7/9$ π -mode, shown in the second subplot. This ensures that the optimized controller will have a band-stop filter. Figure 4.1.12 displays on the left side the analytically computed controller $C_{ana}(z)$ and on the right side the resulting controller $C_{HIFOOd}(z)$ after the optimization. Especially the high frequency behavior around the $7/9$ π -mode is further suppressed, as desired.

The closed-loop behavior in Figure 4.1.13 is marked with light lines to indicate the initial controller settings and with darker lines for the controller optimization by HIFOOd. For

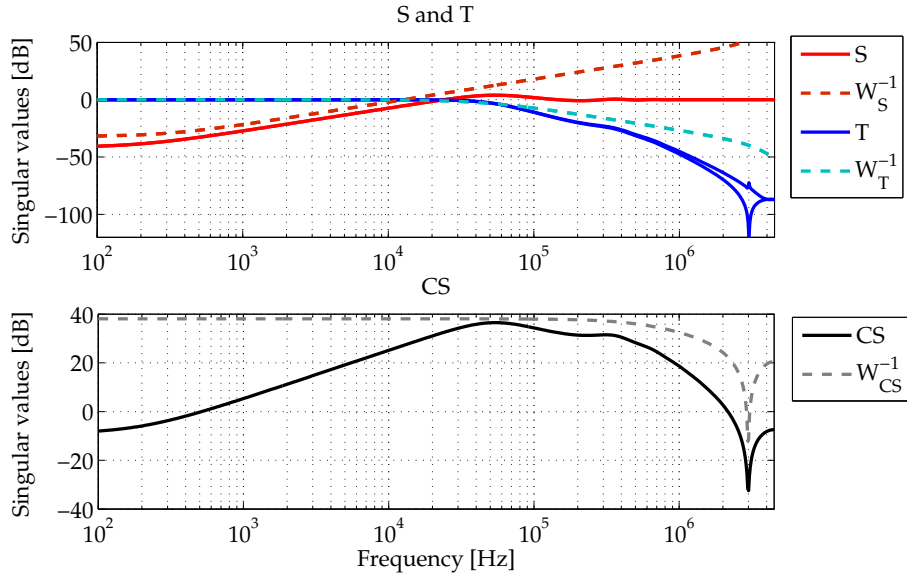


Figure 4.1.11: Used shaping filter for HIFOOD design.

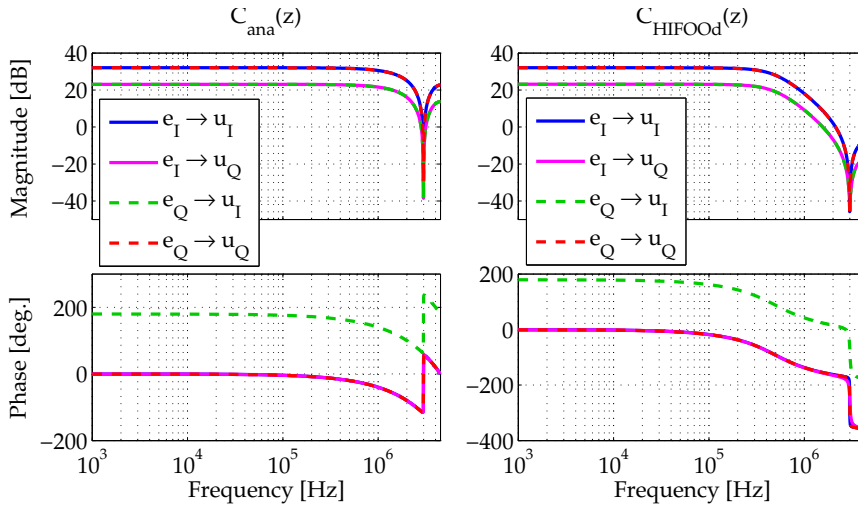


Figure 4.1.12: Analytically computed controller $C_{ana}(z)$ and controller optimization $C_{HIFOOD}(z)$ using HIFOOD.

high frequencies one can see, that decoupling is not fulfilled. This is due to the fact that the controller order is fixed to a second order transfer function of each input-output connection. Ensuring decoupling for all frequencies requires more degrees of freedom by choosing a higher controller order, not given with the current implementation. In addition, the closed-loop plant containing the analytically computed controller shows an intersection point around the $7/9 \pi$ -mode. It is obvious that an excited resonant mode with a weak damping oscillates in the I/Q plane on a perfect circle, hence has the same contribution on channels I and Q .

Considering a flattop length of about 1 ms the frequency range at this application will be from 1 kHz upwards. HIFOOD is used to optimize the high frequency range around the

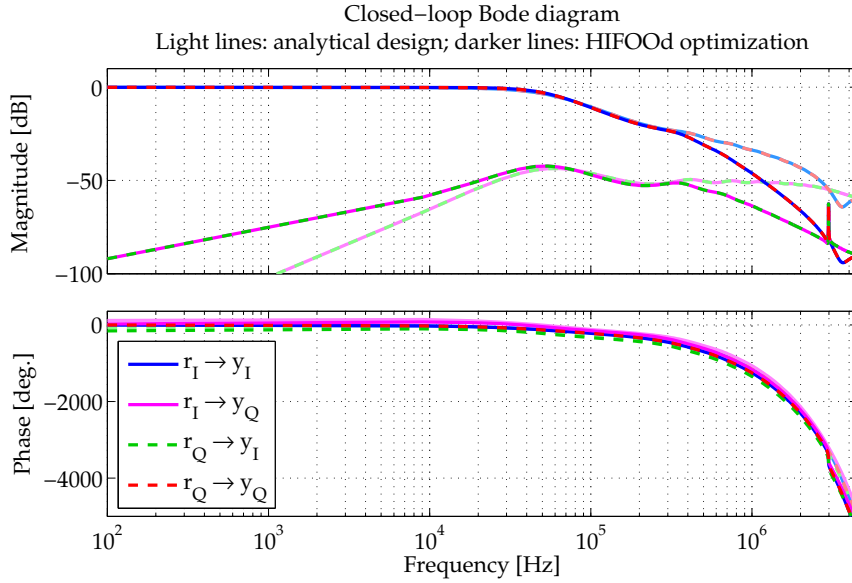


Figure 4.1.13: Closed-loop bode diagram with the analytically computed controller and the optimized controller from the reference signal as input to the output signal.

7/9 π -mode, while the low frequencies remain almost unchanged. Figure 4.1.14 points out a simulation as comparison between the analytically computed controller and the optimized controller.

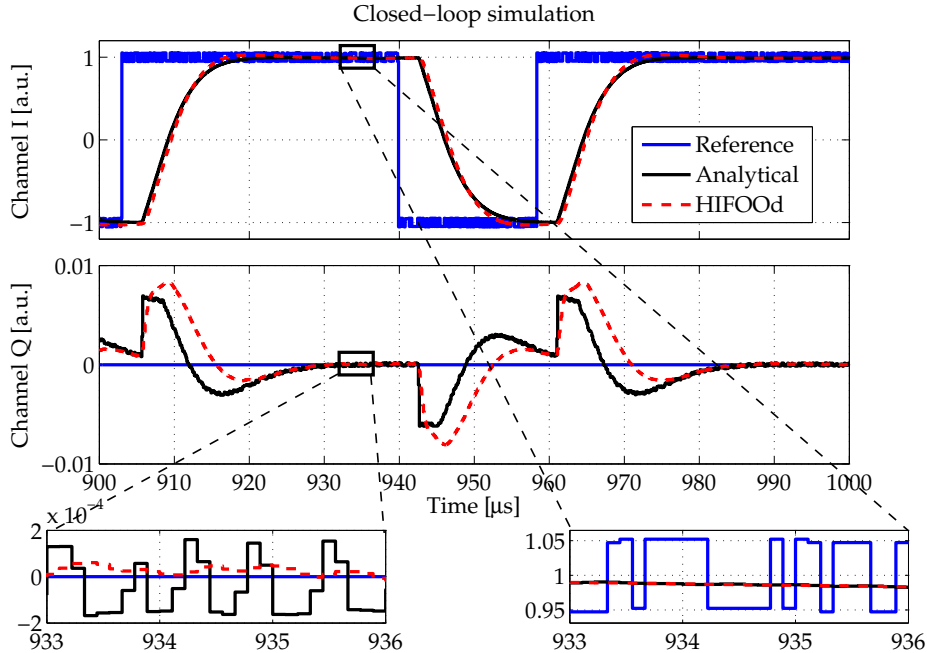


Figure 4.1.14: Simulation of a reference step to one channel and the influence as comparison between the analytically computed and the HIFOOd optimized controller.

A reference trajectory, here a PRB signal with superimposed random high frequency noise,

is applied only to channel I. In case of optimal decoupling, channel Q remains unaffected. However, as seen in Figure 4.1.14, especially for high frequencies, e.g. a step-like reference signal, this is not achieved. Nevertheless, the optimization of the analytically designed controller further improves the noise suppression coming from the neighboring channel.

4.2 Iterative Learning Control

Norm Optimal Iterative Learning Control (NO-ILC) [Ratcliffe et al., 2006] is, since 2010, in most operation situations applied in digital RF field control at FLASH, [Schmidt, 2010]. The pulsed system has shown to be a prime example for NO-ILC because of the quantity and quality of its repetitive behavior, [Rogers et al., 2010]. NO-ILC is used to increase the performance of a system which consequently performs the same task multiple times. It improves the feedforward signal by learning from previous executions (trials, iterations, passes) [Bristow et al., 2006] and accordingly without learning the tracking error would be the same on each trial.

Publications accumulate with a focus on optimization and computation effort. The approach in [Haber et al., 2011] is to minimize the complexity through exploiting the sequentially semi-separable structure of lifted system matrices by using the pseudo-inverse to update the control output. They derived a novel ILC algorithm which is linear in the trial length and reduces the computation time. Within the following sections the focus is on NO-ILC, where model uncertainties are not assumed. Hereby, lifted system representations which make the calculation effort very complex, especially within an implementation on an FPGA, are not considered. The time delay in the system is based on regularity conditions of the plant [Amann et al., 1996]. That means that some components within the system representation are removed and output tables are shifted. Based on the described RF field behavior in Section 3.1, i.e. $SO(2)$ symmetric plant, and further plant upgrades, i.e. MTC system with e.g. a higher sampling rate, the focus is on simplifications of the algorithm. Approaches for complexity reduction of the ILC algorithm thus are welcome and improvements not only reduce required memory space but also computation effort. The latter also helps to minimize possible errors due to fewer parameters to load when updating the ILC output signal. In addition, within a general NO-ILC, a huge amount of data must be loaded, processed and saved.

This section is outlined as follows: Section 4.2.1 introduces the standard NO-ILC. Within Section 4.2.2, fundamental simplifications of the algorithm based on a $SO(2)$ symmetric plant are given. It will be shown, that complexity of the used Norm Optimal ILC can be significantly reduced by exploiting symmetries of the plant. Explicit simplifications of the basic control algorithm using $SO(2)$ symmetric group transformations are given. An alternative ILC representation based on tensors is described in Section 4.2.3. Hereby a decoupling of static and dynamic parts of each calculated ILC matrix leads, for computational reasons, to a reduction by an order of magnitude. Based on such a tensor representation, the Norm Optimal ILC is compressed to a Norm Optimal Tensor ILC (NO-T-ILC). The reduced number of elements to store the ILC parameter in this approach simplifies the calculation, especially for high sampled datasets and therefore long trials. A conclusion of the main results is given in Section 4.3.

4.2.1 Introduction

In the following, the time-dependence within a trial is given by $t = 0, \dots, T$, and the indices k and $k + 1$ represent the previous and current trial, respectively. Given is a discrete linear time-invariant state space model

$$\begin{aligned} x(t+1) &= Ax(t) + Bu(t), \quad x(0) = x_0, \quad 0 \leq t \leq T, \\ y(t) &= Cx(t) \end{aligned} \quad (4.2.1)$$

of the system $G(z)$. The performance index is given by

$$\begin{aligned} J_{k+1}(u_{k+1}) &= \frac{1}{2} \left(\sum_{t=1}^T (r(t) - y_{k+1}(t))^T Q(t) (r(t) - y_{k+1}(t)) \right. \\ &\quad \left. + \sum_{t=0}^{T-1} (u_{k+1}(t) - u_k(t))^T R(t) (u_{k+1}(t) - u_k(t)) \right), \end{aligned} \quad (4.2.2)$$

where the weighting matrices $Q(t)$ and $R(t)$ are of compatible dimensions. This is the familiar performance criterion from linear quadratic optimal control theory.

First, recall the standard Norm Optimal ILC algorithm which is divided into three parts, [Ratcliffe et al., 2006] and [Rogers et al., 2010] and outlined in the following:

The first level solves backwards the Riccati equation for $K(t)$ and, together with $\alpha(t)$, the calculation of the required matrices $\beta(t)$, $\gamma(t)$, $\lambda(t)$ and ω is performed. Since all necessary information are present, this step can be computed before the operation starts.

$$K(t) = A^T K(t+1)A + C^T Q(t+1)C \quad (4.2.3)$$

$$- [A^T K(t+1)B(B^T K(t+1)B + R(t+1))^{-1} B^T K(t+1)A]$$

$$\alpha(t) = (I + K(t)BR^{-1}(t)B^T)^{-1} \quad (4.2.4)$$

$$\beta(t) = \alpha(t)A^T \quad (4.2.5)$$

$$\gamma(t) = \alpha(t)C^T Q(t+1) \quad (4.2.6)$$

$$\omega = R^{-1}(t)B^T \quad (4.2.7)$$

$$\lambda(t) = (B^T K(t)B + R(t))^{-1} B^T K(t)A \quad (4.2.8)$$

The second level calculates backwards the predictive component equation of $\xi_{k+1}(t)$ which is updated between trials.

$$\xi_{k+1}(t) = \beta(t)\xi_{k+1}(t+1) + \gamma(t)e_k(t+1) \quad (4.2.9)$$

The third level updates the control output $u_{k+1}(t)$ and should be done between sampling instants.

$$u_{k+1}(t) = u_k(t) - \lambda(t)[x_{k+1}(t) - x_k(t)] + \omega\xi_{k+1}(t) \quad (4.2.10)$$

Within this section following assumptions must hold:

- Plant model without time delay is available
- ILC input table is shifted w.r.t. time delay

Lets start with an example for the VME and MTCA system which points out the huge matrix dimensions. Assume a system with m outputs, which is here equal to the number of inputs ($m = 2$), n states ($n = 6$) and T defined as trial length ($T = 1300 \mu\text{s} \cdot f_s$) with f_s as sampling frequency, usual values at FLASH. The sizes of each computed ILC matrix are given in Table 4.1. It is obvious, that especially for the MTCA system a huge amount

Table 4.1: ILC Matrix Dimensions for NO-ILC

General	VME system ($f_s=1$ MHz)	MTCA system ($f_s=9$ MHz)
$K(t) \in \mathbb{R}^{(n \cdot T \times n)}$	$K(t) \in \mathbb{R}^{(7806 \times 6)}$	$K(t) \in \mathbb{R}^{(70254 \times 6)}$
$\alpha(t) \in \mathbb{R}^{(n \cdot T \times n)}$	$\alpha(t) \in \mathbb{R}^{(7806 \times 6)}$	$\alpha(t) \in \mathbb{R}^{(70254 \times 6)}$
$\beta(t) \in \mathbb{R}^{(n \cdot T \times n)}$	$\beta(t) \in \mathbb{R}^{(7806 \times 6)}$	$\beta(t) \in \mathbb{R}^{(70254 \times 6)}$
$\gamma(t) \in \mathbb{R}^{(n \cdot T \times m)}$	$\gamma(t) \in \mathbb{R}^{(7806 \times 2)}$	$\gamma(t) \in \mathbb{R}^{(70254 \times 2)}$
$\lambda(t) \in \mathbb{R}^{(m \cdot T \times n)}$	$\lambda(t) \in \mathbb{R}^{(2602 \times 6)}$	$\lambda(t) \in \mathbb{R}^{(23418 \times 6)}$
$\omega \in \mathbb{R}^{(m \times n)}$	$\omega \in \mathbb{R}^{(2 \times 6)}$	$\omega \in \mathbb{R}^{(2 \times 6)}$

of data must be loaded, processed and saved.

The following sections cope with simplifications of those matrices, first, by exploiting SO(2) symmetries of the plant and afterwards, as a tensor style representation.

4.2.2 Norm Optimal ILC for SO(2) Symmetric Systems

Consider a SO(2) symmetric plant which is decomposable into a SISO dynamic scaling part $A_G(z)$ and a fixed rotation matrix $R(\phi_G)$, see (3.1.41) on page 40, such that

$$G(z) = A_G(z)R(\phi_G) \quad (4.2.11)$$

holds. The single-input single-output (SISO) discrete-time state space model of $A_G(z)$ is given as

$$\begin{aligned} x(t+1) &= \tilde{A}x(t) + \tilde{B}u(t) \\ y(t) &= \tilde{C}x(t) \end{aligned} \quad (4.2.12)$$

with a system matrix \tilde{A} , input vector \tilde{B} and output vector \tilde{C} . The SISO model is mapped to a multi-input multi-output (MIMO) model by the Kronecker product of the input

vector \tilde{B} with the rotation matrix $R(\phi_G)$ as well as a block-wise extension of the system and output matrix

$$\begin{aligned} x(t+1) &= \begin{bmatrix} \tilde{A} & 0 \\ 0 & \tilde{A} \end{bmatrix} x(t) + \tilde{B} \otimes \begin{bmatrix} \cos(\phi_G) & -\sin(\phi_G) \\ \sin(\phi_G) & \cos(\phi_G) \end{bmatrix} u(t) , \\ y(t) &= \begin{bmatrix} \tilde{C} & 0 \\ 0 & \tilde{C} \end{bmatrix} x(t) , \end{aligned} \quad (4.2.13)$$

such that the overall model obeys the $SO(2)$ symmetry, see Section 3.1.2. In the following, the focus is on the model structure given by (4.2.13). Having a block diagonal matrix C , the state space system representation for a real eigenvalue is given in Section 3.1.2 by case (a.i), page 24, and for a complex conjugate pair of eigenvalues by case (c.i), page 26. Depending on the identified state space model, this representation may change the internal model structure, while the frequency behavior is unchanged. As seen in Section 3.1.2, the new representation leads to an extended input, output and system matrix of each complex conjugate pair of eigenvalues. In principle this extension has an adverse impact on the computation time of the ILC algorithm, but it will be shown that such a system representation actually helps to reduce the computation time.

Assumptions In order to study possible improvements of the algorithm by a $SO(2)$ symmetric system structure and its effect on the ILC algorithm, especially the resulting ILC matrices, following *ILC conditions* must be satisfied:

- (I) $SO(2)$ symmetric model $G(z)$ of plant according to (4.2.13)
- (II) Output matrix C of $G(z)$ is block diagonal
- (III) ILC weighting

$$R(t) = \begin{bmatrix} \tilde{R}(t) & 0 \\ 0 & \tilde{R}(t) \end{bmatrix}$$

is block diagonal, the upper block is equal to the lower, and symmetric positive-definite

- (IV) ILC weighting

$$Q(t) = \begin{bmatrix} \tilde{Q}(t) & 0 \\ 0 & \tilde{Q}(t) \end{bmatrix}$$

is block diagonal, the upper block is equal to the lower, and symmetric positive-semidefinite

- (V) Matrix gain initialization

$$K(T) = \begin{bmatrix} \tilde{K}(T) & 0 \\ 0 & \tilde{K}(T) \end{bmatrix}$$

is block diagonal, the upper block is equal to the lower block

(VI) Finite trial length $t = 1, \dots, T$.

From engineering expertise, it is convenient to choose identical diagonal blocks for $R(t)$, $Q(t)$ and $K(T)$. The following considered simplifications hold for the special case of equal block diagonal $\tilde{R}(t)$, $\tilde{Q}(t)$ and $\tilde{K}(T)$. For simplicity, the time-dependent weightings $R(t)$ and $Q(t)$ are written time-independent as R and Q .

Simplifications First, consider the backwards computation of the matrix gain $K(t)$, having instead of an initial a final matrix as $K(T)$.

Proposition 4.2.1. *For $SO(2)$ symmetric systems fulfilling conditions (I)-(VI), the ILC matrix gain*

$$K(t) = \begin{bmatrix} \tilde{K}(t) & 0 \\ 0 & \tilde{K}(t) \end{bmatrix}$$

is block diagonal.

Remark 4.2.2. *The matrix gain block matrices are given by the backwards Riccati equation for the SISO state space model of $A_G(z)$, (4.2.12), by*

$$\begin{aligned} \tilde{K}(t) = & \tilde{A}^T \tilde{K}(t+1) \tilde{A} + \tilde{C}^T \tilde{Q} \tilde{C} \\ & - [\tilde{A}^T \tilde{K}(t+1) \tilde{B} (\tilde{B}^T \tilde{K}(t+1) \tilde{B} + \tilde{R})^{-1} \cdot \tilde{B}^T \tilde{K}(t+1) \tilde{A}] . \end{aligned}$$

Thus, the matrix gain $K(t)$ does not directly depend on the rotation part $R(\phi_G)$ of the model.

Proposition 4.2.3. *For a given $SO(2)$ symmetric system fulfilling the conditions (I)-(VI), the matrices $\beta(t)$ and $\gamma(t)$ are block diagonal, while the matrices ω and $\lambda(t)$ are $SO(2)$ symmetric with $R(\phi_G)^{-1} = R(\phi_G)^T$, where*

$$\beta(t) = \left(I + \tilde{K}(t) \tilde{B} \tilde{R}^{-1} \tilde{B}^T \right)^{-1} \tilde{A}^T \otimes \begin{bmatrix} 1 & 0 \\ 0 & 1 \end{bmatrix} , \quad (4.2.14)$$

$$\gamma(t) = \left(I + \tilde{K}(t) \tilde{B} \tilde{R}^{-1} \tilde{B}^T \right)^{-1} \tilde{C}^T \tilde{Q} \otimes \begin{bmatrix} 1 & 0 \\ 0 & 1 \end{bmatrix} , \quad (4.2.15)$$

$$\lambda(t) = \left(\tilde{B}^T \tilde{K}(t) \tilde{B} + \tilde{R} \right)^{-1} \tilde{B}^T \tilde{K}(t) \tilde{A} \otimes R(\phi_G)^T \quad \text{and} \quad (4.2.16)$$

$$\omega = \tilde{R}^{-1} \tilde{B}^T \otimes R(\phi_G)^T \quad (4.2.17)$$

holds.

The proof of proposition 4.2.1 and 4.2.3 is given in Appendix C.

An example for a given $SO(2)$ symmetric plant at FLASH is outlined in the following.

Example at FLASH

From basic physics, the model (3.1.16), page 23, of the RF field at FLASH has a SO(2) symmetric structure and can be represented by a first-order approximation (3.1.43), see page 40, in discrete-time domain with

$$G(z) = \begin{bmatrix} G_1(z) & -G_2(z) \\ G_2(z) & G_1(z) \end{bmatrix} = A_G(z) \cdot \overbrace{\begin{bmatrix} \cos(\phi_G) & -\sin(\phi_G) \\ \sin(\phi_G) & \cos(\phi_G) \end{bmatrix}}^{R(\phi_G)}. \quad (4.2.18)$$

Based on the plant, an optimal controller which decouples the plant is computed (see page 52 ff.), such that the controller fulfills the structure

$$C(z) = \begin{bmatrix} C_1(z) & C_2(z) \\ -C_2(z) & C_1(z) \end{bmatrix} = K_P M_C(z) \cdot \overbrace{\begin{bmatrix} \cos(\phi_G) & \sin(\phi_G) \\ -\sin(\phi_G) & \cos(\phi_G) \end{bmatrix}}^{R(\phi_G)^T = D_C}. \quad (4.2.19)$$

At FLASH, the ILC is implemented in closed-loop operation. The closed-loop model is computed directly by the symmetric plant model and the controller. As seen, $G(z)$ is in first-order approximation SO(2) symmetric with a constant plant phase ϕ_G for all frequencies ω and $C(z)$ decouples the plant, thus is SO(2) symmetric. Both models can be separated into a scaling and rotation part, based on (4.2.18) and (4.2.19), leading to a diagonal loop gain

$$\begin{aligned} L(z) &= C(z) \cdot G(z) \\ &= K_P M_C(z) R(\phi_G)^T \cdot A_G(z) R(\phi_G) \\ &= K_P M_C(z) A_G(z) \mathbf{I}. \end{aligned} \quad (4.2.20)$$

The closed-loop transfer function matrix from the feedforward correction signal $u_{corr}(t)$ to the vector sum $y(t)$, needed to compute the ILC matrices, is given as

$$G_{cl}(z) = (z\mathbf{I} + C(z)G(z))^{-1}G(z) = ((z + K_P M_C(z)A_G(z))\mathbf{I})^{-1}A_G(z)R(\phi_G).$$

By (4.2.18) and (4.2.20) the closed-loop transfer function matrix $G_{cl}(z)$ is SO(2) symmetric. Using the presented SO(2) symmetric ILC algorithm, which computes the necessary ILC matrices for the SISO model $A_G(z)$, leads to a storage and computation reduction by a factor of about four. For the proposed symmetric ILC it is sufficient to store only one block matrix for each ILC matrix, see Table 4.2.

These matrices are computed by the SISO system regarding Proposition 4.2.3, thus in addition either the rotation matrix $R(\phi_G)$ or only ϕ_G , which maps the corresponding ILC matrices back to MIMO, must be stored to update the optimal control signal $u_{k+1}(t)$. The first column shows the resulting matrices for the general Norm Optimal ILC, while the second presents the reduced matrices by using a SO(2) symmetric plant model.

In addition, numerical inaccuracies of the computation of an inverse matrix can result in non-zero off-diagonal blocks within some matrices, while the off-diagonal block is in

Table 4.2: ILC Matrix Dimensions

	General	SO(2) sym.
$K(t)$	$\in \mathbb{R}^{(n \cdot T \times n)}$	$\in \mathbb{R}^{(\frac{n}{2} \cdot T \times \frac{n}{2})}$
$\alpha(t)$	$\in \mathbb{R}^{(n \cdot T \times n)}$	$\in \mathbb{R}^{(\frac{n}{2} \cdot T \times \frac{n}{2})}$
$\beta(t)$	$\in \mathbb{R}^{(n \cdot T \times n)}$	$\in \mathbb{R}^{(\frac{n}{2} \cdot T \times \frac{n}{2})}$
$\gamma(t)$	$\in \mathbb{R}^{(n \cdot T \times m)}$	$\in \mathbb{R}^{(\frac{n}{2} \cdot T \times \frac{m}{2})}$
$\lambda(t)$	$\in \mathbb{R}^{(m \cdot T \times n)}$	$\in \mathbb{R}^{(\frac{m}{2} \cdot T \times \frac{n}{2})}$
ω	$\in \mathbb{R}^{(m \times n)}$	$\in \mathbb{R}^{(1 \times \frac{n}{2})}$
ϕ_G	-	$\in \mathbb{R}^1$

theory zero. Caused by the used backwards computation, where the next matrix depends on the previous, this error may increase over time, especially for long trials.

This section points out that using a SO(2) symmetric model within the ILC controller design reduces the computation effort and memory space. It will be possible to consider slightly nonlinear behavior by just a piecewise adjustment of the considered plant input matrix. At FLASH, the klystron is linearised over a wide range, [Cichalewski and Koseda, 2007]. Without going into detail, such a linearisation can directly act as input matrix correction, corresponding to scaling $A_G(z, t)$ and phase $R(\phi_G)(t)$ adaptation over the trial. In addition this correction allows to adjust possible, e.g. temperature varying, repetitive cross-coupling changes within a trial.

The following section further simplifies the ILC by using a tensor representation for the resulting ILC update matrices. For completeness, the presented Norm Optimal Tensor based ILC approach (NO-T-ILC) is in general not restricted to a SO(2) symmetric structure.

4.2.3 Norm Optimal Tensor ILC (NO-T-ILC)

In the following, a short introduction to a tensor, tensor rank and tensor decomposition is given. The interested reader is referred to e.g. [Kruskal, 1989] and [Kolda and Bader, 2009] for further details.

Full tensors A tensor is a multidimensional array or more precisely the tensor product of N vector spaces, each with its own coordinate system, called an N-th order tensor [Kolda and Bader, 2009]. The basis of this section will be a 3rd order tensor X_3 , see left side of Figure 4.2.1. X_3 is rank-one if it can be written as outer product of 3 vectors, see right side of Figure 4.2.1. Hereby, the vector outer product generates the tensor $X_3 \in \mathbb{R}^{I \times J \times K}$, defined as $X_3 = a \circ b \circ c$, in which the symbol \circ represents the vector outer product. The (i,j,k) element of X_3 is given by $X_3^{i,j,k} = a_i b_j c_k$.

Lets focus on the ILC algorithm given in (4.2.3) to (4.2.10). Within the first step the

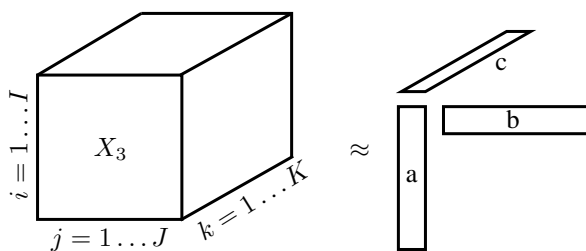


Figure 4.2.1: Rank-one third order tensor.

learning gain $K(t)$ is calculated in a backward prediction. Each $K(t)$ is a quadratic matrix with a dimension of the number of states. If one arranges all $K(t), \forall t$ in series, the first tensor will appear. Since all other matrices, namely $\alpha(t), \beta(t), \gamma(t)$ and $\lambda(t)$, are results of $K(t)$ it is obvious to write these matrices also as tensors.

The resulting three dimensional tensors for the standard Norm Optimal ILC are given by

$$K(t) \in \mathbb{R}^{(n \times n \times T)}, \alpha(t) \in \mathbb{R}^{(n \times n \times T)}, \beta(t) \in \mathbb{R}^{(n \times n \times T)}, \\ \gamma(t) \in \mathbb{R}^{(m \times n \times T)} \text{ and } \lambda(t) \in \mathbb{R}^{(m \times n \times T)} .$$

Tensor rank Although, properties of a tensor and matrix rank are different, the definition of a tensor rank is exact analogues to a matrix rank. One difference is that the rank of a real-valued tensor may be different over \mathbb{R} and \mathbb{C} , for more details about the differences see [Kolda and Bader, 2009]. The smallest number of rank-one tensors, where λ_i is used to normalize a_i, b_i and c_i , that generate a tensor X_3 as their sum is called the rank of X_3 , denoted as $rank(X_3)$, see Figure 4.2.2.

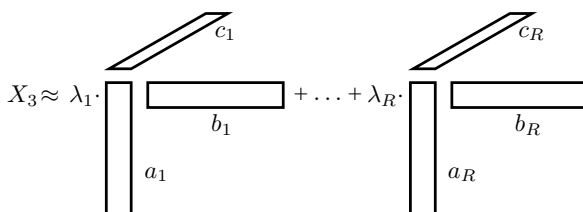


Figure 4.2.2: Tensor CP decomposition of three-way array with rank R .

In [Kruskal, 1989], a weak upper bound for the maximum rank of a third order tensor $X_3 \in \mathbb{R}^{(I \times J \times K)}$ is given as

$$rank(X_3) \leq \min \{IJ, IK, JK\} .$$

Tensor Decomposition and SVD

Hitchcock proposed in 1927 one of the first decompositions, the so-called polyadic form of a tensor, which is the sum of a finite number of rank-one tensors [Hitchcock, 1927]. Nowadays different decompositions, like the Tucker decomposition, which is a higher order

SVD, or the CANDECOMP and PARAFAC decomposition are developed. In this section a combination of CANDECOMP and PARAFAC, the so-called CP decomposition of a third order tensor is used [Kolda and Bader, 2009]. This decomposition of X_3 leads to the so-called factorization matrices A , B and C , see Figure 4.2.3. Here, it will be assumed

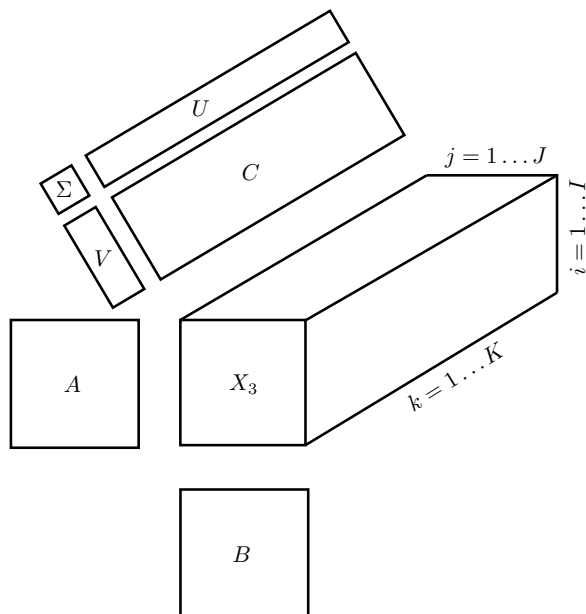


Figure 4.2.3: Full Tensor Decomposition as separation of CP decomposition and SVD of the third factorization matrix C .

that one dimension of X_3 is larger than the other ones, i.e. $K \gg I, J$. In the following K is assumed to be the trial length and I, J are the number of states, input and/or outputs. Hereby, the dimension of C is given by the trial length times the number of states, input and/or outputs. By a singular value decomposition of C the matrix reduces to U , Σ and V .

Tensor CP-Decomposition

Assume X_3 is of dimension $(I \times J \times K)$. If it is possible to reduce the size of the tensor by a special operation, then this reduces the memory needed and in addition simplifies the calculation effort, as seen in the following.

Given is a tensor $X_3 \in \mathbb{R}^{(I \times J \times K)}$. By a tensor CP-decomposition of rank R , the tensor can be constructed by the coefficient λ_r ($r = 1, \dots, R$) and matrices $A \in \mathbb{R}^{(I \times R)}$, $B \in \mathbb{R}^{(J \times R)}$ and $C \in \mathbb{R}^{(K \times R)}$, where λ is used to normalize the column of A and B . This decomposition factorizes a tensor into a sum of component rank-one tensors [Kolda and Bader, 2009].

The tensor X_3 can be reconstructed by

$$X_3 \approx \sum_{r=1}^R \lambda_r a_r \circ b_r \circ c_r, \quad (4.2.21)$$

with $A = \begin{bmatrix} a_1 & a_2 & a_3 & \dots & a_R \end{bmatrix}$, $B = \begin{bmatrix} b_1 & b_2 & b_3 & \dots & b_R \end{bmatrix}$
 and $C = \begin{bmatrix} c_1 & c_2 & c_3 & \dots & c_R \end{bmatrix}$.

Singular Value Decomposition With the assumption that the k -th dimension of X_3 is the largest one, we can use the singular value decomposition of the factor matrix C to rearrange it. This leads to a reduced order of C

$$C = \tilde{U} \cdot \tilde{\Sigma} \cdot \tilde{V}^T \text{ with } \tilde{U} \in \mathbb{R}^{(K \times K)}, \tilde{\Sigma} \in \mathbb{R}^{(K \times I)} \text{ and } \tilde{V} \in \mathbb{R}^{(I \times I)}, \quad (4.2.22)$$

if the lower singular values of C are omitted. The upper $(I \times I)$ block of $\tilde{\Sigma}$ contains the singular values of C . Therefore, only the first I columns of \tilde{U} are necessary such that the resulting matrices can be separated to

$$\tilde{U} = \begin{bmatrix} \hat{U} & X \end{bmatrix} \text{ and } \tilde{\Sigma} = \begin{bmatrix} \hat{\Sigma} \\ 0 \end{bmatrix}, \quad (4.2.23)$$

where X means arbitrary and therefore unused entries. The separation of used and unused entries of the resulting singular value decomposition matrices of (4.2.23) leads to the so-called economy-size SVD [Skogestad and Postlethwaite, 2005], given as

$$C = \hat{U} \cdot \hat{\Sigma} \cdot \hat{V}^T \quad (4.2.24)$$

with $\hat{U} = \begin{bmatrix} \hat{u}_1 & \hat{u}_2 & \dots & \hat{u}_I \end{bmatrix} \in \mathbb{R}^{(I \times K)}$, $\hat{\Sigma} = I \cdot \begin{bmatrix} \hat{\sigma}_1 & \hat{\sigma}_2 & \dots & \hat{\sigma}_I \end{bmatrix} \in \mathbb{R}^{(I \times I)}$
 and $\hat{V} = \begin{bmatrix} \hat{v}_1 & \hat{v}_2 & \dots & \hat{v}_I \end{bmatrix} \in \mathbb{R}^{(I \times I)}$.

Combination of CP and SVD Using the CP-decomposition together with (4.2.24), c_r of (4.2.21) can be replaced by $\hat{U} \cdot \hat{\Sigma} \cdot \hat{v}_r$, in that \hat{v}_r represents the r -th column of \hat{V} .

$$X_3 \approx \sum_{r=1}^I \lambda_r a_r \circ b_r \circ (\hat{U} \cdot \hat{\Sigma} \cdot \hat{v}_r) \quad (4.2.25)$$

It is straightforward to show the general case if the values of σ_i are similar and therefore not negligible. This results in

$$X_3 \approx \sum_{r=1}^R \lambda_r a_r \circ b_r \circ c_r = \sum_{r=1}^R \lambda_r a_r \circ b_r \circ \hat{U} \hat{\Sigma} \hat{v}_r. \quad (4.2.26)$$

The assumption in the following is that each 3-rd factor matrix C is of rank 1. This special case of the singular value decomposition for C leads to $\sigma_1 \gg \sigma_i$ ($i = 2, \dots, n$). Hence, only the first column/row is used in further calculations, leading to

$$X_3 \approx \sum_{r=1}^R \lambda_r a_r \circ b_r \circ (\hat{u}_1 \cdot \hat{\sigma}_1 \cdot \hat{v}_1(r)). \quad (4.2.27)$$

Since the r -th element of $\hat{v}_1(r)$ is constant and in addition λ_r and $\hat{\sigma}_1$ are constant, rewrite (4.2.27) to

$$X_3 \approx \sum_{r=1}^R \lambda_r \hat{\sigma}_1 \hat{v}_1(r) \cdot a_r \circ b_r \circ \hat{u}_1.$$

The vector \hat{u}_1 is the same for each rank ($r = 1, \dots, R$) of the CP-decomposition. This allows to separate the summation part to a matrix

$$M_{X_3} = \sum_{r=1}^R \lambda_r \hat{\sigma}_1 \hat{v}_1(r) \cdot a_r \circ b_r \quad (4.2.28)$$

and by defining

$$\tilde{a}_r = \lambda_r \hat{\sigma}_1 \hat{v}_1(r) \cdot a_r \quad (4.2.29)$$

follows

$$M_{X_3} = \sum_{r=1}^R \tilde{a}_r \circ b_r, \quad (4.2.30)$$

such that the tensor X_3 is decomposable into a matrix M_{X_3} and a vector \hat{u}_1 , i.e.

$$X_3 \approx M_{X_3} \circ \hat{u}_1. \quad (4.2.31)$$

The outer product which connects M_{X_3} and \hat{u}_1 is not the same like for the CP decomposition. But by extending the vector \hat{u}_1 by the number of ranks which are lost by the singular value decomposition one can reproduce the tensor X_3 . Further details are discussed as an example after (4.2.33).

Brief summary: If the singular values of the third factorization matrix C fulfill $\sigma_1 \gg \sigma_i$ with $i = 2, \dots, n$, it follows that the tensor X_3 can be written as the outer product of a matrix M_{X_3} and \hat{u}_1 . Hereby, the dimension of M_{X_3} is given by the number of rows in A times the number of rows in B and \hat{u}_1 represents the number of rows in C , respectively. The matrix M_{X_3} contains a static gain, whereas the vector \hat{u}_1 represents the dynamics of the tensor $X_3(k)$, with $k = 1, \dots, K$.

Norm Optimal ILC - Tensor Representation

The general approach is to rewrite first the ILC matrices, see Section 4.2.1, to tensors and afterwards, separate the static and dynamics of each tensor by a matrix and a vector, respectively. As presented previously, each time-dependent matrix of (4.2.3)-(4.2.8) can be written as tensor by placing the resulting matrices for each time step t in series. This leads to a tensor of dimension 3, e.g. X_3 , which is mostly the case for iterative learning control. The x-y dimension is defined by the number of states, inputs and/or outputs, depending on the respective tensor. The z dimension of the X_3 tensor is defined by the trial length.

It is not necessary to decompose $K(t)$ since this is only used within the first level of the ILC computation. The computation time of this level is not critical, and with $K(t)$ in a tensor representation the calculation time stays almost the same. In addition, $K(t)$ is used to calculate $\beta(t)$, $\gamma(t)$ and $\lambda(t)$. The computation of $\alpha(t)$ is neglected, because it simplifies the calculation of $\beta(t)$, $\gamma(t)$ and $\lambda(t)$. Since only these 3 matrices or tensors are used to calculate the next update step, the focus is on the decomposition of the remaining tensors $\beta(t)$, $\gamma(t)$ and $\lambda(t)$. The latter are calculated in tensor representation from the tensor $K(t)$. Figure 4.2.4 visualizes $K(t)$ at a certain time \tilde{t} . Based on the matrix at

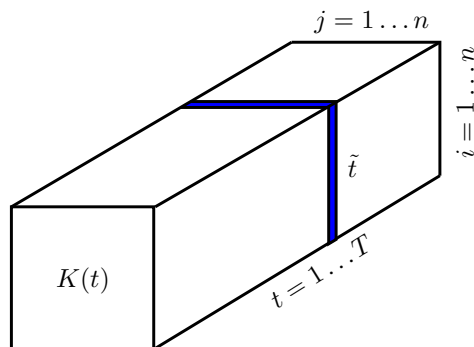


Figure 4.2.4: Tensor $K(t)$ with dimension number of states n times number of states n times trial length T and a depicted time slice \tilde{t} .

time \tilde{t} the previous matrix at $t = \tilde{t} - 1$ is calculated by the ILC algorithm, given in (4.2.3). During the backward prediction, all resulting matrices are stored in a tensor representation starting at $t = T$ down to $t = 1$. For $K(t)$ the algorithm is based on a backwards calculation of the differential Riccati equation with boundary conditions set in the future. Based on $K(t)$ all other tensors within the first step are calculated and a tensor decomposition as well as a singular value decomposition are used to compress each tensor. Due to the observation at FLASH that $\sigma_1 \gg \sigma_i$ ($i = 2, \dots, n$) for $\beta(t)$, $\gamma(t)$ and $\lambda(t)$, each tensor reduces to a matrix and a vector. The resulting matrices and vectors based on (4.2.31) are given by $\beta(t) \approx M_\beta \circ u_\beta$, $\gamma(t) \approx M_\gamma \circ u_\gamma$ and $\lambda(t) \approx M_\lambda \circ u_\lambda$. The comparison of the reduced dimensions of the matrices for a Norm Optimal ILC with respect to a tensor based ILC are given in Table 4.3. The column to the right of each representation is an example for the number of stored elements, if $n = 6$, $m = 2$ and $T = 1300$.

Table 4.3: Comparison of ILC Matrix Dimensions

Coeff.	NO-ILC	E.g.	NO-T-ILC	E.g.
$\beta(t)$	$\in \mathbb{R}^{(n \cdot T \times n)}$	46836	$\in \mathbb{R}^{(n \times n)} \circ \mathbb{R}^{(T \times 1)}$	1337
$\gamma(t)$	$\in \mathbb{R}^{(n \cdot T \times m)}$	15612	$\in \mathbb{R}^{(m \times n)} \circ \mathbb{R}^{(T \times 1)}$	1313
$\lambda(t)$	$\in \mathbb{R}^{(m \cdot T \times n)}$	15612	$\in \mathbb{R}^{(m \times n)} \circ \mathbb{R}^{(T \times 1)}$	1313

The second (4.2.9) and third level (4.2.10) which update the predictive component equa-

tion and ILC output, respectively, can be written in tensor representation as

$$\xi_{k+1}(t) = [M_\beta \circ u_\beta(t)] \cdot \xi_{k+1}(t+1) + [M_\gamma \circ u_\gamma(t)] \cdot e_k(t+1), \quad (4.2.32)$$

$$u_{k+1}(t) = u_k(t) - [M_\lambda \circ u_\lambda(t)] \cdot (x_{k+1}(t) - x_k(t)) + \omega \xi_{k+1}(t), \quad (4.2.33)$$

$$\text{where } M_\beta = \sum_{r=1}^{R_\beta} \tilde{a}_r^\beta \circ b_r^\beta, \quad M_\gamma = \sum_{r=1}^{R_\gamma} \tilde{a}_r^\gamma \circ b_r^\gamma \quad \text{and} \quad M_\lambda = \sum_{r=1}^{R_\lambda} \tilde{a}_r^\lambda \circ b_r^\lambda.$$

Consider the matrix vector interconnections (e.g. $M_\beta \circ u_\beta(t)$) of (4.2.32) and (4.2.33). Those may not be possible due to the reduced rank by SVD of the matrix C , leading to the vector u_p ($p = \beta, \lambda$ or γ). The problem was already introduced on page 75. In the following, an example is presented which considers a possible strategy to correct the matrix vector operation.

Rearrangement due to SVD

Consider only the second part of (4.2.32) as an example, given by

$$\tilde{\xi}_{k+1}(t) = [M_\gamma \circ u_\gamma(t)] \cdot e_k(t+1).$$

Assume, the number of inputs is two $[e_k^1(t+1) \ e_k^2(t+1)]^T$, the number of states is four $[\tilde{\xi}_{k+1}^1(t), \dots, \tilde{\xi}_{k+1}^4(t)]^T$ and the trial length is 10 ($t = 1, \dots, 10$), leading to

$$M_\gamma \in \mathbb{R}^{(4 \times 2)}, u_\gamma \in \mathbb{R}^{(10 \times 1)} \quad \text{and} \quad e_k \in \mathbb{R}^{(2 \times 10)}.$$

The resulting vector $\tilde{\xi}_{k+1} \in \mathbb{R}^{(4 \times 1 \times 10)}$ must hold for the whole calculation. The outer product of $M_\gamma \circ u_\gamma(t)$ holds, if $u_\gamma \in \mathbb{R}^{(10 \times 2)}$. Therefore, one has to extend the dimension of vector u_γ to $u_\gamma = u_\gamma \cdot [1 \ 1]$, where the $[1 \ 1]$ vector is according to the normalized $\hat{v}_1(r)$ element. But, due to the dimension of the input vector $e_k \in \mathbb{R}^{(2 \times 10)}$, it is obvious to scale the incoming error at time t by $u_\gamma(t)$ with the Kronecker product. This can be done either directly after the input of each error or within the backward loop of (4.2.32). Hence, the error vector is modified instead of extending $u_\gamma(t)$ such that the outer product holds again. Similar results are used for the first part of (4.2.32) by weighting the vector $\xi_{k+1}(t+1)$ with $u_\beta(t)$ and generating, after each loop, the tensor ξ_{k+1} backwards from $t = T$ down to $t = 1$.

Based on (4.2.32) and (4.2.33), $u_\beta(t)$ is a weighting on $\xi_{k+1}(t+1)$, $u_\gamma(t)$ weights the error and the state difference is weighted by $u_\lambda(t)$. At each time step t , $u_\beta(t)$, $u_\gamma(t)$ and $u_\lambda(t)$ are only constants and multiplied by the Kronecker product with the appropriate vector.

Finally, the second and third level of the Norm Optimal ILC (NO-ILC), given in Section 4.2.1, can be rewritten in a tensor representation as a Norm Optimal Tensor ILC (NO-T-ILC) by the following equations:

$$\xi_{k+1}(t) = M_\beta \circ [u_\beta(t) \otimes \xi_{k+1}(t+1)] + M_\gamma \circ [u_\gamma(t) \otimes e_k(t+1)] \quad (4.2.34)$$

$$u_{k+1}(t) = u_k(t) - M_\lambda \circ (u_\lambda(t) \otimes [x_{k+1}(t) - x_k(t)]) + \omega \xi_{k+1}(t) \quad (4.2.35)$$

Each Kronecker product of (4.2.34) and (4.2.35) is considered within one time step t . The multiplication for a full trial length can be done with the Hadamard- or Khatri-Rao product [Kolda and Bader, 2009] of the vector u_p ($p = \beta, \lambda$ or γ) and the following matrix. Therefore, the matrix must be separated in single vectors and connected with u_p , which can be done in parallel.

Example at FLASH for MTCA System

In the following example only the MTCA system is considered. The ILC algorithm with the VME system is almost permanently in operation, such that an update of this is not necessary, see [Schmidt, 2010].

Due to limitations of the required FPGA space and since not all states are known, the second and third level are calculated between the trials and hence the ILC tensor $\lambda(t)$ is neglected. Therefore, the state feedback within the ILC algorithm in this application is substituted by an output feedback scheme, i.e. the RF field controller, Section 4.1. See Figure 2.3.1 on page 8 for the considered signal flow.

Assume that the closed-loop system, based on the RF field model, Section 3.1.3, and the RF field controller, Section 4.1.3, is given in discrete-time state space representation as

$$\begin{aligned} x(t+1) &= Ax(t) + Bu_{corr}(t) , \\ y(t) &= Cx(t) , \end{aligned} \tag{4.2.36}$$

$$\text{with } u_{corr}(t) = \begin{bmatrix} u_{corr,I}(t) \\ u_{corr,Q}(t) \end{bmatrix} \quad \text{and} \quad y(t) = \begin{bmatrix} y_I(t) \\ y_Q(t) \end{bmatrix} .$$

First, $K(t)$, see (4.2.3), is calculated and rearranged in a tensor representation. Based on the tensor $K(t)$ the remaining tensors are decomposed in matrix and vector, see (4.2.31). Reconstructing the original tensor by vector outer product shows a fit of about 99%, which is sufficient for the recoverability of the corresponding tensors. The ratio of largest two singular values, i.e. σ_1 and σ_2 , for all third factor matrices is less than 10^{-4} which allows to use an SVD of order one.

Figure 4.2.5 presents the results of a real measurement and displays the initial settings for I and Q , respectively, and the error and feedforward correction signals after the adaptation. The ILC adaptation in between is outlined by the grey dashed lines and presents a set of 300 adaptation trials. Three time values are displayed, i.e. 160 μs for start of filling, 660 μs for start of flattop and 1460 μs for the end of the flattop phase, an usual operation at FLASH. The remaining noisy signals come from a non-filtered test sequence of this NO-T-ILC test. The main aspect of such a representation is the reduced calculation effort and a separation of each ILC matrix to a matrix, which contains a static part and a vector with the dynamic part of each ILC tensor. Together with a state observer the calculation of the third level can be done inside the FPGA and independently from the second level.

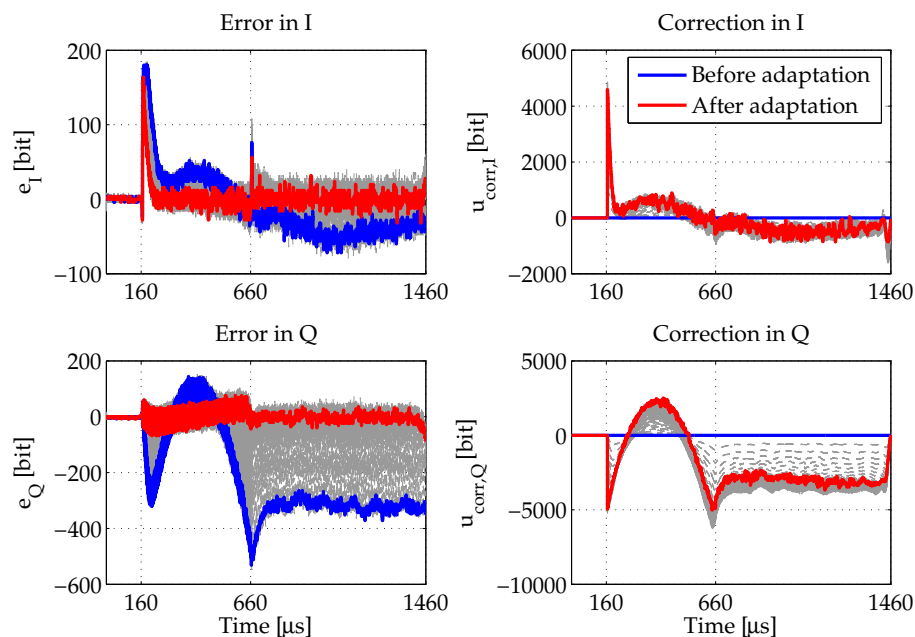


Figure 4.2.5: Measurement of Norm Optimal Tensor ILC (NO-T-ILC) applied at FLASH. The left subplots visualizes the errors in I and Q , the right side the corrections in I and Q .

4.3 Conclusion

This chapter shows that the RF field performance could be improved using a $SO(2)$ symmetric model structure. The RF field feedback controller is designed by a two-step strategy. First, the plant is separated into a SISO like scaling and MIMO like rotation part. An analytically computed controller based on the dynamic SISO part is mapped back to MIMO by the transpose plant rotation matrix. Subsequently, a mixed sensitivity design further optimizes the MIMO controller, where the analytical controller is used as initial controller setting. It has been shown, that the proposed feedback controller design strategy leads to reliable and optimal controller parameters and is highly suitable as RF field feedback controller. This has been verified by measurement results at FLASH.

The second part of this chapter considers simplifications of Norm Optimal Iterative Learning Control algorithm, which makes the algorithm implementable on an FPGA. It has been shown, that it is sufficient to consider an ILC algorithm which is based on the SISO like dynamic scaling part and mapped back to MIMO with either an identity matrix or the plant rotation matrix. The benefit is a reduced set of parameters to be stored; here by a factor of about four. In addition, non-linear behavior, e.g. during the transition from filling to flattop phase, can be included into the ILC algorithm by updating the input matrix within the trial.

Furthermore, a more practical interpretation of the Norm Optimal ILC, namely by a tensor based representation, has been developed. Especially for long, high sampled trials it has been shown, that each ILC matrix can be decomposed to only one vector, with the

length of a trial, and a matrix. This parameter reduction by using a tensor representation and by exploiting the $SO(2)$ symmetric plant leads to a reduced computation effort and makes the algorithm implementable on an FPGA. The tensor based ILC algorithm is verified at FLASH with measurements. The actually used ILC configuration is considered without state information, because no state is measurable. That means that the second and third level of the ILC adaptation is done within one step between the trials. The Norm-Optimal Tensor ILC with all the simplifications works like desired.

Chapter 5

Beam-Based Feedback

Electron bunches are accelerated at FLASH and later at the XFEL to generate X-ray flashes. Each pulse is enabled for about 1 ms (650 μ s for XFEL and 800 μ s for FLASH). In this time up to 2400 bunches with a maximum repetition rate of 3 MHz for FLASH and 2700 bunches with 4.5 MHz as maximum repetition rate for XFEL are injected, [XFEL, 2013]. A precise RF field control, Chapter 4, is a necessary step to provide stable and reproducible photon pulses. In presence of a beam, beam loading compensation is used to keep the RF field within these performance limits [Schmidt, 2010]. The reason for controlling the beam-based measurements is given in Section 1.1. Achieving high beam performance requires a well designed controller strategy which combines beam measurements with the actuator, i.e. the RF field.

This chapter is outlined as follows: Section 5.1 discusses the controller design for bunch arrival time and bunch compression stabilization. After an introduction, three different control strategies are compared. It will be shown, that it is sufficient to consider a lumped controller design within the first section. An example at FLASH displays a significant beam performance improvement. Controlling the beam energy is covered by Section 5.2, where a distributed control scheme is necessary to exchange not only possible beam energy errors. First, possible energy errors are defined and a spatially interconnected plant description is given. The latter is done by rewriting physical equations for the energy gain within an accelerator module. It will be shown, that such sophisticated interconnected controller design for beam energy control is suitable for a linear accelerator.

Parts of this chapter are published in [Pfeiffer et al., 2012a] and [Pfeiffer et al., 2013].

5.1 Bunch Arrival Time and Compression Control

This section describes how the measurements of bunch arrival time t_A and bunch compression C are combined with the RF field measurements to improve the beam performance. The measurements are processed for each single bunch within a bunch train, i.e. a sequence of electron bunches, and used for beam-based feedback to remove undesired machine fluctuations, e.g. residual RF field errors. The bunch arrival time must be stabi-

lized relative to e.g. pump-probe or to experiments where the electron beam is seeded by an external seed laser, the reader is referred to [sFLASH, 2013] for further details. The most challenging goal to meet is reaching the demanded beam performance. In 2010, first beam-based feedback strategies were tested, [Koprek et al., 2010]. Within this previous approach, the RF field setpoint signal is modified with respect to the bunch arrival time and bunch compression errors. It was shown that beam related corrections improve the beam stability. Within this section, the main focus is on improvements of beam-based feedback strategies by combining RF field and beam signals. It will be shown how the analysis of the beam and RF field model helps to further improve the beam performance towards a bunch arrival time jitter of 10 fs.

This section discusses first the theoretical controller design and finalizes with an example at FLASH.

5.1.1 Beam-Based Controller Design

In Section 3.3 the combination of the RF plant and beam model is given. This modeling approach is considered to develop an RF field controller strategy by including beam related measurements. Recall Figure 3.3.1, introduced in Section 3.3 on page 46. The combined model contains the model of the RF field, which maps an input vector field to an output vector field, both in I/Q coordinates. The model of the beam maps amplitude and phase changes to bunch arrival time and bunch compression changes, respectively. It has been shown that the latency for RF field and beam measurements are different, especially for the VME system, where beam signals are two microseconds, i.e. two sampling points, faster at the LLRF controller. This is due to the fact, that the beam signals are measured directly in contrast to the I/Q detection scheme for the RF field. The MTCA system uses a non-I/Q detection scheme such that both time delays can be assumed to be equal. In the following, the focus is on different beam-based controller strategies and can be summarized as follows: First, beam measurements correct the setpoint, followed by an extended MIMO controller and finally a controller approach, which combines RF field and beam errors.

a) Controller design using setpoint correction First results of this approach were shown in [Koprek et al., 2010]. The basic idea of correcting the RF field setpoint, depicted in Figure 5.1.1, leads to an improvement of the beam stability. The setpoint correction is done by a manipulation of the predefined RF field setpoint, leading to a beam-based correction. The setpoint modulation block M is given in I/Q coordinates by

$$\begin{bmatrix} \tilde{r}_{F,I}(k) \\ \tilde{r}_{F,Q}(k) \end{bmatrix} = \overbrace{\left(1 + \frac{\Delta A}{A}\right)}^M \cdot \begin{bmatrix} 1 & -\Delta\phi \\ \Delta\phi & 1 \end{bmatrix} \cdot \begin{bmatrix} r_{F,I}(k) \\ r_{F,Q}(k) \end{bmatrix}. \quad (5.1.1)$$

This approach is the initial point of this section. For further information the reader is referred to [Koprek et al., 2010]. This controller design will not be further studied, since it was shown in Section 3.3 that the beam related measurements are available faster than

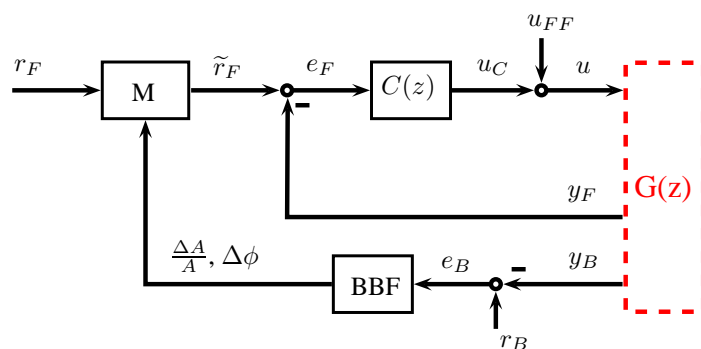


Figure 5.1.1: a) Beam-based feedback by setpoint correction, [Koprek et al., 2010].

the RF field measurements. In principle, the setpoint correction is a cascaded controller strategy with an outer and inner loop, where the outer loop is processed faster than the inner loop, leading to a delimitation by the RF field properties.

b) Controller design using extended MIMO controller We consider an extended MIMO controller, given by

$$\begin{bmatrix} u_{C,I}(k) \\ u_{C,Q}(k) \end{bmatrix} = [C(z)] \cdot \begin{bmatrix} e_{F,I}(k) \\ e_{F,Q}(k) \\ \Delta t_A(k) \\ \Delta C(k) \end{bmatrix}, \quad (5.1.2)$$

where the RF field and beam error acts as input. Hence, the controller has four inputs and two outputs, depicted in Figure 5.1.2. Assume the RF field controller is optimal with

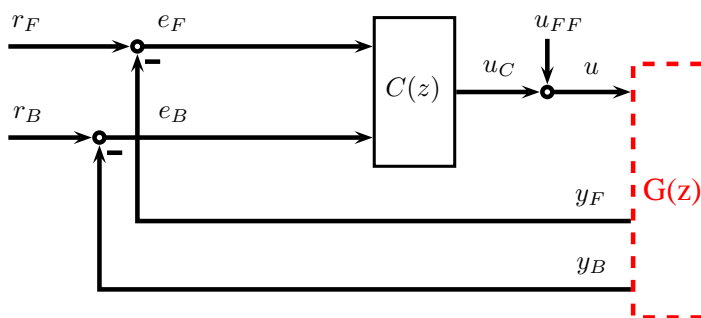


Figure 5.1.2: b) Beam-based feedback by an extended MIMO controller.

respect to beam energy fluctuations, an example is given in [Schmidt, 2010]. Thus it is straightforward to separate the extended controller into an RF field and beam controller

$$\begin{bmatrix} u_{C,I}(k) \\ u_{C,Q}(k) \end{bmatrix} = \begin{bmatrix} C_F(z) & C_B(z) \end{bmatrix} \cdot \begin{bmatrix} e_{F,I}(k) \\ e_{F,Q}(k) \\ \Delta t_A(k) \\ \Delta C(k) \end{bmatrix}, \quad (5.1.3)$$

where both controllers must be designed to be optimal. Therefore, in case of no beam or missing beam information, e.g. not working bunch arrival time detector, the RF field controller must be chosen as optimal w.r.t. bunch energy fluctuations. Assume all controller input signals are available, hence the beam error acts as input to the MIMO controller. The beam controller part must be chosen such that the extended MIMO controller works as desired. As shown in Section 3.2, the bunch arrival time and bunch compression error is mapped by the inverse of the static nonsingular beam model \tilde{G}_B to optimal amplitude and phase changes, (3.2.6) on page 44. Converting amplitude and phase changes to real and imaginary RF field vector changes, leads in principle to a similar error as given by the RF field error. Since the information flow, in terms of time delay, of the measured beam and RF field signals is different, this extension of the MIMO controller is affected by the time delay differences. E.g. consider a bunch arrival time error at time k . This means that the controller changes the output. Thus, the RF field controller part detects the error two sampling instances later and tries to correct this. This can be avoided by adjusting the RF field setpoint with respect to the beam related I/Q changes or by different weights for the RF field and beam error. Using the static matrix of the beam model and superimposing this by the dynamic model of the RF field, allows to design a controller which optimizes the vector modulator input for bunch arrival time and bunch compression errors. The dynamic RF field model must be included into the beam controller design, since additional fundamental modes may be excited.

Consider the beam errors and map those to RF field errors, first to amplitude and phase changes by

$$\begin{bmatrix} \Delta A(k) \\ \Delta \phi(k) \end{bmatrix} = \underbrace{\begin{bmatrix} t_{11} & t_{12} \\ t_{21} & t_{22} \end{bmatrix}}_{\tilde{G}_B^{-1}} \cdot \begin{bmatrix} \Delta t_A(k) \\ \Delta C(k) \end{bmatrix}, \quad (5.1.4)$$

afterwards to I/Q changes by assuming that $\Delta \phi(k)$ is small

$$\begin{aligned} \begin{bmatrix} \Delta I(k) \\ \Delta Q(k) \end{bmatrix} &= \begin{bmatrix} e_{B,I}(k) \\ e_{B,Q}(k) \end{bmatrix} \approx \begin{bmatrix} \cos(\phi_{SP}) & -Q_{SP} \\ \sin(\phi_{SP}) & I_{SP} \end{bmatrix} \cdot \begin{bmatrix} \Delta A(k) \\ \Delta \phi(k) \end{bmatrix} \\ &\approx \underbrace{\begin{bmatrix} \cos(\phi_{SP}) & -Q_{SP} \\ \sin(\phi_{SP}) & I_{SP} \end{bmatrix}}_{\mathcal{M}} \cdot \underbrace{\begin{bmatrix} t_{11} & t_{12} \\ t_{21} & t_{22} \end{bmatrix}}_{\tilde{G}_B^{-1}} \cdot \begin{bmatrix} \Delta t_A(k) \\ \Delta C(k) \end{bmatrix}, \quad (5.1.5) \end{aligned}$$

see Appendix D for the used approximation. As shown, bunch arrival time and bunch compression errors can be rewritten into RF field related errors, here $[\Delta I(k) \quad \Delta Q(k)]^T$. Without going into the details, it is sufficient to change the low frequency gain of the designed SO(2) symmetric RF field controller, which is optimized to decouple the system and to suppress additional fundamental modes. Afterwards, a weighting or trust factor can be defined, which changes the influence of the RF field, respectively beam error. Such an approach is given next, where not the controller is extended, but a sophisticated combination of both errors is used.

c) **Controller design using MIMO controller and error combination** As seen at the end of the previous controller design, i.e. case b), each beam related error can be computed to an RF field error. Thus, instead of extending the RF field MIMO controller, the remaining beam error is mapped back to the I/Q plane and merged with the RF field error, shown in Figure 5.1.3 by function $e_{F,B} = g(e_F, e_B)$. Since the beam is only

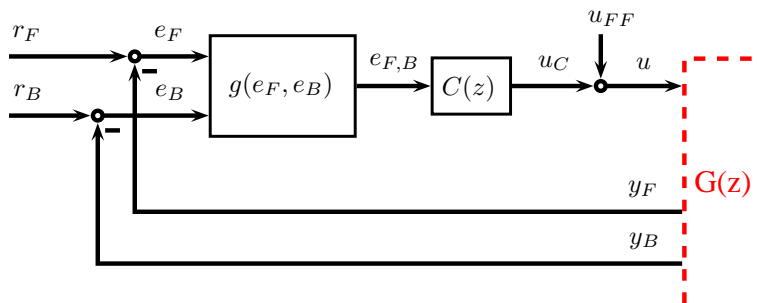


Figure 5.1.3: c) Beam-based feedback by combining the RF field and beam error.

present during flattop time, it is necessary that the RF field error in front of the injected beam is as small as possible, while the beam error acts only as correction of the RF field error. Assume that the RF field measurement has a coarse resolution compared to the beam measurement. Consider Figure 5.1.4: Assume, the beam error stays inside the RF field epsilon ball ϵ_f , which is defined around the operation setpoint as maximal RF field variations, given by $\Delta A_f/A_f < 0.01\%$ and $\Delta\phi_f < 0.01^\circ$, [Brinkmann et al., 2002] or [Altarelli et al., 2006]. Beam measurements with a higher resolution should lead to beam

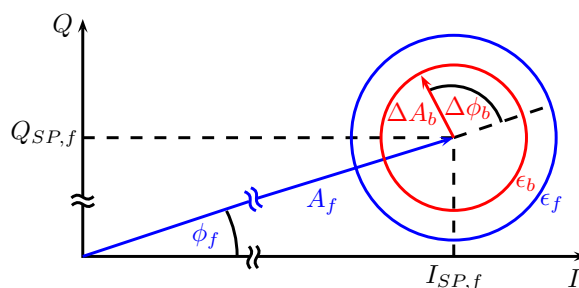


Figure 5.1.4: RF field and beam error for a given sampling instance during flattop with beam information.

corrections inside ϵ_f , such that $\epsilon_f > \epsilon_b$ holds. If the beam corrections leave the ball, an adaptation of the RF field setpoint is necessary, which is considered within Section 5.1.2. Combining or merging RF field and beam errors is shown as one of the important points to improve the beam performance, [Pfeiffer et al., 2012a]. Such an error signal combination was introduced in (5.1.5), where one has to distinguish between the first and second matrix which is multiplied by the beam error. The first matrix \mathcal{M} is a direct consequence of the RF field setpoint, while the second, i.e. \tilde{G}_B^{-1} , mainly depends on the properties of the bunch compressor, see Section 3.2. In case of RF field setpoint changes over the flattop, the first matrix must be adapted. Besides this combination, a second approach is done

by (5.1.1). Necessary for this modulation matrix $M \in \mathbb{R}^{(2 \times 2)}$ is a mapping of the beam error to a relative amplitude and absolute phase change, given by nonsingular transition matrix $G_B^{-1} \in \mathbb{R}^{(2 \times 2)}$, see (3.2.5) on page 44. Note, the combination of RF field and beam errors according to (5.1.1) holds only around the RF field setpoint. The designed controller strategy is depicted in Figure 5.1.5 and shortly outlined. First, calculate the field error e_F , lift up the resulting error to the setpoint, modulate the beam error to the RF field error using (5.1.1) and subtract the setpoint again. The result is an error $e_{F,B}$ which represents field and beam deviations. Two additional gains, used for an independent

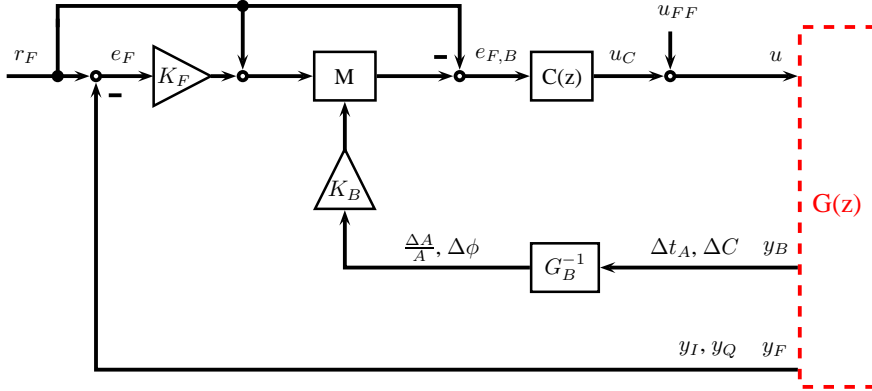


Figure 5.1.5: Cascaded feedback structure for merging field and beam error.

weighting of the RF field by K_F and the beam by K_B , are implemented and optimized with respect to the beam performance. As long as the beam is not present, K_F is set to one and K_B is set to zero, i.e. usual RF field feedback controller. Combining both errors, done by choosing weightings for both measurements, leads to an improvement of beam performance, presented in the following as an example at FLASH.

5.1.2 Example at FLASH

The beam-based feedback strategies to improve the bunch arrival time and bunch compression stability were tested and validated at FLASH. Figure 5.1.6 shows the locations of the beam related measurements, i.e. BAMs and BCs, together with their actuators, i.e. the accelerator modules. The bunch arrival time monitors at FLASH are named by

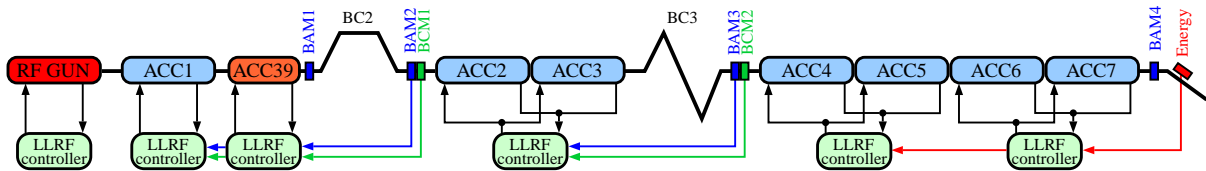


Figure 5.1.6: Beam-based feedback sensor and actuator location at FLASH

their location, e.g. 3DBC2 is located 3 meter downstream (3D) of the first bunch compressor; for historical reasons named BC2. Within this thesis, the BAMs are named by their number within the electron flight direction, see Table 5.1.

Table 5.1: Bunch Arrival Time Monitor Nomenclature

Nomenclature		Location; Comment
Thesis	FLASH	Typ. resolution for bunch with charge of 0.5 nC
BAM1	1UBC2	Upstream of BC2; Sensor for Laser FB ≈ 15 fs - 20 fs
BAM2	3DBC2	Downstream of BC2; Sensor for BBF ACC1 (ACC39) ≈ 17 fs - 22 fs
BAM3	4DBC3	Downstream of BC3; Sensor for BBF ACC23 ≈ 20 fs - 25 fs
BAM4	18ACC7	After main linac; Out of loop measurement ≈ 4 fs - 7 fs

First, only RF field control is considered. A bunch train of 50 bunches with a bunch repetition rate of 500 kHz is injected during flattop. Since the FEL is operated in pulsed mode, each bunch train starts at the same flattop time. Aligning the resulting bunch trains, leads to bunch arrival time measurements shown in Figure 5.1.7. The plot shows

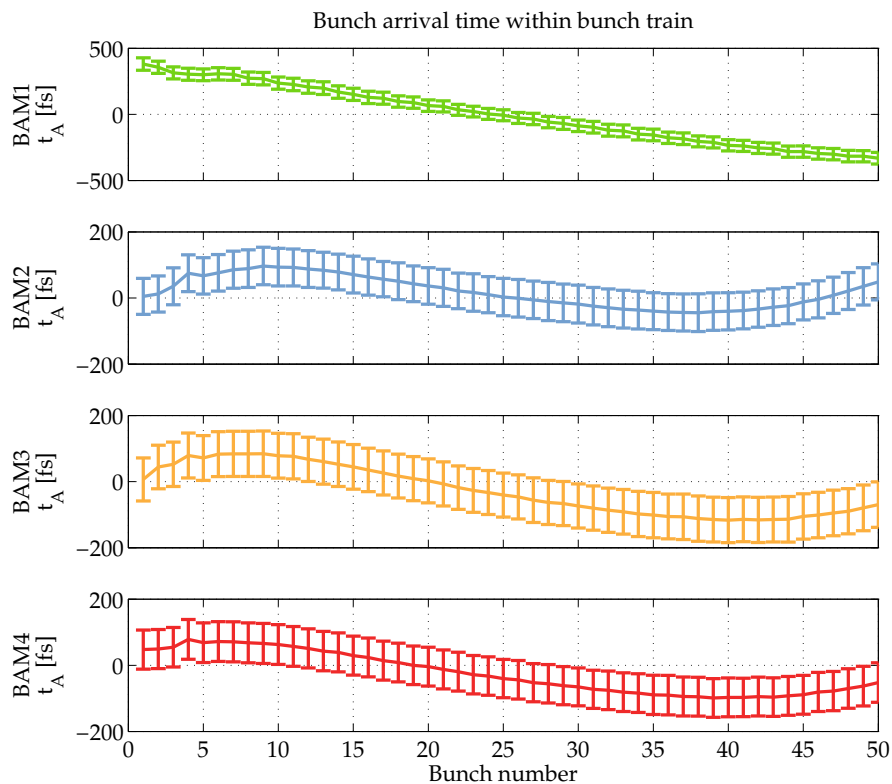


Figure 5.1.7: Bunch arrival time measurements with RF field control and without beam-based feedback. The dataset is taken over two minutes and shows the mean and standard deviation of bunch arrival time. The arrival time range of the first subplot differs from the other.

the mean bunch arrival time and the standard deviation over a time range of 2 minutes for BAM 1 to BAM4. Picking e.g bunch number 1, 5 and 25 of the measurements and plotting these over the considered time range, displays the fluctuations from pulse to pulse as shown in Figure 5.1.8. The shape of the bunch train within each pulse can be assumed

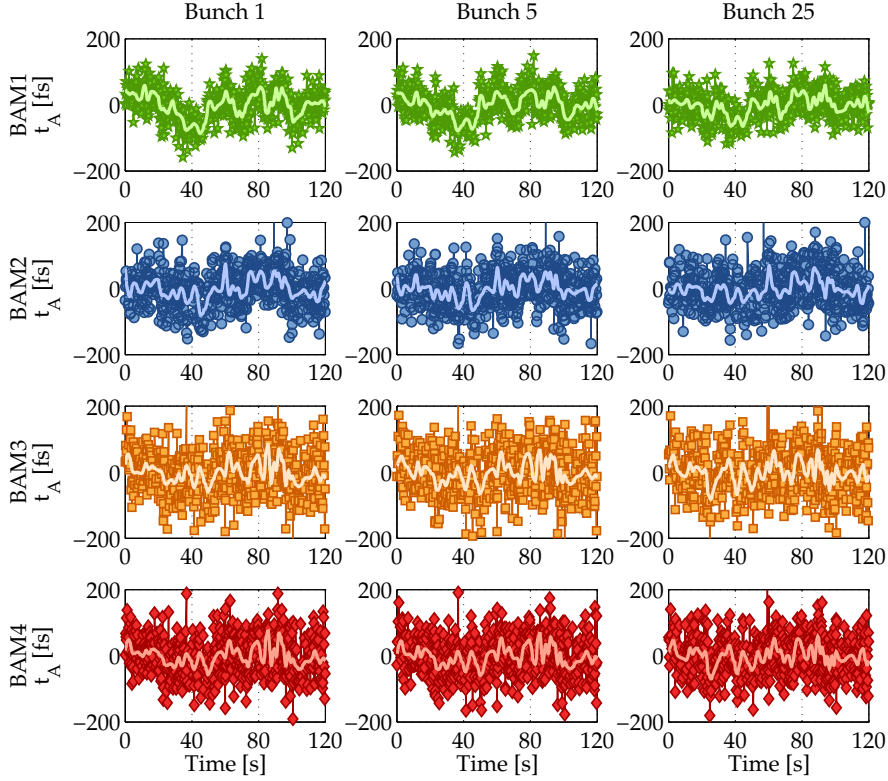


Figure 5.1.8: Usual standard deviation of bunch arrival time without beam-based feedback for a time range of two minutes. The light line within each plot depicts the trend.

to be similar, while the overall bunch train fluctuates by hundreds of femto-seconds. It will be shown, how the standard deviation of the bunch arrival time, the so-called bunch arrival time jitter, and bunch compression jitter of each individual bunch within a bunch train is reduced using the beam information.

Furthermore, repetitive bunch arrival time errors, which determine the bunch train shape are reduced by combining field and beam errors. By doing this, the controller input is a combined error, which is used to adjust the feedforward table by iterative learning control (ILC) algorithm, see Section 4.2.

SP Adaptation and Direct Feedback Approach

Recall the three different beam-based feedback controller strategies, presented in Section 5.1.1. The RF field setpoint modulation, Section 5.1.1.a, was presented in [Koprek et al., 2010]. This approach is compared to the direct feedback control strategy, Section 5.1.1.b. The result is shown in Figure 5.1.9. During this controller performance

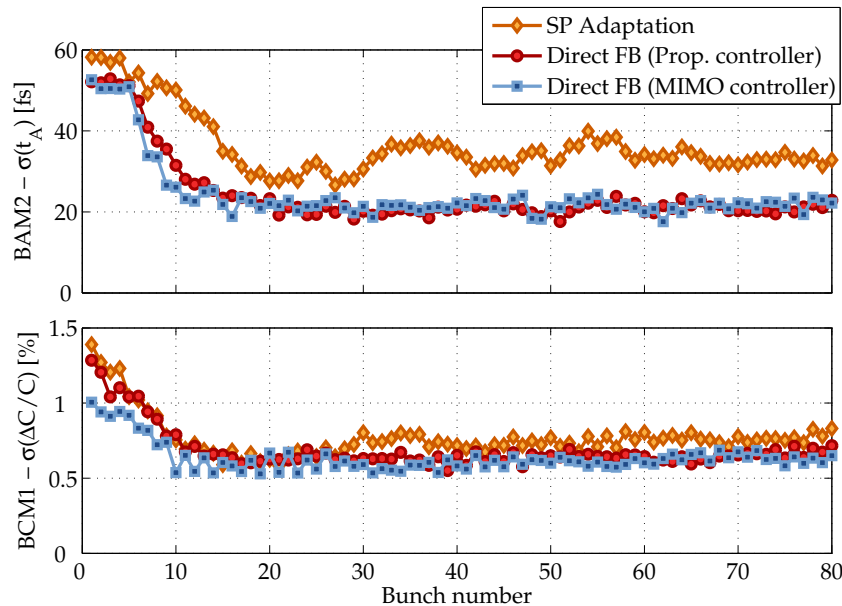


Figure 5.1.9: Controlling the bunch arrival time and bunch compression by setpoint (SP) adaptation and direct feedback (FB) scheme.

comparison, done within a time frame of 30 minutes for the presented three cases, it is assumed that the machine condition is not changing. The advantage of direct feedback control, discussed in Section 5.1.1, is shown in comparison to the setpoint adaptation. It can be seen that the standard deviation of the bunch arrival time and bunch compression can be reduced over the bunch train. Here case b) on page 83 is considered, i.e. *controller design using extended MIMO controller*. This direct feedback approach is used together with a second MIMO controller $C_B(z)$, which is (i) a diagonal proportional controller K_P and (ii) a dynamic controller $C(z)$, identical to the RF field controller $C_F(z)$, see (4.1.10) and (4.1.11) on page 56. During beam time, the field and beam measurements are weighted. In this example, field errors are not considered during beam time, i.e. weighted by zero. Such a weighting is sub-optimal in case of corrupted or missing beam measurements and will be studied in the following section. Nevertheless, it has been shown in theory and by measurements that the direct feedback control scheme together with an optimal controller improves the beam performance significantly.

Implementation at FLASH

Based on the controller design presented in Section 5.1.1.c, Figure 5.1.10 shows the recently implemented beam-based feedback structure at FLASH. Switch S_1 allows to enable

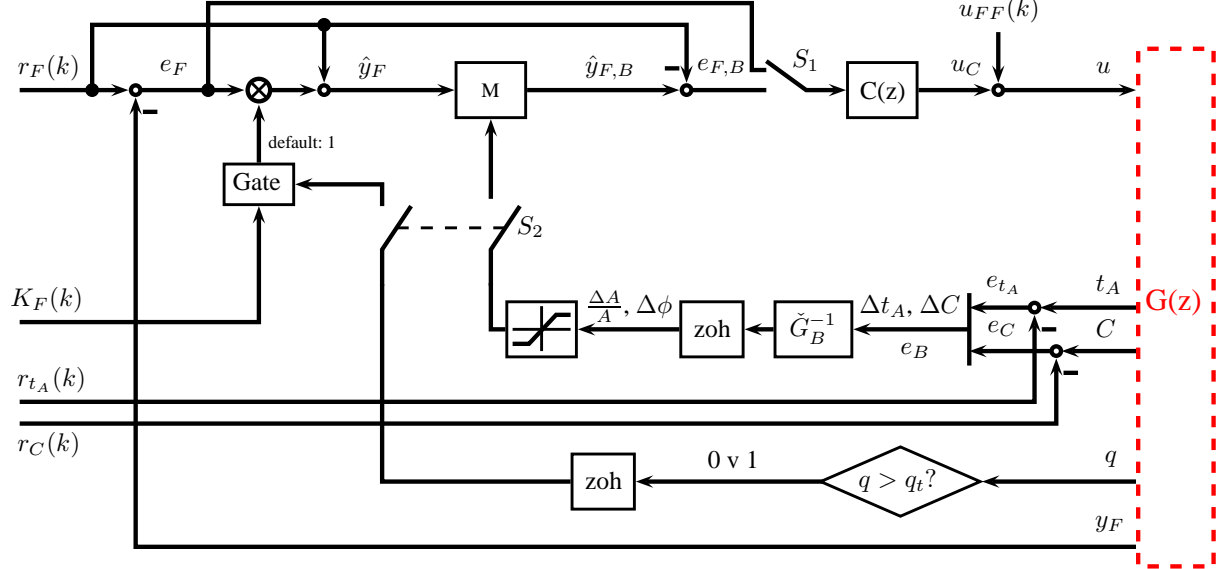


Figure 5.1.10: Beam-based feedback implementation for all RF stations at FLASH.

or disable the beam-based feedback path. By changing the state of S_1 , the internal computation time within the FPGA may change. Since the controller $C(z)$ is optimized for a fixed time delay, the state of S_1 is set once to distinguish between the injector, booster (both are suitable for beam-based feedbacks) and main linac section. From now on S_1 is one, i.e. beam-based feedback path is enabled, which allows to superimpose the beam error with the field error. The second switch S_2 is used to activate the beam-based feedback. The basic functionality, for $S_1=S_2=1$ (beam-based feedback path and beam-based feedback are enabled) is given as follows. First, compute the difference between field setpoint and vector sum. The resulting field error is scaled by $K_F(k)$, which is one in case of no beam. By measuring the beam charge q and defining a threshold value q_t , the predefined value of $K_F(k)$ scales the field error if $q > q_t$, otherwise feed through the field error in case of no beam ($q \leq q_t$). In presence of different beam repetition rates, a zero order hold block keeps the previous values w.r.t. the bunch spacing, e.g. for 500 kHz this value is kept for 2 μ s. Next the field error is modulated by the beam error, which is done around the setpoint as described in Section 5.1.1.c. The beam error is computed from bunch arrival time and compression setpoints and their measurements. The beam scaling factor is part of the transformation matrix $\check{G}_B^{-1} = K_B \cdot G_B^{-1}$, where K_B is a diagonal matrix whose elements correspond to the weighting of bunch arrival time and bunch compression, respectively, see (5.1.6).

$$\begin{bmatrix} \frac{\Delta A}{A} \\ \Delta \phi \end{bmatrix} = \underbrace{\begin{bmatrix} K_{B,1} & 0 \\ 0 & K_{B,2} \end{bmatrix}}_{\check{G}_B^{-1}} \begin{bmatrix} t_{11} & t_{12} \\ t_{21} & t_{22} \end{bmatrix}^{-1} \begin{bmatrix} \Delta t_A \\ \Delta C \end{bmatrix} \quad (5.1.6)$$

If $K_B = \mathbf{I}$, the beam related errors are mapped to optimal amplitude and phase changes, for $K_B \neq \mathbf{I}$, those changes are scaled proportionally. A limiter

$$y(u) = \begin{cases} -a ; & u < -a \\ u ; & -a < u < a \\ a ; & u > a \end{cases}, \quad (5.1.7)$$

for beam related amplitude and phase correction is implemented to avoid undesired large field changes if one of the beam measurements is corrupted. Here, the relative amplitude and phase correction can be limited independently. Within the limits, the input is fed through to the output, while the output is truncated in case of reached predefined limits. First, an optimization of field and beam weighting factors is considered, where the main focus is on improving the bunch arrival time stability.

Optimization of field and beam weighting factor To minimize the arrival time jitter for the user, a gain scan has been performed and is presented in Figure 5.1.11, where the bunch arrival time improvement of the monitor under control is shown, i.e. BAM2 for beam-based feedback with ACC1. If the field weighting is one and the beam

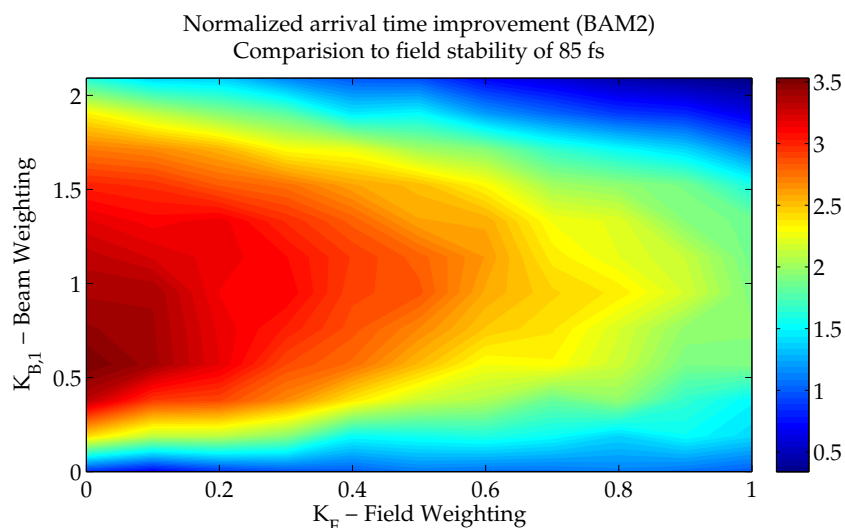


Figure 5.1.11: Arrival time scan for BAM2 with weighting variation in ACC1 for the cascaded beam-based feedback.

weighting is zero, then only field control is active. The resulting bunch arrival time jitter for this special case will be used to normalize the improvements such that a value of one represents only field control. Higher values, given as color code, represent improvements of the bunch arrival time compared to simple field control. If the field gain is kept constant and the beam gain is increased the arrival time stability gets better and after a maximum becomes worse again. This is explainable by different loop delays of the field and beam feedback as on the one hand both feedback loops antagonize each other and on the other hand the individual time delays limit the feedback gain. The lowest arrival time jitter for ACC1 is found at a field gain factor of zero and a beam gain factor of about 0.6.

Hence, without field control the minimal arrival time jitter can be found. However in case of beam cuts, i.e. losses somewhere within the accelerator, the field is driven in open loop since the field weighting factor is zero which may cause problems like oscillations of the ILC algorithm, see Section 4.2. Thus, for safety reasons, it is advisable to drive the system with a small field weighting. In addition consider the out of loop measurement of BAM4, Figure 5.1.12, which shows the bunch arrival time improvements, while the scan was done on ACC1. Furthermore, ACC39 and ACC23 are controlled only by field

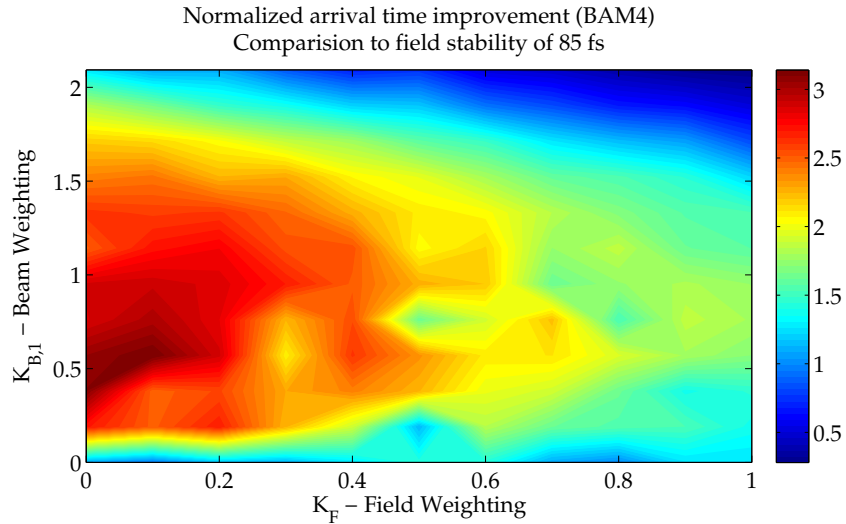


Figure 5.1.12: Arrival time scan as in Figure 5.1.11 for BAM4 with weighting variation in ACC1 in comparison to the out of loop arrival time measurement.

measurements, i.e. without beam information. A wider spread of optimal weighting coefficients for K_F and $K_{B,1}$ is visible. One possible reason, beside ACC39 and ACC23, could be uncorrelated noise sources of the field and beam measurement such that both superimposed weighted errors point, in best case, into the opposite direction. Regarding this, further studies are needed to understand the wider spread of possible weightings. As shown in Figure 5.1.12, beside choosing $K_F = 0$ and $K_{B,1} \approx 0.4$, one can set $K_F \approx 0.1$ and $K_{B,1} \approx 0.6$ such that a similar improvement is reached. Thereby, the field weighting is not zero, such that in presence of beam cuts the field is not driven in open loop.

Improving bunch arrival time Consider Figure 5.1.13, where the improvements by controlling the beam properties are shown. Here, 50 bunches with a bunch repetition rate of 500 kHz are injected. Both, ACC1 and ACC23, are used to control the beam properties. The bunch arrival time jitter is plotted over the number of bunches, for a time range of 2 minutes. Here, BAM1 measures the arrival time upstream of the first bunch compressor (BC2), while BAM2 detects the bunch arrival time after the first BC, which is fed into the LLRF controller of ACC1. The bunch arrival time at BAM3 is fed back to ACC23, while BAM 4 is used as out of loop measurement. BAM3 and BAM4 should show the same arrival time for relativistic electron bunches since there is no further magnetic chicane in between. Figure 5.1.14 presents the correlation of both BAMs for four selected bunches within the bunch train. Caused by the time delay and low closed loop



Figure 5.1.13: Standard deviation of bunch arrival time with applied beam-based feedback to ACC1 and ACC23 at FLASH.

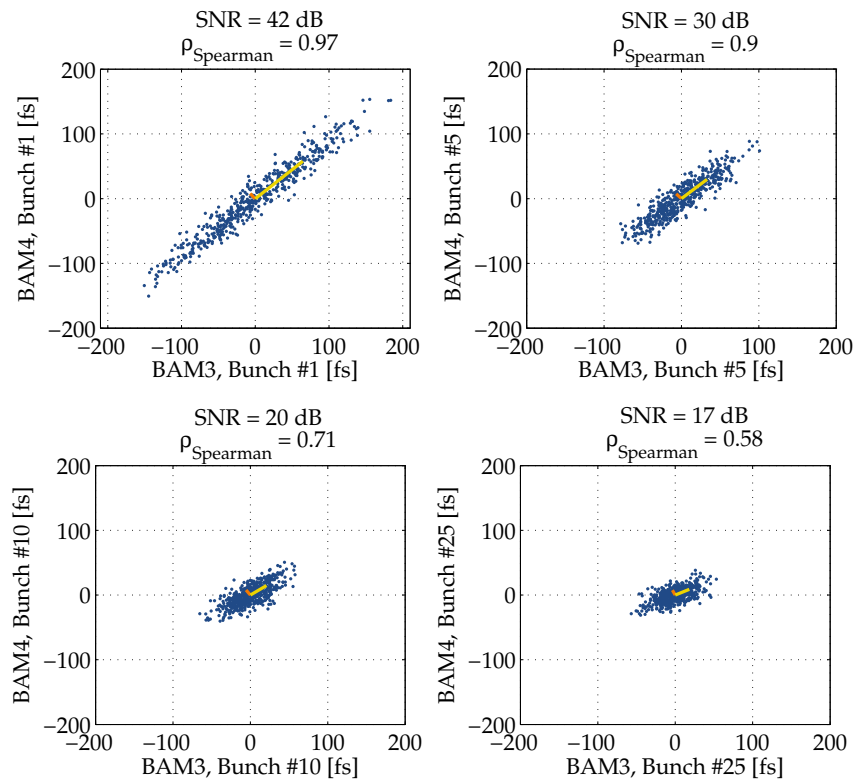


Figure 5.1.14: Correlation between BAM3 and BAM4; the signal-to-noise ratio (SNR) is computed as ratio between the diagonal and off-diagonal spread within the bunch arrival time spread and ρ_{Spearman} is a measure of statistical dependence between the two variables.

controller bandwidth within the feedback structure, the first bunches cannot be controlled, such that the bunch arrival time jitter is comparable to the jitter with only field control. Therefore those bunches show the highest signal-to-noise ratio (SNR). The bunch arrival time jitter over the bunch train is reduced by the beam-based feedback, such that later bunches are closer to the measurement resolution, resulting in a smaller SNR. Consider as example the transition from bunch 1 to bunch 5. After 5 bunches, the bunch arrival time error of BAM4 reduces from about ± 200 fs peak-to-peak down to about ± 75 fs peak-to-peak. Respectively, the standard deviation reduces from 60 fs down to 30 fs, shown in Figure 5.1.13. In the following, the first 10 bunches are not considered within the computation of the bunch arrival time improvement. The reason for this is given on a later stage.

One important advantage of the designed beam-based feedback strategy is the superimposed field and beam error, which acts directly as input for the ILC algorithm, see Figure 2.3.1 on page 8 and Figure 5.1.5. This allows to reduce possible repetitive arrival time spreading within a bunch train without using a second ILC to correct the RF field setpoint, see Figure 5.1.15; and Figure 5.1.16 which display the bunch arrival time jitter for some chosen bunches for a longer time period. Such an algorithm has problems,

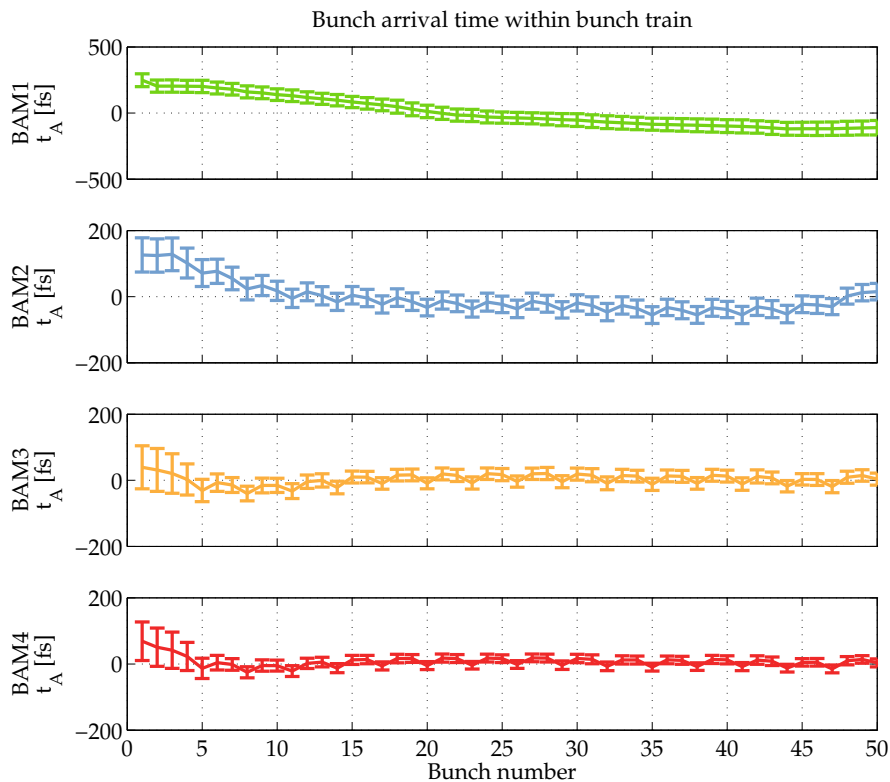


Figure 5.1.15: Bunch arrival time with applied beam-based feedback. The arrival time range of the first subplot differs from the other. The bunch arrival time shape is flattened by modification of RF field error signal, used for iterative learning control.

especially at edges like switching on and off the beam. For the first few bunches this

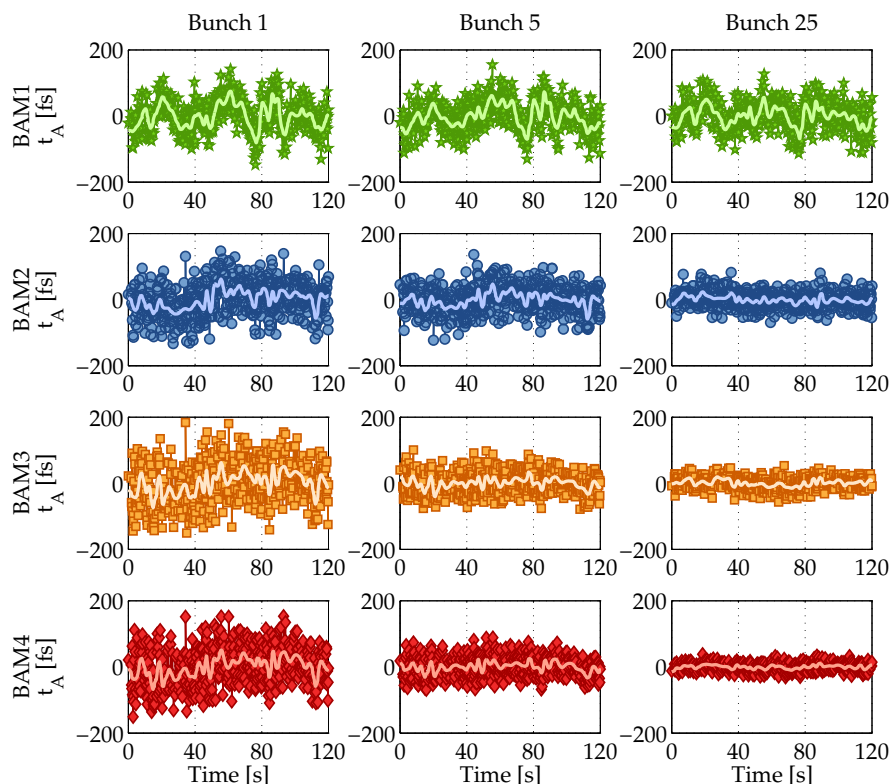


Figure 5.1.16: Usual standard deviation of bunch arrival time with beam-based feedback for a time range of two minutes. The light line within each plot depicts the trend. For comparison reasons, the bunch arrival time axis is not scaled and for all subplots the same.

is not critical, because those are used to stabilize the beam and can be kicked out such that only the stabilized bunches are used for e.g. pump-probe experiments. Figure 5.1.16 gives an example how the arrival time jitter is minimized over a longer time range at FLASH. Starting with the arrival time jitter coming from the GUN (BAM1) the later BAMs, especially BAM4 used as out of loop measurement, show the improvements of the bunch arrival time jitter by a factor of 3 where ACC1 and ACC23 are controlled by the cascaded beam-based feedback structure.

Brief summary: Three different beam-based control strategies were presented. Since the beam related measurements can be mapped to RF field errors, the optimal beam-based controller minimizing the bunch arrival time and bunch compression jitter was chosen as cascaded controller with an inner beam and outer RF field loop. It has been shown, that with the VME system a bunch arrival time stability in femto-second range and performance improvements regarding the bunch compression were reached. The proposed beam-based feedback controller works as desired. However, the beam performance is limited by measurement accuracy and, for high frequency noise, by the closed-loop system bandwidth of about 40 kHz.

MTCA System Integration

The previously presented beam-based feedback controller approach for FLASH needs to be integrated within the MTCA framework. It has been shown, that the basic accelerator structure for FLASH and XFEL, especially for the injector and booster section, are very similar. This allows to give an outlook based on the results from the beam-based feedback tests for the VME system at FLASH. Beside the reduction of the expected time delay for RF field measurements, the main focus is on the higher signal precision, i.e. a higher ADC resolution. This changes, from the theoretical point of view, the size of the ϵ_F ball, see Figure 5.1.4, which requires an adaption of the field and beam weightings. Nevertheless, the outer RF field loop needs to be modulated by beam-based signals, such that the proposed beam-based feedback strategy is highly suitable. The bunch arrival time monitors are currently in a progression stage to improve the bunch arrival time resolution even for small electron bunch charges. Thus, by updating the bunch arrival time monitors for a higher measurement precision, the ϵ_B size will be reduced.

5.2 Beam Energy Control with Information Exchange

As presented in Section 5.1, the bunch arrival time and bunch compression is stabilized by a modulation of the RF field upstream of a bunch compressor. This energy modulation controls the beam performance at the expense of the beam energy stability, which is unacceptable because this is proportional to the wavelength of the laser light generated by the SASE process.

Within this section, the focus is on beam energy control for the European XFEL by an interconnection of the RF field controllers, which follows a distributed control scheme. The interconnection of the RF field controllers is not necessary for FLASH, since the main linac only consists of two RF stations, where the initial and final beam energy measurement can be fed into the first and second RF station of the main linac simultaneously.

First, an introduction which discusses possible beam energy errors and how to avoid those is given. Section 5.2.2 starts with the plant requirements for the considered distributed controller design. It will be shown, that only two measurements for the beam energy, i.e. the initial and final beam energy of the main linac, are not sufficient for high performance beam energy control. Hence, the physical equations describing the energy gain within each accelerator module are rewritten, leading to an observer based controller design. Efficient tools are available to solve the controller synthesis for large scale systems which are outlined at the end of this section. Simulation results, with the assumption that the electron flight time through the main linac is neglectable, complete this section.

5.2.1 Introduction

In the following, a distributed controller design for a linear accelerator such as the European XFEL is developed. At the European XFEL one distinguishes between the injector-, booster- and main-linac sections. The injector and booster section is the first part of an accelerator, where bunch compressors are used to force electrons on different trajectories through the BC to control the beam related measurements, i.e. the bunch arrival time and bunch compression, described in Section 5.1.

Within the second part of the linear accelerator, i.e. the main linac, the beam energy is increased by each RF station up to a final beam energy. At the end, an undulator forces the electron beam on a sinusoidal trajectory, hereby electrons emit light with a wavelength appropriate to their energy. Keeping the final beam energy constant, results in the same laser light wavelength for each electron bunch. Within this section, the focus is on minimizing the final beam energy error by controlling the RF fields of the main linac. It is sufficient to consider mainly two energy errors, caused by a cavity quench and the quench protection system. The shape of the beam energy error is almost known, while the time of action is unknown. In addition, such beam energy errors may occur at several subsystems.

Cavity Quench and Quench Protection At FLASH and the European XFEL, superconducting cavities, build from niobium and operated at a temperature of 2 K, are used to increase the energy of the electrons. At a temperature above 9.2 K, the so-called critical temperature, niobium becomes normal conducting, [Wangler, 1998]. Often impurities and high gradients of the RF field within a cavity lead to a so-called quench state. Field emission can cause local areas to heat up, due to tiny particles, until the RF field within a cavity breaks down. This transition from superconducting to normal conducting causes the loss of the stored energy. A quench detection server detects an undesired energy change. If a cavity quench within an accelerating module occurs, the vector sum signal will decrease due to the RF field drop caused by the quenching cavity. But the RF field controller tries to keep the field error as small as possible. Thus, additional RF power is fed into the remaining cavities. Hence, all neighboring cavities are used to recover zero error by increasing their own RF field. This can result in additional cavity quench events for the remaining cavities as shown in Figure 5.2.1.

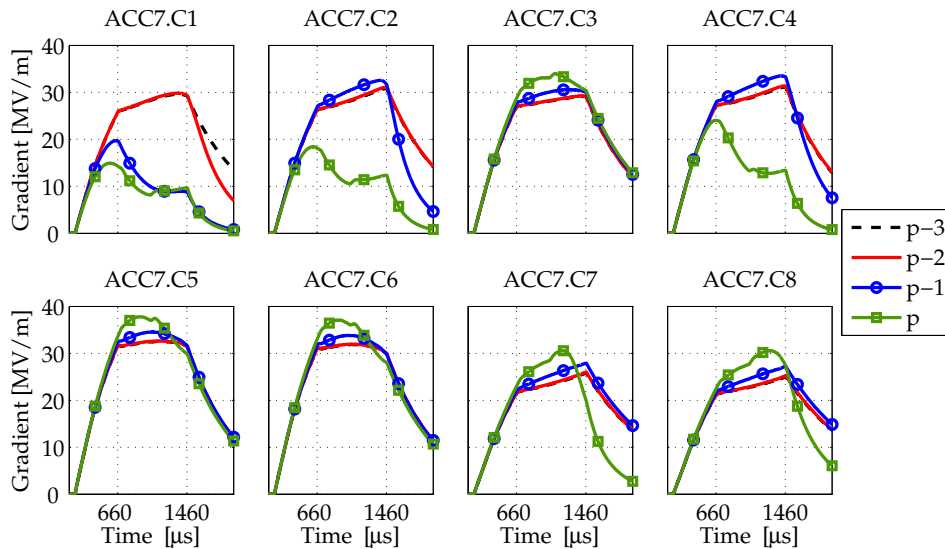


Figure 5.2.1: Presented is a quench sequence for four succeeding pulses starting from pulse (p-3) to pulse (p) for accelerator module ACC7 at FLASH (data is taken during ILC studies in 2012, [ILC, 2013]). Cavity 1 (ACC7.C1) changes at pulse (p-2) the loaded Q (different slope during decay), while in the following pulses the RF field controller tries to keep closed-loop operation, leading to cavity quench events for some remaining cavities.

First, a strategy is considered to avoid cavity quenches, followed by a strategy to recover the RF station, [Branlard et al., 2012].

Pre-Limiter One possibility is to define an upper RF field limit for each cavity, i.e. a pre-limiter. If a cavity reaches this limit, the RF field setpoint is decreased over time until the RF field falls below this limit. Therefore, a pre-limiter helps to avoid cavity quenches. Within the following simulation results, such a behavior is considered as ramp-like energy error.

Adjust the RF field setpoint If a sudden cavity quench occurs, in case the pre-limiter is deactivated or not fast enough, one could instantaneously lower the RF field setpoint, to avoid feeding additional RF power to the cavities. Therefore, the RF field setpoint must be decreased to keep the remaining cavities in closed-loop operation; in the following, this is simulated as step-like energy error. This error is an extremum since the stored energy within the cavity decreases by an exponential decay.

The resulting energy error for both scenarios should be compensated by the remaining RF stations. It is assumed that no control action is taken to bring the disturbed RF station back to its normal operation. To distinguish between RF fields, which are used to increase the energy of the electron beam, and the beam energy, two setpoints are defined: the RF field setpoint, which can be changed by the quench protection system, and an energy gain setpoint, respectively.

Only in the case that an event within an RF station occurs, the resulting error will be transmitted to the neighboring RF stations and only the RF field setpoint will be changed. Otherwise, the local RF field feedbacks are active, such that the field error is as small as possible.

5.2.2 Distributed Controller Design

It will be shown, that a linear accelerator, more precisely the main linac, can be approximated by a finite chain of subsystems in spatial domain. In addition, the controller design considers the possibility to control the overall system by neighboring subsystems to the left and right, while in theory only one direction would be possible. Since measurements for the control variable, i.e. the beam energy, are only available for the first and last RF station, physical equations are rewritten to approximate this variable for the remaining RF stations. The system equations in spatial and time domain are combined to a generalized plant. Each accelerator module itself is an enclosed subsystem, such that remaining errors, as well as the control signals, must be distributed digitally. First an introduction to the considered RF field model and possible simplifications are given.

RF Field Model for Homogeneous Distributed Controller Design The physical plant behavior and the system identification is described in Section 3.1. The resulting two-input two-output linear time-invariant model in discrete-time takes the form

$$\begin{aligned}x(k+1) &= \Phi x(k) + \Gamma u(k) \\ y(k) &= Cx(k) ,\end{aligned}$$

with $u(k) \in \mathbb{R}^2$ as input to the vector modulator and $y(k) \in \mathbb{R}^2$ as output, i.e. the vector sum. Figure 3.1.15, see page 38, displays the frequency response of the identified SO(2) symmetric model without time delay.

Within this section the following *distributed control assumptions* are chosen:

- RF field model of each subsystem is SO(2) symmetric with:
 - Constant rotation matrix $R(\phi_G)$ for all frequencies
 - Additional fundamental modes are neglected
 - Remaining scaling part $A_G(z)$ is identical for all RF stations
- Definition of an energy gain setpoint for each RF station
- Allow information exchange with both neighboring RF stations
 - without communication delay
 - with a constant and not changing communication delay
- Finite chain of RF stations

The first assumption is a necessary condition to consider each RF station as identical. Therefore, the focus is only set on the system bandwidth, i.e. no additional fundamental modes are included into the plant model. This assumption is required since each RF station may have additional fundamental modes at different frequencies, while within the distributed controller design all subsystems are assumed to be equal. The mode suppression part can be included afterwards by using the symmetric controller design described in Section 4.1.2. This allows to extend the resulting distributed controller by additional block-wise matrices, representing the eigenvalues, input and output matrices for the additional fundamental mode suppression. If it is not possible to equalize the individual subsystems, the reader is referred to [Dullerud and D’Andrea, 2004] who proposed a method for non-identical subsystems. The second assumption distinguishes between local RF field control and energy control by an information exchange. The energy gain setpoint is stored such that the beam energy gain without error can be recovered for the disturbed RF station. The third assumption, i.e. information exchange between neighboring RF stations, is necessary for a distributed control approach. The fourth copes with a real physical plant with boundary conditions and is designed as in [Langbort and D’Andrea, 2003], who model the distributed plant as infinite interconnection by using the *method of images*. It will be shown that this is a valid assumption even for a linear accelerator. Communication delays are neglected during the first simulation results, while the last subsection copes with communication delays.

An introduction of the used distributed control design for spatially interconnected systems, based on [D’Andrea and Dullerud, 2003], is given in Appendix E.

Distributed Plant Representation for a Free-Electron Laser

The main linac consists of RF station A5 to A25, depicted in Figure 5.2.2, which accelerate the beam to the final target energy. The beam energy at the entrance of the main linac can be measured by an Energy Beam Position Monitor (EBPM) within the last bunch

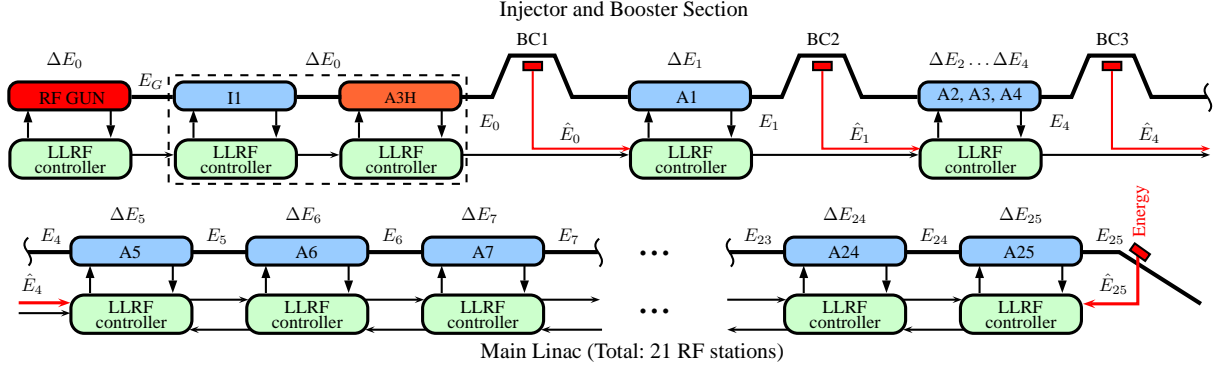


Figure 5.2.2: Main linac of the XFEL consisting of 21 RF stations.

compressor, see Section 2.4. The beam energy exiting the main linac can be measured by combining beam position measurements to an energy signal. Both measurements are used to control the initial and target beam energy as depicted in Figure 5.2.2. Along the main linac the beam energy must be estimated by the energy gain of the contributing RF stations. In the following, the contribution of each RF station is denoted by $\Delta E(k, \mathbf{s})$ with discrete time steps k and spatial domain parameter by \mathbf{s} . The beam energy $E(k, \mathbf{s})$ denotes the beam energy at the RF station exit. Then the final beam energy can be expressed as sum of the initial beam energy and all energy gains:

$$E(k, 25) = E(k, 4) + \sum_{\mathbf{s}=5}^{25} \Delta E(k, \mathbf{s}) . \quad (5.2.1)$$

In the following a strategy is developed, which allows to reduce the final beam energy error by an interconnected control scheme. First an introduction in increasing the beam energy by a single accelerator module is given, followed by the interconnection of all accelerator modules within the main linac.

Energy gain for an accelerator module It is assumed, that the electrons increase their energy within an accelerator module only by the real part of the electric field. Other effects like a not perfectly calibrated beam phase are neglected. Hereby, the energy gain inside the cavities is given as

$$\Delta E(k, \mathbf{s}) = E(k, \mathbf{s}) - E(k, \mathbf{s} - 1) \quad (5.2.2)$$

$$= q \cdot A(k, \mathbf{s}) \cdot \cos(\phi(k, \mathbf{s})) , \quad (5.2.3)$$

where q is the elementary charge, and $A(k, \mathbf{s})$ and $\phi(k, \mathbf{s})$ are the RF field amplitude and phase at spatial location \mathbf{s} . Assume that the energy within the main linac is controlled by keeping the RF field phase constant and changing only the RF field amplitude. Set the RF field phase $\phi(k, \mathbf{s}) = 0$ for all subsystems, i.e. an usual on-crest operation. By this, only one channel, i.e. the real part of the RF field, is necessary to control the amplitude and therefore the beam energy. The second channel, i.e. the imaginary channel is zero by $\phi(k, \mathbf{s}) = 0$, which leads to an energy gain

$$\Delta E(k, \mathbf{s}) = q \cdot y_I(k, \mathbf{s}) , \quad (5.2.4)$$

where $q = -e$ is the charge for an electron and $y_I(k, i)$ is the real part of the RF field, [Towiwat, 2011]. For simplicity, the proportional conversion from voltage to energy, i.e. from the unit volt [V] to electron volt [eV], which is a multiplication of the RF field voltage with the electron charge, is absorbed in the output signal

$$\Delta E^F(k, \mathbf{s}) = \frac{\Delta E(k, \mathbf{s})}{q} = y_I(k, \mathbf{s}) , \quad (5.2.5)$$

where $\Delta E^F(k, \mathbf{s})$ is a modified charge free energy gain. As before, all absolute beam energies are modified as $E^F(k, \mathbf{s}) = E(k, \mathbf{s})/q$, which will not change the control problem. If the RF field phase is non-zero, the second channel can be adjusted afterwards by a rotation matrix which maps the amplitude change to a complex vector field change. Nevertheless, the RF field phase has to be kept constant.

Energy error for an accelerator module Beside the RF field setpoint $r^{RF}(k, \mathbf{s})$ define an energy gain setpoint $r^E(k, \mathbf{s})$. During normal operation both setpoints are equal. As discussed in Section 5.2.1, in case of an error, e.g. cavity quench, the RF field setpoint is changed to recover closed-loop operation. Hence, (5.2.2) and (5.2.4) are combined to

$$\begin{aligned} E^F(k, \mathbf{s}) &= E^F(k, \mathbf{s} - 1) + y_I(k, \mathbf{s}) , \\ E^F(k, \mathbf{s}) &= E^F(k, \mathbf{s} - 1) + r^E(k, \mathbf{s}) - \epsilon(k, \mathbf{s}) , \end{aligned}$$

where

$$\epsilon(k, \mathbf{s}) = r^E(k, \mathbf{s}) - y_I(k, \mathbf{s}) \quad (5.2.6)$$

represents the beam energy error within an accelerator module.

Energy error for the FEL Including the beam energy error $\epsilon(k, \mathbf{s})$, defined in (5.2.6), into (5.2.1) and assuming that the charge is absorbed by the energy leads to

$$E^F(k, 25) = E^F(k, 4) + \sum_{\mathbf{s}=5}^{25} r^E(k, \mathbf{s}) - \epsilon(k, \mathbf{s}) . \quad (5.2.7)$$

It is obvious, that the final beam energy error

$$\epsilon_E(k) = \epsilon(k, 4) + \sum_{\mathbf{s}=5}^{25} \epsilon(k, \mathbf{s}) \quad (5.2.8)$$

is the sum of the initial beam energy error and all beam energy errors within the main linac. Assume that the beam energy measuring system at the end of the main linac measures a beam energy error $\epsilon_E(k)$. Recall that only one energy detector can be used to control energy errors within the main linac, e.g. by correcting the RF field of the last RF station.

Controllability and Observability With the assumption that only the real part of the RF field, i.e. $y_I(k)$, is needed to control the beam energy and by exploiting symmetry properties of the plant, see Section 3.1.4 on page 40, the resulting two by two linear time-invariant model can be decomposed into two SISO transfer functions. Each of the resulting SISO systems, given in spatial domain \mathbf{s} , is represented in state space form as

$$\begin{aligned} x(k+1, \mathbf{s}) &= A_G x(k, \mathbf{s}) + B_G u(k, \mathbf{s}) , \\ y(k, \mathbf{s}) &= C_G x(k, \mathbf{s}) , \end{aligned} \quad (5.2.9)$$

with $x \in \mathbb{R}$ as state variable, $u \in \mathbb{R}$ as input to the vector modulator and $y \in \mathbb{R}$ as output, i.e. the vector sum; the numerical values are taken from (3.1.43) with frequency response corresponding to Figure 3.1.15 as

$$A_G = 0.9998 \quad \text{and} \quad B_G = C_G = 0.0194 .$$

It is assumed, that all accelerator modules can be modeled by the same transfer function, i.e. they represent a homogeneous chain of subsystems. Therefore, the main linac consisting of 21 subsystems is represented in state space form as

$$\begin{aligned} \begin{bmatrix} x(k+1, 5) \\ x(k+1, 6) \\ \vdots \\ x(k+1, 25) \end{bmatrix} &= \begin{bmatrix} A_G & 0 & \cdots & 0 \\ 0 & A_G & \cdots & 0 \\ \vdots & \vdots & \ddots & \vdots \\ 0 & 0 & \cdots & A_G \end{bmatrix} \begin{bmatrix} x(k, 5) \\ x(k, 6) \\ \cdots \\ x(k, 25) \end{bmatrix} + \begin{bmatrix} B_G & 0 & \cdots & 0 \\ 0 & B_G & \cdots & 0 \\ \vdots & \vdots & \ddots & \vdots \\ 0 & 0 & \cdots & B_G \end{bmatrix} \begin{bmatrix} u(k, 5) \\ u(k, 6) \\ \vdots \\ u(k, 25) \end{bmatrix} , \\ \epsilon_E(k) &= \begin{bmatrix} -C_G & -C_G & \cdots & -C_G \end{bmatrix} \begin{bmatrix} x(k, 5) \\ x(k, 6) \\ \vdots \\ x(k, 25) \end{bmatrix} + \epsilon(k, 4) , \end{aligned} \quad (5.2.10)$$

with $u(k, \mathbf{s}) \in \mathbb{R}^{21}$ as input to each vector modulator, $\epsilon(k, 4)$ as energy error input to the main linac and $\epsilon_E(k) \in \mathbb{R}$ as output. The output represents the final energy error (5.2.8) as sum of energy errors from each accelerator module, i.e. the sign-inverted vector sum signals (5.2.6). It is straightforward to show that the system (5.2.10) is controllable, since the controllability matrix

$$\mathcal{C}(A, B) = \begin{bmatrix} B & AB & A^2B & \cdots & A^{n-1}B \end{bmatrix} \quad (5.2.11)$$

has full rank for the given numerical values, while the system is not observable, i.e. the observability matrix

$$\mathcal{O}(C, A) = \begin{bmatrix} C^T & (CA)^T & (CA^2)^T & \cdots & (CA^{n-1})^T \end{bmatrix}^T \quad (5.2.12)$$

has a rank lower than the system order; the observability rank is one for the given values. Based on the energy measurement at the end of the main linac, it is not possible to detect the location \mathbf{s} at which an energy error is first generated. This is an undesired case, because if a cavity at the beginning of the main linac quenches and the beam energy is

not corrected close to the disturbed RF station, an adjustment of steerer and quadrupole magnets, which have a low bandwidth in the order of hertz, is probably necessary to provide a matched beam optics and straight beam orbit through the accelerator. In addition, it may happen, that a cavity quench occur within the last RF station if the RF field needed to correct an energy disturbance is above an RF field limit. Hence, it is preferable to control the beam energy close to the disturbed module.

To recap: The plant model of spatially interconnected control variable, i.e. beam energy error, shows that the system is controllable, while it is not observable with only one beam energy detector. To cope with non-observability of the system, a scheme which distribute locally computed beam energy errors is chosen. It will be shown that such a spatially interconnected system together with a distributed control scheme minimizes beam energy errors locally by exploiting a proper beam energy error distribution to neighboring RF stations.

Spatially interconnected system The desired and in the following developed interconnection structure of the closed-loop system including the plant, with performance input $d(k, \mathbf{s})$, performance output $z(k, \mathbf{s})$, and the controller is shown in Figure 5.2.3.

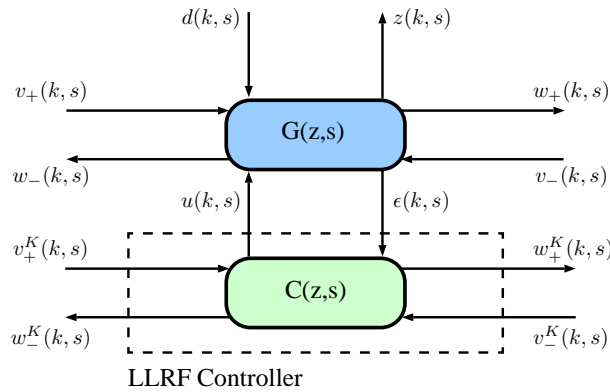


Figure 5.2.3: Closed-loop system including the plant $G(z, \mathbf{s})$ with performance input and output, the controller $C(z, \mathbf{s})$ and the interconnections to neighboring subsystems.

First, the energy quantities are redefined as $v(k, \mathbf{s})$ and $w(k, \mathbf{s})$ representing the energy error input and output, respectively, of the spatial interconnection.

In case of a FEL, the beam energy is increased towards the positive flight direction of the electrons by ΔE within each RF station, see (5.2.3). The RF stations are depicted in Figure 5.2.4 by the real system, where the location of each RF station is defined with a spatial domain parameter \mathbf{s} . An electron bunch passing a disturbed accelerator module will have an energy error $\epsilon(k, \mathbf{s})$ in positive flight direction, which is shown in (5.2.6). Since the electron bunches travel with almost speed of light through a FEL, it is not possible to control each bunch directly, e.g. by latencies of the measured signals. Therefore, only the following bunches can be controlled, which allows to approximate the system behavior. This and the fact that an electron energy error is not directly detectable within the main linac lead to an energy error distribution structure, implementable as an additional layer

of a distributed control scheme, which is illustrated in Figure 5.2.4. In addition, each

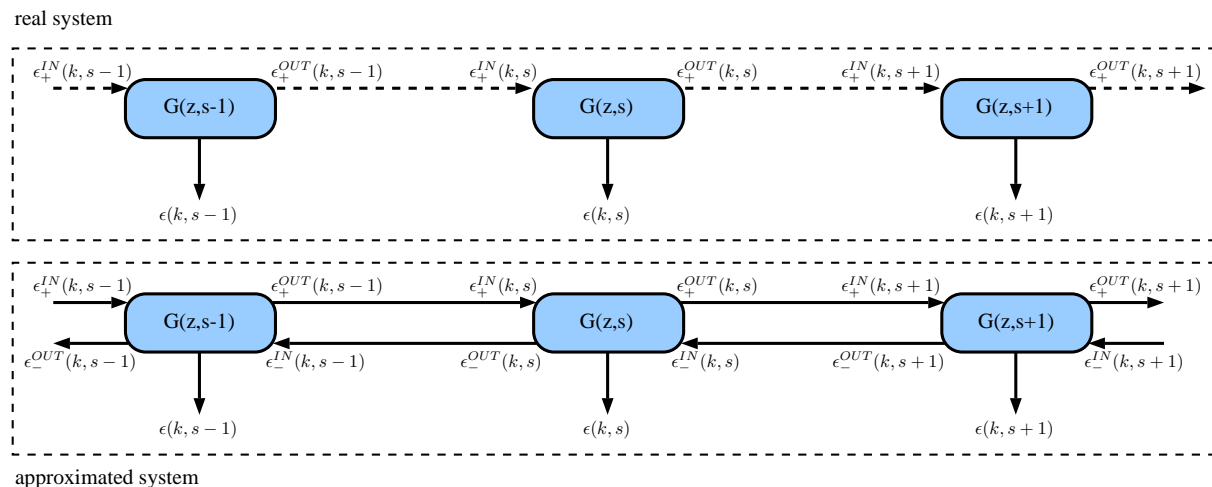


Figure 5.2.4: Beam energy error distribution of the real system, i.e. only in positive direction, and the approximated system, which allows an energy error distribution in both directions.

accelerator module may have a different operating RF field setpoint caused by the quench limit, i.e. the energy gain of each subsystem may differ. Hence, only energy errors within an RF station are considered. Lets assume, that an energy error at an RF station is correctable by both neighboring RF stations and is distributed by the same amount, i.e. by a factor K_w , to the left and right, respectively. Additional energy errors by other RF stations are distributed in the same way and added:

$$\epsilon_+^{OUT}(k, \mathbf{s}) = K_w \left(\epsilon_+^{IN}(k, \mathbf{s}) + \epsilon(k, \mathbf{s}) \right) , \quad (5.2.13)$$

$$\epsilon_-^{OUT}(k, \mathbf{s}) = K_w \left(\epsilon_-^{IN}(k, \mathbf{s}) + \epsilon(k, \mathbf{s}) \right) , \quad (5.2.14)$$

where $+$ indicates the positive direction (the electron flight direction) and $-$ the negative direction and $\epsilon(k, \mathbf{s})$ either an energy error input or output of an RF station. Adding (5.2.13) and (5.2.14) and select $K_w = 1/2$, it follows that the full energy error is distributed. To distinguish between inputs and outputs, the beam energy errors (5.2.13) and (5.2.14) are interconnected in a distributed scheme, see Figure 5.2.3 , as

$$w_+(k, \mathbf{s}) = K_w (v_+(k, \mathbf{s}) + \epsilon(k, \mathbf{s})) , \quad (5.2.15)$$

$$w_-(k, \mathbf{s}) = K_w (v_-(k, \mathbf{s}) + \epsilon(k, \mathbf{s})) , \quad (5.2.16)$$

with v as interconnection input and w as output, respectively. The pre-factor K_w is used as additional tuning variable and accomplish the plant model. This allows to distribute a weighted energy error signal to the neighboring RF stations, which is discussed at the end of this section.

Boundary conditions The interconnected controller is designed by assuming an infinite interconnection, which is not true for a FEL. In [Langbort and D'Andrea, 2003]

a boundary condition is given allowing this assumption. They make use of symmetries coming from the *method of images* reflecting a *Neumann boundary condition*. Hence, by mirroring the plant at each end infinite times, the interconnected system itself becomes infinite. Recall, the energy error $\epsilon(k, \mathbf{s})$ is not measurable at neighboring modules, this information needs to be transmitted and is modeled as additional layer. This allows to make use of the proposed boundary condition. Hereby, a non-singular matrix M must be found displaying those images, depicted and simplified in Figure 5.2.5 for three subsystems.

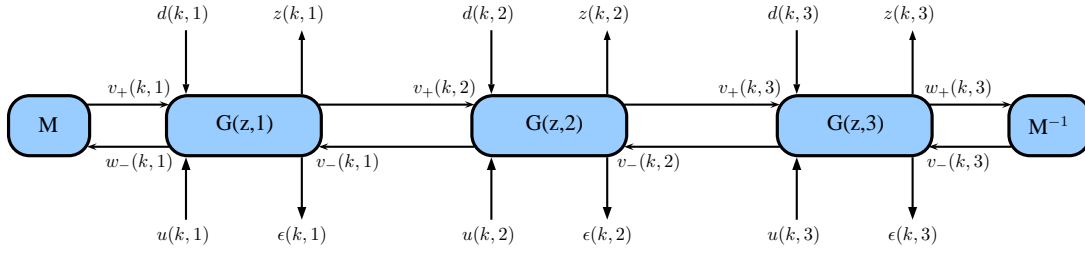


Figure 5.2.5: Finite system with 3 interconnected modules and boundary condition matrix M , [Langbort and D’Andrea, 2003].

In the following, the boundary condition matrix M is defined for this application as $M=1$, such that for the example depicted in Figure 5.2.5

$$\begin{aligned} v_+(k, 1) &= w_-(k, 1) \quad \text{and} \\ v_-(k, 3) &= w_+(k, 3) \end{aligned}$$

holds; for XFEL redefine the first ($\mathbf{s}=5$) and last ($\mathbf{s}=25$) interconnection as

$$\begin{aligned} v_+(k, \mathbf{s}) &= w_-(k, \mathbf{s}) \quad ; \quad \mathbf{s} = 5 \quad \text{and} \\ v_-(k, \mathbf{s}) &= w_+(k, \mathbf{s}) \quad ; \quad \mathbf{s} = 25 . \end{aligned}$$

This can be justified as follows: recall that the energy error is transmitted through an additional layer between the RF stations. It is obvious, that an energy error at the last RF station can be corrected only by the RF stations upstream. Hence, the energy error to the open side is connected upstream to distribute the overall error. Further details about boundary conditions can be found in [Langbort and D’Andrea, 2003].

Construction of a generalized plant Next, the generalized plant using the mathematical definitions of the previous subsections is defined. Hence, obtain a state space model of a subsystem of the approximated plant by

$$\begin{bmatrix} x(k+1, \mathbf{s}) \\ (\Delta_{\mathbf{s}, \mathbf{m}} v(k))(\mathbf{s}) \\ \epsilon(k, \mathbf{s}) \end{bmatrix}_{x_0(\mathbf{s})} = \begin{bmatrix} A_{\mathbf{T}\mathbf{T}} & A_{\mathbf{T}\mathbf{S}} & B_{\mathbf{T}} \\ A_{\mathbf{S}\mathbf{T}} & A_{\mathbf{S}\mathbf{S}} & B_{\mathbf{S}} \\ C_{\mathbf{T}} & C_{\mathbf{S}} & D \end{bmatrix} \cdot \begin{bmatrix} x(k, \mathbf{s}) \\ v(k, \mathbf{s}) \\ u(k, \mathbf{s}) \end{bmatrix}, \quad (5.2.17)$$

where $x_0(\mathbf{s}) = x(0, \mathbf{s})$ and

$$\begin{aligned} A_{\mathbf{T}\mathbf{T}} &= A_G, & A_{\mathbf{T}\mathbf{S}} &= \begin{bmatrix} 0 & 0 \end{bmatrix}, & B_{\mathbf{T}} &= B_G, \\ A_{\mathbf{S}\mathbf{T}} &= \begin{bmatrix} -K_w \cdot C_G \\ -K_w \cdot C_G \end{bmatrix}, & A_{\mathbf{S}\mathbf{S}} &= \begin{bmatrix} K_w & 0 \\ 0 & K_w \end{bmatrix}, & B_{\mathbf{S}} &= \begin{bmatrix} 0 \\ 0 \end{bmatrix}, \\ C_{\mathbf{T}} &= -C_G, & C_{\mathbf{S}} &= \begin{bmatrix} 0 & 0 \end{bmatrix}, & D_{\mathbf{T}} &= 0. \end{aligned}$$

The equations in (5.2.9) describe the temporal behavior, i.e. the first and last row in (5.2.17). Using the plant approximation, the temporal states of a neighboring subsystem are not affected by the interconnected signals $v(k, \mathbf{s})$. The interconnection matrices in (5.2.17) are designed accordingly to (5.2.15) and (5.2.16) with the tuning parameter K_w . Within a small signal model, where only errors are considered, $\epsilon(k, \mathbf{s})$ is represented as

$$\epsilon(k, \mathbf{s}) = -y_I(k, \mathbf{s}) = -C_G \cdot x(k, \mathbf{s}).$$

A simplified notation for (5.2.17) is introduced as

$$\begin{bmatrix} \Delta_{\mathbf{m}\mathbf{G}} r^G(k, \mathbf{s}) \\ \epsilon(k, \mathbf{s}) \end{bmatrix} = \begin{bmatrix} A^G & B_u^G \\ C_y^G & D_{yu}^G \end{bmatrix} \cdot \begin{bmatrix} r^G(k, \mathbf{s}) \\ u(k, \mathbf{s}) \end{bmatrix}, \quad (5.2.18)$$

with

$$\Delta_{\mathbf{m}\mathbf{G}} r^G(k, \mathbf{s}) = \begin{bmatrix} x(k+1, \mathbf{s}) \\ (\Delta_{\mathbf{S}, \mathbf{m}} v(k))(\mathbf{s}) \end{bmatrix} \quad \text{and} \quad r^G(k, \mathbf{s}) = \begin{bmatrix} x(k, \mathbf{s}) \\ v(k, \mathbf{s}) \end{bmatrix},$$

where e.g. A^G is the upper left A block of (5.2.17) containing the temporal, spatial and coupling matrices.

In the following, the tuning parameter K_w is chosen such that the plant interconnection itself is stable, hence, well-posed which is fulfilled if $(\Delta_{\mathbf{S}, \mathbf{m}} - A_{SS})$ is invertible. In the following, it is assumed that $0 < K_w < 1$ which is needed to describe bounded energy distributions. Remember that for the real plant the energy error is defined only in positive direction, where this factor is one. By rewriting the physical equations for both directions, the error is split-up with a factor of $K_w = 1/2$. Since this is an approximation of the real plant, K_w is introduced as tuning parameter for the energy error exchange. This factor can be used to ensure that the beam energy is controlled only by RF stations that are close to the disturbed RF station, outlined in the following paragraph.

Choice of the tuning factor K_w Assume a beam energy error is observed in one of the accelerator modules and controlled only by the local RF field controller, i.e. without controller information exchange. Recall that the energy error signal is not observed by neighboring modules directly. Instead, the energy error is weighted by K_w , transmitted to the neighboring RF stations, see (5.2.15) and (5.2.16), and added to the energy error signal of that RF station according to

$$\epsilon_C(k, \mathbf{s}) = \epsilon(k, \mathbf{s}) + v_+(k, \mathbf{s}) + v_-(k, \mathbf{s}), \quad (5.2.19)$$

where $\epsilon_C(k, \mathbf{s})$ is the input of the local RF field controller. It is desirable to control the beam energy by RF stations close to a disturbed RF station to minimize second order effects to other subsystems, e.g. the adjustment of magnets within the FEL. For this reason, K_w is tuned such that the sum of the squared beam energy error $J(K_w)$ is minimized in spatial domain:

$$\min_{K_w} \overbrace{\sum_{s=6}^{25} \epsilon(k, \mathbf{s})^2}^{J(K_w)} . \quad (5.2.20)$$

Since only the local controller is active, the minimization is done at the end of a pulse without considering the transient behavior. Figure 5.2.6 shows the simulated squared beam energy error if an error, i.e. an energy drop of 60 MeV, is induced. If K_w is

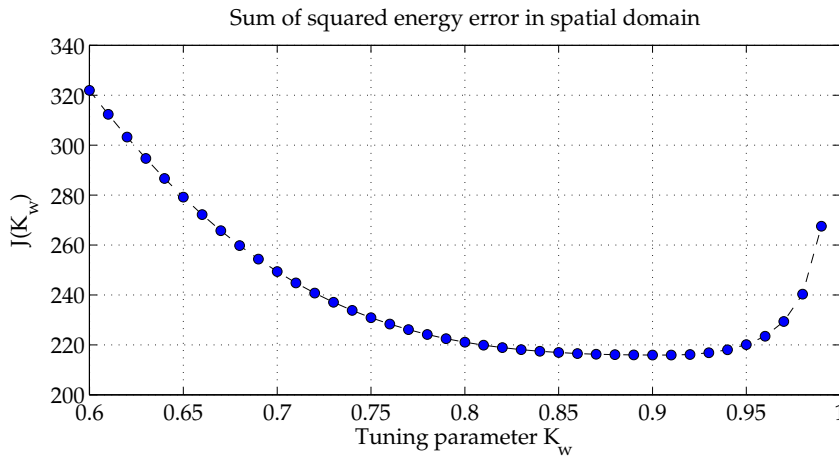


Figure 5.2.6: Sum of squared energy error along the spatial domain as function of tuning factor K_w .

small, little information is shared with the neighboring modules, while increasing the value facilitates local control of the beam energy. If the value is too high, the error is distributed through the whole chain of subsystems and every RF station tries to contribute to this error. Hence, the sum of the squared beam energy error becomes larger. In the following distributed controller design and simulation results a value of $K_w = 0.9$ is used.

Connection to Distributed Controller

The interconnection of the RF stations is done by using the energy error signal $\epsilon(k, \mathbf{s})$ as input to the controller block, shown in Figure 5.2.7. The optimal output will be computed and fed back into the plant. In addition, we will allow interconnections of the designed controller, as usual for a distributed controller design.

Usually, the controller interconnection has a similar or even the same structure as the plant interconnection. The main focus of the presented controller design approach is set to a distributed controller design for spatially interconnected systems as described

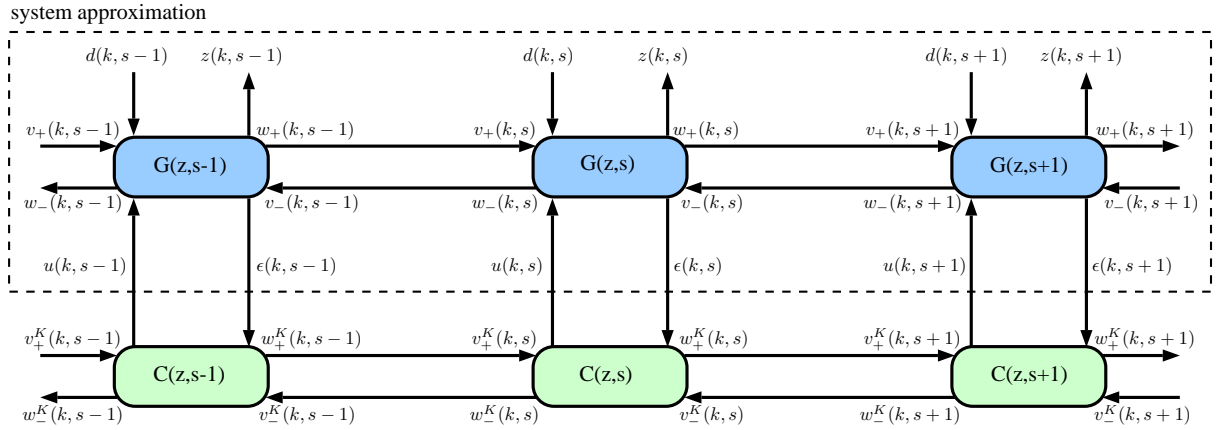


Figure 5.2.7: Distributed controller design task consisting of the approximated plant model and the controller interconnection scheme.

by [D’Andrea and Dullerud, 2003], which results in an optimal and robust interconnected controller for a predefined closed-loop behavior. This behavior is defined by setting shaping filters within the controller design. The following equations are used to describe the plant, the shaping filters and the connection to the designed controller:

$$\begin{bmatrix} \Delta_{\mathbf{m}^G} r^G(k, \mathbf{s}) \\ z(k, \mathbf{s}) \\ \epsilon(k, \mathbf{s}) \end{bmatrix} = \begin{bmatrix} A^G & B_d^G & B_u^G \\ C_z^G & D_{zd}^G & D_{zu}^G \\ C_y^G & D_{yd}^G & D_{yu}^G \end{bmatrix} \cdot \begin{bmatrix} r^G(k, \mathbf{s}) \\ d(k, \mathbf{s}) \\ u(k, \mathbf{s}) \end{bmatrix}. \quad (5.2.21)$$

The second block row displays matrices needed to include shaping filters, see *Controller Optimization using HIFOOD* in Section 4.1.2 with performance input $d(k, \mathbf{s})$ and output $z(k, \mathbf{s})$, respectively. The performance output variables are taken to be

$$z_1(k, \mathbf{s}) = W_u u(k, \mathbf{s}) \quad \text{and} \quad z_2(k, \mathbf{s}) = W_\epsilon \epsilon(k, \mathbf{s}), \quad (5.2.22)$$

with W_u as penalty to the control effort and W_ϵ as weight for the error signal. Furthermore, the performance input is partitioned into

$$d(k, \mathbf{s}) = \begin{bmatrix} d_1(k, \mathbf{s}) \\ d_2(k, \mathbf{s}) \end{bmatrix},$$

where $d_1(k, \mathbf{s})$ is taken as control input $u(k, \mathbf{s})$ and $d_2(k, \mathbf{s})$ as energy error, and W_{d_1} and W_{d_2} are the corresponding shaping filters. The framework of spatially interconnected systems proposed in [D’Andrea and Dullerud, 2003] provides an efficient way of solving the controller synthesis problem for a large scale system with many subsystems. The synthesis problem can be solved by solving an LMI problem for a single subsystem with the generalized plant model given in (5.2.21) which leads to the controller $C(z, \mathbf{s})$ and is depicted in Figure 5.2.7. The resulting controller takes the form

$$\begin{bmatrix} \Delta_{\mathbf{m}^K} r^K(k, \mathbf{s}) \\ u(k, \mathbf{s}) \end{bmatrix} = \begin{bmatrix} A^K & B^K \\ C^K & D^K \end{bmatrix} \cdot \begin{bmatrix} r^K(k, \mathbf{s}) \\ \epsilon(k, \mathbf{s}) \end{bmatrix}. \quad (5.2.23)$$

By rewriting the state $r^K(k, \mathbf{s})$ in the same way as in (5.2.18), the controller $C(z, \mathbf{s})$ takes the form

$$\begin{bmatrix} x^K(k+1, \mathbf{s}) \\ w_+^K(k, \mathbf{s}) \\ w_-^K(k, \mathbf{s}) \\ u(k, \mathbf{s}) \end{bmatrix} = \begin{bmatrix} A_{\mathbf{T}\mathbf{T}}^K & A_{\mathbf{T}\mathbf{S}}^K & B_{\mathbf{T}}^K \\ A_{\mathbf{S}\mathbf{T}}^K & A_{\mathbf{S}\mathbf{S}}^K & B_{\mathbf{S}}^K \\ C_{\mathbf{T}}^K & C_{\mathbf{S}}^K & D^K \end{bmatrix} \cdot \begin{bmatrix} x^K(k, \mathbf{s}) \\ v_+^K(k, \mathbf{s}) \\ v_-^K(k, \mathbf{s}) \\ \epsilon(k, \mathbf{s}) \end{bmatrix} \quad (5.2.24)$$

and results in the same controller order as the plant.

5.2.3 Simulation Results for XFEL

A good assumption, even during the RF field controller design, see Section 4.1.2 on page 51, is to neglect the plant time delay of 2.22 μs , due to the low bandwidth of the system. In addition, the controller will be implemented on an FPGA such that a low controller order is desired. The controller can be written in a decoupled form as presented in Section 4.1.2, as

$$U(z, \mathbf{s}) = C(z, \mathbf{s})E(z, \mathbf{s}) \quad , \quad \text{where} \quad (5.2.25)$$

$$C(z, \mathbf{s}) = \begin{bmatrix} K_{P,I}(\mathbf{s})M_{C,I}(z, \mathbf{s}) & 0 \\ 0 & K_{P,Q}(\mathbf{s})M_{C,Q}(z, \mathbf{s}) \end{bmatrix} R(\phi_G)^T(\mathbf{s}) \quad , \quad (5.2.26)$$

with $U(z)$ as controller output, $E(z)$ as input, i.e. RF field error, $K_P(\mathbf{s})$ and $M_C(z, \mathbf{s})$ as proportional gain and mode suppression part and $R(\phi_G)^T$ as static decoupling matrix. The latter allows to design two SISO controllers, i.e. an independent design of $K_{P,I}$ which is updated by $C(z, \mathbf{s})$ and $M_{C,I}$, included afterwards to suppress additional fundamental modes. The second SISO controller for the imaginary channel needs not to be updated and follows from Section 4.1.2.

The synthesis problem for the discrete-time distributed controller is solved with the help of *The Multidimensional System Toolbox* [D'Andrea, 1999]. The controller obtained this way is labeled $C(z, \mathbf{s})$ in Figure 5.2.7.

As explained previously, the error signal $\epsilon(k, \mathbf{s})$ needs to be propagated through the system, since the system structure itself is not able to detect energy errors from neighboring subsystems. This leads to a modified plant with an additional error interconnection block, given in state space form as

$$\begin{bmatrix} w_+(k, \mathbf{s}) \\ w_-(k, \mathbf{s}) \\ \epsilon_C(k, \mathbf{s}) \end{bmatrix} = \begin{bmatrix} K_w & 0 & K_w \\ 0 & K_w & K_w \\ 1 & 1 & 1 \end{bmatrix} \cdot \begin{bmatrix} v_+(k, \mathbf{s}) \\ v_-(k, \mathbf{s}) \\ \epsilon(k, \mathbf{s}) \end{bmatrix} \quad ,$$

where $\epsilon_C(k, \mathbf{s})$ is input to the designed controller $C(z, \mathbf{s})$ and $\epsilon(k, \mathbf{s})$ is the local energy error (5.2.6). The modification of the error signal is given by (5.2.19) and displayed in Figure 5.2.8. The approximated plant distributes an energy error signal $\epsilon(k, \mathbf{s})$ to the neighboring RF stations, scaled by K_w .

The controller is designed as described in the last subsection. Only energy errors in one channel are considered for the interconnected controller. The control signals can be

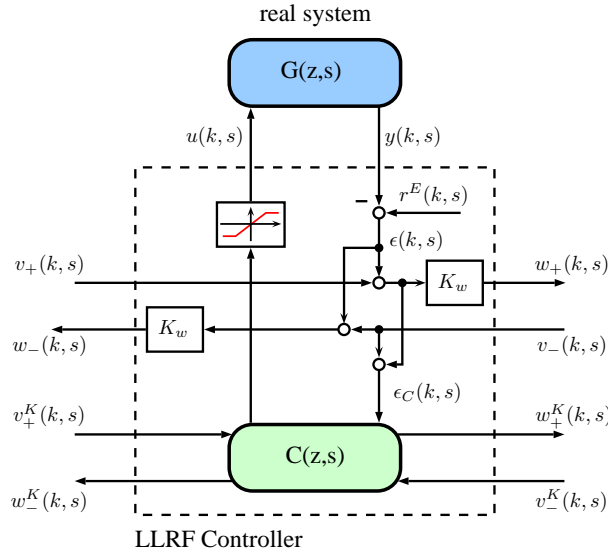


Figure 5.2.8: Closed-loop system as in Figure 5.2.7, but here showing the physical model of an accelerator module $G(z,s)$ and the error propagation layer explicitly. The output limiter displays a restricted actuator action.

mapped by the RF field phase to a two-dimensional vector field. The controller design focus is set to increase the rise time and to lower the peak overshoot and steady-state error. The values for the weights used for simulation are taken as:

$$W_u = 0.1, W_\epsilon = 1, W_{d_1} = 0.1 \text{ and } W_{d_2} = 0.05.$$

Two different kinds of errors, introduced in Section 5.2.1, are considered and shown in Figure 5.2.9. First, a step-like energy error, an extremum case which corresponds to

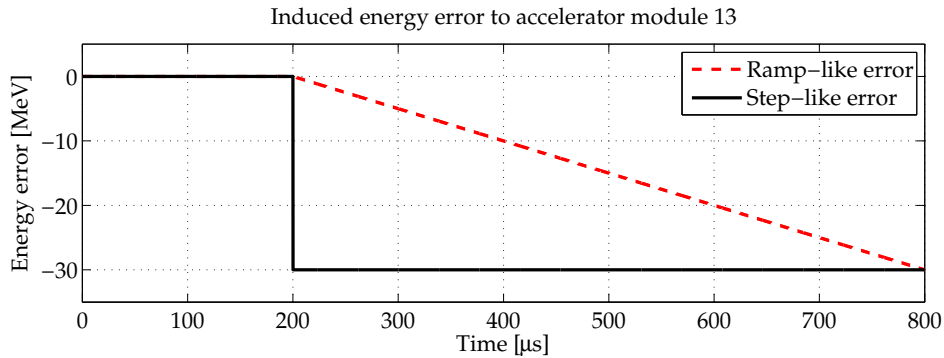


Figure 5.2.9: Error due to pre-limiter and limiter injected in module 13.

an active limiter reducing instantaneously the RF field setpoint, followed by a ramp-like energy error, which represents an active pre-limiter. The simulation of the system analysis is done without communication delay. An outlook including the communication delays is given within the last section. The communication delay results in increase oscillations in most cases and should be part of the generalized plant. However, this would significantly

increase the plant and controller order, which is not desired for an implementation on an FPGA.

Without communication delay

A simulation of the designed distributed controller together with the interconnected plant for a step-like error is shown in Figure 5.2.10. The beam energy error is visualized in

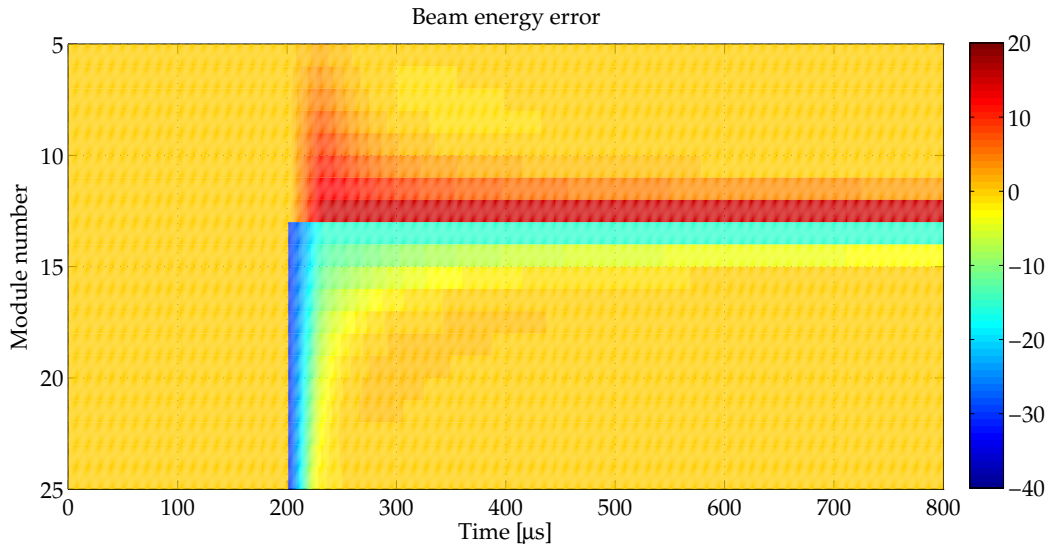


Figure 5.2.10: Response to step-like energy error at RF station 13 along the bunch path, controlled by the distributed control scheme. The plant model contains the internal plant delays.

temporal and spatial domain. The color code represents the error distribution. The final beam energy error after the last accelerator module, i.e. module 25, is shown in Figure 5.2.11, where three cases are considered. The imposed energy error at module 13 is the same as the final beam energy error if this information is not shared with the neighboring RF stations. To keep the controller order small, the controller synthesis was done without internal plant delay. The comparison between the simulation with and without plant delay shows almost no difference. This is due to the fact, that a plant delay changes the plant phase for high frequencies, while the reached closed-loop bandwidth for superconducting cavities is in the order of tens of kilohertz. Figure 5.2.12 shows the temporal and spatial energy error for an induced ramp-like error in module 13, controlled by the neighboring RF stations. The final beam energy error with and without plant delay is compared in Figure 5.2.13. It can be seen, that neglecting plant delays for this application affects the fast transient behavior which results in overshoots and damped oscillations. Integral action during the controller design is not considered, leading to a steady state error, which is correctable by iterative learning control within the next few pulses. Remember, the controller input signal, i.e. the beam energy error signal, is used to adapt the feedforward signal from pulse to pulse, hence an uncritical case.

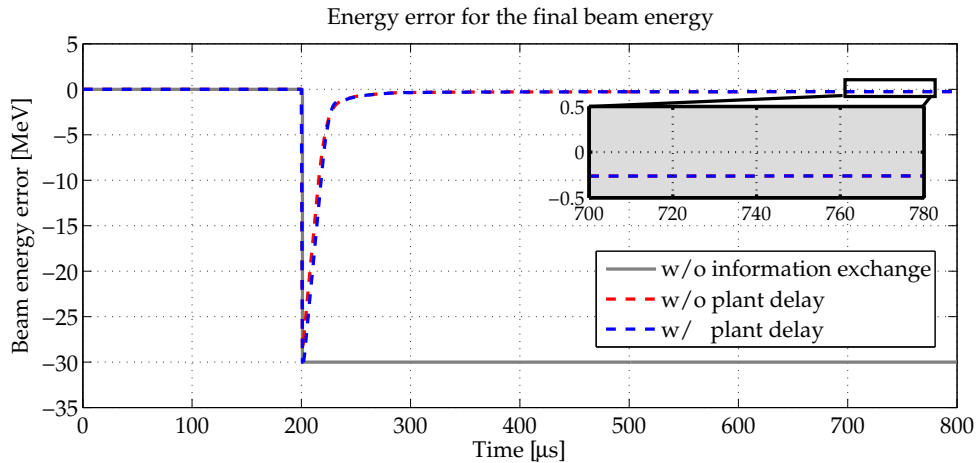


Figure 5.2.11: Final energy error for step-like energy error at RF station 13 for three different cases.

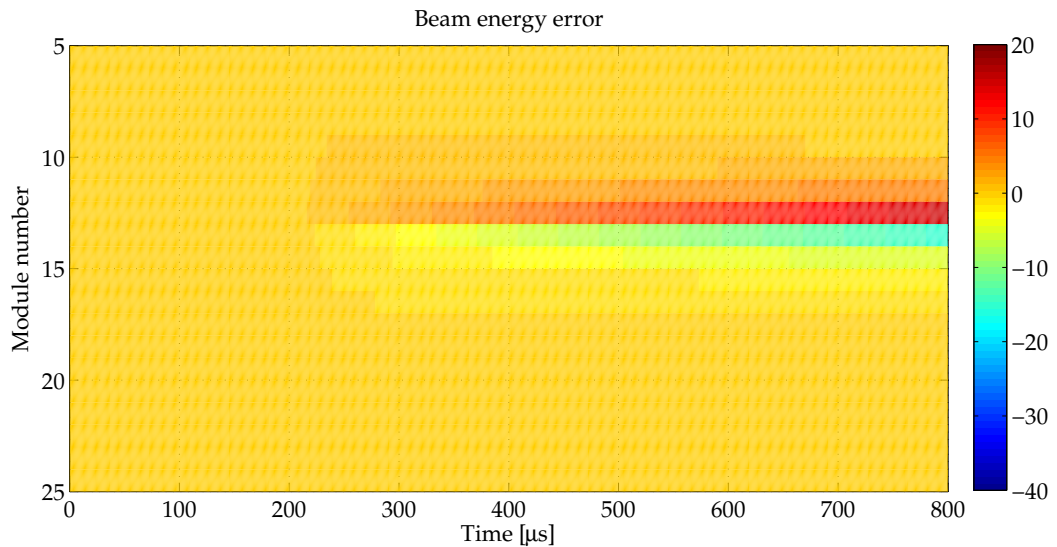


Figure 5.2.12: Ramp-like energy error at RF station 13 along the bunch path, controlled by the distributed control scheme.

It has been shown that the controller is able to drive the system in case of RF field, thus, energy errors. The energy error and the controller state information is exchanged between neighboring RF stations on both sides to recover zero energy error. Till now the consideration was done by assuming that the controller exchanges information without communication delay. If this communication fails, the overall distributed controller is not connected, such that the last energy monitor detects an energy change which results in a feedback only by using the last RF station. If the overall communication fails, the distributed plant is not able to correct energy errors caused by, e.g., cavity quenches.

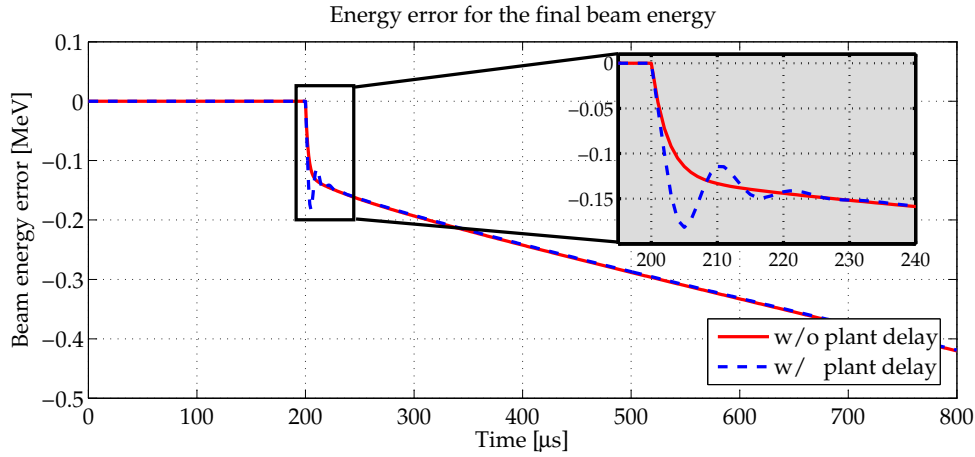


Figure 5.2.13: Final energy error for ramp-like energy error at RF station 13, as comparison with and without internal plant delay.

5.2.4 Outlook - Communication Delays

In the previous distributed controller design, the time delays during the controller synthesis were neglected. This includes the enclosed plant time delay, a good assumption as seen in Section 4.1 and within the previous simulation results. In addition the communication delays between the LLRF controllers, as shown in Figure 5.2.14, were not considered. It

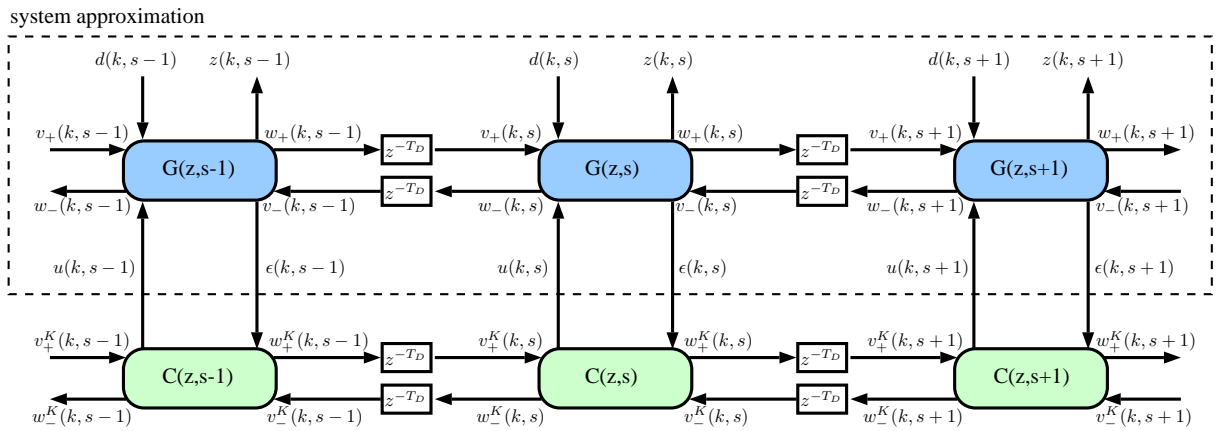


Figure 5.2.14: Spatially interconnected system with included communication time delays.

is shown in the following simulations, that the interconnected system tends to become a stable weakly damped oscillation if communication delays are included. To cope with this effect, without extending the controller order itself, one possibility is to readjust the tuning factor K_w , considered in the following.

Readjustment of K_w Similar to the optimization of the tuning parameter K_w on page 107, a tuning parameter scan is shown in Figure 5.2.15 including a communication delay of 1 μ s. Hereby, the tuning parameter is updated within the plant model and the

controller synthesis is done for each K_w . As presented before, in case of zero commu-

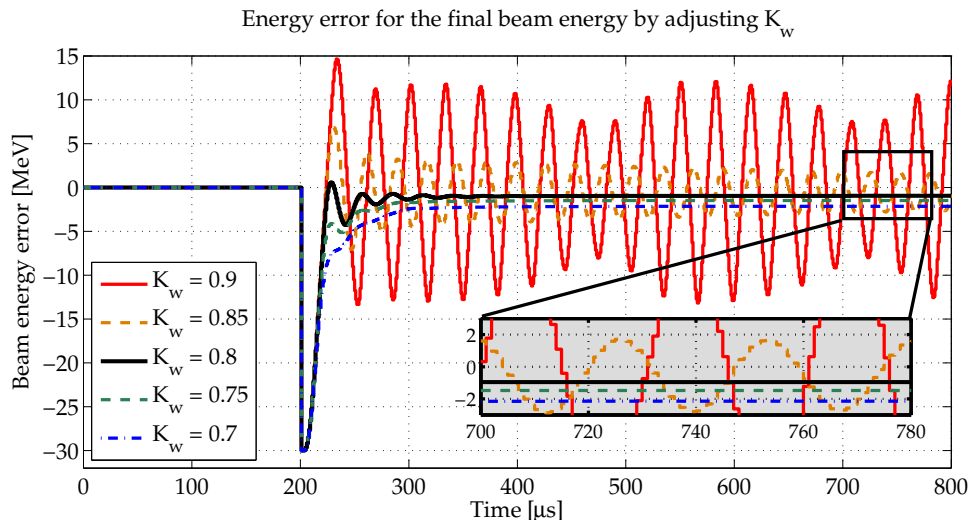


Figure 5.2.15: Tuning parameter variation of K_w and the resulting final beam energy error with communication delay of $1 \mu\text{s}$ and an applied step-like error signal, see Figure 5.2.9.

nication delay, the best results are achieved with a tuning factor of about $K_w = 0.9$, while including a communication delay of $1 \mu\text{s}$ moves the optimal tuning parameter towards lower values, e.g. $K_w = 0.8$, presented in Figure 5.2.15. Nevertheless, using such optimization methods avoids to extend the plant model order, thus the controller order. Figure 5.2.16 shows the simulation results for both occurring energy errors for two different tuning parameters, i.e. the optimal without communication delay ($K_w = 0.9$) and the chosen parameter with communication delays ($K_w = 0.8$). In principle it seems to be sufficient to readjust the tuning parameter K_w to avoid oscillations in case of communication delays. Since the RF field error, hence the energy error, is controlled by an iterative learning control algorithm, see Section 4.2, the remaining error will be reduced within the next few pulses to an uncritical level. Therefore, the required performance specifications in relative amplitude and phase, hence in beam energy accuracy, will be met.

It has thus been demonstrated, that a distributed control scheme significantly reduces the final beam error, thus appearing to be a key element for reaching high beam energy performance. Nevertheless, further improvements, e.g. observer based control or the interconnection of iterative learning control in a distributed scheme, perhaps improves the beam performance. For further research, [Eichler et al., 2013] proposes a strategy which guarantees robust stability for an interconnected system with uncertain time-varying time delays with integral quadratic constraints.

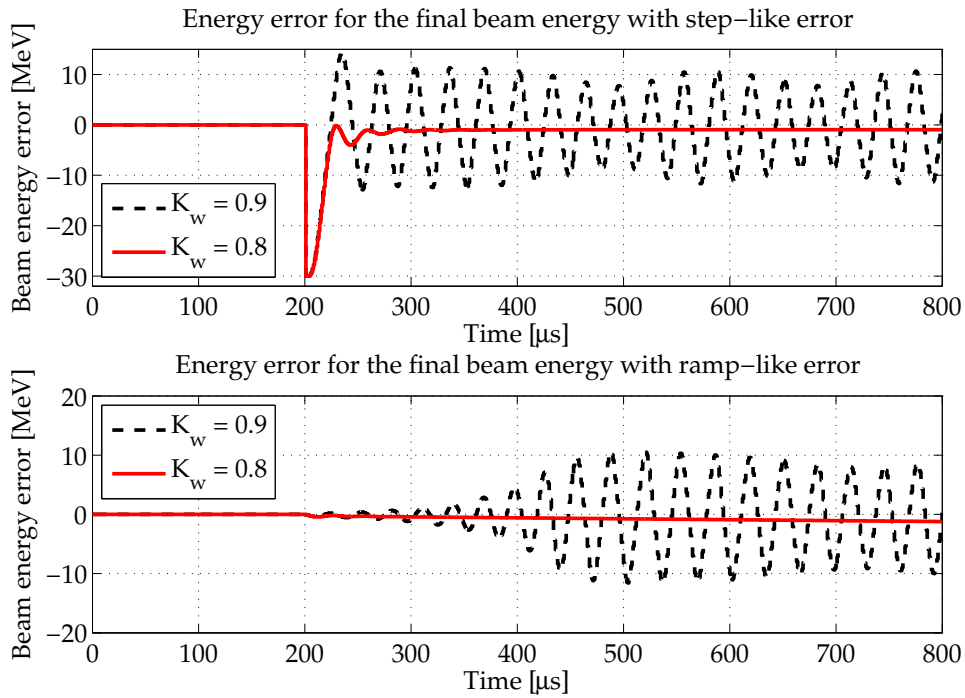


Figure 5.2.16: Adjustment of K_w and the resulting final energy error with plant time delay and with communication delay of $1 \mu\text{s}$ in a distributed control scheme; Figure 5.2.9 shows the energy error signal.

5.3 Conclusion

The beam-based controller design by a superposition of the RF field with beam information has been presented. The free-electron laser, hence the beam-based controller design, is separated into two parts. First, a lumped beam-based controller design within the first part of a FEL has been presented. The controller design follows a cascaded feedback structure and combines the bunch arrival time and bunch compression measurements with the RF field. Hereby the RF field error, which is the input to the RF field controller is superimposed by the mentioned beam related measurements, leading to significant improvements of the beam stability in bunch arrival time and bunch compression.

The second part considers beam energy control within the main linac. It has been shown that the beam energy must be estimated and have to be transmitted to the neighboring RF stations as long as the beam energy is not measurable after each accelerator module. Presented is a distributed control scheme with interconnections between the LLRF controller. This allows to exchange beam error information and controller states. Simulation results present the beam performance gain by exchanging information and controlling the FEL in a distributed control scheme. Furthermore, it has been shown, that communication delays have a negative impact on the beam energy performance. Nevertheless, without extending the controller order an adjustment of one parameter seems to be sufficient to handle communication delays.

Chapter 6

Summary and Outlook

In this thesis the problem of beam-based controller design for free-electron lasers is addressed. Future FELs require a high performance controller design to ensure equidistant laser light flashes which have the same peak brilliance and wavelength for each laser pulse. The requirement on the FEL pulses are directly related to requirement on the electron beam. The proposed controller design includes beam-based measurements, i.e. the arrival time, compression and energy of electron bunches, which are controllable by adjusting the acceleration fields inside the accelerator modules. The actuator, i.e. the RF field, is modeled with high accuracy based on the special $SO(2)$ symmetric group. It has been shown, that the actuator dynamics, separated in its real and imaginary part, obeys this symmetry. Based on this, an optimal RF field feedback controller and simplifications regarding the feedforward drive adaptation by norm optimal iterative learning control were found and measurement results, displaying the improvements, were presented. The beam-based signals are proportional to RF field signals, e.g. bunch arrival time and compression changes are proportional to RF field amplitude and phase changes, which are seen as static mapping matrix around a given RF field setpoint. The beam-based controller makes use of a linearised mapping from beam measurements to the real and imaginary RF field vector field. Measurement results at FLASH show significant improvements of beam-based controller, i.e. bunch arrival time and bunch compression, as comparison to only RF field control. Proposed is a cascaded feedback controller, with an inner beam-based loop and an outer RF field loop. These beam-based corrections, done within the first part of the linear accelerator, are on the expense of the beam energy. The main linear accelerator increases the beam energy up to a desired final beam energy value which defines the laser light wavelength. The beam energy is directly measurable at two positions, i.e. the initial and final beam energy, of the main linear accelerator. In case of an error within the main linac the only possibility is to minimize this occurring disturbance by adjusting the RF field within the last accelerator module. In this thesis an alternative approach is considered which allows to control beam energy errors close to a disturbed module. Hereby, the temporal system equations and physical equations describing the energy gain in spatial domain are rewritten in a spatially interconnected plant model. Making use of an interconnected controller, the controller design task is to find an optimal controller for both, the spatial interconnection and temporal dynam-

ics. Simulation results present the performance gain by exchanging information between neighboring controllers. By including communication delays, which are present for real plant integration, the interconnected controller tends to become a stable weakly damped oscillation. This is minimized by adjusting one parameter within the controller synthesis.

6.1 Outlook

In the following, a number of relevant problems of further research concerning free-electron lasers are discussed and outlined.

Distributed control scheme with communication delays Communication delays between neighboring controllers have a negative impact on beam energy control. Further research concerning this communication delays within the controller synthesis should lead to reliable controller without adjusting additional tuning parameters. In [Eichler et al., 2013] the stability analysis for an interconnected system with uncertain time-varying time delays by integral quadratic constraints is considered. Further controller synthesis extensions, including time-varying communication delays, packet losses and interconnection breaks, must be considered for an integration at XFEL to guarantee robust beam energy stability.

Distributed iterative learning control The beam energy error is connected to RF field properties, more precisely to the RF field error, where repetitive errors are minimized from pulse to pulse using an iterative learning algorithm. The interconnected control scheme exchanges beam energy information between RF stations. Hence, the extension of an interconnected iterative learning control algorithm may provides a faster reduction of repetitive beam energy errors. Within this thesis it has be shown that the developed tensor based ILC is implementable directly within the LLRF controller, which is interconnected to the neighboring controller, hence those are able to exchange information.

Integration of normal conducting cavity It is foreseen to equip FLASH with a normal conducting cavity. This, together with low latency measurements and low latency drive signals, allows to increase the control bandwidth by a factor of about 10. Nevertheless, the drawback is a limited control action such that the proposed controller design for bunch arrival time and bunch compression needs to exchange information between the superconducting RF station and normal conducting module. Hereby, the control action needs to be separated into different frequency ranges, e.g. the normal conducting module covers high frequency disturbance rejection and the superconducting modules those for low frequencies, respectively.

Optical synchronization system The previously described beam-based controller design and by using a fast actuator to minimize fast errors from the electron beam ensures an optimal electron beam w.r.t. arrival time, compression and energy of the electron

bunch. However, since the latter are stabilized to a high level, the main task for further user experiments is a stable clock distribution via optical fibre links, [Schulz et al., 2013]. This problem can be divided into two parts. Firstly, make sure that the master laser oscillator generates equidistant laser pulses for synchronization. Secondly, stabilize the travel time of the laser pulses within the fibre links which distributes the clock signal to other subsystems. Those fibre links are sensitive w.r.t. temperature and humidity variations. The latter must be compensated by a control strategy, especially for the XFEL with fibre length in kilometer range.

Appendix A

Introduction Lie Groups and Subgroup SO(2)

A short introduction to Lie groups, especially the subgroup SO(2), is given in the following. Those occur in abundance throughout physics and mathematics; a variety of books is available, e.g. [Gilmore, 1974], [Srinivasa Rao, 1988] and [Sepanski, 2007]. Considering the *general linear group of dimension n*

$$GL(n, \mathbb{F}) = \{g \in M_{n,n}(\mathbb{F}) \mid g \text{ is invertible}\} , \quad (\text{A.0.1})$$

with $M_{n,n}$ as set of $n \times n$ matrices over \mathbb{F} , where \mathbb{F} is either \mathbb{C} or \mathbb{R} . A Lie group is a group and a manifold so that the multiplication map and inverse map is smooth, [Sepanski, 2007]. The *orthogonal group* is a Lie group, given by

$$O(n) = \{g \in GL(n, \mathbb{R}) \mid g^T g = \mathbf{I}\} , \quad (\text{A.0.2})$$

with g^T as transpose of g . The *special orthogonal group of dimension n*, as short hand notation SO(n), is a closed subgroup of the *orthogonal group*. This group is often denoted as *rotation group*, defined by

$$SO(n) = \{g \in O(n) \mid \det g = 1\} . \quad (\text{A.0.3})$$

Within this thesis the *special orthogonal group of dimension two* is considered, which can be expressed as a two-dimensional rotation matrix

$$R(\phi) = \begin{bmatrix} \cos \phi & -\sin \phi \\ \sin \phi & \cos \phi \end{bmatrix} . \quad (\text{A.0.4})$$

This matrix rotates points in the xy-Cartesian plane counter-clockwise through a rotation angle ϕ about the origin. Obviously, the determinant of $R(\phi)$ is one for all angles ϕ , thus $R(\phi)$ obeys the SO(2) symmetry. Lets choose a complex vector $x \in \mathbb{C}$ which is decomposable into an amplitude part A and phase part ϕ ,

$$x = A \cdot e^{i\phi} = A \cdot (\cos \phi + i \sin \phi) = \text{Re}\{x\} + i \text{Im}\{x\} , \quad (\text{A.0.5})$$

with i as imaginary unit, and $\text{Re}\{x\}$, $\text{Im}\{x\}$ as real and imaginary part of x , respectively. The phase of the complex variable $x \in \mathbb{C}$ is rotated by an angle ϕ_1

$$\tilde{x} = x \cdot e^{i\phi_1} = (\text{Re}\{x\} + i \text{Im}\{x\}) \cdot (\cos \phi_1 + i \sin \phi_1) \quad (\text{A.0.6})$$

$$= (\text{Re}\{x\} \cos \phi_1 - \text{Im}\{x\} \sin \phi_1) + i (\text{Re}\{x\} \sin \phi_1 + \text{Im}\{x\} \cos \phi_1) , \quad (\text{A.0.7})$$

leading to a new complex vector \tilde{x} . The one dimensional complex problem is mapped into a two-dimensional problem by separating the real and imaginary part, which obeys a matrix vector operation

$$\begin{bmatrix} \text{Re}\{\tilde{x}\} \\ \text{Im}\{\tilde{x}\} \end{bmatrix} = \begin{bmatrix} \cos \phi_1 & -\sin \phi_1 \\ \sin \phi_1 & \cos \phi_1 \end{bmatrix} \cdot \begin{bmatrix} \text{Re}\{x\} \\ \text{Im}\{x\} \end{bmatrix} , \quad (\text{A.0.8})$$

in which the rotation matrix is $\text{SO}(2)$ symmetric.

Appendix B

3rd Harmonic RF Module at FLASH

B.1 Phase Space Linearisation

Since 2010 an additional module, namely ACC39, is installed, [Vogel et al., 2010]. The main purpose of this module, which is operated with a three times higher frequency ($f_0 = 3.9$ GHz), is to linearise the longitudinal phase space of the electron bunch; detailed information can be found in [Vogel et al., 2007] and [Edwards et al., 2010]. The accelerating amplitude seen by the electron beam for an acceleration by ACC1 and ACC39 is $A_{(ACC1+ACC39)} = A_{ACC1} \cdot \cos(-\phi_{beam}) + A_{ACC39} \cdot \cos(180^\circ + 3 \cdot \phi_{beam})$. The electron bunches leaving the RF gun typically have a length of about 2 mm, depending on the bunch charge. It is straightforward to show that this corresponds to about 3 degree of the RF field phase upstream the first BC. ACC39 linearises the RF field of the first accelerator module, such that an electron bunch, which is accelerated by ACC1 and ACC39, have a linear energy chirp, shown in Figure B.1.1.

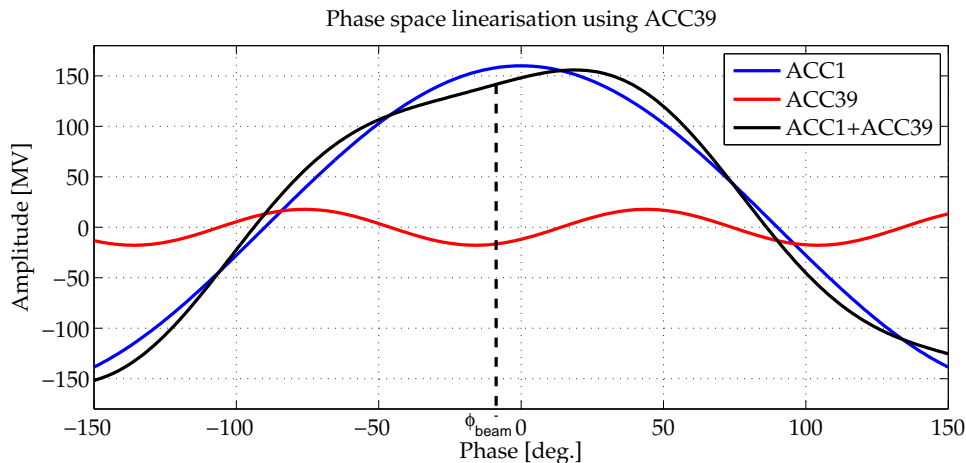


Figure B.1.1: Phase space linearisation at beam phase $\phi_{beam} = 8$ deg. corresponds to -8 deg. RF field phase for ACC1. ACC39 is operated as decelerating module with an RF field phase of 180 deg. $+ 3\phi_{beam}$, here -156 deg., and 1/9 lower amplitude than ACC1, see [Vogel et al., 2007].

All RF field phases are shifted w.r.t. the phase of ACC1. Assume a beam phase of 8 deg., i.e. an RF field phase of -8 deg. in ACC1; an usual off-crest operation. With an electron bunch length of 3 deg., the amplitude and phase must be linearised by ACC39 around $-8 \text{ deg.} \pm 1.5 \text{ deg.}$, visualized in Figure B.1.2 as centered black line, where Figure B.1.1 is zoomed into the region of interest.

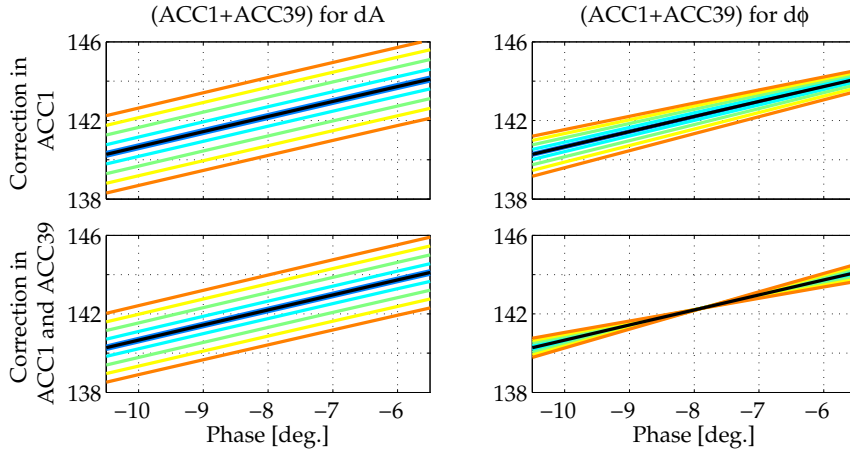


Figure B.1.2: Simulation of phase linearisation for corrections (from nominal setpoint) only in ACC1 (two upper subplots) or corrections in ACC1 and ACC39 (two subplots below). Here an amplitude correction up to $\pm 2 \text{ MV}$ (left side) and a phase correction up to $\pm 2 \text{ deg.}$ (right side) is assumed. The initial setpoint correction is in- and decreased in steps of ± 0.1 , ± 0.5 , ± 1.0 , ± 1.5 and ± 2.0

The colored lines are correction signals, either amplitude or phase corrections, which shows in the upper two subplots the effect of amplitude or phase changes by ACC1. In general, such amplitude or phase changes must be compensated by ACC39. Thus an information exchange between both modules is necessary, since changes of the phase of ACC1 (upper right subplot) leads to amplitude variations. If the module is able to exchange those phase corrections to the neighboring module, here ACC39, this amplitude change can be corrected, see lower right subplot. Consider Figure B.1.3, where the first derivative of each function is shown and compare the upper and lower two subplots. Amplitude variations caused by corrections of ACC1 lead to derivative changes, more precisely to bunch compression changes, if this is not corrected by ACC39. However, such an additional correction in ACC39 causes a higher sensitive to compression, i.e. a larger spread of the derivatives. Therefore, if the bunch compression is corrected, i.e. the slope of the amplitude is changed, the system is more sensitive to the performance of phase control. Hence, by using a beam-based feedback strategy which corrects simultaneously the RF field of ACC1 and ACC39 an information exchange between both modules is necessary.

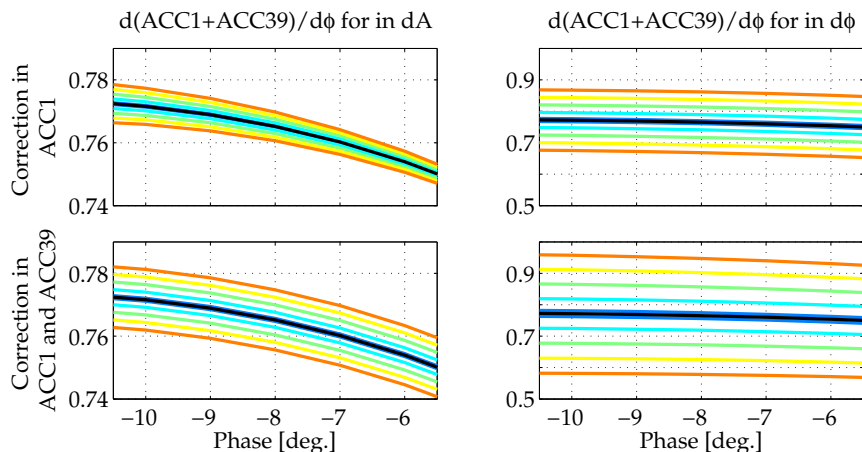


Figure B.1.3: First derivative of the functions given in Figure B.1.2 showing the sensitivity and linearity over the considered phase range.

B.2 Modeling the 3rd Harmonic RF Module

Using the developed SO(2) symmetric grey box structure, Section 3.1.2 on page 23, to identify the parameters of the mathematical model for the 3rd harmonic RF station, shows that a non-symmetric modeling approach facilitates the cross-validation. Hence, the SO(2) symmetric modeling procedure is extended to allow the parameter identification for slightly SO(2) symmetric disturbances.

Extension to symmetry disturbances

To identify also non-symmetric elements of the system, an example of adapting the input or output sub-matrices is given. For real eigenvalues, e.g. with representation given in (a.i) on page 24, the disturbed input matrix

$$\hat{\Gamma}_r = \begin{bmatrix} b_1 & -b_2 \\ k_2 b_2 & k_1 b_1 \end{bmatrix}, \quad (\text{B.2.1})$$

can be defined by introducing two variables k_1 and k_2 . In case for $k_1 = k_2 = 1$ the model is SO(2) symmetric again. The input sub-matrix of the high frequency behavior, e.g. for case (c.i), see page 26, is adapted to

$$\hat{\Gamma}_c = \begin{bmatrix} b_{11} & b_{12} & k_2 b_{21} & k_2 b_{22} \\ -b_{21} & -b_{22} & k_1 b_{11} & k_1 b_{12} \end{bmatrix}^T. \quad (\text{B.2.2})$$

An example of such a non-symmetry system is given by modeling the third harmonic RF station. The procedure, including data preconditioning and detrending follows from Section 3.1.3.

The plant model is shown in Figure B.2.1 and the cross-validation is presented in Figure B.2.2. Hereby, one has to consider that the identified model is a small signal model,

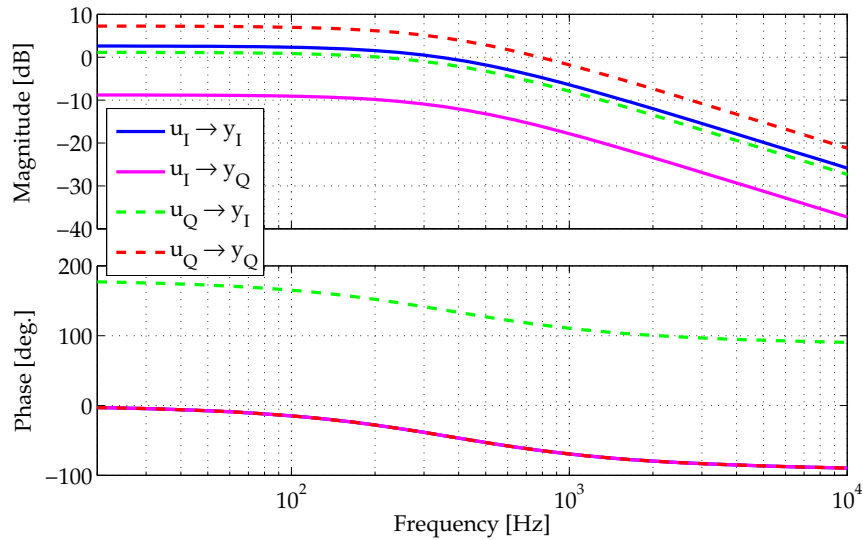


Figure B.2.1: Small signal model for ACC39; identified with the non-symmetric modeling approach.

hence it is valid around the operating point for a small excitation signal. It can be seen that a disturbance, i.e. the excitation signal itself, has a stronger effect on channel Q, since the drift of the error signal is much larger compared to channel I. The RF station was operated with a phase setpoint of 45 degree during the system identification, hence it is expected that the error variation is similar on both channels. Further studies which

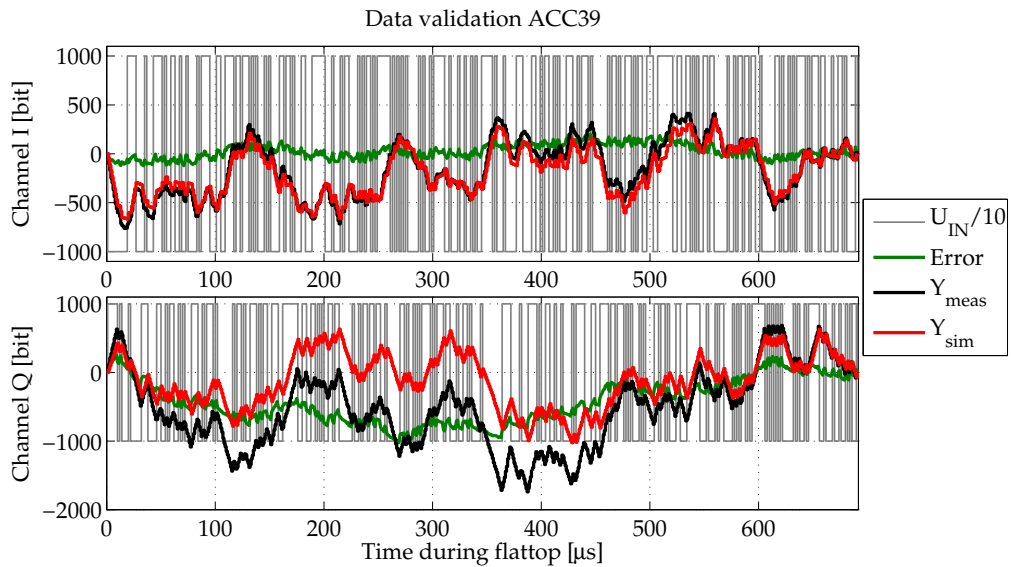


Figure B.2.2: Cross-validation for the measured and simulated system response of ACC39.

clarify the variation in error signal are necessary.

Appendix C

Iterative Learning Control - Proofs

In the following, extend the SISO dynamic scaling part $A_G(z)$ back to MIMO by multiplication with fixed rotation matrix $R(\phi_G)$ as $G(z) = A_G(z)R(\phi_G)$. The SISO discrete-time state space model of $A_G(z)$ is given as

$$\begin{aligned} x(t+1) &= \tilde{A}x(t) + \tilde{B}u(t) , \\ y(t) &= \tilde{C}x(t) \end{aligned} \quad (\text{C.0.1})$$

and mapped to a MIMO model by the Kronecker product of the input vector \tilde{B} with the rotation matrix $R(\phi_G)$ and a block-wise extension of the system and output matrix as

$$\begin{aligned} x(t+1) &= \overbrace{\begin{bmatrix} \tilde{A} & 0 \\ 0 & \tilde{A} \end{bmatrix}}^A x(t) + \tilde{B} \otimes \underbrace{\begin{bmatrix} \cos(\phi_G) & -\sin(\phi_G) \\ \sin(\phi_G) & \cos(\phi_G) \end{bmatrix}}_{R(\phi_G)} u(t) , \\ y(t) &= \underbrace{\begin{bmatrix} \tilde{C} & 0 \\ 0 & \tilde{C} \end{bmatrix}}_C x(t) . \end{aligned} \quad (\text{C.0.2})$$

Proof of Proposition 4.2.1

Proof. The proof is based on the ILC algorithm given in Section 4.2.1, page 66, and the ILC assumptions given on page 68. Lets assume $K(T) = \mathbf{0}$ and compute $K(T-1)$, which depends only on the output matrix C and the weighting Q . Since C is designed to be block diagonal and from the assumption that Q is block diagonal,

$$K(T-1) = C^T Q C = \begin{bmatrix} \tilde{K}(T-1) & 0 \\ 0 & \tilde{K}(T-1) \end{bmatrix}$$

is block diagonal. The second element $K(T-2)$ is computed from

$$\begin{aligned} K(T-2) &= A^T K(T-1)A + C^T Q C \\ &\quad - [A^T K(T-1)B(B^T K(T-1)B + R)^{-1} \cdot B^T K(T-1)A] . \end{aligned}$$

The matrix $K(T-2)$ is a summation of three matrices. The first term of the sum is block diagonal, since A and thus A^T and $K(T-1)$, which is the second term of the sum, are block diagonal. The third matrix is computed by

$$M_3 = -[A^T K(T-1)B(B^T K(T-1)B + R)^{-1} \cdot B^T K(T-1)A] .$$

Lets start with the inverse part of M_3 , i.e.

$$\widehat{M} = (B^T K(T-1)B + R)^{-1} .$$

The input matrix B is the Kronecker product of

$$B = \tilde{B} \otimes \begin{bmatrix} \cos(\phi_G) & -\sin(\phi_G) \\ \sin(\phi_G) & \cos(\phi_G) \end{bmatrix} = \begin{bmatrix} \tilde{B} \cos(\phi_G) & -\tilde{B} \sin(\phi_G) \\ \tilde{B} \sin(\phi_G) & \tilde{B} \cos(\phi_G) \end{bmatrix}$$

and the transpose of B is

$$B^T = \tilde{B}^T \otimes \begin{bmatrix} \cos(\phi_G) & -\sin(\phi_G) \\ \sin(\phi_G) & \cos(\phi_G) \end{bmatrix}^T = \begin{bmatrix} \tilde{B}^T \cos(\phi_G) & \tilde{B}^T \sin(\phi_G) \\ -\tilde{B}^T \sin(\phi_G) & \tilde{B}^T \cos(\phi_G) \end{bmatrix} .$$

Thus, \widehat{M} is computed by

$$\begin{aligned} \widehat{M} &= (B^T K(T-1)B + R)^{-1} \\ &= \left(\begin{bmatrix} \tilde{B}^T \cos(\phi_G) & \tilde{B}^T \sin(\phi_G) \\ -\tilde{B}^T \sin(\phi_G) & \tilde{B}^T \cos(\phi_G) \end{bmatrix} \begin{bmatrix} \widetilde{K}(T-1) & 0 \\ 0 & \widetilde{K}(T-1) \end{bmatrix} \right. \\ &\quad \left. \cdot \begin{bmatrix} \tilde{B} \cos(\phi_G) & -\tilde{B} \sin(\phi_G) \\ \tilde{B} \sin(\phi_G) & \tilde{B} \cos(\phi_G) \end{bmatrix} + \begin{bmatrix} \tilde{R} & 0 \\ 0 & \tilde{R} \end{bmatrix} \right)^{-1} \\ &= \begin{bmatrix} \tilde{B}^T \widetilde{K}(T-1) \tilde{B} + \tilde{R} & 0 \\ 0 & \tilde{B}^T \widetilde{K}(T-1) \tilde{B} + \tilde{R} \end{bmatrix}^{-1} \\ &= \begin{bmatrix} \widetilde{M}_{3,1}^{-1} & 0 \\ 0 & \widetilde{M}_{3,1}^{-1} \end{bmatrix} , \end{aligned} \tag{C.0.3}$$

which is block diagonal. It is straight forward to show, that the remaining part of $K(T-2)$ obtains the block diagonal structure, such that $K(t)$ is the sum of three block diagonal terms, which is block diagonal for SO(2) models with diagonal weighting matrices $R(t)$ and $Q(t)$ and a block diagonal output matrix C . If $K(T) \neq \mathbf{0}$, but block diagonal as given in assumptions on page 68, it is already shown above that $K(t)$ remains block diagonal. \square

Proof of Proposition 4.2.3

Proof. Lets focus first on the computation of

$$\alpha(t) = (I + K(t)BR^{-1}B^T)^{-1},$$

followed by the other matrices involved in the Norm Optimal ILC. First, consider the inner part

$$\begin{aligned} BR^{-1}B^T &= \left(\begin{bmatrix} \tilde{B} \cos(\phi_G) & -\tilde{B} \sin(\phi_G) \\ \tilde{B} \sin(\phi_G) & \tilde{B} \cos(\phi_G) \end{bmatrix} \begin{bmatrix} \tilde{R} & 0 \\ 0 & \tilde{R} \end{bmatrix}^{-1} \begin{bmatrix} \tilde{B}^T \cos(\phi_G) & \tilde{B}^T \sin(\phi_G) \\ -\tilde{B}^T \sin(\phi_G) & \tilde{B}^T \cos(\phi_G) \end{bmatrix} \right)^{-1} \\ &= \begin{bmatrix} \tilde{B}\tilde{R}^{-1}\tilde{B}^T & 0 \\ 0 & \tilde{B}\tilde{R}^{-1}\tilde{B}^T \end{bmatrix}. \end{aligned}$$

As seen in Proposition 4.2.1 on page 69, $K(t)$ is block diagonal, thus

$$\begin{aligned} \alpha(t) &= \begin{bmatrix} I + \tilde{K}(t)\tilde{B}\tilde{R}^{-1}\tilde{B}^T & 0 \\ 0 & I + \tilde{K}(t)\tilde{B}\tilde{R}^{-1}\tilde{B}^T \end{bmatrix}^{-1} \\ &= \begin{bmatrix} (I + \tilde{K}(t)\tilde{B}\tilde{R}^{-1}\tilde{B}^T)^{-1} & 0 \\ 0 & (I + \tilde{K}(t)\tilde{B}\tilde{R}^{-1}\tilde{B}^T)^{-1} \end{bmatrix} \end{aligned}$$

is block diagonal. Since the result of $\beta(t)$ and $\gamma(t)$ are multiplications by block diagonal matrices, $\beta(t)$ and $\gamma(t)$ remains block diagonal and are given by

$$\begin{aligned} \beta(t) &= \alpha(t)A^T = (I + \tilde{K}(t)\tilde{B}\tilde{R}^{-1}\tilde{B}^T)^{-1} \tilde{A}^T \otimes \begin{bmatrix} 1 & 0 \\ 0 & 1 \end{bmatrix} \text{ and} \\ \gamma(t) &= \alpha(t)C^T Q = (I + \tilde{K}(t)\tilde{B}\tilde{R}^{-1}\tilde{B}^T)^{-1} \tilde{C}^T \tilde{Q} \otimes \begin{bmatrix} 1 & 0 \\ 0 & 1 \end{bmatrix}. \end{aligned}$$

Next, consider the computation of $\lambda(t)$. Since the first factor was derived in (C.0.3), so substitute $K(T-1)$ by $K(t)$.

$$\begin{aligned} \lambda(t) &= (B^T K(t)B + R)^{-1} B^T K(t)A \\ &= \begin{bmatrix} \tilde{B}^T \tilde{K}(t) \tilde{B} + \tilde{R} & 0 \\ 0 & \tilde{B}^T \tilde{K}(t) \tilde{B} + \tilde{R} \end{bmatrix}^{-1} \begin{bmatrix} \tilde{B}^T \cos(\phi) & \tilde{B}^T \sin(\phi) \\ -\tilde{B}^T \sin(\phi) & \tilde{B}^T \cos(\phi) \end{bmatrix} \begin{bmatrix} \tilde{K}(t) & 0 \\ 0 & \tilde{K}(t) \end{bmatrix} \begin{bmatrix} \tilde{A} & 0 \\ 0 & \tilde{A} \end{bmatrix} \\ &= \begin{bmatrix} (\tilde{B}^T \tilde{K}(t) \tilde{B} + \tilde{R})^{-1} & 0 \\ 0 & (\tilde{B}^T \tilde{K}(t) \tilde{B} + \tilde{R})^{-1} \end{bmatrix} \\ &\quad \begin{bmatrix} \tilde{B}^T \cos(\phi_G) \tilde{K}(t) \tilde{A} & \tilde{B}^T \sin(\phi_G) \tilde{K}(t) \tilde{A} \\ -\tilde{B}^T \sin(\phi_G) \tilde{K}(t) \tilde{A} & \tilde{B}^T \cos(\phi_G) \tilde{K}(t) \tilde{A} \end{bmatrix} \\ &= (\tilde{B}^T \tilde{K}(t) \tilde{B} + \tilde{R})^{-1} \tilde{B}^T \tilde{K}(t) \tilde{A} \otimes \begin{bmatrix} \cos(\phi_G) & \sin(\phi_G) \\ -\sin(\phi_G) & \cos(\phi_G) \end{bmatrix} \\ &= (\tilde{B}^T \tilde{K}(t) \tilde{B} + \tilde{R})^{-1} \tilde{B}^T \tilde{K}(t) \tilde{A} \otimes R(\phi_G)^T. \end{aligned}$$

Obviously $\lambda(t)$ is a result of a multiplication by B^T and thus follows a SO(2) symmetry. The multiplication of the block diagonal matrix R^{-1} with a SO(2) symmetric matrix B^T results in a SO(2) symmetric matrix

$$\begin{aligned}\omega &= R^{-1}B^T = R^{-1} \begin{bmatrix} \tilde{B}^T \cos(\phi_G) & \tilde{B}^T \sin(\phi_G) \\ -\tilde{B}^T \sin(\phi_G) & \tilde{B}^T \cos(\phi_G) \end{bmatrix} = \tilde{R}^{-1}\tilde{B}^T \otimes \begin{bmatrix} \cos(\phi_G) & \sin(\phi_G) \\ -\sin(\phi_G) & \cos(\phi_G) \end{bmatrix} \\ &= \tilde{R}^{-1}\tilde{B}^T \otimes R(\phi_G)^T .\end{aligned}$$

□

Appendix D

Amplitude/Phase to I/Q Linearisation

The goal is to find a matrix \mathcal{M} which maps small amplitude and phase corrections to I/Q changes, where \mathcal{M} needs to be a matrix operation as

$$\begin{pmatrix} \Delta I \\ \Delta Q \end{pmatrix} = \underbrace{\begin{bmatrix} \mathcal{M}_{11} & \mathcal{M}_{12} \\ \mathcal{M}_{21} & \mathcal{M}_{22} \end{bmatrix}}_{\mathcal{M}} \cdot \begin{pmatrix} \Delta A \\ \Delta \phi \end{pmatrix} ,$$

which must be implementable on an FPGA.

Consider a complex vector field

$$x = A \cdot e^{i\phi} = A(\cos(\phi) + i \sin(\phi)) = A \cos(\phi) + iA \sin(\phi) = x_I + ix_Q , \quad (\text{D.0.1})$$

where a small correction Δx results in a new complex vector field

$$y = x + \Delta x = (A + \Delta A) \cdot e^{i(\phi + \Delta\phi)} = (A + \Delta A)(\cos(\phi) + i \sin(\phi))(\cos(\Delta\phi) + i \sin(\Delta\phi)) ,$$

in that ΔA and $\Delta\phi$ is an amplitude and phase correction, respectively. A separation of the real and imaginary part of y leads to

$$\begin{aligned} y_I &= A[\cos(\phi) \cos(\Delta\phi) - \sin(\phi) \sin(\Delta\phi)] + \Delta A[\cos(\phi) \cos(\Delta\phi) - \sin(\phi) \sin(\Delta\phi)] , \\ y_Q &= A[\cos(\phi) \sin(\Delta\phi) + \sin(\phi) \cos(\Delta\phi)] + \Delta A[\cos(\phi) \sin(\Delta\phi) + \sin(\phi) \cos(\Delta\phi)] . \end{aligned} \quad (\text{D.0.2})$$

With the assumption that $\Delta\phi$ is sufficiently small

$$\cos(\Delta\phi) \approx 1 \quad \text{and} \quad \sin(\Delta\phi) \approx \Delta\phi$$

holds. Hence, (D.0.2) for small corrections can be rewritten as

$$\begin{aligned} y_I &= A[\cos(\phi) - \sin(\phi)\Delta\phi] + \Delta A[\cos(\phi) - \sin(\phi)\Delta\phi] , \\ y_Q &= A[\cos(\phi)\Delta\phi + \sin(\phi)] + \Delta A[\cos(\phi)\Delta\phi + \sin(\phi)] , \end{aligned} \quad (\text{D.0.3})$$

and inserting $x_I = A \cos(\phi)$ and $x_Q = A \sin(\phi)$ from (D.0.1)

$$\begin{aligned} y_I &= \overbrace{x_I - x_Q \Delta\phi + \Delta A \cos(\phi) - \Delta A \sin(\phi) \Delta\phi}^{\Delta I = y_I - x_I} , \\ y_Q &= \overbrace{x_Q + x_I \Delta\phi + \Delta A \sin(\phi) + \Delta A \cos(\phi) \Delta\phi}^{\Delta Q = y_Q - x_Q} , \end{aligned} \quad (\text{D.0.4})$$

both equations are separable in initial vector x_I and x_Q and corrections ΔI and ΔQ . Assuming that $\Delta A \Delta\phi \ll \Delta A$ and $\Delta\phi$ allows to use a matrix operation which maps amplitude and phase corrections to I/Q changes by

$$\begin{pmatrix} \Delta I \\ \Delta Q \end{pmatrix} = \underbrace{\begin{pmatrix} \cos(\phi) & -x_Q \\ \sin(\phi) & x_I \end{pmatrix}}_{\mathcal{M}} \cdot \begin{pmatrix} \Delta A \\ \Delta\phi \end{pmatrix} ,$$

with x_I and x_Q as RF field setpoint.

Given is a second approach to determine the matrix \mathcal{M} by the total derivative of I and Q . The real and imaginary part of a complex vector, see (D.0.1), are given as

$$I = A \cos(\phi) \quad \text{and} \quad Q = A \sin(\phi) .$$

The total derivative of the functions I and Q are

$$dI = \frac{\partial I}{\partial A} dA + \frac{\partial I}{\partial \phi} d\phi \quad \text{and} \quad dQ = \frac{\partial Q}{\partial A} dA + \frac{\partial Q}{\partial \phi} d\phi ,$$

in matrix representation

$$\begin{bmatrix} \Delta I \\ \Delta Q \end{bmatrix} = \begin{bmatrix} dI \\ dQ \end{bmatrix} = \begin{bmatrix} \frac{\partial I}{\partial A} & \frac{\partial I}{\partial \phi} \\ \frac{\partial Q}{\partial A} & \frac{\partial Q}{\partial \phi} \end{bmatrix} \begin{bmatrix} dA \\ d\phi \end{bmatrix} = \begin{bmatrix} \frac{\partial I}{\partial A} & \frac{\partial I}{\partial \phi} \\ \frac{\partial Q}{\partial A} & \frac{\partial Q}{\partial \phi} \end{bmatrix} \begin{bmatrix} \Delta A \\ \Delta\phi \end{bmatrix} ,$$

with matrix elements

$$\begin{aligned} \frac{\partial I}{\partial A} &= \cos(\phi) & , & & \frac{\partial I}{\partial \phi} &= -A \sin(\phi) , \\ \frac{\partial Q}{\partial A} &= \sin(\phi) & , & & \frac{\partial Q}{\partial \phi} &= A \cos(\phi) , \end{aligned}$$

which are the elements of \mathcal{M} from the first approach.

Appendix E

Introduction to Distributed Control

During the last years, new strategies have been developed to synthesize controller for large scale interconnected systems, which are typically spatially distributed and separable in a chain of subsystems. These subsystems can be homogeneous and/or heterogeneous. In the following, only homogeneous subsystems are considered. A theoretical background in controlling a distributed system with non-identical subsystems is given in [Dullerud and D’Andrea, 2004]. The main purpose of considering an infinite chain of identical subsystems, which are interconnected, is to study the ability to synthesize an interconnected controller which is designed by a single subsystem and can be used to control the overall system chain. A short introduction based on [D’Andrea and Dullerud, 2003] is given in the following.

Assume a chain of identical subsystems with short hand notation $G(z, \mathbf{s}) = G_{\mathbf{s}}$ as depicted in Figure E.0.1, where each subsystem can be described by

$$\begin{bmatrix} x(k+1, \mathbf{s}) \\ w_+(k, \mathbf{s}) \\ w_-(k, \mathbf{s}) \\ z(k, \mathbf{s}) \\ y(k, \mathbf{s}) \end{bmatrix}_{x_0(\mathbf{s})} = \begin{bmatrix} A_{\mathbf{T}\mathbf{T}} & A_{\mathbf{T}\mathbf{S}} & B_{\mathbf{T},xd} & B_{\mathbf{T},xu} \\ A_{\mathbf{S}\mathbf{T}} & A_{\mathbf{S}\mathbf{S}} & B_{\mathbf{S},wd} & B_{\mathbf{S},wu} \\ C_{\mathbf{T},z} & C_{\mathbf{S},z} & D_{zd} & D_{zu} \\ C_{\mathbf{T},y} & C_{\mathbf{S},y} & D_{yd} & D_{yu} \end{bmatrix} \cdot \begin{bmatrix} x(k, \mathbf{s}) \\ v_+(k, \mathbf{s}) \\ v_-(k, \mathbf{s}) \\ d(k, \mathbf{s}) \\ u(k, \mathbf{s}) \end{bmatrix}, \quad (\text{E.0.1})$$

with an initial state $x(0, \mathbf{s}) = x_0(\mathbf{s})$; k and \mathbf{s} are discrete-time and spatial location, respectively.

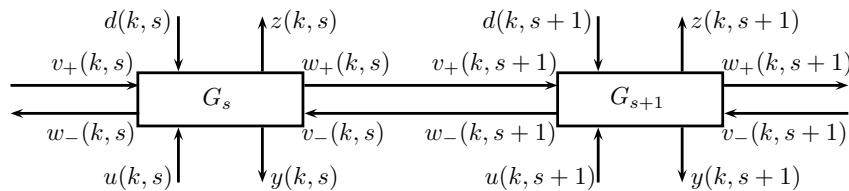


Figure E.0.1: Spatially interconnected system $G_{\mathbf{s}} = G(z, \mathbf{s})$ with a fictive input $d(k, \mathbf{s})$ and fictive output $z(k, \mathbf{s})$, the plant input $u(k, \mathbf{s})$ and plant output $y(k, \mathbf{s})$ and the interconnection $v(k, \mathbf{s})$ as input and $w(k, \mathbf{s})$ as output, respectively.

The interconnection of subsystems follows

$$\begin{aligned} v_+(k, \mathbf{s} + 1) &= w_+(k, \mathbf{s}) , \\ v_-(k, \mathbf{s} - 1) &= w_-(k, \mathbf{s}) , \end{aligned} \quad (\text{E.0.2})$$

where $v(k, \mathbf{s})$ is the input and $w(k, \mathbf{s})$ the output of the spatial interconnection to neighboring subsystem. Often the signals are considered at a fixed time. Thus it is convenient to separate the spatial (index \mathbf{S}) and temporal (index \mathbf{T}) parts of a signal [D'Andrea and Dullerud, 2003]. By using $\mathbf{m} = (m_0, m_+, m_-)$, in which m_0 is the number of internal temporal subsystem states $x(k, \mathbf{s})$, m_+ as size of interconnection variables $v_+(k, \mathbf{s})$ and m_- as size of interconnection variables $v_-(k, \mathbf{s})$ in positive and negative direction, respectively. The spatial shift operator is defined as

$$\Delta_{\mathbf{s}, \mathbf{m}} = \begin{bmatrix} \mathbf{S}I_{m_+} & 0 \\ 0 & \mathbf{S}^{-1}I_{m_-} \end{bmatrix} , \quad (\text{E.0.3})$$

such that the interconnection can be substituted as

$$(\Delta_{\mathbf{s}, \mathbf{m}}v(k))(\mathbf{s}) = w(k, \mathbf{s}) . \quad (\text{E.0.4})$$

By this, the interconnected system representation is given by

$$\begin{bmatrix} x(k+1, \mathbf{s}) \\ (\Delta_{\mathbf{s}, \mathbf{m}}v(k))(\mathbf{s}) \\ z(k, \mathbf{s}) \\ y(k, \mathbf{s}) \end{bmatrix}_{x_0(\mathbf{s})} = \begin{bmatrix} A_{\mathbf{T}\mathbf{T}} & A_{\mathbf{T}\mathbf{S}} & B_{\mathbf{T},xd} & B_{\mathbf{T},xu} \\ A_{\mathbf{S}\mathbf{T}} & A_{\mathbf{S}\mathbf{S}} & B_{\mathbf{S},wd} & B_{\mathbf{S},wu} \\ C_{\mathbf{T},z} & C_{\mathbf{S},z} & D_{zd} & D_{zu} \\ C_{\mathbf{T},y} & C_{\mathbf{S},y} & D_{yd} & D_{yu} \end{bmatrix} \cdot \begin{bmatrix} x(k, \mathbf{s}) \\ v(k, \mathbf{s}) \\ d(k, \mathbf{s}) \\ u(k, \mathbf{s}) \end{bmatrix} , \quad (\text{E.0.5})$$

for the subsystem $G(z, \mathbf{s})$. Furthermore, if and only if $(\Delta_{\mathbf{s}, \mathbf{m}} - A_{\mathbf{S}\mathbf{S}})$ is invertible in spatial domain, then the interconnected system is well-posed and hence itself stable, further details in [Langbort and D'Andrea, 2003] and [D'Andrea and Dullerud, 2003]. The proposed framework of spatially interconnected systems provides an efficient way of solving the controller synthesis problem for a large scale system with many subsystems, because it reduces the problem to solving a synthesis problem for a single unit with generalized plant model (E.0.5). Moreover, the synthesis problem can be solved by solving an LMI problem, for which efficient solvers are available. The resulting controller takes the form

$$\begin{bmatrix} x^K(k+1, \mathbf{s}) \\ \begin{bmatrix} w_+^K(k, \mathbf{s}) \\ w_-^K(k, \mathbf{s}) \end{bmatrix} \\ u(k, \mathbf{s}) \end{bmatrix} = \begin{bmatrix} A_{\mathbf{T}\mathbf{T}}^K & A_{\mathbf{T}\mathbf{S}}^K & B_{\mathbf{T}}^K \\ A_{\mathbf{S}\mathbf{T}}^K & A_{\mathbf{S}\mathbf{S}}^K & B_{\mathbf{S}}^K \\ C_{\mathbf{T}}^K & C_{\mathbf{S}}^K & D^K \end{bmatrix} \cdot \begin{bmatrix} x^K(k, \mathbf{s}) \\ \begin{bmatrix} v_+^K(k, \mathbf{s}) \\ v_-^K(k, \mathbf{s}) \end{bmatrix} \\ y(k, \mathbf{s}) \end{bmatrix} . \quad (\text{E.0.6})$$

The control design objective is to find a controller $C(z, \mathbf{s})$ such that the closed-loop system is well-posed, stable, and contractive, [D'Andrea and Dullerud, 2003]. The controller interconnection to neighboring controllers as well as the subsystems is depicted in Figure E.0.2.

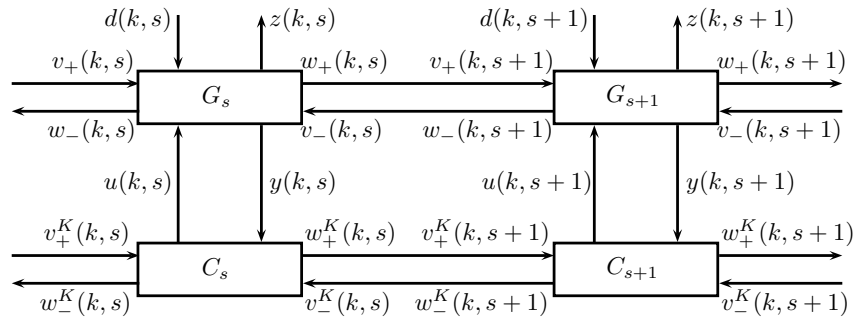


Figure E.0.2: Spatially interconnected system, where subsystem G_s is connected to the computed spatially interconnected controller $C_s = C(z, \mathbf{s})$ with the controller interconnections $v^K(k, \mathbf{s})$ as input and $w^K(k, \mathbf{s})$ as output in positive and negative direction, respectively.

Appendix F

Symbols and Abbreviations

Symbols

A, B, C, D, Φ, Γ	state-space matrices
$A_G(z)$	amplitude scaling part of transfer function matrix $G(z)$
$C(z)$	controller transfer function
E	energy
f_S, T_S	sampling frequency, sampling time
$G(z)$	transfer function of a plant
i	imaginary unit
K	proportional factor
$R(\phi_G)$	rotation matrix with rotation phase ϕ_G
R_L	shunt impedance
$R(t), Q(t)$	weighting matrices
Q, Q_L	quality factor, loaded quality factor
q	charge
T_d	time-delay
V	voltage
v, w	interconnected signals
$\Delta\omega, \Delta f$	detuning of the cavity
$\Delta A/A$	relative amplitude variation
$\Delta\phi$	absolute phase variation
Δt_A	bunch arrival time variation
ΔC	bunch compression variation
\mathbf{s}	spatial domain parameter
\mathbf{I}	identity matrix
$\text{Re}\{x\}$	real part of vector field x
$\text{Im}\{x\}$	imaginary part of vector field x
\mathbb{R}	set of real numbers
\mathbb{C}	set of complex numbers

ϵ	beam energy error
λ	eigenvalue
σ	standard deviation, also jitter or root mean square (rms)
ω_0	resonance frequency
$\omega_{1/2}$	system bandwidth ($\omega_{1/2} = \omega_0 - \omega$)
$\ G(z)\ _\infty$	H_∞ norm of $G(z)$ - system norm induced by signal two norm
\otimes	Kronecker product
\circ	vector outer product
σ_i	singular value i from a matrix

Subscripts

+	positive direction (beam flight direction)
-	negative direction
<i>acc</i>	acceleration
<i>ana</i>	analytical
<i>B</i>	beam
<i>C</i>	controller
<i>cl</i>	closed-loop
<i>corr</i>	correction
<i>F</i>	field
<i>f</i>	final
<i>FF</i>	feedforward
<i>I</i>	in-phase
<i>i</i>	initial
<i>ident</i>	identified
<i>Kly</i>	klystron
<i>meas</i>	measured
<i>Q</i>	quadrature
S	spatial domain
<i>sim</i>	simulated
<i>SP</i>	setpoint
T	temporal domain
<i>VM</i>	vector modulator

Superscripts

<i>E</i>	related to an energy
<i>F</i>	related to an RF Field
<i>K</i>	spatially interconnected controller
<i>T</i>	transpose

Abbreviations

ACCx	Accelerator module number x (FLASH)
A _x	Accelerator module number x (XFEL)
ADC	Analog-Digital Converter
BAM	Bunch Arrival Time Monitor
BBF	Beam-Based Feedback
BC	Bunch Compressor
BCM	Bunch Compression Monitor
DAC	Digital-Analog Converter
DESY	Deutsches Elektronen Synchrotron
EBPM	Energy Beam Position Monitor
FEL	Free-Electron Laser
FLASH	Free-Electron Laser in Hamburg
FPGA	Field Programmable Gate Array
FWHM	Full Width at Half-Maximum
HIFOO(d)	H-Infinity Fixed Order Optimization (in discrete-time)
HOM	Higher Order Mode
I	In-phase or real part of a complex vector field
IF	Intermediate Frequency
ILC	Iterative Learning Control
linac	linear accelerator
LLRF	Low Level Radio Frequency
LMI	Linear Matrix Inequality
LTI	Linear Time-Invariant
MIMO	Multi-Input Multi-Output
NO-ILC	Norm Optimal Iterative Learning Control
NO-T-ILC	Norm Optimal Tensor Iterative Learning Control
PRB	Pseudo Random Binary
Q	Quadrature or imaginary part of a complex vector field
RF	Radio Frequency
rms	root mean square
SASE	Self Amplified Spontaneous Emission
SISO	Single-Input Single-Output
SLAC	Stanford Linear Accelerator Center
SNR	Signal-to-Noise Ratio
SO(2)	Special Orthogonal group of dimension 2
TESLA	TeV-Energy Superconducting Linear Accelerator
MTCA	also MTCA.4, Micro Telecommunications Computing Architecture standard, [MTCA.4, 2013]
VME	Versa Module Eurocard standard
w/	with
w/o	without
w.r.t.	with respect to
XFEL	X-ray Free-Electron Laser

Bibliography

- Altarelli, M., Brinkmann, R., Chergui, M., Decking, W., Dobson, B., Düsterer, S., Grübel, G., Graeff, W., Graafsma, H., Hajdu, J., Marangos, J., Pflüger, J., Redlin, H., Riley, D., Robinson, I., Rossbach, J., Schwarz, A., Tiedtke, K., Tschentscher, T., Vartaniants, I., Wabnitz, H., Weise, H., Wichmann, R., Witte, K., Wolf, A., Wulff, M. and Yurkov, M. (2006). *XFEL, the European X-ray free-electron laser: Technical design report*. Hamburg: DESY XFEL Project Group. ISBN 978-3935702171.
- Amann, N., Owens, D. H. and Rogers, E. (1996). Iterative learning control for discrete-time systems with exponential rate of convergence. *IEE Proceedings Control Theory and Applications* **143**(2), 217–224.
- Baboi, N. (2001). *Studies on Higher Order Modes in Accelerating Structures for Linear Colliders*. Ph.D. thesis, University of Hamburg.
- Baboi, N. (2013). Personal Discussion.
- Barany, E. (2001). Identification in the presence of symmetry: oscillator networks. *Automatic Control, IEEE Transactions on* **46**(3), 476–481.
- Behrens, C., Nicoletti, D., Schmidt, B. and Wesch, S. (2010). Upgrade and Evaluation of the Bunch Compression Monitor at the Free-electron Laser in Hamburg (FLASH). In *1st International Particle Accelerator Conference*, pages 912–914.
- Bock, M. K. (2012). *Measuring the Electron Bunch Timing with Femtosecond Resolution at FLASH*. Ph.D. thesis, University of Hamburg.
- Branlard, J., Ayvazyan, V., Hensler, O., Schlarb, H., Schmidt, C., Walla, M., Cichalewski, W. and Jałmużna, W. (2012). LLRF Automation for the 9mA ILC Tests at FLASH. In *26th Linear Accelerator Conference*.
- Brinkmann, R., Faatz, B., Flöttmann, K., Rossbach, J., Schneider, J. R., Schulte-Schrepping, H., Trines, D., Tschentscher, T. and Weise, H. (2002). *TESLA XFEL: First Stage of the X-Ray Laser Laboratory, Technical Design Report, supplement*.
- Bristow, D. A., Tharayil, M. and Alleyne, A. G. (2006). A survey of iterative learning control, A learning-based method for high-performance tracking control. *IEEE Control Systems* **26**(3), 96–114.

- Brown, K. L.** (1975). *A First- and Second-Order Matrix Theory for the Design of Beam Transport Systems and Charged Particle Spectrometers*. SLAC Report 75.
- Cichalewski, W. and Koseda, B.** (2007). Characterization and compensation for nonlinearities of high-power amplifiers used on the FLASH and XFEL accelerators. *Measurement Science and Technology* **18**(8), 2372–2378.
- D’Andrea, R.** (1999). Software for modeling, analysis, and control design for multidimensional systems. In *Proceedings of the IEEE International Symposium on Computer Aided Control System Design*, pages 24–27.
- D’Andrea, R. and Dullerud, G. E.** (2003). Distributed control design for spatially interconnected systems. *IEEE Transactions on Automatic Control* **48**(9), 1478–1495.
- Deacon, D., Elias, L. R., Madey, J. M., Ramian, G., Schwettmann, H. A. and Smith, T. I.** (1977). First Operation of a Free-Electron Laser. *Physical Review Letters* **38**(16), 892–894.
- Dullerud, G. E. and D’Andrea, R.** (2004). Distributed control of heterogeneous systems. *Automatic Control, IEEE Transactions on* **49**(12), 2113–2128.
- Edwards, H., Behrens, C. and Harms, E.** (2010). 3.9 GHz Cavity Module for Linear Bunch Compression at FLASH. In *25th International Linear Accelerator Conference, LINAC10*.
- Eichler, A., Hoffmann, C. and Werner, H.** (2013). Robust Stability Analysis of Interconnected Systems with Uncertain Time-Varying Time Delays via IQCs. In *Proceedings of the 52th IEEE Conference on Decision and Control*.
- Elias, L. R., Fairbank, W. M., Madey, J. M., Schwettmann, H. A. and Smith, T. I.** (1976). Observation of Stimulated Emission of Radiation by Relativistic Electrons in a Spatially Periodic Transverse Magnetic Field. *Physical Review Letters* **36**(13), 717–720.
- Fagnani, F. and Willems, J. C.** (1991). Representations of symmetric linear dynamical systems. In *Proceedings of the 30th IEEE Conference on Decision and Control*, pages 17–18.
- FEL Beam Dynamics Group** (2013). XFEL Lattice Definition Version 8.3. Online: <http://www.desy.de/xfel-beam/index.html>.
- FLASH** (2013). Free-electron laser FLASH. Online: <http://flash.desy.de/>.
- Gdaniec, P.** (2010). *Grey-Box Identification and advanced Learning Feedforward Controller Design Methods for Free Electron Lasers*. Masters Thesis, TU Hamburg-Harburg, Institute of Control Systems.
- Gerth, C., Ludwig, F. and Schmidt, C.** (2009). Beam Based Measurements of the RF Amplitude Stability at FLASH using a Synchrotron Radiation Monitor. In *9th European Workshop on Beam Diagnostics and Instrumentation for Particle Accelerators*.

- Gilmore, R.** (1974). *Lie groups, Lie algebras and some of their applications*. New York: Wiley. ISBN 0471301795.
- Haber, A., Franjee, P. R. and Verhaegen, M.** (2011). Fast and Robust Iterative Learning Control for Lifted Systems. In *Proceedings of the 18th IFAC World Conference*, pages 3617–3622.
- Hacker, K.** (2010). *Measuring the Electron Beam Energy in a Magnetic Bunch Compressor*. Ph.D. thesis, Hamburg University.
- Hitchcock, F. L.** (1927). The expression of a tensor or a polyadic as a sum of products. *Journal of Mathematics and Physics* **6**, 164–189.
- Hoffmann, M.** (2008). *Development of a Multichannel RF Field Detector for the Low-Level RF Control of the Free-Electron Laser at Hamburg*. Ph.D. thesis, TU Hamburg-Harburg.
- ILC** (2013). International Linear Collider. Online: <http://www.linearcollider.org/ILC>.
- Ising, G.** (1925). Prinzip einer Methode zur Herstellung von Kanalstrahlen hoher Voltzahl. *Arkiv för matematik, astronomi och fysik* **18**(30).
- Jugo, J. and Arredondo, I.** (2005). Analysis and control design of MIMO systems based on symmetry properties. In *Proceedings of the 44th IEEE Conference on Decision and Control and European Control Conference. CDC-ECC '05*, pages 6887–6892.
- Kirchhoff, S., Schmidt, C., Lichtenberg, G. and Werner, H.** (2008). An iterative learning algorithm for control of an accelerator based Free Electron Laser. In *Proceedings of the 47th IEEE Conference on Decision and Control*, pages 3032–3037.
- Kolda, T. G. and Bader, B. W.** (2009). Tensor Decompositions and Applications. *SIAM Review* **51**(3), 455–500.
- Koprek, W., Behrens, C., Bock, M. K., Felber, M., Gessler, P., Schlarb, H., Schmidt, C., Schulz, S., Steffen, B., Szewiński, J. and Wesch, S.** (2010). Intra-train Longitudinal Feedback for Beam Stabilization at FLASH. In *32nd International Free Electron Laser Conference*.
- Kruskal, J. B.** (1989). *Rank, Decomposition, and Uniqueness for 3-Way and N-Way Arrays*. In *Multiway Data Analysis*, R. Coppi and S. Bolasco (Eds.), North-Holland. ISBN 0-444-87410-0.
- Langbort, C. and D’Andrea, R.** (2003). Imposing boundary conditions for a class of spatially-interconnected systems. In *Proceedings of the American Control Conference*, pages 107–112.
- Langkowski, H.** (2008). *Fixed-Order H_∞ Controller Design for the Free Electron Laser FLASH*. Diplomarbeit, TU Hamburg-Harburg, Institute of Control Systems.

- Ljung, L.** (1999). *System Identification, Theory for the User*. Prentice-Hall Inc. USA, 2 edition. ISBN 0-13-656695-2.
- Löhl, F.** (2009). *Optical Synchronization of a Free-Electron Laser with Femtosecond Precision*. Ph.D. thesis, University of Hamburg.
- Madey, J. M.** (1971). Stimulated Emission of Bremsstrahlung in a Periodic Magnetic Field. *Journal of Applied Physics* **42**(5), 1906–1913.
- Mavrič, U., Felber, M., Gerth, C., Schlarb, H., Jałmużna, W. and Piotrowski, A.** (2012). Preliminary Measurement Results of the Upgraded Energy BPM at FLASH. In *Proceedings of the 3rd International Particle Accelerator Conference*.
- MTCA.4** (2013). MTCA.4 for Industry and Research. Online: <http://mtca.desy.de>.
- Pfeiffer, S., Bock, M. K., Schlarb, H., Schmidt, C., Lichtenberg, G., Werner, H. and Jałmużna, W.** (2012a). Fast Feedback Strategies for Longitudinal Beam Stabilization. In *Proceedings of the 3rd International Particle Accelerator Conference*, pages 26–28.
- Pfeiffer, S. and Lichtenberg, G.** (2013). Iterative Learning Control for SO(2) Symmetric Systems. In *11th IFAC International Workshop on Adaptation and Learning in Control and Signal Processing*, pages 158–163.
- Pfeiffer, S., Lichtenberg, G., Schmidt, C. and Schlarb, H.** (2012b). Tensor Techniques for Iterative Learning Control of a Free-Electron Laser. In *Proceedings of the 2012 IEEE Multi-Conference on Systems and Control*, pages 160–165.
- Pfeiffer, S., Lichtenberg, G., Schmidt, C., Schlarb, H. and Werner, H.** (2012c). Design of an Optimal and Robust Controller for a Free-Electron Laser Exploiting Symmetries of the RF-System. In *Proceedings of the 51th IEEE Conference on Decision and Control*, pages 4253–4258.
- Pfeiffer, S., Schmidt, C., Lichtenberg, G. and Werner, H.** (2011). Grey Box Identification for the Free Electron Laser FLASH exploiting Symmetries of the RF-System. In *Proceedings of the 18th IFAC World Congress*, pages 10770–10775.
- Pfeiffer, S., Werner, H., Schmidt, C. and Schlarb, H.** (2013). Distributed Controller Design for a Free-Electron Laser. In *Proceedings of the American Control Conference*, pages 6553–6558.
- Photon Science DESY** (2013). Photon Science DESY. Online: http://photon-science.desy.de/facilities/flash/facility_information/.
- Popov, A. P., Werner, H. and Millstone, M.** (2010). Fixed-structure discrete-time Hinf controller synthesis with HIFOO. In *Proceedings of the 49th IEEE Conference on Decision and Control*, pages 3152–3155.

- Przygoda, K., Poźniak, T., Napieralski, A. and Grecki, M.** (2010). Piezo control for Lorenz Force detuned SC cavities of DESY FLASH. In *1st International Particle Accelerator Conference*.
- Ratcliffe, J. D., Lewin, P. L., Rogers, E., Hatonen, J. J. and Owens, D. H.** (2006). Norm-optimal iterative learning control applied to gantry robots for automation applications. *IEEE Transactions on Robotics* **22**(6), 1303–1307.
- Rogers, E., Owens, D. H., Werner, H., Freeman, C. T., Lewin, P. L., Kichhoff, S., Schmidt, C. and Lichtenberg, G.** (2010). Norm-Optimal Iterative Learning Control with Application to Problems in Accelerator-Based Free Electron Lasers and Rehabilitation Robotics. *European Journal of Control* **16**(5), 497–522.
- Schilcher, T.** (1998). *Vector sum control of pulsed accelerating fields in lorentz forced force detuned superconducting cavities*. Ph.D. thesis, Hamburg University.
- Schmidt, C.** (2010). *RF System Modeling and Controller Design for the European XFEL*. Ph.D. thesis, Hamburg University of Technology.
- Schmidt, C., Pfeiffer, S., Branlard, J., Schlarb, H. and Jałmużna, W.** (2012). Precision Regulation of RF Fields with MIMO Controllers and Cavity-based Notch Filters. In *26th Linear Accelerator Conference*.
- Schmüser, P., Dohlus, M. and Rossbach, J.** (2008). *Ultraviolet and Soft X-Ray Free-Electron Lasers: Introduction to Physical Principles, Experimental Results, Technological Challenges*, volume 229 of *Springer Tracts in Modern Physics*. Berlin and Heidelberg: Springer-Verlag Berlin Heidelberg.
- Schulz, S., Czwalinna, M., Felber, M., Predki, P., Schefer, S., Schlarb, H. and Wegner, U.** (2013). Femtosecond-precision synchronization of the pump-probe optical laser for user experiments at FLASH. In *SPIE Optics + Optoelectronics*.
- Sepanski, M. R.** (2007). *Compact Lie Groups*. Graduate Texts in Mathematics. Springer. ISBN 0387302638.
- sFLASH** (2013). DESY - sFLASH - An experiment at FLASH for a seeded VUV-FEL. Online: <http://sflash.desy.de/>.
- Skogestad, S. and Postlethwaite, I.** (2005). *Multivariable feedback control: Analysis and design*. Chichester: Wiley, 2 edition. ISBN 9780470011676.
- Srinivasa Rao, K. N.** (1988). *The rotation and Lorentz groups and their representations for physicists*. New York: Wiley Eastern. ISBN 0470210443.
- Stulle, F.** (2004). *A Bunch Compressor for small Emittances and high Peak Currents at the VUV Free-Electron Laser*. Ph.D. thesis, University of Hamburg.
- Towiwat, T.** (2011). *An Approach of Distributed Control for the European XFEL-Project*. Masters Thesis, TU Hamburg-Harburg, Institute of Control Systems.

- Vogel, E.** (2007). High gain proportional rf control stability at TESLA cavities. *Physical Review Special Topics - Accelerators and Beams* **10**.
- Vogel, E.** (2013). Personal Discussion.
- Vogel, E., Albrecht, C., Baboi, N. and et al.** (2010). Test and Commissioning of the Third Harmonic RF System for FLASH. In *1st International Particle Accelerator Conference*.
- Vogel, E., Dohlus, M., Edwards, H., Harms, E., Huening, M., Jensch, K. and Khabiboulline, T.** (2007). Considerations on the Third Harmonic RF of the European XFEL. In *13th International Workshop on RF Superconductivity*.
- Wangler, T. P.** (1998). *Principles RF Linear Accelerators*. Weinheim and Germany: Wiley-VCH Verlag GmbH. ISBN 9783527618408.
- Wesch, S.** (2012). *Echtzeitbestimmung longitudinaler Elektronenstrahlparameter mittels absoluter Intensitäts- und Spektralmessung einzelner kohärenter THz Strahlungspulse*. Ph.D. thesis, University of Hamburg.
- Wideröe, R.** (1928). Über ein neues Prinzip zur Herstellung hoher Spannungen. *Archiv für Elektrotechnik* **21**(4), 387–406.
- XFEL** (2013). European XFEL. Online: <http://www.xfel.eu>.

Lebenslauf

Persönliche Daten

Name	Pfeiffer
Vorname	Sven
Geburtsdatum	18.02.1979
Geburtsort, -land	Finsterwalde, Deutschland

Schulausbildung

09/1985 - 06/1989	Grundschule Lugau
09/1989 - 06/1995	Gesamtschule Doberlug-Kirchhain
08/1995 - 06/1998	Sängerstadt-Gymnasium Finsterwalde
06/1998	Abitur

Wehrdienst

07/1998 - 04/1999	Grundwehrdienst Fallschirmjägerbataillon in Doberlug-Kirchhain
-------------------	---

Ausbildung

09/1999 - 01/2003	Ausbildung zum Energieelektroniker Fachrichtung Betriebstechnik FELS WERKE GmbH, NL Hennersdorf
-------------------	---

Hochschulstudium

10/2004 - 04/2010	Technische Universität Hamburg-Harburg Studiengang Elektrotechnik Vertiefungsrichtung Mess-, Steuerungs- und Regelungstechnik
-------------------	---

Beruflicher Werdegang

05/2003 - 05/2004	Elektroniker für Betriebstechnik, Schönborner Armaturen GmbH
06/2004 - 09/2004	Energieelektroniker - Betriebstechnik, Vedior Personaldienstleistungen
06/2005 - 11/2005	Studentische Hilfskraft, Technologiezentrum Hamburg-Finkenwerder, Institut für Flugzeug-Systemtechnik
05/2010 - 05/2013	Wissenschaftliche Hilfskraft mit Hochschulabschluss zum Zwecke der Vorbereitung auf die Promotion, Deutsches Elektronen-Synchrotron in Hamburg
seit 05/2013	Wissenschaftlicher Mitarbeiter, Deutsches Elektronen-Synchrotron in Hamburg